

PHOSPHORESCENCE QUENCHING STUDIES OF ZINC SUBSTITUTED
HEME-PROTEINS AND NOVEL APPLICATIONS OF A WATER SOLUBLE
HEMICARCERAND IN BIOCHEMISTRY

by

KATARZYNA IZABELA JANKOWSKA

A Dissertation submitted to the

Graduate School-Newark

Rutgers, The State University of New Jersey

in partial fulfillment of the requirements

for the degree of

Doctor of Philosophy

Graduate Program in Chemistry

written under the direction of

Professor Piotr Piotrowiak

and approved by

Newark, New Jersey

October, 2012

ABSTRACT OF THE DISSERTATION

PHOSPHORESCENCE QUENCHING STUDIES OF ZINC SUBSTITUTED HEME-PROTEINS AND NOVEL APPLICATIONS OF A WATER SOLUBLE HEMICARCERAND IN BIOCHEMISTRY

By KATARZYNA IZABELA JANKOWSKA

Dissertation Director:
Professor Piotr Piotrowiak

Electron transfer (ET) reactions play a crucial role in biological systems. They occur at critical steps of numerous metabolic pathways and are studied in a variety of ways. One of the methods involves photoinduced ET investigation of chemically modified proteins, which are labeled or transformed to be photoactive. The most popular class of redox active proteins which allow modifications facilitating the study of ET reactions are heme proteins such as cytochromes. Their properties include colored prosthetic groups, varied oxidation states, and diverse biological functions which have provided a rich and fertile ground for study by chemists, biophysicists and biologists. The native iron-containing heme dissipates the excitation energy through rapid radiationless transitions which lead to extremely short excited state lifetimes in the femtosecond range. The replacement of iron by diamagnetic zinc at the porphyrin center dramatically changes the photophysics of the enzyme. Proteins containing zinc porphyrins exhibit both fluorescence and long lived phosphorescence. Thanks to their emissive nature, they are

amenable to highly sensitive single photon counting techniques, which permit kinetic studies over a very broad range of concentrations and time scales.

A large part of the research reported here has focused on examining intermolecular interactions in zinc substituted heme proteins probed by phosphorescence quenching. First, photoinduced ET reactions between zinc substituted cytochrome P450_{cam} (ZnP450) and small organic compounds capable of accessing the protein's hydrophobic channel and binding close to active site in a fashion that mimics its native substrate, camphor, were investigated. The heme – to - zinc protoporphyrin exchange revealed the existence of two conformers of the substituted protein (F420 and F450) which exhibited different photochemical and photophysical properties. The ET behavior of form F420 suggests that hydrophobic redox-active ligands are able to penetrate the hydrophobic channel and locate themselves in the direct vicinity of the Zn-porphyrin. In contrast, the slower ET quenching rates observed in the case of F450 indicate that the association is weak and occurs outside of the protein channel. Therefore, we conclude that form F420 corresponds to the open structure of the native cytochrome P450_{cam}, while form F450 has a closed or partially closed channel that is characteristic of the camphor-containing cytochrome P450_{cam}.

Both forms of ZnP450 were examined in the presence of ligands possessing long aliphatic chains to explore electron and energy transfer processes in those systems. The triplet state lifetime of form F420 decreases in all studied cases, while the emission of ³F450 remains unchanged in the presence of the selected ligands. The ET and TT rates obtained from ³F420 quenching allowed the calculation of the separation between the Zn-center and quenchers. The estimated D-A distances are consistent with those previously

obtained from X-ray structures of native cytochrome P450 and imply ligation close to the active center. Moreover, similarly as in native P450, quenchers with a hydrophobic tether induce conformational changes in ZnP450. These data show that ZnP450 mimics the behavior of the native enzyme and can be used to study protein - ligand and protein - protein interactions.

In the second part of this thesis a water soluble octacarboxyhemicarcerand was used as a shuttle to transport redox-active substrates across the aqueous medium and deliver them to the target protein. Hydrophobic electron donors and acceptors were encapsulated within the hemicarcerand, and photoinduced electron transfer between the Zn-substituted cytochrome *c* and the host-guest complexes was used to probe the association between the negatively charged hemicarceplex and the positively charged protein. ET mediated by the protein-bound hemicarcerand is much faster than that due to diffusional encounters with the respective free donor or acceptor in solution. The results show that the hemicarcerand is capable of exhibiting ‘induced fit’ behavior characteristic of protein-protein interactions. The kinetic behavior of these systems depends on the relative strength of the protein-hemicarcerand and guest-hemicarcerand interactions. When $K_{\text{encaps}} \gg K_{\text{assoc}}$, the hemicarcerand transports the ligand to the protein while protecting it from the aqueous medium. But if $K_{\text{assoc}} > K_{\text{encaps}}$ the docked cage can act as an artificial receptor.

In addition, the water soluble Cram-type hemicarcerand has been used as a gas capture device. This project involved encapsulation studies of hydrophobic gases such as sulfur hexafluoride or butane. The interactions between the guest and the host were probed by 1D relaxation and 2D NOESY experiments. The host:guest complex in a ratio

of 1:1 was the dominant form for both studied gases, however additional NMR signals in the case of butane suggest imprisonment of two guests. The encapsulation of the second molecule is possible thanks to structural flexibility of a hemicarcerand, which can adapt to the guest. Furthermore, the fundamental question of the gas-like vs. liquid like behavior of the guest(s) in the inner phase environment of the hemicarcerand has been addressed. Our observations imply liquid like behavior for the 1:1 host: guest complex and solid-like behavior for the 1:2 host: butane complex, thus agreeing with Cram's conjecture that the cage interior can be designed to be vacuum-like, liquid-like, or even solid-like depending on the fraction of the space occupied by the guest(s).

The presented work not only contributes new knowledge about photoinduced electron and energy transfer reactions in proteins but also introduces interesting materials for bio-sensing, biomedical or biocatalytic applications.

Acknowledgements

I would like to express my utmost gratitude to my Advisor, Prof. Piotr Piotrowiak for giving me an opportunity to pursue my doctoral study in his group. I would also like to thank him for helpful support, guidance, patience and encouragement throughout my PhD studies. It has truly been a great and enjoyable experience, one which I will never forget.

I would like to thank Prof. Frank Jordan, Prof. Richard Mendelsohn from Dept. of Chemistry, Rutgers University, Newark, NJ and Prof. Ralf Warmuth from Dept. of Chemistry & Chemical Biology at Rutgers University, New Brunswick, NJ for readily agreeing to be on my committee, their time devoted on reading and correcting my thesis and their helpful advice and encouragement.

I would like to thank Dr Lazaros Kakalis for time and assistance in NMR measurements, Dr Lars Gundlach who provided valuable help with time-resolved spectroscopy and data analysis and Dr Cynthia Pagba for time in teaching me protein substitution.

I also thank my professors who taught me throughout my graduate program.

I am grateful to all current and former members in Prof. Piotrowiak group for their relentless support and most of all your friendship. I have thoroughly enjoyed my time here. In addition, I would also like to thank all the staffs of Chemistry Department for their assistance.

Finally, I am very grateful to my family and friends for their continuous support and encouragements.

This work wouldn't have been possible without you all.

Table of Contents

ABSTRACT OF THE DISSERTATION	II
ACKNOWLEDGEMENTS	VI
TABLE OF CONTENTS	VII
LIST OF ABBREVIATIONS	IX
LIST OF TABLES.....	XIV
LIST OF ILLUSTRATIONS	XV
LIST OF APPENDICES	XXII
CHAPTER 1. INTRODUCTION.....	1
1.1 PORPHYRIN	2
1.2 METALLOPORPHYRINS AND HEME PROTEINS.....	5
<i>Zinc porphyrins</i>	8
<i>Iron to zinc substitution</i>	9
1.3 PHOTOCHEMISTRY	10
1.4 ELECTRON TRANSFER.....	12
<i>Marcus Theory</i>	15
1.5 ENERGY TRANSFER.....	18
<i>Förster resonance energy transfer</i>	19
<i>Triplet-triplet energy transfer</i>	21
1.6 TRANSFER MECHANISMS	23
1.7 REFERENCES I	27
CHAPTER 2. PHOSPHORESCENCE QUENCHING STUDIES OF ZINC SUBSTITUTED CYTOCHROME P450.....	31
2.1 MATERIALS AND METHODS	41
<i>Materials: The e</i>	41
<i>Expression and Purification</i>	42
<i>The Zn-Substitution of Cytochrome P450_{cam}:</i>	42
<i>Sample preparation for ET studies:</i>	44
<i>Instrumentation and spectroscopic methods:</i>	45
<i>Data analysis and MO calculations:</i>	48
2.2 RESULTS AND DISCUSSION	49
<i>Spectroscopic characterization of ZnP450</i>	49
<i>Electron transfer reaction between ZnP450 and small organic ligands</i>	56
<i>Bidirectional photoinduced electron transfer studies of zinc substituted cytochrome P450_{cam} with tethered ligands</i>	62
<i>Triplet - triplet energy transfer reactions of zinc substituted cytochrome P450_{cam}</i>	72
2.3 CONCLUSIONS	79
2.4 REFERENCES II.....	82
CHAPTER 3. ELECTROSTATIC DOCKING OF A SUPRAMOLECULAR HOST-GUEST ASSEMBLY TO CYTOCHROME C PROBED BY BIDIRECTIONAL PHOTOINDUCED ELECTRON TRANSFER	86

3.1 MATERIALS AND METHODS	95
<i>Materials</i>	95
<i>Zinc-substitution of cytochrome c</i>	95
<i>Guest encapsulation and binding to the protein</i>	98
<i>Photophysical properties</i>	98
<i>Data analysis</i>	99
3.2 RESULTS AND DISCUSSION	100
<i>Electrostatic association between Zn-cytochrome c and the hemicarcerand</i>	100
<i>Photoinduced electron transfer between Zn-cytochrome c and the encapsulated guests</i>	104
<i>The binding site</i>	115
3.3 CONCLUSIONS	123
3.4 REFERENCES III	125
CHAPTER 4. GAS TRAPPING INSIDE THE WATER SOLUBLE CRAM-TYPE HEMICARCERAND.	131
4.1 MATERIALS AND METHODS	136
<i>Materials:</i>	136
<i>Sample preparation and encapsulation:</i>	136
<i>Measurements</i>	137
<i>Data Analysis</i>	142
4.2 RESULTS AND DISCUSSION	143
<i>Butane encapsulation</i>	143
<i>SF₆ trapping</i>	154
4.3 CONCLUSIONS	158
4.4 REFERENCES IV	160
5. SUPPORTING INFORMATION	163
<i>Supporting information for chapter 2</i>	163
<i>Supporting information for chapter 3</i>	170
<i>Supporting information for chapter 4</i>	171
CURRICULUM VITAE	176

List of abbreviations

ϵ_0	the permittivity of vacuum
ϵ_{opt}	optical dielectric constant
ϵ_{static}	static dielectric constant
1D	one-dimensional
^1M	molecule in its first excited singlet state
2D	two-dimensional
^3M	molecule in its first excited triplet state
5chs	5-coordinated high-spin state
6cls	6-coordinated low-spin state
A	acceptor
A/D	analog-to-digital converter
Ab	absorption
AM1	Austin Model 1
APM	avalanche photodiode
Arg	L-arginine
Asp	L-aspartic acid
Az	azulene
bC	β carotene
BME	β -mercaptoethanol
BQ	benzoquinone
cage	water soluble Cram-type hemicarcerand
Cam	camphor
CC	cytochrome <i>c</i>
CD	circular dichroism
CHT	cycloheptatriene
Co2	coenzyme Q2
Co4	coenzyme Q4
COSY	correlation spectroscopy
CQ	chloranil
CYP101	cytochrome P450 _{cam}
Cys	L-cysteine

D	donor
D-A	donor- acceptor system
D-B-A	donor-bridge-acceptor system
DFT	density functional theory
DME	dimethyl ether
DMF	dimethylformamide
DMS	dimethyl sulfide
DPH	1,6-diphenyl-1,3,5-hexatriene
DPO	1,8-diphenyl-1,3,5,7-octatetraene
DQ	duroquinone
DTT	dithiothreitol
E	energy
E_c	crossover barrier
E^{ox}	oxidation potential
E^{red}	reduction potential
ET	electron transfer
F420	open form of zinc substituted cytochrome P450
F450	closed form of zinc substituted cytochrome P450
FC	and the Fran-Condon weighted density of states
Fc	ferrocene
$Fc(COOH)_2$	1,1'-ferrocenedicarboxylic acid
Fe(II)PPDME	protoporphyrin IX dimethyl ester
FePP	iron protoporphyrin IX
FeUP	iron uroporphyrin
Fl	fluorescence
FRET	Förster resonance energy transfer
FROG	frequency resolved optical gating
FTMA	11-ferrocenyltrimethylundecylammonium bromide
g_N	nuclear g factor
H_{AB}	electronic coupling
His	L-histidine
HOESY	heteronuclear Overhauser effect spectroscopy
HOMO	highest occupied molecular orbital
HPLC	high performance liquid chromatography

HS	high-spin species
I	transmitted intensity at a given wavelength,
I_0	intensity of the incident light at a given wavelength
Im	imidazole
IPTG	isopropyl β -D-1-thiogalactopyranoside
IR	infrared
ISC	intersystem crossing
J	donor acceptor spectral overlap in FRET
J	spin-spin splitting, J-coupling
k	reaction rate
K	specific orbital interactions such as overlap dependence on specific orientation of redox partners
K_a	association constants
K_{assoc}	association constant
k_B	Boltzmann constant
K_{encaps}	encapsulation constant
k_{ET}	electron transfer rate
k_{nr}	rate coefficient for non-radiative deexcitation
k_r	rate coefficient for radiative deexcitation
k_{TT}	triplet-triplet energy transfer rate
Leu	L-leucine
LS	low-spin species
LUMO	lowest unoccupied molecular orbital
M	molecule
M^*	electronically excited molecule
Mb	myoglobin
Met	L-metionine
MO	molecular orbital
MRI	magnetic resonance imaging
n	refractive index
NADH	nicotinamide adenine dinucleotide
N-MeIm-	N-methylimidazole
NMR	nuclear magnetic resonance
NOESY	nuclear Overhauser effect spectroscopy

NOPA	noncollinear optical parametric amplifier
oET	oxidative photoinduced ET
<i>P</i>	products
P450 _{cam}	cytochrome P450 cam
PAD	photodiode array detector
PC	computer
<i>PC</i>	packing coefficient
PCS	PCS-150 modules
PDB	protein data bank
Pdx	putidaredoxin
Ph	phosphorescence
Phe	L-phenylalanine
PL	photoluminescence
PMT	photomultiplier tubes
PP	protoporphyrin IX
ppm	parts-per-million
<i>R</i>	reactant
R	distance
R ₀	Förster radius
r _A	the effective radius of the acceptor
r _D	the effective radius of the donor
R _{DA}	donor-acceptor separation
ReA	retinal
rET	reductive photoinduced ET
RF	radio frequency
RH	substrate
S ₀	singlet state
<i>SS</i>	singlet-singlet
<i>T_l</i>	longitudinal (or spin-lattice) relaxation time
TMA	dodecyl trimethyl ammonium chloride
T _n	n-th triplet state
TOCSY	total correlation spectroscopy
TPPS	tetrakis(4-sulfonatophenyl) porphyrin
<i>TS</i>	triplet-singlet

TT	triplet-triplet
Tyr	L-tyrosine
UV	ultraviolet
UV-Vis	ultraviolet and visible radiation
Val	L-valine
Vis	visible
Zn(Meso-IX-DME)	mesoporphyrin IX dimethyl ester
ZnCC	Zn-substituted cytochrome <i>c</i>
ZnMb	Zn-substituted myoglobin
ZnOPE-	zinc octaethylporphyrin
ZnP	zinc porphyrin
ZnP450	zinc substituted cytochrome P450 _{cam}
ZnPP	zinc protoporphyrin IX
ZnTPP	zinc tetraphenylporphyrin
β	decay constant
γ	the magnetonic ratio
ΔA_b	absorption difference
ΔE	energy gap
Δe	the transferred charge
ΔG	Gibbs free energy
δ_i	chemical shift
$\Delta \nu_{1/2}$	line widths
κ^2	orientation factor
λ	reorganization energy
λ_i	vibrational/internal reorganization energy
λ_s	solvatational reorganization energy
ν_i	frequency
τ	lifetime
Φ	quantum yield

List of tables

Table 1. Selected absorption maxima of iron porphyrin and heme proteins.....	7
Table 2. Solvent and ligand effects on the zinc porphyrin spectrum.	8
Table 3. Instrument settings for Varian Cary Eclipse Fluorescence Spectrophotometer.....	46
Table 4. Absorption and emission maxima of zinc substituted heme proteins: F450 and F420 – the forms of zinc substituted cytochrome P450	52
Table 5. Triplet state decay rates and deuterium isotope effects measured for both forms of ZnP450 _{cam}	55
Table 6. The thermodynamic parameters and the measured electron transfer reaction rates of both forms of ³ ZnP450 _{cam}	57
Table 7. Normalized fluorescence intensity of forms F420 and F450 in the presence of quinones.	59
Table 8. Fluorescence lifetime of F420 and F450 estimated by fitting to convoluted reference sample (± 0.1ns) with single exponential functions.....	67
Table 9. Experimental rates, association constants, binding energies and thermodynamic parameters for the electron transfer reaction between ³ F420 and the quenchers: FTMA, CoQ2 and CoQ4.....	69
Table 10. Energy transfer rates (k_{TT}), ΔG°_{TT} and donor-acceptor separation (R_{DA}) for ³ F420 – triplet energy acceptor complexes.....	76
Table 11. Single exponential phosphorescence lifetime of zinc substituted cytochrome <i>c</i> in the presence and absence of empty hemicarcerand at different pH and room temperature.	102
Table 12. Experimental rates and thermodynamic parameters for the electron transfer reaction between ³ ZnCC and host-guest complexes as well as free donors and acceptors in solution.....	110
Table 13. Quenching rates in the presence of encapsulated ferrocene and 1,1’- ferrocenedicarboxylic acid at different pH and room temperature.....	114
Table 14. ¹ H longitudinal relaxation time for butane in the presence of cage.	152
Table 15. ¹ H longitudinal relaxation time for cage nuclei in the presence of butane.....	152
Table 16. Chemical shifts δ in the ¹⁹ F NMR and the ¹⁹ F longitudinal relaxation times for the SF ₆ in the absence and presence of cage.....	155

List of illustrations

Figure 1. Spectrum of electromagnetic radiation.	1
Figure 2. Structure of a free-base and metal porphyrin.	3
Figure 3. Absorbtion spectrum of zinc porphyrin (ZnPP).	4
Figure 4. Four-orbital model for porphyrin.	5
Figure 5. Structures of some natural hemes.	6
Figure 6. Metal-porphyrin substitution.	10
Figure 7. Jabłoński diagram.	10
Figure 8. Schematic representation for oxidative and reductive photoinduced electron transfer.	13
Figure 9. Schematic representation of free energy cross section of two electronic states in adiabatic and nonadiabatic reactions.	14
Figure 10. Driving force dependence of nonadiabatical ET rates predicted by the semiclassical Marcus theory.	17
Figure 11. Reactant – product potential energy surfaces for ET reactions.	18
Figure 12. Schematic representation of Förster resonance energy transfer.	19
Figure 13. Schematic representation of exchange energy transfer.	21
Figure 14. Two possible mechanisms for electron and triplet energy transfer reactions: single step tunneling from donor D to acceptor A with a reaction rate k_T (green path) or multistep hopping onto H with a reaction rate k_{H1} , from which the charge is transferred to A with the transfer rate k_{H2}	23
Figure 15. The distance dependences of the rates of single-step and two-step electron tunneling reactions at room temperatures.	26
Figure 16. Structure of cytochrome P450 _{cam} in the presence and absence of camphor: side and upper view. Molecular surface representation of P450 showing the open and closed conformation.	33
Figure 17. Edge-on and stereoscopic view of the the P450 _{cam} heme region bound to camphor with neighboring aliphatic and aromatic residues important for the protein-substrate hydrophobic contacts.	34

Figure 18. Model of the specific complex between Pdx and cytochrome P450 _{cam}	35
Figure 19. The catalytic cycle of cytochrome P450.	37
Figure 20. Electronic absorption spectra of ZnP450 and ferric P450 _{cam} . Inset: Circular dichroism obtained by Morishima <i>et al.</i>	38
Figure 21. The quenchers selected for the study of photoinduced electron transfer properties of ZnP450 _{cam}	39
Figure 22. Quenchers selected for the TT energy transfer study.....	41
Figure 23. HPLC system.....	43
Figure 24. UV-vis spectra of the HPLC fractions resulting from the protein substitution performed as described in the Material and Methods section.	44
Figure 25. Schematic diagram of UV-vis spectrometer and a spectrofluorometer.	46
Figure 26. Set-up for the time-resolved fluorescence experiments.	47
Figure 27. Absorption spectra of two fractions of zinc substituted cytochrome P450 _{cam} collected at different elution times. The fraction containing primarily form F420 is shown in blue, fraction containing form F450 in red.	50
Figure 28. Fluorescence and phosphorescence spectra of ZnP450 _{cam} fractions collected at different elution times. Emission spectra of fraction containing primarily form F420 excited at 420 nm are shown in blue, emission spectra of fraction containing form F450 excited at 450 nm is shown in red.	51
Figure 29. The triplet-state lifetimes measured on a 1:2 mixture of forms F420 and F450 of ZnP450 _{cam} excited at 420 nm and 450 nm and monitored at 590 nm and 768 nm, respectively. The amplitudes at $t = 0$ were normalized.....	52
Figure 30. HPLC results for ZnP450 substituted in the absence and presence of camphor.	54
Figure 31. Left: absorption spectrum of ZnP450 after equilibration for 3 hours in the presence and absence of camphor and K ⁺ ions. Right: F450 to F420 conversion upon binding with imidazole.	54
Figure 32. Normalized decay kinetics of ³ ZnP450 _{cam} in H ₂ O and D ₂ O solutions of 40 mM KPi, 0.1 M camphor, pH = pD = 7.4, excited at 420 and 450 nm.	55
Figure 33. Phosphorescence spectra and normalized decay profiles of ZnP450 in the presence of quinones excited at 420 and 450 nm at pH = 7. 4.	58

Figure 34. Changes in the appearance of the UV-Vis spectra upon addition of quinones to ZnP450.....	58
Figure 35. Fluorescence spectra of ZnP450 _{cam} excited at 420 nm and at 450 nm in aerated solution in the presence of quinones at pH=7.4.	59
Figure 36. The results of reductive quenching of the excited state of ZnP450 _{cam} in the presence of electron donors.	60
Figure 37. Protein absorption changes induced by the quenchers.....	62
Figure 38. The quenching results for ZnP450 _{cam} in the presence of tether ligands.....	63
Figure 39. Titration of ZnP450 by FTMA and TMA at pH = 7.4; absorption differences of ZnP450+FTMA and ZnP450 at 426 and 450 nm and the spectrum of ZnP450 after equilibration with 0.35 mM FTMA.....	64
Figure 40. Titration of FeP450 by FTMA and TMA at pH = 7.4, with 1 mM camphor or without camphor; absorption differences of FeP450 and FeP450+FTMA at 392 and 417 nm (lower row, left) and the spectrum of FeP450 with or without camphor, as well as in the presence of 0.4mM K ⁺ ions, pH=7.4.....	65
Figure 41. Normalized decay kinetics of ¹ F420, excited at 420 nm and emission monitored at 590 ±10 nm in the presence of quenchers.	66
Figure 42. Normalized emission decay profiles of 2×10 ⁻⁶ ZnP450 in the presence of FTMA, CoQ2 and CoQ4 when excited at 420 nm, with emission monitored at 590 nm and when excited at 450 nm and emission monitored at 768 nm at pH=7.4.....	67
Figure 43. Ligand association with ZnP450. Both forms F420 and F450 display the same conformation upon ligation with a tether-bearing partner.	68
Figure 44. Concentration dependence of electron transfer kinetics of ³ F420 with FTMA, CoQ2 and CoQ4 at pH=7.4. Ligand structures and the tether lengths are shown on the right.	68
Figure 45. The relevant molecular orbitals participating in the ET reactions with ZnP450: HOMO of FTMA and LUMO of CoQ2 and CoQ4.....	70
Figure 46. Proposed binding preferences of FTMA, coenzyme CoQ2 and coenzyme CoQ4 to ZnP450 deduced from the ET results.....	71
Figure 47. Energy levels of the triplet and singlet states of the selected acceptors and the F420 and F450 forms of ZnP450.....	72
Figure 48. TT energy transfer results for ³ F420.	73

Figure 49. Absorption differences of ZnP450+quencher subtracted from reference spectrum of ZnP450.....	74
Figure 50. Fluorescence spectra of ZnP450 excited at 420 and 450nm in the presence and absence of triplet energy acceptor.	74
Figure 51. Temperature dependent triplet energy transfer in the F420+Az complex.	75
Figure 52. Spin density distribution in retinal molecule; retinoic acid association inside the hydrophobic channel of cytochrome P450, PDB: 2VE3 and propose ligand association with ZnP450: DPO with its spin density inside the protein hydrophobic channel.	77
Figure 53. The logarithm of (V/V_0) versus donor- acceptor separation (R_{DA}).	78
Figure 54. Examples of host molecules: (A) resorcinarene, (B) knot, (C) cyclodextrin, (D) cucurbituril (D) hemicarcerands and polyimine capsules made from cavitands C^y , and di- (L^x) and triamines T.....	87
Figure 55. Cram-type water soluble hemicarcerand used in this study.	89
Figure 56. The X-ray structure of cytochrome <i>c</i> showing the basic lysine residues (blue) distributed on its surface (upper row) and the heme (red) axially ligated with histidine and methionine residues (orange) (PDB file:1AKK).	89
Figure 57. The mitochondrial electron-transport chain carried out by four inner membrane-associated enzyme complexes, cytochrome <i>c</i> and the mobile electron carrier ubiquinone (Q).	90
Figure 58. Left: Schematic planar projection of the front hemisphere of CC indicating the high affinity binding domain for cytochrome peroxidase (orange circle), cytochrome <i>c</i> oxidase (dark yellow) with some distances between the heme (red rectangular) and lysine residues involved in binding CC's partners (blue circle); Right: The structure of cytochrome <i>c</i> -cytochrome <i>c</i> ₁ complex determined by Lange and Hunte.	91
Figure 59. The encapsulated ligands: electron donors (ferrocene and ruthenocene), electron acceptor (duraquinone) and redox inactive guests (adamantane and naphthalene).	93
Figure 60. Schematic representation of: (1) encapsulation of the guest molecule within the hydrophobic cavity of octacarboxyhemicarcerand; (2) binding of the complete hemicarceplex to the target protein.....	94
Figure 61. UV-Vis spectrum monitored during the metal exchange in cytochrome <i>c</i>	96

Figure 62. UV-Vis spectrum of ZnCC and ZnCC+Cage with ratio 1:10 after purification and lyophilization, dissolved in phosphate buffer at pH = 7 to achieve the desired concentration.....	97
Figure 63. Homebuilt photon counting system with Cube 404 nm diode laser as a light source.....	98
Figure 64. Phosphorescence spectra and normalized decay profiles of ZnCC in the absence and presence of the empty hemicarcerand at pH = 7.....	102
Figure 65. Temperature dependence of the triplet lifetime of ZnCC in the absence and presence of the empty octacarboxyhemicarcerand at pH = 7 (a) and pH=9 (b).	103
Figure 66. Duroquinone encapsulated within the octacarboxyhemicarcerand.....	105
Figure 67. Room temperature kinetics of the incarceration of duroquinone (DQ).	107
Figure 68. Phosphorescence spectra and emission time profiles of cytochrome c with empty cage, encapsulated ferrocene and in the presence of ferrocene dicarboxylic acid at pH=7.....	109
Figure 69. The free energy diagram for the reaction of $^3\text{ZnCC}$ with DQ@Cage, Fc@Cage, Ru@Cage and the redox inactive Naph@Cage.....	111
Figure 70. Electron transfer kinetics of $^3\text{ZnCC}$ with Fc@Cage and DQ@Cage. The DQ@Cage trace has been corrected for the quenching by the free duroquinone, $k_{\text{DQ@Cage}} = k_{\text{measured}} - k_{\text{DQ}}$	112
Figure 71. Electrostatic potential on the surface of fully protonated, singly ionized and fully deprotonated hemicarcerand (upper row) as well as Fc(COOH) ₂ and quinones.	115
Figure 72. Left: The effective radii of cytochrome c and the hemicarceplex. Right: The location of the hemicarceplex–cytochrome c binding interface based on the R_{DA} radius of 16.5 Å.	119
Figure 73 (a) Location of the negative charges and the relative fully relaxed energies of the distinct quadruply de-protonated octacarboxyhemicarcerand (in kcal/mol, AM1 in vacuo). (b) Examples of the distorted fully protonated hemicarcerand with corresponding energies relative to the D_{4h} minimum (in kcal/mol, AM1 in vacuo).	120
Figure 74. Capture of the guest by the octacarboxyhemicarcerand associated with cytochrome c.....	122

Figure 75. Novel applications of the hemicarcerand: a molecular shuttle (purple) or an artificial receptor (orange).	124
Figure 76. Cram-type hemicarcerand used by Rudkevich <i>et al</i> vs the Cram-type hemicarcerand used for butane and SF ₆ trapping in work reported here.....	132
Figure 77. The general scheme.	133
Figure 78. Properties of butane and sulfur hexafluoride.	134
Figure 79. The set up for the encapsulation of hydrophobic gases.	137
Figure 80. The inversion recovery sequence.	138
Figure 81. The inversion recovery experiment and the exponential growth of the longitudinal magnetization with increasing t_1	139
Figure 82. The dependence of longitudinal relaxation times T_1 on the correlation time τ_C , viscosity and molecular size.	139
Figure 83. Puls sequence for COESY.....	140
Figure 84. The cycle-NOE sequence.	140
Figure 85. The TOCSY sequence. The spin-lock mixing time, τ_m , replaces the single mixing pulse of the basic COSY experiment.	141
Figure 86. The NOESY pulse sequence.	142
Figure 87. 1D ¹ H NMR for: a) free cage, b) the same solution of cage after bubbling with butane; c) gas-saturated sample obtained by additional bubbling with butane (dark green); and d) the highlighted region (4-8.5 ppm) for all three spectra (a,b and c) together, green arrow indicate the signal increase upon encapsulation.....	143
Figure 88. Cram-type hemicarcerand with labeled protons and 1D ¹ H NMR for cage and cage in the presence of butane (green) with assigned protons.....	145
Figure 89. 2D COSY for the cage+butane sample at 5°C.....	145
Figure 90. 2D TOCSY for the cage+butane sample at 5°C.....	146
Figure 91. 2D NOESY for the cage+butane sample at 5°C showing the interaction of the cage protons.	146
Figure 92. 2D NOESY for cage+butane at 5°C showing the butane region with labeled cross-peaks between the butane protons outside and inside the cage.....	148

Figure 93. 2D NOESY for the cage+butane sample at 5°C showing the interaction between a cage and butane molecules.	148
Figure 94. Encapsulated butane inside the cage: a) The hemicarcerand with highlighted cage protons giving the cross-peak with bound butane aligned along the long north-south axis of a cage. Side and upper view of entrapped butane in b) cis-conformation aligned along the south-west axis of a cage, c) cis- and d) trans-conformation aligned along the long north-south axis of a cage; e) two butane molecules trapped inside the cage in their equilibrium geometries (in cis and trans conformation) as well as the corresponding energy difference between the complexes in kcal/mol (AM1 in vacuo).	150
Figure 95. 1D ^1H NMR spectra of the cage and butane at 5°C and 25°C. Free butane signal is highlighted by light blue circles.	151
Figure 96. Longitudinal relaxation time for bound and free butane and a cage at 5 and 25°C.	152
Figure 97. 1D ^1H NMR for a) free cage and cage after bubbling with SF_6 with labeled protons (a-g) and b) the 4-8 ppm region showing the spectral changes upon gas encapsulation at 20°C.	154
Figure 98. 1D ^{19}F NMR for a) SF_6 in D_2O solution (green); b) SF_6 in the presence of the cage (orange) at 20°C.	155
Figure 99. Temperature variation of ^{19}F longitudinal relaxation time (T_1) (left) and the ^{19}F chemical shift of SF_6 (right) in the absence (green) and the presence of cage.	156
Figure 100. The saturation transfer experiment. Left graph shows 1D ^{19}F cycle-NOE NMR spectrum for the SF_6 inside the cage. NOE peak corresponding to the SF_6 outside the cage is phased positive and the saturated ^{19}F peak corresponding to SF_6 inside the cage is phased negative. Right plot shows the intensity of the unsaturated resonance when the exchanging resonance is saturated for a given length of time.	158

List of appendices

Appendix 1. Gaussian line shape analysis of the contributions of conformers F420 and F450 to the overall spectra of the HPLC fractions of ZnP450 rich in F450 and F420.	163
Appendix 2. Fluorescence excitation and emission spectra of ZnP450 collected under aerobic conditions.	164
Appendix 3. The thermodynamic parameters for both forms of ZnP450 complexed with the quenchers.	164
Appendix 4. Phosphorescence spectra of ZnP450 in the presence of FTMA. CoQ2 and CoQ4.....	165
Appendix 5. Spectral features of ZnP450 in the presence of TMA.....	166
Appendix 6. Normalized fluorescence decays of ¹ ZnP450 (F420) (40 mM KPi, 0.1M camphor, pH=7.4) in the presence of FTMA, CoQ2 and CoQ4 (5×10^{-5} M) at pH=7.4, excited at 420 nm with 590±10 nm band pass filter, fitted to the single exponential functions to convoluted reference sample.....	167
Appendix 7. Normalized fluorescence decays of ¹ ZnP450 (F450) (40 mM KPi, 0.1M camphor, pH=7.4) in the presence of FTMA, CoQ2 and CoQ4 (5×10^{-5} M) at pH=7.4, excited at 450 nm with 670±10 nm band pass filter, fitted to the single exponential functions to convoluted reference sample.....	168
Appendix 8. Normalized emission decay profiles of 2×10^{-6} ZnP450 in the presence of energy transfer quenchers (saturated solutions except of AnCOOH (20 μM), ReA (70 μM) and bC (70 μM)) excited at 450 nm and emission monitored at 768 nm pH=7.4.	169
Appendix 9. Thermodynamic parameters for F420 complexed with the triplet energy acceptors and computational values of internal reorganization energies λ_i for redox partners.	169
Appendix 10. Titration of Zn-cytochrome <i>c</i> with the empty cage at pH = 9 monitored by UV-Vis spectroscopy.....	170
Appendix 11. ET quenching of Zn-cytochrome <i>c</i> phosphorescence by tetracarboxynaphthalene, encapsulated ruthenocene and ferrocene at pH = 7, T = 25 °C.	170
Appendix 12. 2D NOESY for cage+butane sample at 5°C and 25°C, showing the butane region.	171

Appendix 13. NMR spectra comput at the Hartree-Fock level, 3-21G basis set using the Spartan 06 software packing by Wavefunction, Inc.	171
Appendix 14. 1D ^1H NMR for butane in D_2O at 25°C two days after gas bubbling.	172
Appendix 15. 1D ^1H NMR for butane in D_2O at 25°C week after gas bubbling.	173
Appendix 16. 1D ^1H NMR spectrum for Cage and butane at 25°C showing integration results with respect to six methyl group of cage at 1.6 ppm.....	174
Appendix 17. 1D ^1H NMR spectrum for Cage and butane at 5°C showing integration results with respect to six methyl group of cage at 1.6 ppm.....	175

Chapter 1. Introduction

Many inventions are inspired by nature, thus better understanding of natural phenomena enhances human creativity. Enzymes as well as any other biomolecules interact with each other in highly specific and selective manner in order to perform their particular functions. The structural and kinetic investigations of these systems not only help to understand how the processes are driven in living creatures, but also supply valuable data for biomedical and chemical engineering.

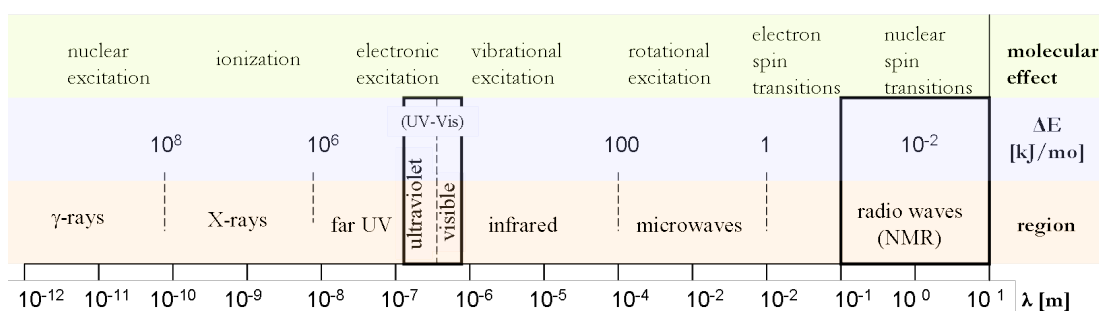


Figure 1. Spectrum of electromagnetic radiation.

A number of spectroscopic techniques, which detect the absorbed, emitted or scattered energy by molecules upon interaction with electromagnetic radiation can be applied for structural and kinetic investigations. Since the different types of electromagnetic radiation occur in different regions of the electromagnetic spectrum in form of heat, light, ultraviolet, or other electromagnetic waves, they provide different information about certain characteristic features (Figure 1). For example, absorption of the relatively high-energy UV-Vis photon by an atom or a molecule causes its electronic excitation. Absorption of the lower energy radiation (IR) causes vibrational and rotational

excitation of groups of atoms while, absorption in the low-energy radio-frequency part of the spectrum causes excitation of nuclear spin states (NMR).

In this thesis intermolecular and intramolecular interactions were studied mainly by applying optical and radio wave spectroscopy. Optical spectroscopic techniques are used to study photochemical properties of molecules. Those techniques include electronic absorption (UV-vis), photoluminescence (PL), infrared red (IR) absorption, Raman scattering, as well as time-resolved techniques such as photon counting, transient absorption or time-resolved luminescence. The main part of this thesis has focused on the study intramolecular interaction of zinc substituted heme proteins, the enzymes which possess chromophores in their active centers. The spectroscopic properties of these molecules allow us to apply optical techniques which are summarized in the material and methods of the next chapters. The last part of this report summarizes the results of gas encapsulation inside the Cram type hemicarcerand probed by NMR spectroscopy. Thus detailed information about NMR spectroscopy and the techniques used are summarized in the last chapter. This section is focused to present the optical properties of porphyrin and principle of the photochemical processes which were investigated in zinc substituted heme proteins.

1.1 Porphyrin

Porphyrin, a naturally occurring macrocyclic compound, plays a pivotal role in nature. The high diversity and the large number of its derivatives makes this compound very important from chemical, industrial and technological points of view. This is mainly

because the properties of porphyrins can be easily modified by a metal exchange or by change of the substituents of the macrocyclic ring. The porphyrin ring (Figure 2) is build from four pyrrole subunits linked by α carbon atoms via methine bridges ($=CH-$) and forms highly- conjugated aromatic system containing $22-\pi$ electrons, of which 18 are delocalized.

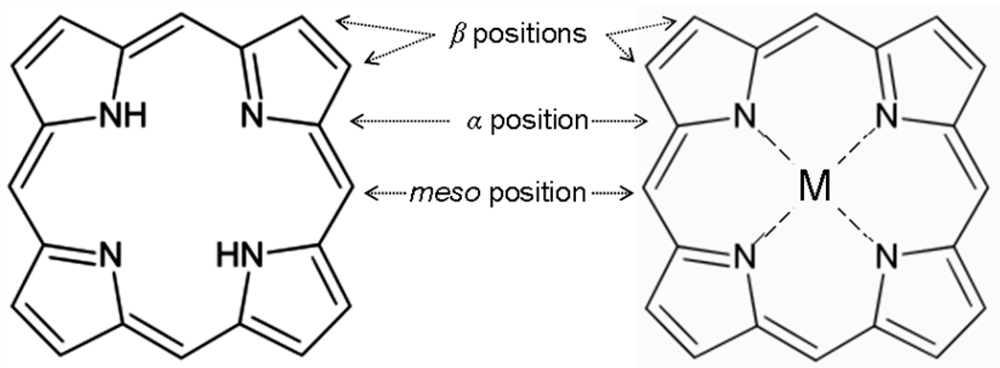


Figure 2. Structure of a free-base and metal porphyrin.

The porphyrin ring is able to complex a metal in its center with the coordination number of four, five or six. The metal conjugations are stabilized by a nitrogen lone pair of electrons from the σ orbitals and $\pi - \pi$ interactions between the metal and nitrogen atoms.^{1,2} Porphyrins have strong color and exhibit very intense absorption bands in the visible region. The typical metalloporphyrin absorption spectrum is characterized by an intense Soret band due to a transition to the second excited state ($S_0 \rightarrow S_2$) at about 400-420 nm and two weak $Q(\alpha, \beta)$ transitions to the first excited state ($S_0 \rightarrow S_1$) at about 550 - 600 nm (Figure 3).³

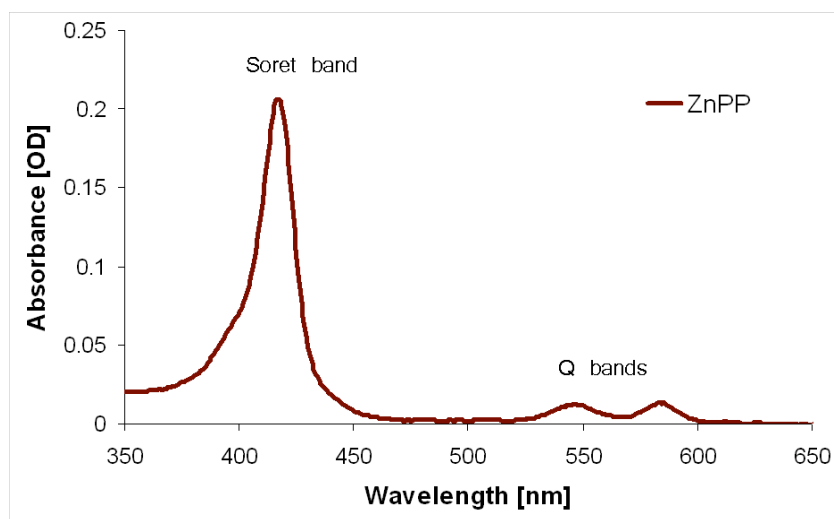


Figure 3. Absorbance spectrum of zinc porphyrin (ZnPP).

The origin of this spectrum arises from a $\pi \rightarrow \pi^*$ transition between two HOMOs and two LUMOs. The HOMOs represent two π orbitals, an a_{1u} and an a_{2u} , while the LUMOs are a degenerate set of e_g orbitals (Figure 4). As was explained by Gouterman,⁴ transitions between these orbitals gave rise to two excited states. Due to orbital mixing these two energy states split, a higher energy state with greater oscillator strength corresponds to the Soret band, while the lower energy state give rise to the Q-bands.⁵

The spectroscopic properties of a metalloporphyrin depend in part on the metal that is bound in its center. Closed shell metal ions which have a d orbital either empty or fully occupied (d_0 , d_{10}), have only a small effect on the electronic spectrum of the porphyrin. On the other hand, metal ion in which d orbitals is not fully occupied (d_6 - d_9) causes a hypsochromic (blue) shift in the spectrum. The mixing of the metal $d\pi$ orbitals with the π^* orbitals of the porphyrin ring in these metalloporphyrins results also in a decrease of the fluorescent yield.⁶

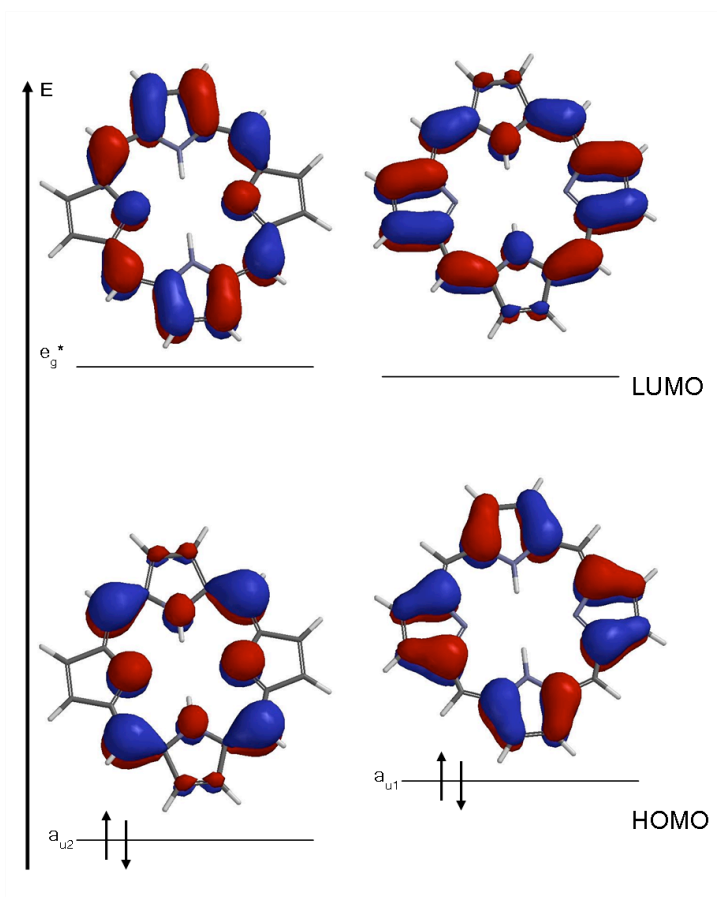


Figure 4. Four-orbital model for porphyrin.

1.2 Metalloporphyrins and heme proteins

Metalloporphyrins play important biochemical functions in nature. Magnesium porphyrin derivatives, chlorophylls, are light harvesting molecules, essential in the process of photosynthesis.⁷ Cobalamin, also called vitamin B12, is important in cell metabolism.⁸ Finally, the large group of heme proteins: hemoglobin, myoglobin, or cytoglobin are responsible for storage and activation of molecular oxygen, while cytochromes are involved in electron transport, catalysis as well as in active membrane transport.⁹

There are several types of natural hemes which differ by substituents of the porphyrin ring (Figure 5) and as a consequence of binding to their apoproteins. All of them have characteristic reddish-brown color due to the presence of the iron ion in the center of the heterocyclic ring.

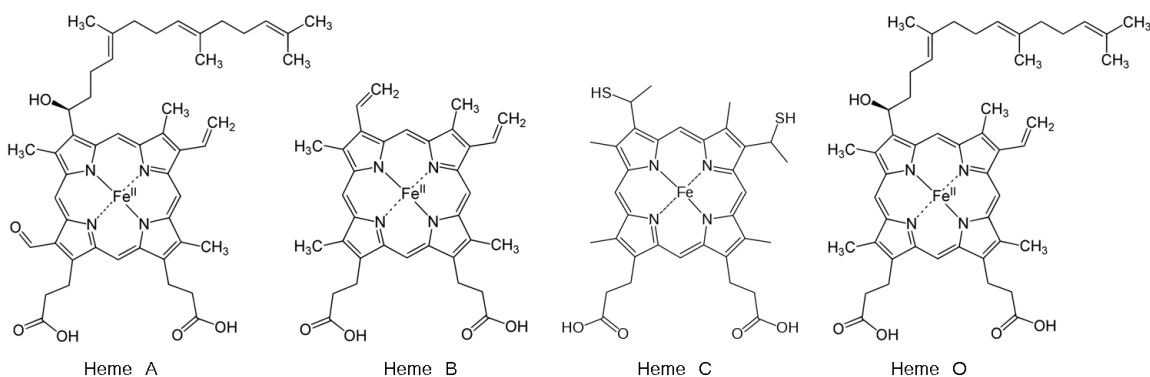


Figure 5. Structures of some natural hemes.

Because the spectral features of the heme depend on the iron oxidation state, peripheral substituents, axial ligands, spin state and nearby amino acid residues, the electronic absorption spectroscopy is used extensively to obtain conformational information on heme proteins (Table 1).¹⁰ Aside from the four nitrogen atoms of the porphyrin ring, the primary coordination sphere of the iron in heme proteins is dominated by histidine, as found in myoglobin or hemoglobin. This ligation causes bathochromic a shift of the Soret band. The binding of sulfur donors or carbon monoxide may lead to even larger red-shifts and resulting in a so called hyperporphyrin spectrum with an additional “hyper band” at around 370-380 nm.¹¹ The high spin pentacoordination and mono-histidine ligation dominate in heme proteins. In these enzymes the heme iron provides an open site for the binding of a substrate such as oxygen in the case of hemoglobin or myoglobin.

Table 1. Selected absorption maxima of iron porphyrin and heme proteins.^{12,13,14,15,16,17}

	hyper	Soret	β	α
H ₂ TPPS (a) ^a		412	516; 555	582; 635
Fe(III)TPPS (a)		393	528	686
Fe(II)TPPS (a)		421	556	608
Fe(II)PP (d)		424	527	556
Fe(II)UP+OH (n) ^b		394	593	
Fe(II)PPDME+N-MeIm (c) ^c		409	522	558
Fe(II)PPDME+Pyridine (p) ^d		420	527	557
Fe(II)PPDME+Im (c) ^e		428	538	568
Fe(II)PP+Im (d)		426	527	556
Fe(II)PP+Im (e) ^f		425	530	560
Fe(II)PPDME+OC ₆ H ₃ -3,4Me ₂ ^g		434	563	593
Fe(II)PPDME+C ₆ H ₅ CH ₂ S ⁻ (c)	376	470	561	
Fe(II)PPDME+p-NO ₂ C ₅ H ₄ S ⁻ (c)	376	455	555	611
Fe(III)peroxidase-His ^h		408	505	645
Fe(II) cytochrome c+His/Met ⁱ		416	520	550
Fe(II) cytochrome c+His/His		423	527	555
Fe(II)-P450-cys ^j		409	544	
Fe(III)-P450-cys-/H ₂ O		417	535	571
Fe(III)-P450-cys-/CO	363	446	550	
Fe-P450 +C ₆ H ₅ CH ₂ SH	377	465	557	
Fe(II)-P450-cys/DMS ^{-k}		446	541	568

^a acetate buffer , TPPS- tetrakis(4-sulfonatophenyl) porphyrin

^b NaOH solution, pH=9, FeUP-Iron uroporphyrin

^c Methylene Chloride, N-MeIm-N-Methylimidazole

^d In pyridine/water

^e DMSO, FePP – iron protoporphyrin IX;

^f sodium dodecyl sulfate/0.01 M NaOH solution; Im-imidazole

^g Fe(II)PPDME - protoporphyrin IX dimethyl ester, OC₆H₃-3,4Me₂- 3,4.dimethy I phenoxide

^h His-histidine

ⁱ Met-metionine

^j Cys-cysteine

^k DMS, dimethyl sulfide

Often when the protein is substrate free, heme is weakly coordinated by a water molecule, as in cytochrome P450. The low spin, six-coordinate heme environment is found in cytochromes involved in the electron transfer chain, such as cytochrome *b5* or cytochrome *c*.

Zinc porphyrins

Table 2. Solvent and ligand effects on the zinc porphyrin spectrum.^{20, 5}

	hyper	Soret	β	α
ZnTPP (b) ^{lm}		422	549	588
ZnTPP in DMF		425	559	599
ZnPP in DMF/H ₂ O buffer ⁿ		414	544	583
ZnTPP + C ₄ H ₉ SH (b)		426	558	599
ZnTPP + C ₄ H ₉ S ⁻ (b)	378	449	587	633
Zn(Meso-IX-DME) (t) ^o		404	532	569
Zn(Meso-IX-DME) + SBU ⁻ (t)	354	438	562	596
ZnTPP + Im (b)		431	566	606
ZnTPP + N-MeIm (b)		430	565	605
ZnPP + Pyridine (t)		428	562	602
ZnTPP + CN ⁻ (b)		437	577	618
ZnPP + H ₂ O buffer		412	544	582
ZnPP + Pyridine		425	551	588
ZnOPE (t) ^p		405	532	568
ZnOPE+ Im (t)		415	543	578
Zn cytochrome c		423	536	574
Zn myoglobin		428	553	595
Zn hemoglobin		423	550	587

Iron-porphyrins lose the absorbed energy mainly by radiationless transitions because of the open shell configurations of the metal ion (4s² 3d⁶) but the same

^l ZnTPP - Zinc tetraphenylporphyrin

^m (b) in benzene; (t) in toluene

ⁿ ZnPP – Zinc protoporphyrin IX

^o Mesoporphyrin IX dimethyl ester

^p ZnOPE-zinc octaethylporphyrin

porphyrins with closed shell metal such as zinc ($4s^2 3d^{10}$) exhibit both fluorescence and phosphorescence.¹⁸ In addition, as in case of iron porphyrin, the absorption of zinc porphyrin (ZnP) is determined by its microenvironments (Table 2)^{19,20} and thus the zinc porphyrin analogues have been extensively used in biological systems.

Iron to zinc substitution

Metal substitutions in heme proteins have been widely applied to change proteins properties. The modified molecule adapt different optical quality, and thanks to that, other spectroscopic methods can be employed to evaluate protein structure and its inter- or intra- molecular interactions. Years of studies on this kind of systems have shown that most of the modified proteins remain in their native conformation.²¹ Since substituted proteins containing zinc protoporphyrin (ZnPP) exhibit both fluorescence and phosphorescence¹⁹ with long lived triplet excited state (ms range), energy or electron transfer processes can be monitored in these systems. Moreover, because the triplet excited state of zinc substituted protein is able to accept or donate an electron, bidirectional redox chemistry can be investigated as well. The substitution methods depend mainly on the strength of heme-protein binding. If a heme is covalently attached to a protein, it is possible to exchange only the metal, but if a prosthetic group is stabilized by weak non-covalent interactions, the whole porphyrin is replaced (Figure 6).

The detailed iron to zinc substitution methods for cytochrome c and cytochrome P450_{cam} will be described in next chapters.

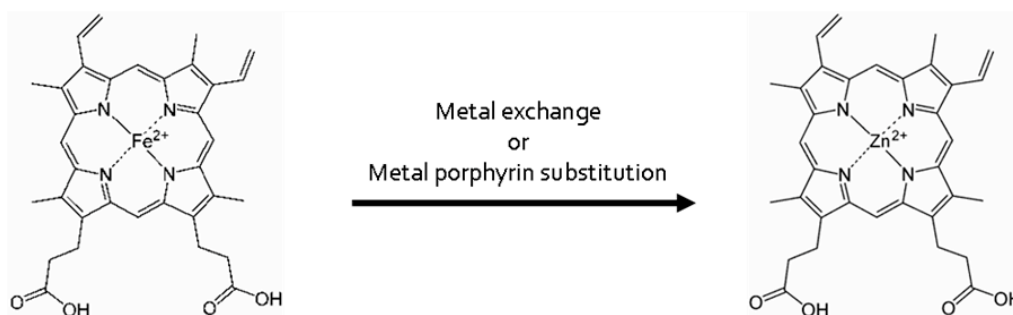


Figure 6. Metal-porphyrin substitution.

1.3 Photochemistry

Fundamental biological processes involve chemical reactions produced by light. These processes include light absorption, formation of excited electronic states, transfer of excitation energy or photoinduced electron transfer. The molecule (M), which has absorbed a photon of light with the energy $h\nu$, is promoted to an excited electronic state S_1 . The possible sequence of events following the absorption of a visible or UV photon (Ab) is summarized in Jabłoński diagrams²² (Figure 7).

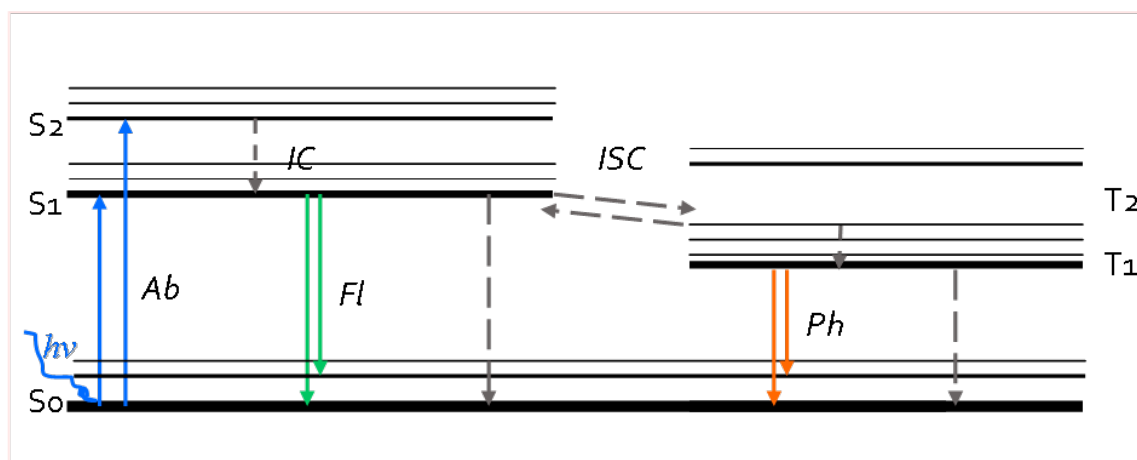


Figure 7. Jabłoński diagram.

The excited molecule (M^*) can undergo non-radiative relaxation and dissipate the excess vibrational energy via intermolecular collisions, through vibrational relaxation. If vibrational energy levels strongly overlap electronic energy levels, a possibility exists that the excited molecule can transition from a vibrational level of one electronic state to another vibrational level a lower electronic state. This process is called internal conversion (IC). The M^* can also experience radiationless transitions to a different excited electronic state with a different spin multiplicity via intersystem crossing (ISC).

The additional electronic energy can also be lost by spontaneous photoluminescence. As a consequence, M^* returns to its ground state emitting a photon of light with the lower energy $M^* \rightarrow M + h\nu$. If this emission occurs without changing the total electronic spin, the molecule relaxes via fluorescence (Fl), if the excited molecules undergo conversion to a triplet state (T_1), it subsequently relaxes through phosphorescence (Ph).

Because the excited molecule possesses an excess energy, it is more likely to undergo chemical reactions than when it is in its ground state S_0 . The absorption of light can causes several kinds of chemical processes. M^* may decompose, isomerize or promote a bimolecular chemical reaction.²³

The excess energy from the M^* can be transferred to acceptor molecule without photon emission (FRET) or the emission of light can be quenched by another molecule (quencher) during collision. Some quenchers act by inducing intersystem crossing, other cause electron exchange (Dexter interaction) or undergo photoinduced electron transfer (ET). These emission quenching processes are described below in more detail.

1.4 Electron transfer

Electron transfer (ET), or the act of moving an electron from one place to another, is amongst the simplest of chemical processes, yet plays a central and critical role in all aspects of life. Schematically can be described as follows (1):



Where D acts as the electron donor and A is the electron acceptor.

Electron transfer induced by a photon is a key reaction initiating photosynthesis. In photoinduced electron transfer the excited molecule can accept or donate an electron, i.e. can be either an electron donor or electron acceptor. The direction of ET is determined by the oxidation and reduction potential of the ground and excited state of the D-A pair.

If the electron from the donor's lowest unoccupied molecular orbital (LUMO) is transferred to the acceptor's LUMO, oxidative photoinduced ET occurs (oET), (2):



If the donor transfers the electron from its highest occupied molecular orbital (HOMO) to the acceptor's HOMO when A is in the excited state, reductive photoinduced ET (rET) is observed (3):



In both cases a radical cation and a radical anion are formed (Figure 8).

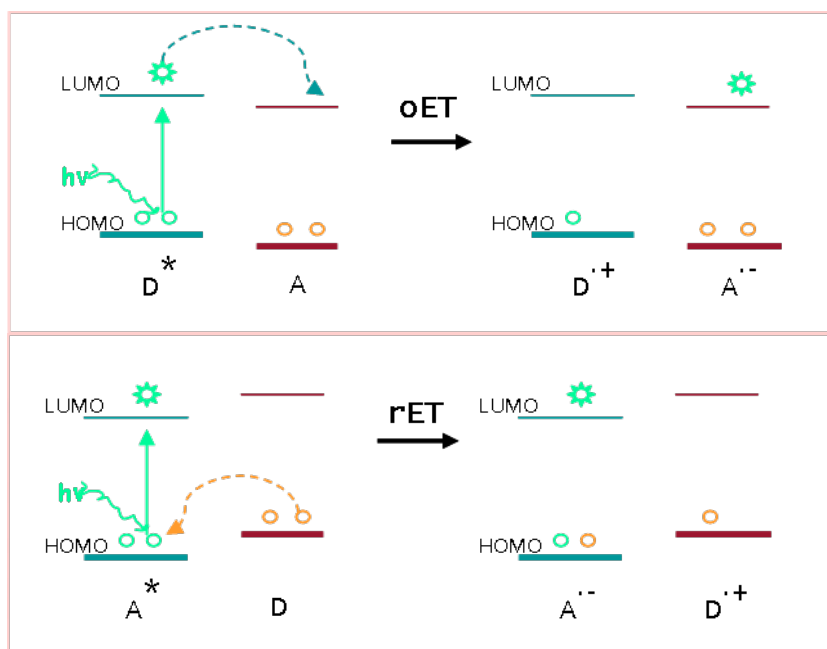


Figure 8. Schematic representation for oxidative (oET) and reductive (rET) photoinduced electron transfer.

The electronic coupling H_{AB} that leads to the transfer mixes the diabatic states that define the potential with the electron on the donor or on the acceptor in the region of their crossing (Figure 9). If the mixing is strong, there is substantial electronic coupling of the reactant pair ($2H_{AB}$; $H_{AB} \gg k_B T$) and the process is adiabatic. The rate of transfer can be described by equation 4:²⁴

$$k = \frac{k_B T}{h} e^{-\left(\frac{\Delta G^\ddagger}{k_B T}\right)} \quad (4)$$

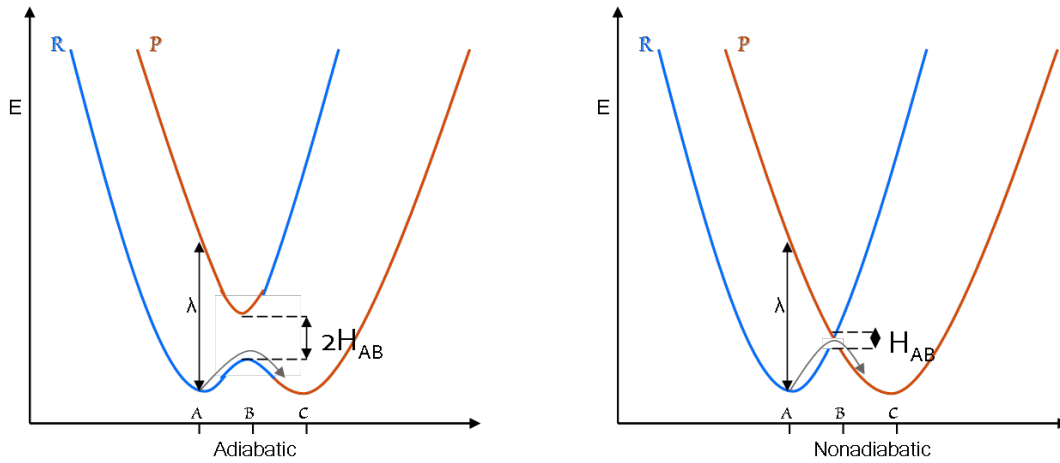


Figure 9. Schematic representation of free energy cross section of two electronic states in adiabatic (left) and nonadiabatic (right) reactions. A and C denote nuclear coordinates for the equilibrium configuration of the reactants R and products P, respectively; B refers to the nuclear configuration at the intersection of the two potential-energy surfaces (transition state).

A nonadiabatic ET reaction is characterized by weak electronic interaction between the reactant and product at the transition state ($H_{AB} \ll k_B T$). Following the Franck-Condon approximation, the coupling is directly related to the strength of the electronic interaction between D and A, and is expected to drop off exponentially with the separation between donor and acceptor orbitals (equations 5).

$$|H_{AB}|^2 = |H_0|^2 e^{-\beta(R_{DA}-R_0)} \quad (5)$$

Where β is exponential decay constant and $|H_0|^2$ is electronic coupling element at the contact distance R_0 for the donor and acceptor.

The rate of nonadiabatic ET can be described by the Marcus' theory of electron transfer^{25,26}.

Marcus Theory

Quantum mechanical treatments of electron transfer follow the Golden Rule (equation 6) expressing the ET rate as a product of an electronic coupling and the Franck-Condon weight density of states (FC):

$$k = \frac{2\pi}{\hbar} |H_{AB}|^2 FC \quad (6)$$

FC characterizes the nuclear motion along the reaction coordinate that accompanies the ET event. Marcus evaluated this expression for the transfer rate and showed that, when the molecular vibrations of the reactant and the product required for the molecule to reach the transition state are treated as harmonic oscillators, k_{ET} can be expressed by coupling the matrix H_{AB} , the free energy of reaction ΔG° and the reorganization energy λ (equation 7):

$$k(R_{DA}) = \left(\frac{\pi}{\hbar^2 \lambda k_B T} \right)^{1/2} \cdot |H_{AB}|^2 \cdot e^{-\frac{(\Delta G^\circ + \lambda)^2}{4\lambda k_B T}} \quad (7)$$

Where the free energy of activation has a quadratic dependence on the ΔG° (equation 8):

$$\Delta G^\ddagger = \frac{(\Delta G^\circ + \lambda)^2}{4\lambda} \quad (8)$$

The energy of nuclear reorganization λ required for system to reach the intersection is composed of the solvation (λ_s) and vibrational (λ_i) components (equation 9).

$$\lambda = \lambda_i + \lambda_s \quad (9)$$

In a two- sphere model of reactants the solvent reorganization energy can be estimated with the help of the Born equation (equation 10):

$$\lambda_s = \left(\frac{\Delta e^2}{4\pi\epsilon_0} \right) \left(\frac{1}{2r_D} + \frac{1}{2r_A} - \frac{1}{R_{DA}} \right) \left(\frac{1}{\epsilon_{optic}} - \frac{1}{\epsilon_{static}} \right) \quad (10)$$

where r_A and r_D are the effective radii of the donor and the acceptor and R_{DA} is the donor-acceptor separation, ϵ_{static} and $\epsilon_{\text{opt}} = n^2$ are the static and optical dielectric constants, respectively, Δe is the transferred charge and ϵ_0 is the permittivity of vacuum. The internal reorganization energy can be expressed by equation 11:

$$\lambda_i = \sum_j \frac{f_j^r f_j^p}{f_j^r + f_j^p} |\Delta q_j|^2 \quad (11)$$

where f_i^r is the j th normal mode force constant of the reactants and f_j^p that of the products, Δq_j is the change in equilibrium value of the j th normal coordinate. The internal reorganization energy is usually small compared to the external component and is often determined by computing the energy difference between the two equilibrium geometries of the molecule in its final and initial state.

The total reorganization energy (λ_{12}) can be also obtained from the reorganization energy for self exchange reactions (λ_{11} and λ_{22}) (equation 12):

$$\lambda_{12} \cong \frac{1}{2} (\lambda_{11} + \lambda_{22}) \quad (12)$$

Where λ_{12} is the reorganization energy for transition state and λ_{11} and λ_{22} are the reorganization energy for self exchange reactions.

Empirically, the dependence of the ET rate constant on the donor – acceptor separation R_{DA} (center to center) can be expressed by equation 13, where k_0 has a maximum value close to the frequency of a single molecular vibration ($k_B T/h \approx 1 \times 10^{13} \text{ s}^{-1}$).²⁷

$$k = k_0 \cdot e^{(-\beta \cdot R_{DA})} \quad (13)$$

Where

$$k_0 = \left(\frac{\pi}{\hbar^2 \lambda k_B T} \right)^{1/2} \cdot |H_{AB}|^2 \quad (14)$$

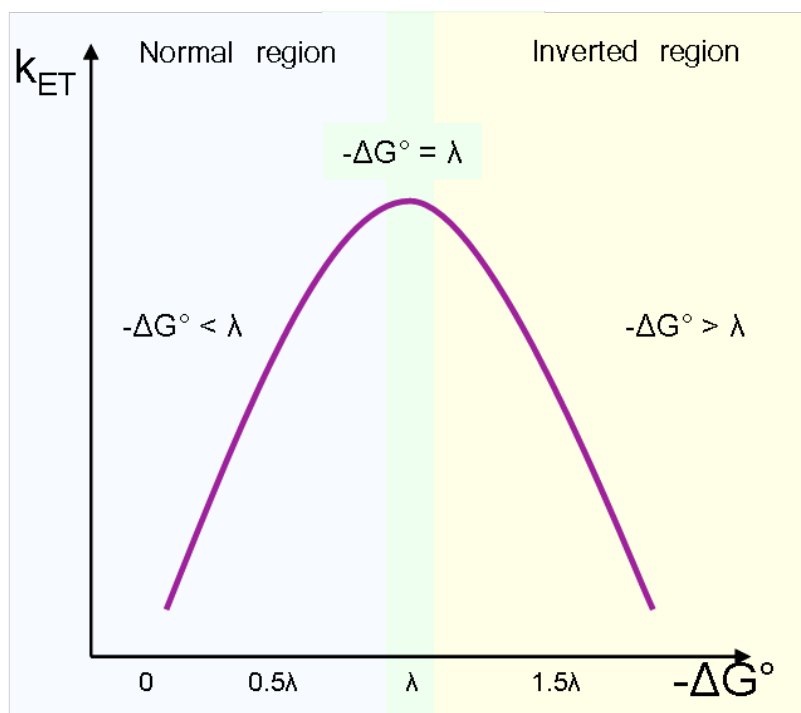


Figure 10. Driving force dependence of nonadiabatic ET rates predicted by the semiclassical Marcus theory.

The Marcus equation (7) shows the nonlinear behavior expected for the dependence of the electron transfer rate k_{ET} on the reaction free energy (Figure 10). At low driving forces, ET rates increase when the driving free energy of the reaction $-\Delta G^0$ increases and $-\Delta G^0 < \lambda$. This “normal” or Arrhenius like behavior only holds for the region in ΔG^0 until a maximum rate is observed for $-\Delta G^0 = \lambda$. As the driving free energy increases and become greater than λ , the ET rate decreases. This regime is known as the “inverted region”. The inverted behavior means that extra vibrational excitation is needed to reach the curve crossing as the acceptor well is lowered. Inverted region kinetics for bimolecular ET reaction is rare mainly due to the limiting influence of the diffusion rate of the reactants on the effective reaction rate. The schematic representation of free energy

surfaces of the reactant (R) and products (P) for nonadiabatic reactions in described regions is shown in Figure 11.

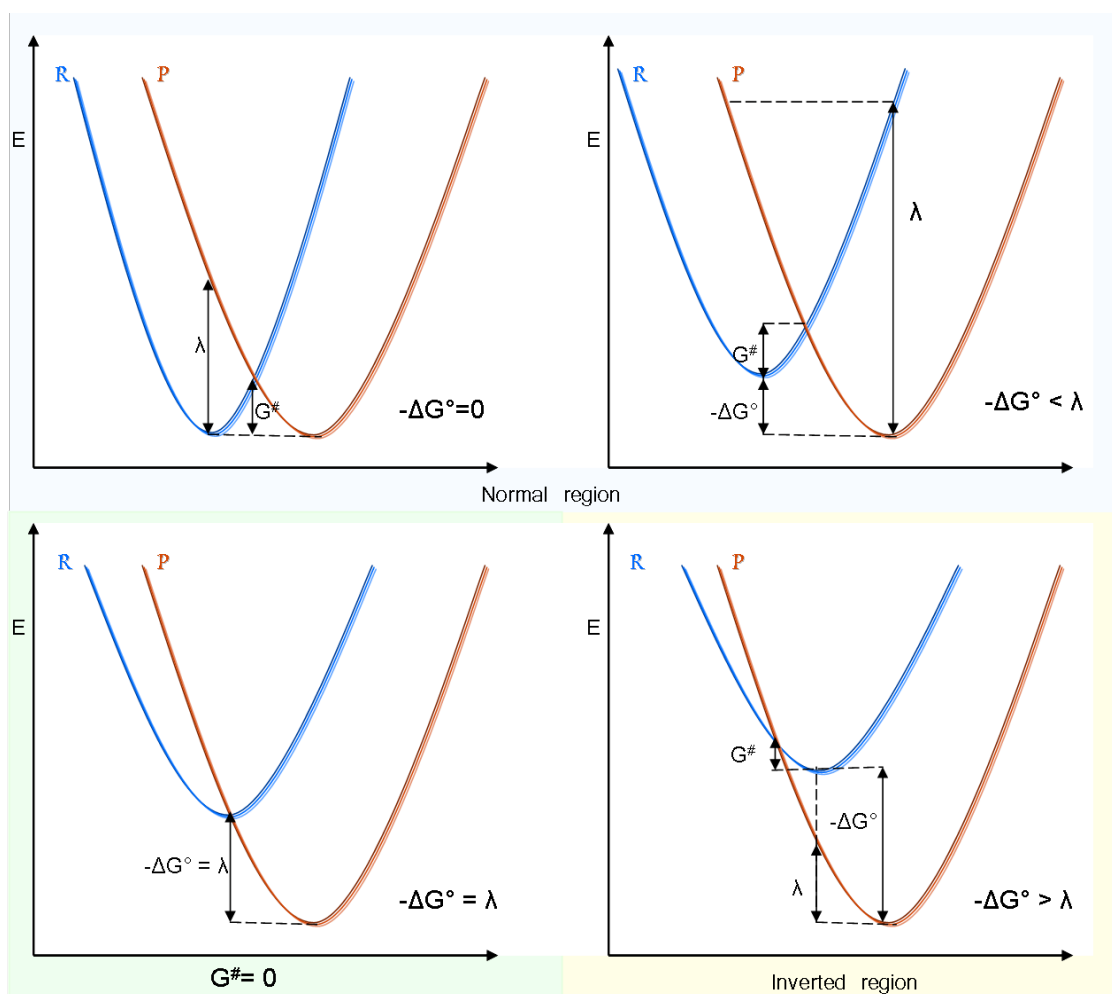
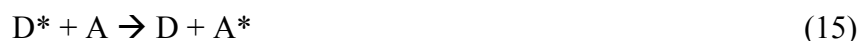


Figure 11. Reactant – product potential energy surfaces for ET reactions.

1.5 Energy Transfer

Another crucial process essential for biological reactions is the energy transfer. Electronic energy can be transferred by at least three mechanisms: potentially long - range simultaneous electron transitions in donor -acceptor pair, where energy is transferred over distances 10-100 Å due to dipole-dipole interactions (FRET); a short -

range ($<10 \text{ \AA}$) electron exchange between the donor and acceptor molecular orbitals (Dexter) and radiative energy transfer, which involves sequential donor emission and reabsorption of the photon by the acceptor. The general scheme of these processes is as follows (15):



Singlet-singlet (*SS*) energy transfer can proceed by all three of these mechanisms. Triplet-triplet (*TT*) energy transfer in which electronic transitions of both the donor and the acceptor are spin forbidden is driven only by Dexter mechanism. Examples of the overall spin-forbidden triplet-singlet (*TS*) energy transfer are known, but are relatively rare.^{28, 29, 30}

Förster resonance energy transfer

Förster resonance energy transfer (FRET) is a spectroscopic process by which energy is passed nonradiatively between molecules. When the donor chromophore (D) is excited by incident light and its emission spectrum overlaps with the absorption wavelength of an acceptor (A), the excited state energy from the donor may transfer to the acceptor through dipole-dipole coupling (Figure 12).³¹

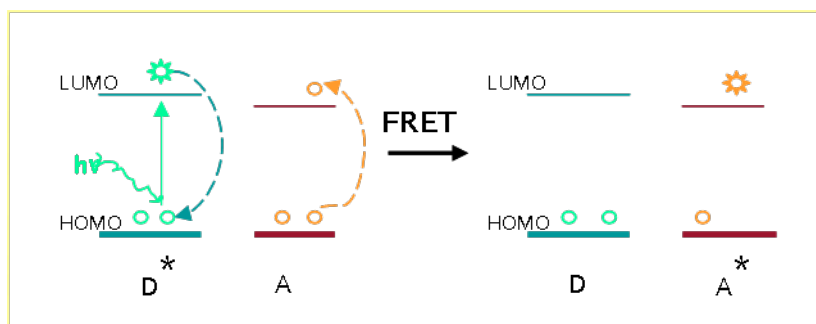


Figure 12. Schematic representation of Förster resonance energy transfer (FRET).

As a consequence of this process the donor fluorescence intensity and excited state lifetime decrease, and the acceptor becomes electronically excited. If the acceptor is fluorescent it may then emit a photon of light. If the acceptor is not a good fluorophore, the energy is dissipated as heat through vibrational relaxation.

The rate of the energy transfer is determined by the distance between the donor and acceptor (equation 16),³²

$$k_T = \frac{1}{\tau_0} \left(\frac{R_0}{R} \right)^6 \quad (16)$$

where R_0 is the Förster radius, which is the distance at which FRET is 50% efficient. It depends on the orientation factor κ^2 , the donor quantum yield Φ_D , the D-A spectral overlap J and the refractive index n of the medium (equation 17).³³

$$R_0 = (8.79 \cdot 10^{-23} \kappa^2 \Phi_D J n^{-4})^{1/6} \quad (17)$$

The efficiency of energy transfer (E) depends on the donor-acceptor distance, R , with an inverse 6th-power law (equation 18):

$$E = \frac{R_0^6}{(R_0^6 + R^6)} = \frac{k_T}{(k_r + k_{nr} + k_T)} = 1 - \frac{\tau}{\tau_0} \quad (18)$$

where τ_0 and τ is the donor lifetime in the absence or in the presence of acceptor, respectively ($\tau_0 = 1/(k_r + k_{nr})$; $\tau = 1/(k_r + k_{nr} + k_T)$) and k_r and k_{nr} are the rate coefficients for radiative and non-radiative deexcitation.³⁴

Since FRET is a sensitive method to study long range processes within or between molecules, is used extensively to measure the distances between the dyes attached to molecules, to study conformational changes in proteins or in the analysis of intermolecular interactions.^{31, 33}

Triplet-triplet energy transfer

While FRET occurs within 100 Å, the exchange interaction or Dexter mechanism occurs via overlap of electron clouds and requires collision between the molecules. In these process the excited donor transfers its electron from the lowest unoccupied molecular orbital (LUMO) to the acceptor's LUMO, while the acceptor transfers an electron from its highest occupied molecular orbital (HOMO) to the donor's HOMO (Figure 13). Both HOMO and LUMO of the acceptor must be within the HOMO-LUMO gap of a donor to allow such an electron transfer process.

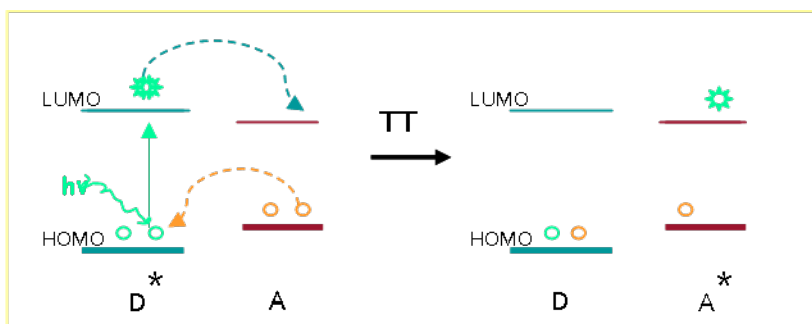


Figure 13. Schematic representation of exchange energy transfer.

Dexter energy transfer is a short-range phenomenon that decreases with e^{-R} and depends on spatial overlap of donor and quencher molecular orbitals.

The energy transfer rate is given by Dexter equation 19:

$$k_{TT(R)} = \frac{2\pi}{\hbar} K J_D \cdot e^{-2R/L} \quad (19)$$

where J_D is the normalized spectral overlap between donor emission and acceptor absorption spectra, K is related to the specific orbital interactions such as overlap dependence on specific orientation of D^* and A , R is the edge to edge displacement

between the donor and acceptor and L is the average van der Waals radius.^{35, 36, 37} If the donor and acceptor are weakly coupled, the Dexter mechanism exhibits features similar to nonadiabatic electron transfer with the rates following the Golden Rule (equation 6). It has been experimentally proved by Closs *et al.*^{38, 39} that the electron exchange energy transfer can be treated as simultaneous two electron transfer. As a result, the coupling matrix H_{AB} and consequently the energy transfer rate have an exponential dependence on the R_{DA} similar to that described by Marcus (equation 14). In contrast to electron transfer, triplet energy transfer does not involve a major redistribution of charges between the donor and the acceptor. As a result, the magnitude of the solvent reorganization energy λ_{sol} is very small, typically smaller than 5 kcal/mol⁴⁰. On the other hand, the magnitude of λ_i associated with the $S_0 \rightarrow T_1$ transitions is much larger, hence these values dominate the overall reorganization energy in triplet transfer.

Similarly as in ET, the steepness of the exponential decay of coupling matrix H_{AB} is captured by the coupling constant (β) for TT with respect to R_{DA} . Since the TT reaction is a simultaneous electron and hole transfer, the coupling constant β_{TT} can be treated as the sum of the electron and hole coupling constants ($\beta_{HT} + \beta_{ET}$). Closs *et al.*^{38, 39} measured the reaction rates of TT and ET for D-bridge-A systems and found that the β_{ET} values are about two times smaller than the obtained β_{TT} . Recent computational studies of Subotnik *et al.*⁴¹ evaluated the Closs *et al.* experiments and have showed that the theoretical coupling constant nicely agrees with the experimental data.

1.6 Transfer mechanisms

Studies of charge and energy transfer in donor-bridge-acceptor (D-B-A) systems have demonstrated two general transport mechanisms: strongly distance-dependent single-step tunneling and weakly distance-dependent multistep hopping (Figure 14), in which energy, an electron or an electron hole can transiently be localized, so the reaction is broken into several tunneling steps. The dominant mechanism is determined by the arrangement and electronic properties of the redox centers.

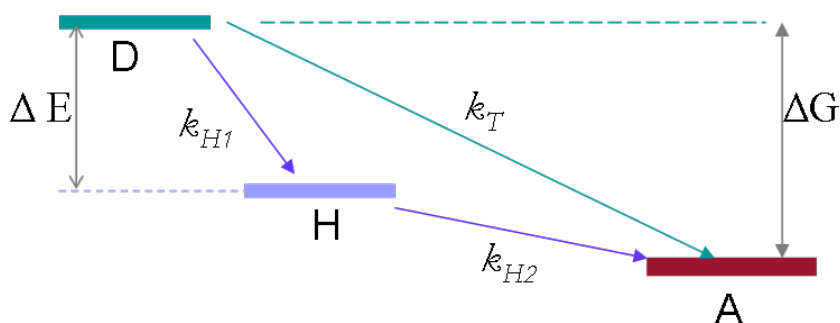


Figure 14. Two possible mechanisms for electron and triplet energy transfer reactions: single step tunneling from donor D to acceptor A with a reaction rate k_T (green path) or multistep hopping onto H with a reaction rate k_{H1} , from which the charge is transferred to A with the transfer rate k_{H2} (purple path). ΔG is the free energy change for the reaction between the donor and acceptor, while E is the energy gap between the donor and the intermediate states H.

Activating the hopping mechanism requires matching the energy levels of the donor and the intermediate states (H). In this case an electron from the donor reduces the bridge states first and then the electron is forwarded to the acceptor. In this case, electron transfer rates may demonstrate weak dependence on distance. In situations when the transient reduction of the bridging medium is thermodynamically impossible, a tunneling

mechanism that exponentially depends on distance becomes important for electron transport. ET tunneling over to distance greater than the direct interaction between D and A ($R > 10 \text{ \AA}$), can be described by a superexchange model. The superexchange model was formulated by McConnell, who described the overall electronic coupling (H_{DA}) in a system, in which the donor (D) and acceptor (A) are separated by n identical repeat units (H). In this model, H_{DA} depends on electronic couplings between the donor and the first bridging unit (h_{DH}), between adjacent bridging units (h_{HH}), and between the last bridging unit and the acceptor (h_{HA}) as well as on the energy gap (ΔE) between the donor and intermediate states H_i , (20).⁴²

$$H_{DA} = \frac{h_{DH}}{\Delta E} \cdot \left(\frac{h_{HH}}{\Delta E} \right)^{n-1} \cdot h_{HA} \quad (20)$$

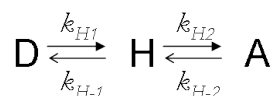
Because in cases of intermolecular electron transfer in solution, the positions of D and A are not restricted by a covalent bridge, Beratan and Onuchic developed a generalization of the McConnell superexchange coupling model. They accommodated the structural complexity of a protein matrix, in which the medium between D and A is decomposed into smaller subunits linked by covalent bonds, hydrogen bonds, or through-space jumps. Each contact is assigned a coupling decay value (ϵ_C , ϵ_H , ϵ_S) and the total coupling of a single pathway is given as a repeated product of the couplings for the individual links (21):

$$H_{DA} = \prod \epsilon_C \prod \epsilon_H \prod \epsilon_S \quad (21)$$

where ϵ_H , ϵ_S , ϵ_C are the coupling-decay factors for hydrogen bonds, van der Waals contacts, and single covalent bonds respectively.^{43,44}

Gray and Winkler compare the tunneling and hopping mechanisms in proteins.

They considered two-step hopping:



This model predicts a biological electron-transport chain ($\Delta G^\circ_{\text{DA}}=0$) reaction with a single endergonic step. In the case when $\Delta G^\circ_{\text{DH}} = -\Delta G^\circ_{\text{HA}}$ and $r_{\text{DH}} = r_{\text{HA}}$, shown in Figure 15, the charge transport up to 20 Å is much faster through single step tunneling, but over this range electron flow transport is facilitated by a hopping mechanism.

Recently Voityuk has formulated expressions for the threshold barrier, which may be useful to predict the ET mechanism in natural and artificial redox systems. Following Gray and Winkler, he considered two-step hopping but in these cases the rate of the back ET $\text{A} \rightarrow \text{H}$ is negligibly small ($k_{\text{H-2}}$ is set to be zero).⁴⁵ He has shown that the ET mechanism can be determined using three quantities ΔE , ΔG , and R_{DA} and by calculating the crossover barrier E_{C} for a system, where $E_{\text{C}} = (\Delta G/2) + (3/4)k_{\text{B}}T\beta R_{\text{DA}}$. According to this model single-step tunneling will be operative when the energy gap ΔE between D and H is larger than E_{C} ($\Delta E > E_{\text{C}}$), while hopping will dominate when $\Delta E < E_{\text{C}}$. Importantly, since both ET and TT transfer can be treated as electron transport reactions as expressed by the Marcus equation, the same mechanisms and models can be applied in analyzing those transfer reactions.^{46, 47, 48}

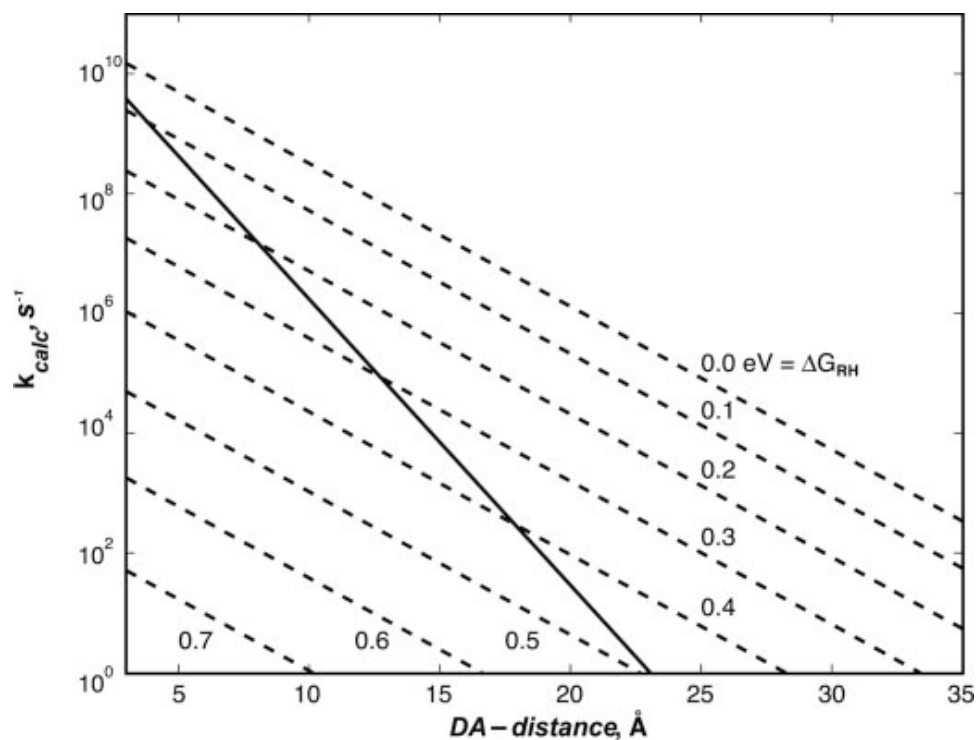


Figure 15. The distance dependences of the rates of single-step and two-step electron tunneling reactions at room temperatures. The solid line indicates theoretical distance dependence for the single-step, ergoneutral ($\Delta G_{RP}=0$) tunneling process ($\beta=1.1$ Å). Dashed lines indicate distance dependence calculated for two-step ergoneutral tunneling ($D \rightleftharpoons H \rightleftharpoons A$) with the indicated free-energy changes for the $D \rightleftharpoons H$ step.⁴⁸

1.7 References I

-
- ¹ L. R. Milgrom The colours of life: An introduction to the chemistry of porphyrins and related compounds *OUP, Oxford*, 1997.
- ² D. Dolphin The porphyrins *Academic Press, New York*, 1978.
- ³ I. T. Oliver and W. A. Rawlinson The absorption spectra of porphyrin a and derivatives *Biochem J.* 1955; *61*, 641–646.
- ⁴ M. Gouterman, G. H. Wagnière, and L. C. Snyder Spectra of porphyrins: Part II. Four orbital model *Journal of Molecular Spectroscopy* 1963, *11*, 108-127.
- ⁵ M.-Y. R. Wang and B. M. Hoffman Systematic Trends in Metalloporphyrin, Optical Spectra *J. Am. Chem. Soc.*, 1984, *106*, 4235-4240.
- ⁶ D. Marsh, L. Mink Microscale synthesis and electronic absorption spectroscopy of etraphenylporphyrin H₂(TPP) and metalloporphyrins ZnII(TPP) and NiII(TPP) *J. Chem. Educ.* 1996, *73*, 1188-1190.
- ⁷ J. M. Berg, J. L. Tymoczko, L. Stryer Biochemistry 5th edition. *New York: W H Freeman* 2002.
- ⁸ M. Wolak, G. Stochel, and R. van Eldik Mechanistic studies on the interaction of reduced cobalamin (Vitamin B_{12r}) with nitroprusside *J. Am. Chem. Soc.*, 2003, *125*, 1334–1351.
- ⁹ G. Simonneaux and A. Bondon Mechanism of electron transfer in heme proteins and models: The NMR approach *Chem. Rev.* 2005, *105*, 2627-2646.
- ¹⁰ J. A. Wyer and S. B. Nielsen Absorption in the Q-band region by isolated ferric heme+ and heme+(histidine) in vacuo *J. Chem. Phys.* 2010, *133*, 084306.
- ¹¹ C. J. Reedy, B. R. Gibney Heme protein assemblies *Chem Rev.* 2004, *104*, 617-49.
- ¹² R. Huszánk, G. Lendvay, and O. Horváth Air-stable, heme-like water-soluble iron(II) porphyrin: in situ preparation and characterization *J Biol Inorg Chem* 2007, *12*, 681–690.
- ¹³ J. A. Shelnutt Electronic structure of the porphyrin ring in an electrostatically bound π - π complex. Methylviologen-metallouroporphyrin complexes *J. Phys. Chem.* 1984, *88*, 6121-6127.

-
- ¹⁴ H. H. Ruf, and P. Wende Hyperporphyrin spectra of ferric dimercaptide-hemin complexes. Models for ferric cytochrome P450-thiol complexes *J. Am. Chem. Soc.*, 1977, 99, 5499-5500
- ¹⁵ R. W. Larsen, E. W. Findsen, and R. E. Nalliah Ligand photolysis and recombination of Fe(II) protoporphyrin complexes in dimethyl sulfoxide *Inorganica Chimica Acta* 1995, 234, 101-107.
- ¹⁶ J. M. Vanderkooi, F. Adar, and M. Erecinska Metallocytochromes c : Characterization of electronic absorption and emission spectra of Sn^{4+} and Zn^{2+} cytochromes c *Eur. J. Biochem.* 1976, 64, 381-387.
- ¹⁷ T. Egawa, T. Hishiki, Y. Ichikawa, Y. Kanamori, H. Shimada, S. Takahashi, T. Kitagawa, and Y. Ishimura Refolding processes of cytochrome P450cam from ferric and ferrous acid forms to the native conformation *J. Biol. Chem.* 2004, 279, 32008–32017.
- ¹⁸ A. Harriman Luminescence of porphyrins and metalloporphyrins. Zinc(II), nickel(II) and manganese(II) porphyrins *J. Chem. Soc., Faraday Trans.* 1980, 1, 76.
- ¹⁹ J. Feitelson and N. Barboy Triplet-state reactions of zinc protoporphyrins, *J. Phys. Chem.* 1986, 90, 271-274.
- ²⁰ M. Nappa and J. S. Valentine The influence of axial ligands on metalloporphyrin visible absorption spectra. Complexes of tetraphenylporphinatozinc *JASC*, 1978, 100, 5075-5080.
- ²¹ S. Ye, C. Sben, T. M. Cotton, and N. M. Kosti Characterization of zinc-substituted cytochrome c by circular dichroism and resonance Raman spectroscopic methods *J. Inorg. Biochemistry* 1997, 65, 219-226.
- ²² A. Jablonski and W. Szymanowski Thermal rotations of fluorescent molecules and duration of luminescence *Nature* 1935, 135, 582.
- ²³ I. N. Levine Physical chemistry 3rd Edition, *McGraw-Hill, Inc* 1988.
- ²⁴ N. S. Hush Adiabatic theory of outer sphere electron transfer reactions in solution *Trans. Faraday Soc.* 1961, 57, 557-580
- ²⁵ R. A. Marcus and N. Sutin Electron transfers in chemistry and biology *Biochimica et Biophysica Acta* 1985, 811, 265-322.
- ²⁶ R. A. Marcus On the theory of oxidation-reduction reactions involving electron transfer *J. Chem. Phys.* 1956, 24, 966-978.

-
- ²⁷ R. A. Marcus Electron transfer reactions in chemistry. Theory and experiment *Pure & Appl. Chem.* 1997, 69, 13-29.
- ²⁸ R. G. Bennett, R. P. Schwenker, and R. Kellogg Radiationless intermolecular energy transfer. II. Triplet→singlet transfer *J. Chem. Phys.* 1964, 41, 3040-3041.
- ²⁹ N. J. Two, I. E. Kochevar, Y. Noguchi, and M.-F. Chow Electronic excitation transfer in polymers. 3. Singlet-singlet, triplet-singlet, and triplet-triplet energy transfers. Evidence for triplet migration among pendant phenyl groups of polystyrene *J. Am. Chem. Soc.* 1978, 100, 3170–3177.
- ³⁰ T.-S. Fang, J. Lin, R. Schneider, T. Yamada and L. A. Singer Studies on triplet-singlet energy transfer with 1,3-dibromo-9,10-bis-[phenylethynyl]-anthracene *Chemical Physics Letters* 1982, 92, 283-287.
- ³¹ P. R. Selvin The Renaissance of fluorescence resonance energy transfer *Nature Structural Biology*, 2000, 7, 730-734.
- ³² J. R. Lakowicz Principles of fluorescence spectroscopy *Springer*, 2006.
- ³³ G. U. Nienhaus Exploring protein structure and dynamics under denaturing conditions by single-molecule FRET analysis *Macromolecular Bioscience* 2006, 6, 907–922.
- ³⁴ T. H. Förster, 10th Spiers memorial lecture; Transfer mechanisms of electronic excitation Discuss. Faraday Soc. 1959, 27, 7-17.
- ³⁵ D. L. J. Dexter, A theory of sensitized luminescence in solids *Chem. Phys.* 1953, 21, 836-850.
- ³⁶ S. Speiser Photophysics and mechanisms of intramolecular electronic energy transfer in bichromophoric molecular systems: solution and supersonic jet studies *Chem. Rev.* 1996, 96, 1953-1976.
- ³⁷ C. B. Murphy, Y. Zhang, T. Troxler, V. Ferry, J. J. Martin, and W. E. Jones, Jr. Probing Förster and Dexter energy-transfer mechanisms in fluorescent conjugated polymer chemosensors *J. Phys. Chem. B* 2004, 108, 1537-1543.
- ³⁸ G. L. Closs, P. Piotrowiak, J. M. MacInnis, and G. R. Fleming Determination of long distance intramolecular triplet energy transfer rates. A quantitative comparison with electron transfer *J. Am. Chem. Soc.* 1988, 110, 2652-2653.
- ³⁹ G. L. Closs, M. D. Johnson, J. R. Miller, and P. Piotrowiak A connection between intramolecular long-range electron, hole, and triplet energy transfers *J. Am. Chem. Soc.*, 1989, 111, 3751-3753.

-
- ⁴⁰ I. Place, A. Farran, K. Deshayes, and P. Piotrowiak Triplet energy transfer through the walls of hemicarcerands: Temperature dependence and the role of internal reorganization energy *J. Am. Chem. Soc.* 1998, *120*, 12626-12633
- ⁴¹ J. E. Subotnik, J. Vura-Weis, A.J. Sodt, and M.A. Ratner Predicting accurate electronic excitation transfer rates via Marcus theory with Boys or Edmiston-Ruedenberg localized diabaticization *J. Phys. Chem. A* 2010, *114*, 8665–8675.
- ⁴² McConnell, H. M. Intramolecular charge transfer in aromatic free radicals. *J. Chem. Phys.* 1961, *35*, 508–515.
- ⁴³ J. R. Winkler Electron tunneling pathways in proteins *Current Opinion in Chemical Biology* 2000, *4*, 192–198
- ⁴⁴ H. B. Gray and J. R. Winkler Electron tunneling through proteins *Quarterly Reviews of Biophysics* 2003, *36*, 341–372.
- ⁴⁵ A. A. Voityuk Long-range electron transfer in biomolecules. Tunneling or hopping? *J. Phys. Chem. B* 2011, *115*, 12202–12207.
- ⁴⁶ J. Vura-Weis, S. H. Abdelwahed, R. Shukla, R. Rathore, M. A. Ratner, M. R. Wasielewski. Crossover from single-step tunneling to multistep hopping for molecular triplet energy transfer *Science* 2010, *328*, 1547.
- ⁴⁷ C. Curutchet, A. A. Voityuk Triplet-triplet energy transfer in DNA: A process that occurs on the nanosecond timescale *Angew. Chem., Int. Ed.* 2011, *50*, 1820.
- ⁴⁸ H. B. Gray and J. R. Winkler Long-range electron transfer *PNAS* 2005, *102*, 10 3534-3539

Chapter 2. Phosphorescence Quenching Studies of Zinc Substituted Cytochrome P450

Metal substitution of heme proteins is widely applied in the study of biologically relevant electron transfer reactions. The most popular class of redox active proteins which allow modifications facilitating the study of ET reactions are heme proteins such as cytochromes. They are excellent model systems because they are naturally involved in electron transport and the spectroscopic and redox properties of heme group can be easily manipulated. Due to large spin-orbit coupling the native iron-containing heme dissipates the excitation energy through rapid radiationless transitions which leads to extremely short excited state lifetimes in the femtosecond range.⁴⁹ Consequently, native heme proteins are not very good targets for photoinduced electron transfer investigations. In order to overcome this problem various methods were developed to exchange the metal in the prosthetic group. The replacement of iron by diamagnetic zinc at the porphyrin (PP) center dramatically changes the photophysics of the enzyme. Proteins containing zinc porphyrins (ZnPP) exhibit both fluorescence (nanoseconds) and long lived phosphorescence¹⁹ (milliseconds at room temperature in deoxygenated solutions). Studies on Zn-substituted cytochrome *c* (ZnCC) and myoglobin (ZnMb) have shown that the exchange of iron (II) to zinc (II) porphyrin does not alter the conformation of these proteins.²¹ Importantly, the singlet and triplet excited states of zinc substituted proteins are able to accept or donate electron from good acceptors or donors, thus maintaining the key redox properties of the native protein. Thanks to their emissive nature, they are amenable to highly sensitive single photon counting techniques, which permit kinetic studies over a very broad range of concentrations and time scales. Optical spectroscopy

experiments on Zn-substituted cytochrome *c* and its modified variants laid the fundamental groundwork for the understanding of electron transfer dynamics in proteins. Zinc substitution of cytochrome P450 open opportunities to study electron and energy transfer processes in this enzyme as well.

Replacement of the heme moiety in cytochrome P450_{cam} by ferriprotoporphyrin IX, as well as manganese, cobalt and zinc substitutions of cytochrome P450_{cam} were reported.^{50,51,52,53,54} The primary challenge in these substitutions arises because the heme is not covalently bound to the backbone of cytochrome P450, nevertheless, it appears to play an significant role in maintaining the overall structure of the properly folded enzyme. This liability leads to poor substitution yields and the presence of non-native conformers in the reconstituted protein. The metal substitution in cytochrome P450 involves first the complete removal of the heme from the enzyme which is then replaced by a zinc protoporphyrin IX. The Gunsalus group, which established the substitution method, performed the heme removal and replacement by iron protoporphyrin IX to check the quality of the substituted enzyme and has shown that the FeP450 exhibits an absorption spectrum and same enzymatic activity similar to the native form.⁵¹

P450 is an important member of the heme monooxygenase family which catalyzes a vast variety of processes including drug metabolism, carcinogenesis, degradation of xenobiotics, the biosynthesis of steroids, lipids and secondary metabolites.⁵⁵ The camphor metabolizing cytochrome P450_{cam} isolated from *Pseudomonas putida* is the most widely utilized representative of this group and very often serves as a model for other cytochromes P450 since all shares a common protein fold. Cytochrome P450_{cam} consists of 414 amino acids with a molecular weight of 46,600 Da. Its triangular – prism

structure is predominately helical consisting of 12 α -helices, named A- L, and five β -sheets. The protein core is formed by a four-helix bundle composed of three parallel helices, D, L, and I, and one antiparallel helix E. The active site, heme, is confined inside the protein pocket formed by the distal I-helix and proximal L-helix and ligated by a cysteine residue 357. The substrate entry channel includes the F, G helices, FG loop and Bo helix, folds over the heme and I helix to place the substrate close to heme center and is dominated by hydrophobic amino acid residues which are responsible for the substrate coordination.⁵⁶

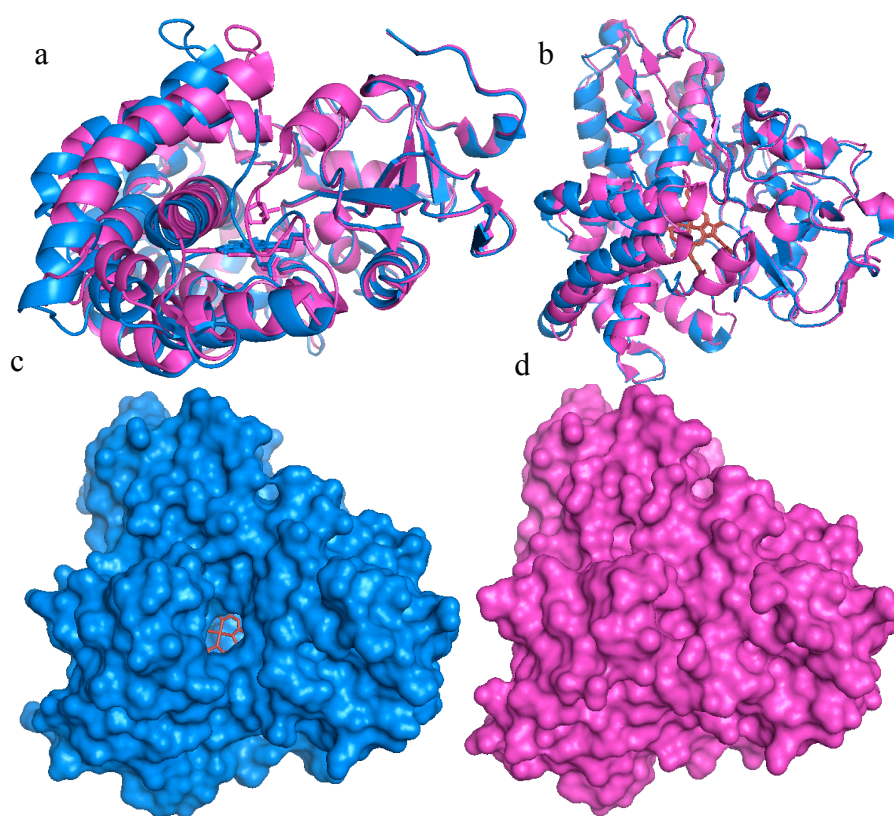


Figure 16. Structure of cytochrome P450_{cam} in the presence (pink) and absence (blue) of camphor: a) side and b) upper view. Molecular surface representation of P450 showing the open (c) and closed (d) conformation (PDB: 3L63, 3L62).⁵⁷

A recent report by Goodin *et al.*⁵⁷, who determined the X-ray structure of the native P450_{cam} in the presence and absence of camphor, has shown that the protein displays dynamic behavior and exhibits different structures when it binds its partner (Figure 16). The substrate-free protein exhibits a more open structure with the access channel exposed to the solvent while upon the binding of camphor the protein adopts a tighter, closed structure, in which the access channel narrows and restricts the ingress and egress of substrates. The presence of the open conformation was previously postulated by Gray *et al.* and Goodin *et al.* on the basis of their work on the ligation of native P450_{cam} to synthetic “molecular wires”^{58, 59, 60, 61} and suggested that conformational dynamics and plasticity play an important role in P450 substrate access and recognition.

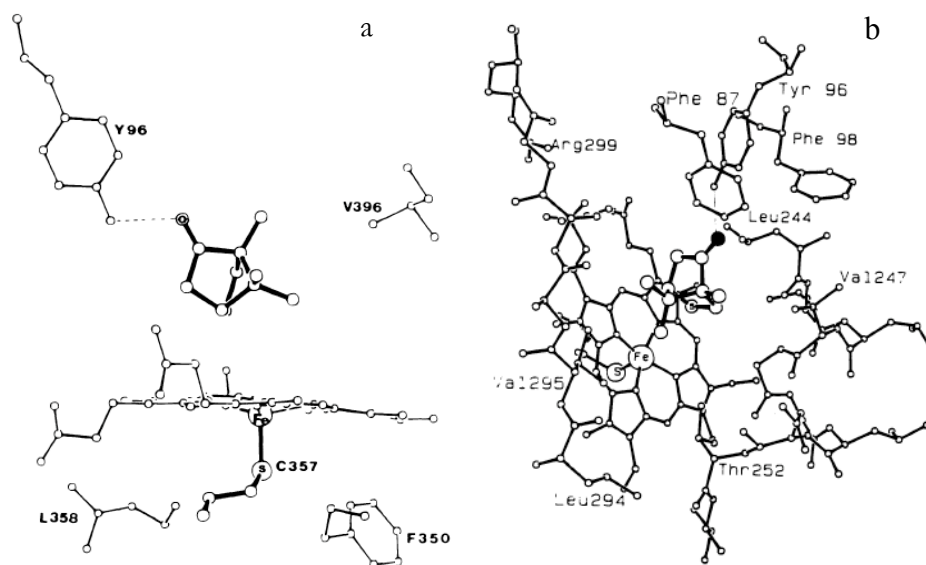


Figure 17. Edge-on (A) and stereoscopic view (B) of the the P450_{cam} heme region bound to camphor with neighboring aliphatic and aromatic residues important for the protein-substrate hydrophobic contacts.⁶²

The channel leading from the protein’s surface to the active site near the heme is approximately 22 Å deep.⁵⁸ Camphor is located at the end of this active pocket 5.3 Å

away from the porphyrin center where it is stabilized via a hydrogen bond formed between carbonyl its moiety and the hydroxyl group of Tyr96. Additionally, a number of hydrophobic amino acids located inside the channel such as Val295, Val247, Leu244 and Phe87 play a role in substrate binding via van der Waals contacts (Figure 17).

Cytochrome P450_{cam} has a specific binding site for potassium ion in the B₀ helix which is required to drive the formation of the characteristic high-spin state of the heme Fe⁺³ upon substrate binding. The presence of K⁺ enhances camphor binding and increases the stability of the enzyme, but high concentration of K⁺ alone does not induce any change in the open conformation. This suggests that K⁺ binding is not sufficient to drive the closure of the active site channel in the absence of camphor. Thus the ordering of the B₀ helix and K⁺ coordination appear to be driven by substrate binding.⁶³

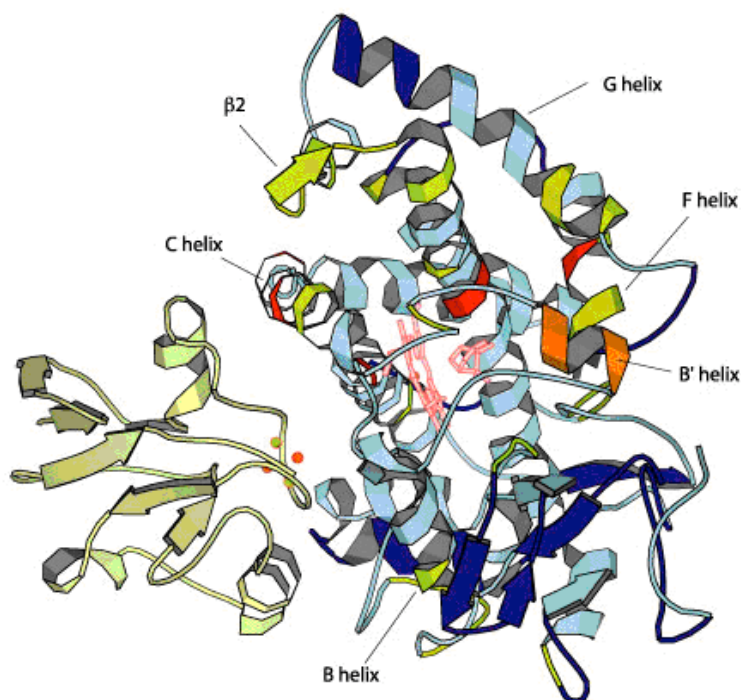


Figure 18. Model of the specific complex between Pdx (yellow) and cytochrome P450_{cam} from Pochapsky *et al.*⁶⁴

To perform its function, the monooxygenase reaction, the enzyme requires a multienzyme system composed of putidaredoxin (an iron-sulfur protein), putidaredoxin reductase (a flavoprotein) and NAD(P)H as the electron supplying components. Putidaredoxin (Pdx) binds to the proximal surface of cytochrome P450_{cam} enabling direct electron transfer from the [2Fe–2S] cluster to the heme (Figure 18). This association is driven primarily via electrostatic attraction and involves formation of a salt bridge between the negatively charged group of Asp38 in Pdx and Arg112 in the positively charged patch of cytochrome P450.⁶⁵

The catalytic cycle of cytochrome P450_{cam} is presented in Figure 19.⁶⁶ In the resting state the enzyme is six-coordinated and holds a water molecule as a distal ligand (1) while the ferric (Fe^{III}) five *d*-electrons occupy the lower MOs leading to a low spin species (LS). The appearance of the substrate (RH) inside the protein's active channel causes water displacement and generates the five-coordinated ferric species (2). These cause the iron to buckle out of the porphyrin's plane and consequently, the five *d*-electrons prefer to occupy the *d*-block in a high spin (HS) fashion. This complex becomes a good electron acceptor and is easily reduced by the reductase domain, the 2Fe-2S ferredoxin putidaredoxin (Pdx), to form the HS substrate bound ferrous (Fe^{II}) complex (3). This form is a good dioxygen binder, which triggers O₂ binding and leads to production of the LS ferrous-dioxygen complex (4). This form accepts another electron from Pdx and becomes the twice reduced ferric-dioxo species (5). Importantly, while the first electron can be accepted from any donor with the appropriate reduction potential, the second electron transfer specifically requires the presence of Pdx for full activity. As a good Lewis base, the ferric dioxo complex undergoes protonation and accepts two

protons prior to the release of a water molecule from the oxyferyl radical cation species (7). The high-valent iron oxo complex (Fe^{IV}) transfers the oxygen atom to the substrate. The hydroxylated substrate is released from the protein pocket, which triggers water ligation.

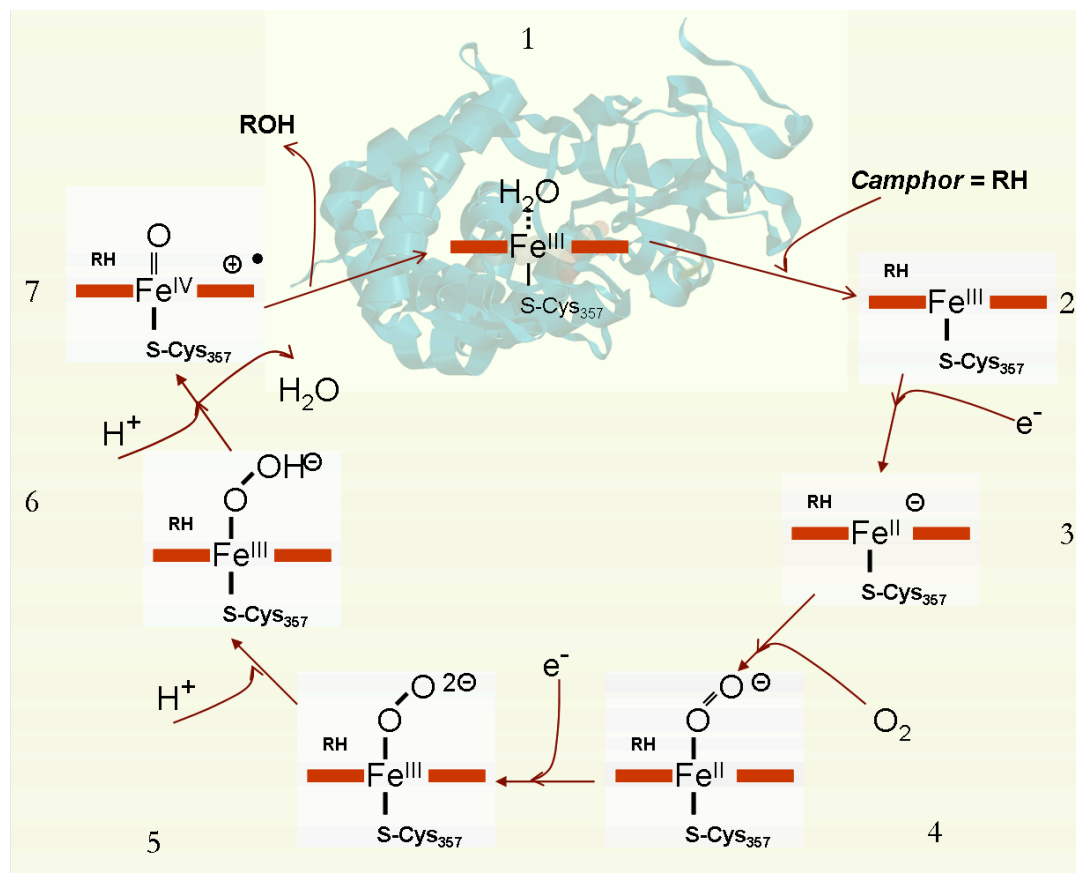


Figure 19. The catalytic cycle of cytochrome P450.

Since the heme spectrum is sensitive to environmental changes and ligation, each state exhibits different absorption maxima. In the substrate free P450 the protein channel is filled by water and the enzyme absorb the maximum light at 417nm. The camphor-bound enzyme possesses a characteristic absorption spectrum with a maximum at 392 nm for the ferric form and at 409 nm when iron is in its ferrous state. Importantly, in the

presence of carbon monoxide the protein (Fe^{+3}) exhibits so called hyper spectrum with a characteristic Soret band at 450nm and hyper band around 370 nm.

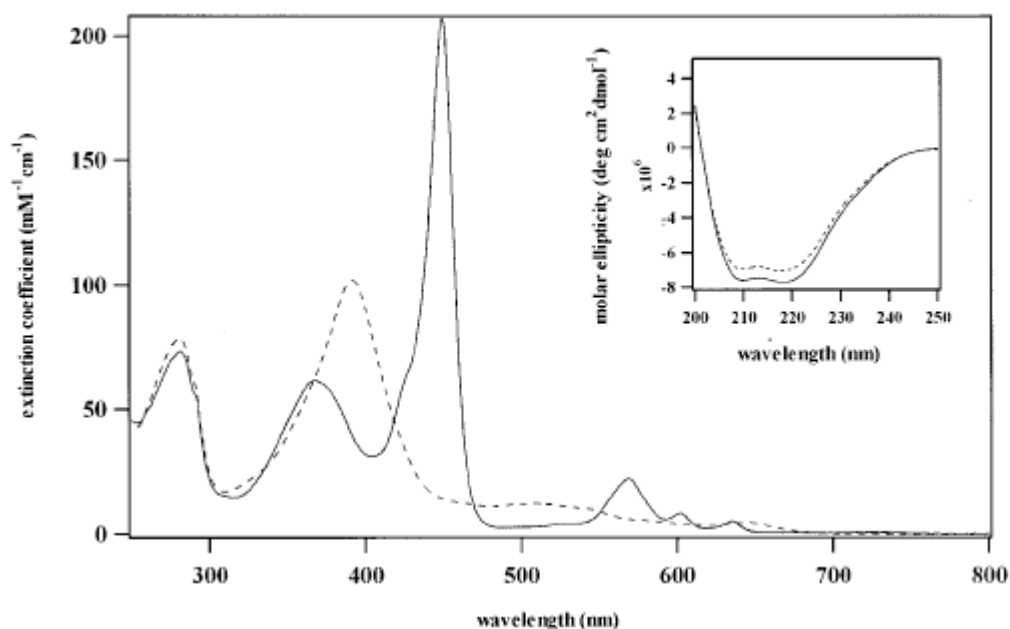


Figure 20. Electronic absorption spectra of ZnP450 (solid curve) and ferric P450_{cam} (dashed line). Inset: Circular dichroism obtained by Morishima *et al.*⁵⁴

The replacement of heme with a zinc protoporphyrin IX by Morishima *et al.* resulted in the formation of Zn-substituted cytochrome P450 (ZnP450) with unusual for Zn-proteins photophysical properties.⁵⁴ The spectrum of ZnP450 has very similar features as the native cytochrome P450 bound to carbon monoxide with a maximum at 450 nm (Figure 20) which indicate sulfur ligation to the Zn-porphyrin in the enzyme. In order to confirm that the metal substitution in P450_{cam} does not perturb the protein structure Morishima *et al.* measured the CD spectra of ZnP450. The α -helical content was 45% and 50% for P450_{cam} and ZnP450, respectively, which indicate that the zinc substitution only slightly perturb the protein secondary structure.

The hydrophobic nature of the protein channel favors organic ligand association inside the active pocket. Such positioning puts the binding partners in sufficiently close proximity to facilitate electron and energy transfer processes. The ligands for the study of photoinduced electron and energy transfer in ZnP450 were chosen based on their redox and structural properties. The first group contains small redox partners (Figure 21). The acceptors, small quinones, are involved in numerous redox reactions in natural biological systems, albeit in nature they often carry lipophilic side chains.⁶⁷ The donors, ferrocene and its derivatives, are strong reductants known to be capable of transferring electrons to the excited states of other zinc substituted proteins.⁶⁸

The size of these ligands is comparable to camphor and as a consequence they should bind to the Zn-substituted protein in a very similar fashion, leading to efficient reductive (ferrocenes) and oxidative (quinones) electron transfer quenching of the excited state of ZnP450_{cam}.

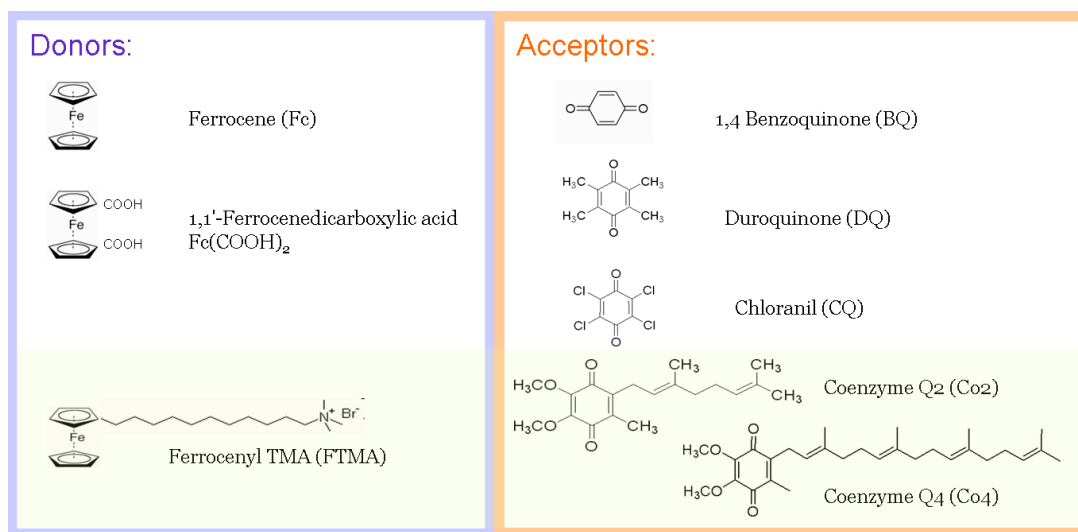


Figure 21. The quenchers selected for the study of photoinduced electron transfer properties of ZnP450_{cam}.

The quenchers from a second group selected for these studies (Figure 21) possess the long aliphatic tethers which vary in length, structure and electrochemical properties. Coenzymes Q2 and Q4, as the derivatives of coenzyme Q10, which serves as an electron carrier in the cellular electron transport chain,⁶⁹ should easily accept electrons from the protein. The water soluble ferrocene derivative, FTMA, should be able to donate an electron to the excited protein as well. The long hydrophobic chains which they carry should fit and stabilize them inside the protein hydrophobic pocket, and place them close to the active center, as was previously observed in the conformational studies of P450_{cam} with “molecular wires”.⁵⁹ The association between ZnP450 and the ET ligands was probed spectroscopically by monitoring the protein absorption and emission spectra.

The distance dependence of ET reaction as well as triplet-triplet energy transfer (TT) can be used to estimate the separation between the donor and acceptor in a manner similar to FRET. For that purpose FRET is employed extensively in biophysical or biochemical analysis^{31, 70} but only few reports can be found where TT has been applied to examine interactions in biological systems. The technique has been utilized mainly to evaluate intramolecular attractions between two attached chromophores or between a donor attached to protein and its tryptophan or tyrosine residue.^{71, 72, 73} Here we explore TT studies in biosystems and present examples of intermolecular triplet energy transfer reactions between a zinc substituted cytochrome P450 and TT acceptors associated close to protein active center. Among the TT quenchers selected for these studies (Figure 22) small ligands as well as substrates with long hydrophobic chain can be found. The thermodynamic and spectroscopic properties of these compounds and ZnP450 disfavor FRET of ET reactions but support TT energy transfer. Since only association inside the

protein channel provides D-A separation small enough for TT reactions, any changes observed in protein triplet states imply electron exchange between zinc porphyrin and the ligand associated inside the protein pocket. As in case of ET reactions, the association between ZnP450 and TT quencher was probed by the phosphorescence lifetime of $^3\text{ZnP450}$.

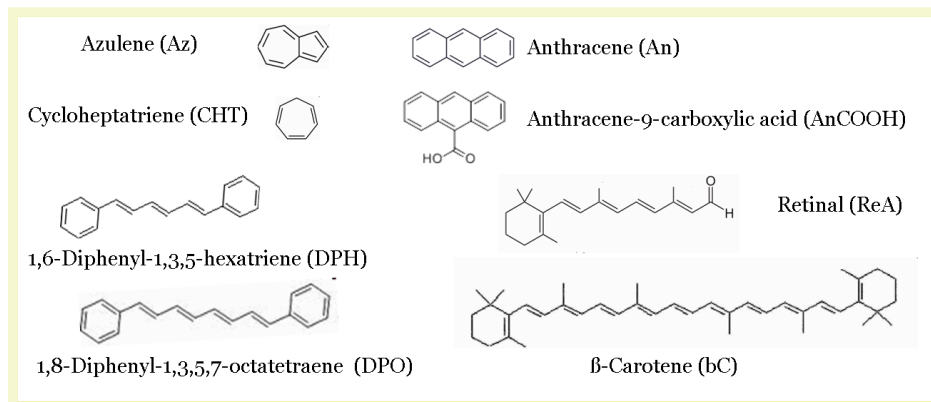


Figure 22. Quenchers selected for the TT energy transfer study.

2.1 Materials and methods

Materials: The escherichia coli vector containing CYP101 was a gift from Prof. S. G. Sligar. Culture media were prepared at Genentech's media preparation facility. Isopropyl β -D-1-thiogalactopyranoside (IPTG), dithiothreitol (DTT) and 5-aminolevulinic acid were purchased from Pro-Omega. Ni-NTA agarose was obtained from Qiagen Inc. Zinc protoporphyrin IX, d-camphor, β -mercaptoethanol (BME), ferrocene (Fc), 1,1'-ferrocenedicarboxylic acid ($\text{Fc}(\text{COOH})_2$), benzoquinone (BQ), chloranil (CQ) duroquinone (DQ), coenzyme Q2 and Q4, azulene (Az), cycloheptatriene (CHT), 1,6-diphenyl-1,3,5-hexatriene (DPH), 1,8-diphenyl-1,3,5,7-octatetraene (DPO), and retinal (ReA) were purchased from Sigma Aldrich Co, dodecyl trimethyl ammonium chloride (TMA), β - carotene (bC) from Fluka while 11-

ferrocenyltrimethylundecylammonium bromide (FTMA) from Dojindo Laboratories.

Deuterium oxide (99.9%) was obtained from MP Biomedicals, LLC.

Expression and Purification of 6xHis-tagged Fe-cytochrome P450_{cam} was done following the Sligar *et al.* protocols.⁷⁴ The purified protein solution was dialyzed for about 6 hours against a 200 μ M camphor solution containing BME (1.4 ml/L) prior to lyophilization. The lyophilized P450_{cam} was stored at -20°C.

The Zn-Substitution of Cytochrome P450_{cam}: The Zn-substituted cytochrome P450_{cam} was prepared as described by Gunsalus *et al.*^{51,52} and later by Morishima *et al.*⁵⁴ with small modifications during the protein purification. Briefly: 100mg of P450_{cam} was dissolved in 15ml of ice-cold 0.1 M histidine solution (pH 7.8). Next, the pH of the protein solution was lowered to 2.7 on ice by 1.0 M HCl. To extract the heme, an equivolume of 2-butanone was added to the protein solution. The aqueous apoprotein solution was collected and dialyzed against 2 L of 0.6 mM NaHCO₃ overnight. The apoprotein was subsequently dialyzed against 2 L of 0.1 M histidine containing 40% (v/v) glycerol overnight. This process reduced the volume of the apoprotein solution. The dialyzate was purged with purified argon gas, after 2h 1M dithiothreitol (DTT) was added to the apoprotein in equivolume to give a final concentration of 20 mM DTT. After another hour an equal volume of previously degassed 0.1M histidine solution containing 10% saturated camphor was added using a gas-tight syringe and then 5 mg of Zinc porphyrin IX dissolved in 0.5 ml DMF were added dropwise to the apoprotein solution. The mixture was purged with argon for another 48 h at room temperature. The solution was concentrated to about 5 ml using Amico Ultra centrifugal filter devices and then purified by double HPLC (Figure 23).

The crude ZnP450 was purged first by ProteinPak column (Waters Inc.) for the HPLC system equilibrated against buffer containing 40 mM potassium phosphate, 0 to 1 mM d-camphor, pH = 7.8, to remove the unbound porphyrin. The collected protein fractions were subsequently purified by the HiprepQ ion exchange HPLC column. The sample was loaded onto the column in 40 mM potassium phosphate, 0 to 1 mM d-camphor, pH = 7.8, and eluted with a linear 0-400 mM KCl gradient in 40 mM potassium phosphate, 0 to 1 mM d-camphor at pH = 7.8. The protein was eluted with ~150 mM KCl. Finally, the purified protein was dialyzed against 40 mM potassium phosphate, 0 to 1 mM d-camphor, pH = 7.4, overnight. All manipulations of the ZnP450 were performed in the dark.

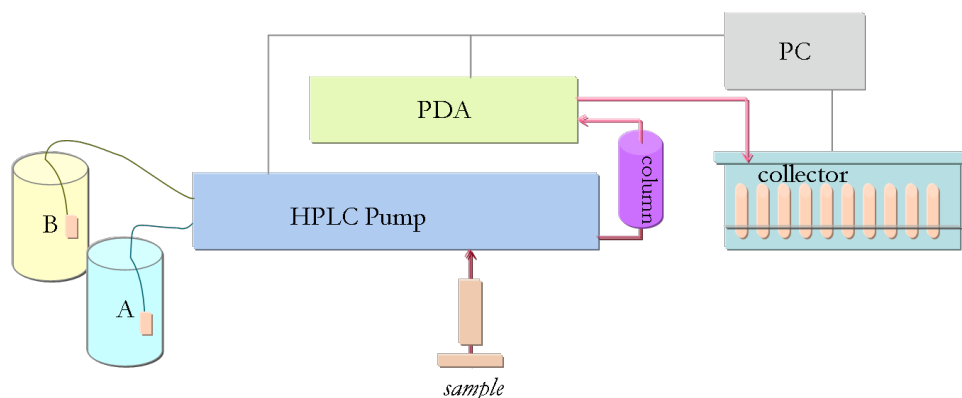


Figure 23. HPLC system: Waters 1525 Binary HPLC Pump with integral vacuum degasser performs with a maximum operating pressure of 4000 psi, has two pump channels, A and B and is equipped with the Waters 2996 UV-Vis Photodiode Array Detector (PDA) capable of recording the spectrum of the eluted sample from 190 nm to 800nm with 1.2 nm resolution. The injected sample is purified on the HPLC column and then the fractions are collected using Waters Fraction Collector III. The system is controlled by EmpowerPro software.

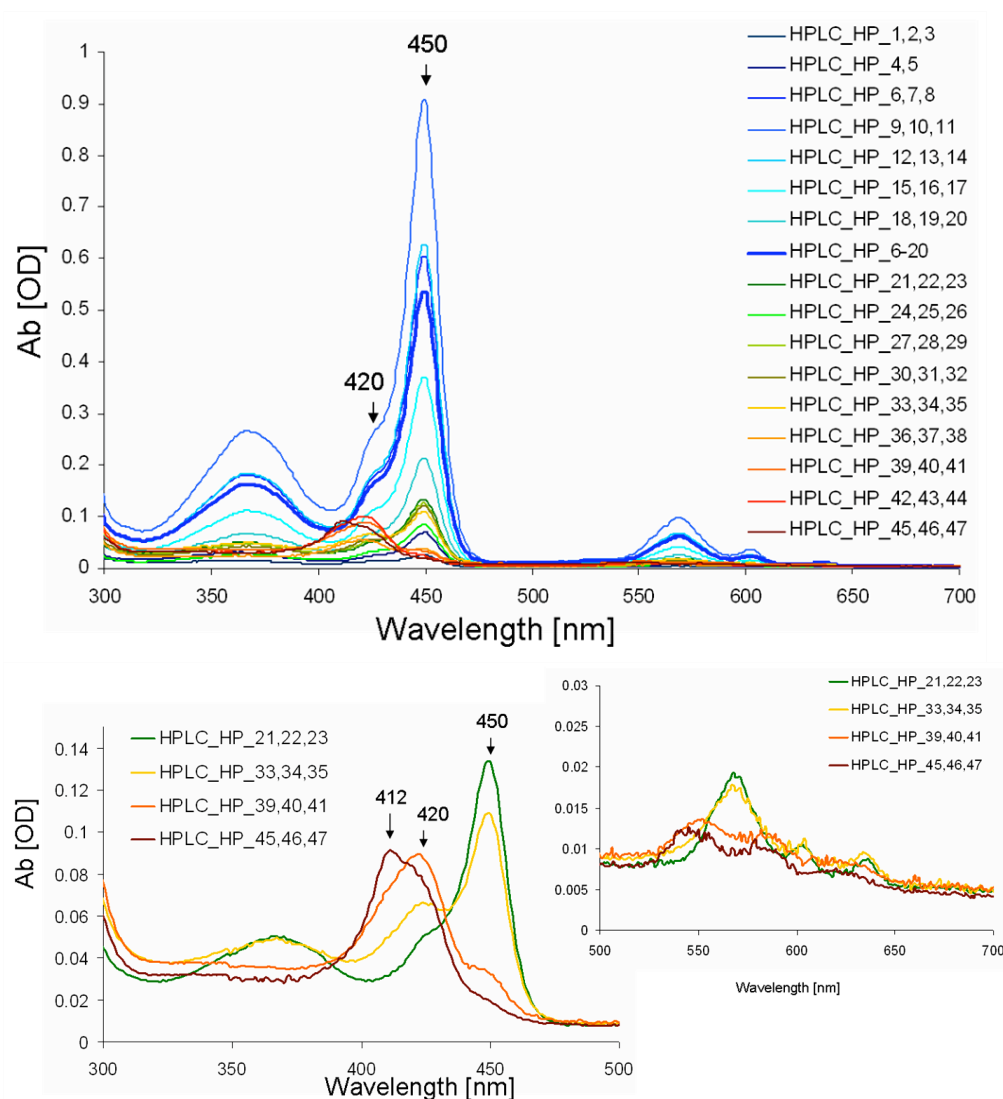


Figure 24. UV-vis spectra of the HPLC fractions resulting from the protein substitution performed as described in the Material and Methods section. Main fractions collected for the measurements contained a mixture of F420 and F450 (HPLC_HP_6-20), in which the F450 was the dominant form.

The complete set of the UV-vis spectra acquired during a typical HPLC separation of the products of the zinc substitution of P450_{cam} is shown in Figure 24. The main fractions collected for measurements contained the mixture of F420 and F450 (HPLC_HP_6-20), where the F450 was the dominant form. Repeated attempts to completely separate these two forms from one another were not successful. In all cases

both conformers were present, however, it was possible to collect fractions which contained primarily F420 (HPLC_HP_36-41), which were followed by the unfolded protein fractions with the characteristic Soret band at 412 nm. Because the fractions which contain primarily F420 are present in the elution only in low concentration and since they may contain the unfolded protein with a closely lying Soret band at 412 nm, this part of protein was not used for the electron transfer studies.

Sample preparation for ET studies: The appropriate amount of quencher was dissolved in 40 mM potassium phosphate, 0.1 mM d-camphor pH = 7.4 buffer (standard buffer) and mixed with equal volume of 2-10 μ M ZnP450. Because of low solubility, the ferrocene (Fc) was introduced to the protein solution at its saturated concentration. Additionally, in order to increase the quencher concentration, the quinones were first dissolved in few μ l of DMF. In each case, the reference sample of the ZnP450 was suspended in the same buffer as the samples containing the quencher. For the isotope effect experiments the purified protein solution was concentrated to minimal volume and then dissolved in deuterated buffer to give the final ratio $\text{H}_2\text{O}:\text{D}_2\text{O} = 1:35$. The F420:F450 ratio in the samples used for the electron transfer studies was kept close to 1:2.

Instrumentation and spectroscopic methods: Absorption spectra were recorded using Cary 500 Scan UV-Vis NIR spectrophotometer. Fluorescence, phosphorescence and triplet lifetime measurements were carried out using Varian Cary Eclipse Fluorescence Spectrophotometer (Figure 25, Table3) following excitation at 420 nm or 450 nm.

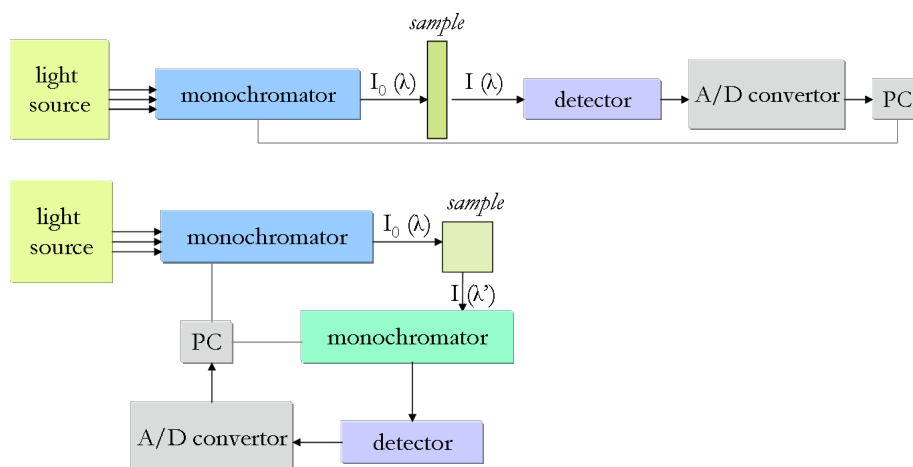


Figure 25. Schematic diagram of UV-vis spectrometer (upper scheme) and a spectrofluorometer (lower scheme).

Table 3. Instrument settings for Varian Cary Eclipse Fluorescence Spectrophotometer

Parameters	Fluorescence	Phosphorescence	Lifetime
Excitation λ , nm	420, 450	420, 450	420, 450
Emission λ , nm	460 - 800	550 - 900	590, 768
Excitation slit, nm	5	5	5
Emission slit, nm	10	10	20
Detector voltage, V	800	1000	1000
Scan rate, nm/min	120	-	-
Total decay time, ms	-	20	-
Decay time, ms	-	0.2	0.10
Gate time, ms	-	5	0.05
Averaging time, ms	500	100	-
Data interval, nm	1.0	1.0	-
Number of cycles	-	-	100 ($\times 3$)

The differences in the photophysical properties of F450 and F420 allow the analysis of both species in parallel by changing excitation wavelengths. If the sample containing both forms was excited at 450 nm only the triplet state of F450 was observed, but when it was excited at 420 nm, the phosphorescence and delayed fluorescence of F420 as well as the triplet state of F450 were seen. Because the phosphorescence of F450 (a maximum at 768 nm) overlaps the phosphorescence of F420 (maximum at 732 nm) the $^3\text{F420}$ was

monitored at the delayed fluorescence peak at 590 nm (Table 3). Additionally, time resolved measurements helped to distinguish the observed component. The decay kinetics of the $^3\text{F}_{450}$ was fit satisfactorily with a single exponential function, however the decay of $^3\text{F}_{420}$ was analyzed as biexponential function, where one component had a lifetime characteristic of $^3\text{F}_{450}$.

Time-resolved fluorescence experiments were carried out using a noncollinear optical parametric amplifier (NOPA) as the excitation source and a photodiode as the detector (Figure 26). NOPA was pumped by a home-built multipass Ti:sapphire amplifier operating at a 1.25 kHz repetition. The samples were excited at 420 or 450 nm. The emitted photons passed through 590 ± 10 nm or 670 ± 10 nm bandpass filters and were detected by a Hamamatsu photodiode (H5783-01) recorded by the PCS-150 modules (Becker & Hickl GmbH) with the synchronization provided by a high speed avalanche photodiode APM-400-N (Becker & Hickl GmbH). The obtained fluorescence signals were convoluted with a system response function. The data were analyzed using an Origin software package. Attempts to deconvolute the response signal were ineffective, as a result the system response signal was convoluted with the number of single exponential functions with a known lifetime and compared with the signal spectrum.

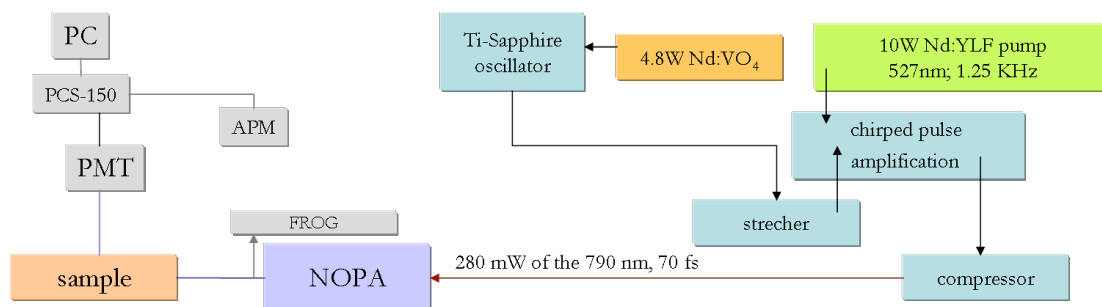


Figure 26. Set-up for the time-resolved fluorescence experiments.

Data analysis and MO calculations: The total reorganization energy in an electron transfer reaction consists of the medium component resulting from the rearrangement of the solvent dipoles around the new distribution of charges and the internal or vibrational reorganization, associated with the structural relaxation of the product states. Born theory can be applied to estimate the upper limit for the solvent reorganization energy for the donor and acceptor (equation 10).^{75, 38, 39, 76, 77,}

$$\lambda_{\text{sol}} = (e^2/4\pi\epsilon_0) \cdot (1/2r_D + 1/2r_A - 1/R_{\text{DA}}) \cdot (1/\epsilon_{\text{opt}} - 1/\epsilon_{\text{static}})$$

where r_A and r_D are the effective radii of the donor and the acceptor and R_{DA} is the donor-acceptor separation, ϵ_{static} is the low frequency (dc) dielectric constant of the solvent and $\epsilon_{\text{opt}} = n^2$ is the optical dielectric constant of the intervening medium. All other symbols have their standard meaning. λ_{sol} reaches maximum at infinite donor-acceptor separation, $R_{\text{DA}} \rightarrow \infty$. Since the terms are additive, the contributions of the donor and the acceptor can be evaluated separately.

The internal, or vibrational, reorganization energy for the donor or acceptor was calculated at the B3LYP DFT level with the 6-31G* basis set (Spartan '06). We followed the standard procedure of first calculating the unrelaxed energy of the product species in the optimized geometry of the neutral species and then allowing the product species to relax. The overall reorganization energy of the quencher is $\lambda_{\text{sol}} + \lambda_{\text{vib}}$.

Since the self exchange reorganization energy of ZnP450 has been assumed to be 1.2eV by Morrishima *et al.*⁵⁴ the reorganization energy of this enzyme is $\lambda_{\text{ZnP450}}/2$.

The nuclear reorganization energies for TT reaction associated with the $S_0 \leftrightarrow T_1$ transitions in the donor and acceptors were calculated at the AM1 level. To obtain the reorganization energy of a triplet energy acceptor, its T_1 energy was first calculated in the

frozen geometry of the S_0 state, which subsequently was allowed to relax to the optimum triplet geometry. The reorganization energy of the energy donor (ZnPP) was obtained by first calculating the S_0 energy in the frozen optimized geometry of the T_1 state and then allowing it to relax to the S_0 optimum. All calculations employed Spartan 06.

2.2 Results and discussion

Spectroscopic characterization of ZnP450

UV-Vis measurements of the purified ZnP450 revealed that the substituted protein exists as a mixture of two forms, F450 and F420 (Figure 27). The main product of the Zn-porphyrin substitution, form F450, which was described by Morishima *et al.*⁵⁴ exhibits a red shifted Soret band at 449 nm and an intense hyper-band at 367 nm. Such hyper-bands are characteristic of the zinc porphyrin derivatives after ligation with thiol ions (Chapter 1, Table 2). The second form, F420, displays the expected photophysical properties that are consistent with other zinc substituted heme proteins which all show a Soret band in the vicinity of 420 nm. Gaussian line shape fitting locates the maximum of the F420 Soret band at 424 nm, i.e. remarkably close to that of ZnCC (Appendix 1).

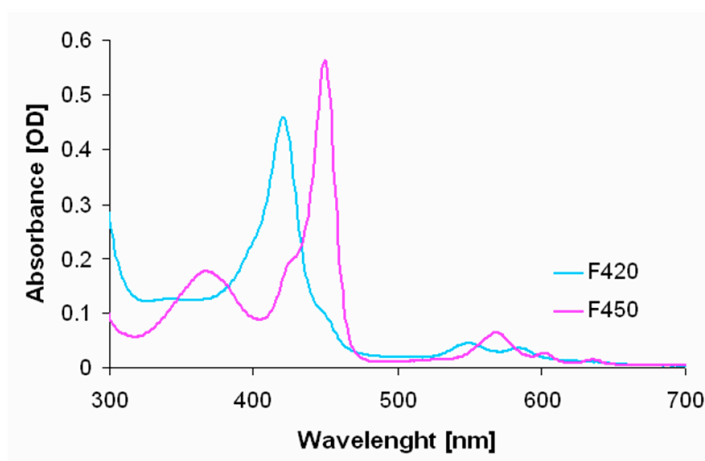


Figure 27. Absorption spectra of two fractions of zinc substituted cytochrome P450_{cam} collected at different elution times. The fraction containing primarily form F420 is shown in blue, fraction containing form F450 in red.

Similarly, the fluorescence spectrum of form F420 has the appearance that is characteristic of zinc substituted heme proteins, with maxima at 592 nm and 646 nm. In contrast, the fluorescence of the F450 is considerably red shifted, with maxima at 606 nm and 667 nm (Figure 28, Appendix 2). Both forms exhibit delayed fluorescence. Form F420 has weak phosphorescence at 723 nm with a long lifetime of approximately 7-14 ms, depending on the preparation and experimental conditions, characteristic also for other zinc proteins.¹⁶ The phosphorescence of form F450 at 768 nm is much more intense, probably at least in part as a result of the large S_1 - T_1 gap and hence slower repopulation of the S_1 state. Excitation at 450 nm produces exclusively the F450 T_1 state and as a result the phosphorescence decay is purely monoexponential, with $\tau_{F450} = 1.67$ ms (Figure 29).

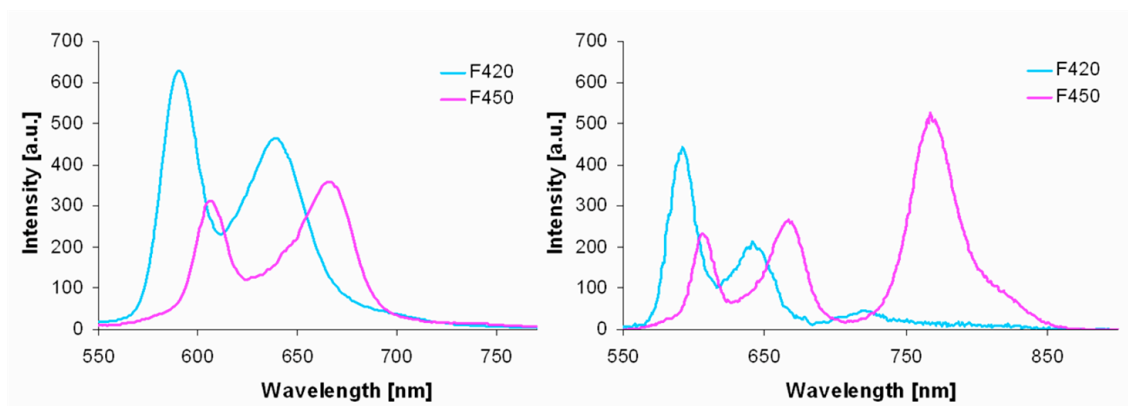


Figure 28. Fluorescence (left) and phosphorescence (right) spectra of ZnP450_{cam} fractions collected at different elution times. Emission spectra of fraction containing primarily form F420 excited at 420 nm are shown in blue, emission spectra of fraction containing form F450 excited at 450 nm is shown in red.

Due to the spectral overlap excitation at 420 nm always leads to a mixture of the F420 and F450 triplet states. As a consequence, the resulting phosphorescence decay is biexponential and consists of a major 10 ms component that belongs to the form F420, as well as a minor short-lived F450 contribution with the aforementioned $\tau_{F450} = 1.67$ ms. The unusually short triplet state lifetime at room temperature and the large S-T splitting found for form F450 are not consistent with the other Zn-substituted cytochromes. In contrast, the S-T gap as well as the triplet lifetime of form F420 is very similar to those of ZnCC (Table 1).

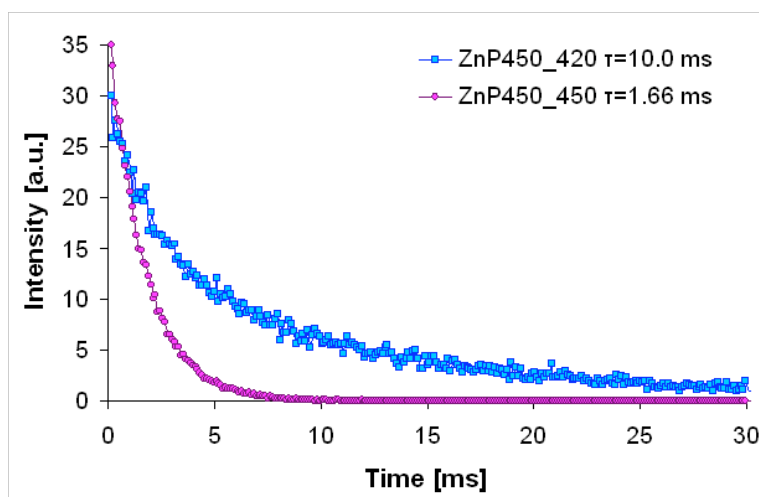


Figure 29. The triplet-state lifetimes measured on a 1:2 mixture of forms F420 and F450 of ZnP450_{cam} excited at 420 nm (blue) and 450 nm (red) and monitored at 590 nm and 768 nm, respectively. The amplitudes at $t = 0$ were normalized.

Table 4. Absorption and emission maxima of zinc substituted heme proteins: F450 and F420 – the forms of zinc substituted cytochrome P450; ZnCC- zinc substituted cytochrome c; ZnMb- zinc substituted myoglobin. The most relevant wavelengths are highlighted in boldface.

		Absorption				Fl ^q (S)		Ph ^a (T)	S-T gap
F450^r	nm	367	449	568	602	607	669	768	--
	cm ⁻¹	27200	22300	17600	16600	16500	14900	13000	3500
F420^{r, s}	nm	340	424	551	584	592	641	723	--
	cm ⁻¹	29900	23800	18200	17100	16900	15600	13800	3100
ZnCC ^t	nm	346	423	549	584	591	644	726	--
	cm ⁻¹	28900	23600	18200	17100	16900	15500	13800	3100
ZnMb ^u	nm	356	428	553	595	595	647	735	--
	cm ⁻¹	28100	23400	18100	16800	16800	15500	13600	3200

^q Abbreviations used in this table: Fl – fluorescence; Ph – phosphorescence.

^r This work

^s The F420 is more sensitive to environmental changes, few nm shifts (± 2 nm) in absorbance spectrum was observed if the pH or ionic strength changed.

^t H. Anni, J. M. Vanderkooi, and L. Mayne *Biochemistry* 1995, *34*, 5744-5753.

^u S. Papp J. M. Vanderkooi, Owen, C. S., Holtom, G. R., and Phillips C. M. *Biophys. J.* 1990, *58*, 177-186.

We determined that the initial ratio of F420/F450 depends on the concentration of camphor during the exchange of the prosthetic group (Figure 30). The substitution was performed in the presence of different camphor concentration (0 – 1 mM) and under all conditions that we have explored, the F450 is more abundant. The F420 content was higher at lower camphor concentrations. The ratio F420:F450 changed from 1:2.8 to 1:1.4 when camphor was eliminated from all buffers used in substitution. The F420:F450 ratio in fractions used for the electron and energy transfer studies was kept close to 1:2. In this case substitution was performed in the presence of 0.1 mM camphor. The amount of form F450 changed if additional camphor was introduced to the protein solution which was substituted and processed without camphor (Figure 31). Goodin *et al.*⁵⁷ similarly observed that redissolving a crystal of the “open conformation” of the native P450_{cam} yielded a mixed solution of P420 and P450. The resulting equilibrium was shifted if additional camphor was introduced into the solution. On the other hand, F450 to F420 conversion was observed when imidazole was present in the protein solution. The structure of the wild-type P450_{cam} crystallized with imidazole is very similar to the substrate-free conformation,⁷⁸ which suggests that the F420 is the open, substrate-free analog of native P450_{cam} while F450 is the closed, camphor bound form (Figure 16).

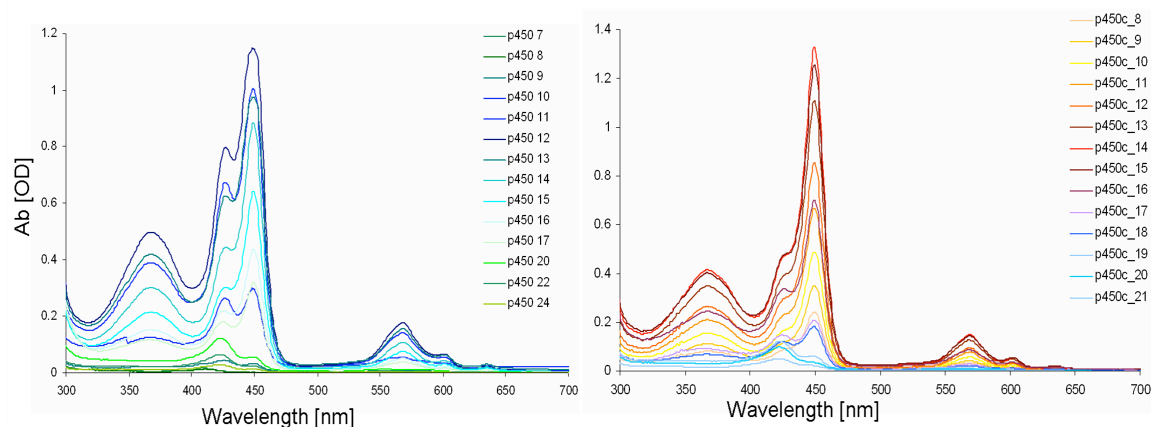


Figure 30. HPLC results for ZnP450 substituted in the absence (left) and presence (right) of camphor.

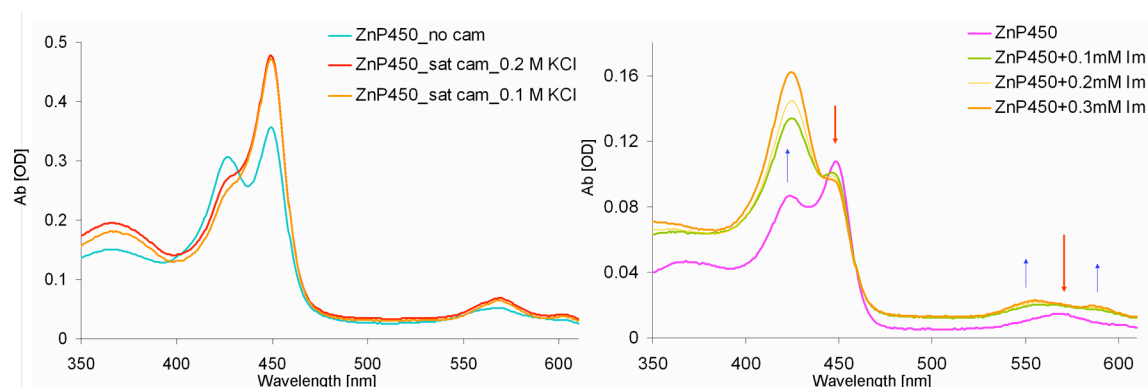


Figure 31. Left: absorption spectrum of ZnP450 after equilibration for 3 hours in the presence and absence of camphor and K^+ ions. Right: F450 to F420 conversion upon binding with imidazole.

In order to learn more about the conformers of $ZnP450_{cam}$, the magnitude of the solvent deuterium/hydrogen isotope effect on the triplet lifetime was measured. Since the prosthetic group in $P450_{cam}$ is located deep inside the protein channel, the magnitude of the isotope effect should reflect the ligand and solvent accessibility of the zinc porphyrin. Upon the H_2O to D_2O exchange an increase in triplet lifetime was observed for both forms (Figure 32, Table 5).

Table 5. Triplet state decay rates and deuterium isotope effects measured for both forms of ZnP450_{cam}.

	$k_{\text{H}_2\text{O}}$ [s^{-1}]	$k_{\text{D}_2\text{O}}$ [s^{-1}]	$k_{\text{H}_2\text{O}}/k_{\text{D}_2\text{O}}$
F450	602	484	1.24
F420	96	73	1.32

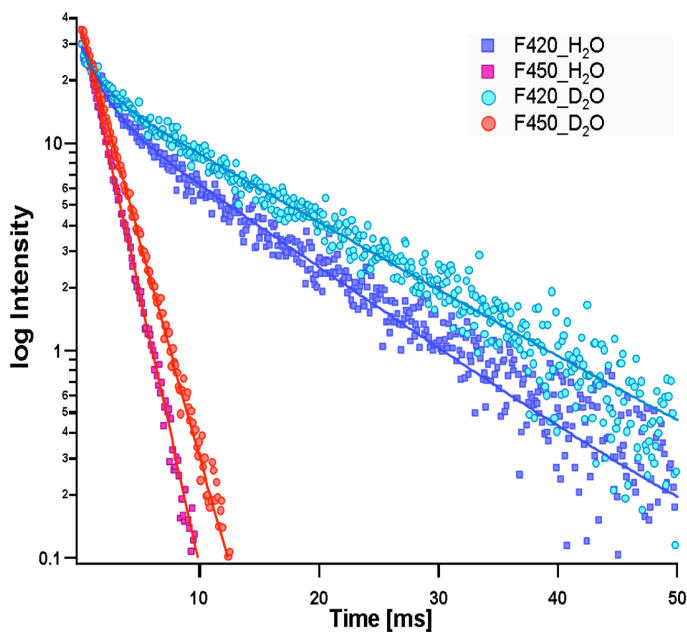


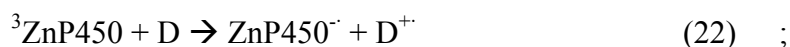
Figure 32. Normalized decay kinetics of $^3\text{ZnP450}_{\text{cam}}$ in H_2O and D_2O solutions of 40 mM KPi, 0.1 M camphor, $\text{pH} = \text{pD} = 7.4$, excited at 420 and 450 nm. As explained in the text, the F420 traces contain a small F450 contribution at early times.

The decay of $^3\text{F450}$ was somewhat less affected ($k_{\text{H}_2\text{O}}/k_{\text{D}_2\text{O}} = 1.2$) than that of $^3\text{F420}$ ($k_{\text{H}_2\text{O}}/k_{\text{D}_2\text{O}} = 1.3$) suggesting that the active site of F420 is more readily accessible to the solvent. This can mean that either the substrate channel in F450 is partially collapsed, or that the access to the porphyrin is blocked by an axial ligand coordinated to the Zn center. The earlier mentioned large bathochromic shift and the appearance of an intense hyper-band in F450 are also consistent with the presence of a strongly coordinating ligand in the axial position. It should be mentioned that both in the case of F420 and F450 the magnitude of the isotope effect is smaller than when the zinc porphyrin is fully exposed

to the solvent, as observed by Winkler *et al.*,⁷⁹ who for chemically denatured Zn-cytochrome *c* obtained $k_{\text{H}_2\text{O}}/k_{\text{D}_2\text{O}} = 1.5$.

Electron transfer reaction between ZnP450 and small organic ligands

Having demonstrated the existence of two forms of ZnP450_{cam} we used photoinduced electron transfer to evaluate the redox activity and ligand binding ability of forms F420 and F450. Since depending on the redox properties of its partner, ³ZnP450_{cam} can act either as an electron donor or acceptor it was possible to examine electron transfer from and to the triplet state of the protein. The general reaction scheme for the oxidative (21) and reductive (22) electron transfer quenching is shown below:



The selected acceptors, benzoquinone, duroquinone and chloranil form complexes with the protein and efficiently quench the phosphorescence of ³F450 and ³F420 (Table 6, Figure 33). Time-resolved photon counting measurements show that for all the acceptors the quenching is much more rapid for F420 than for F450. In both cases the measured rates follow the expected driving force dependence and increase with increasing driving force, suggesting that the ET reactions lie in the Marcus “normal region”.

Additionally, the presence of the acceptors causes changes in the protein absorption spectrum around 420 nm, which reflect the alteration of the immediate vicinity of the porphyrin (Figure 34). The changes are accompanied by a major decrease in the fluorescence intensity of F420 but much less so in the case of F450 (Figure 35, Table 7). The possibility that the observed reduction of fluorescence is due to Förster energy transfer can be excluded because quinones do not absorb light at the emission

wavelengths of F420 or F450. It is much more plausible that the lowering of the fluorescence yield is caused by fast electron transfer from the singlet state, which effectively competes with the intersystem crossing. Because of the limited time resolution of our photon counting setup, we were not able to fully resolve the fluorescence quenching dynamics.

Table 6. The thermodynamic parameters and the measured electron transfer reaction rates of both forms of $^3\text{ZnP450}_{\text{cam}}$.

	$E^{\text{red}} [\text{V}]^{\text{v}}$	ΔG^0	$k_{\text{ET}} [\text{s}^{-1}]$
F420 + DQ	-0.49^{w}	-0.43	2.0×10^3
F450 + DQ		-0.32	4.0×10^2
F420 + BQ	-0.16^{w}	-0.75	5.9×10^3
F450 + BQ		-0.64	8.2×10^2
F420 + CQ	0.32^{w}	-1.08	1.6×10^4
F450 + CQ		-0.97	7.0×10^3
	$E^{\text{ox}} [\text{V}]^{\text{v}}$		
F450 + Fc	0.55^{x}	0.24	0
F420 + Fc		0.13	3.6×10^3
F450 + Fc(COOH) ₂	0.64^{y}	0.33	0
F420 + Fc(COOH) ₂		0.22	2.0×10^2

^v Potentials versus normal hydrogen electrode.

^w A. P. Darmanyan, and W. S. Jenks, *J. Phys. Chem. B* 1999, 103, 3323-3331.

^x T. Kuwana, D. E. Bublitz, and G. Hoh, *J. Am. Chem. Soc.* 1960, 82, 5811-5817.

^y D. Quaranta, R. McCarty, V. Bandarian, and C. Rensing, *J. Bacteriol.* 2007, 189, 5361-5371.

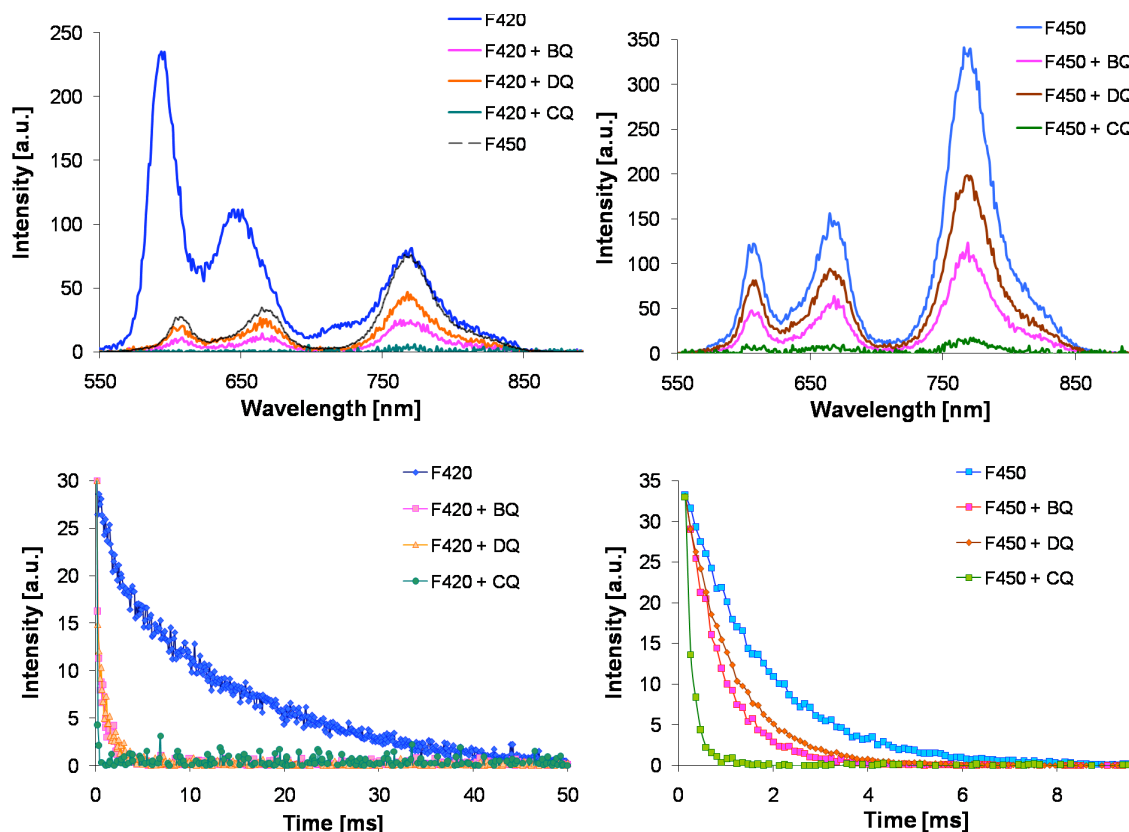


Figure 33. Phosphorescence spectra and normalized decay profiles of ZnP450 (1×10^{-6} M) in the presence of quinones (5×10^{-4} M) excited at 420 (left) and 450 nm (right) at pH = 7.4. Note that the phosphorescence of F420 is almost completely quenched in the presence of acceptors and that the residual emission observed upon 420 nm excitation (top, left) has the characteristics of $^3\text{F450}$ (black line).

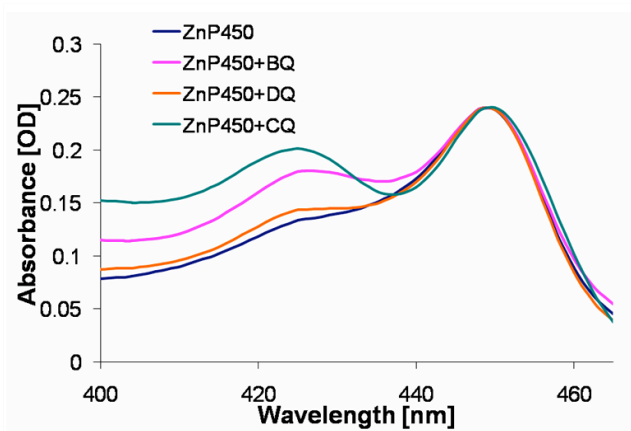


Figure 34. Changes in the appearance of the UV-Vis spectra upon addition of quinones (5×10^{-5} M) to ZnP450 (1×10^{-6} M).

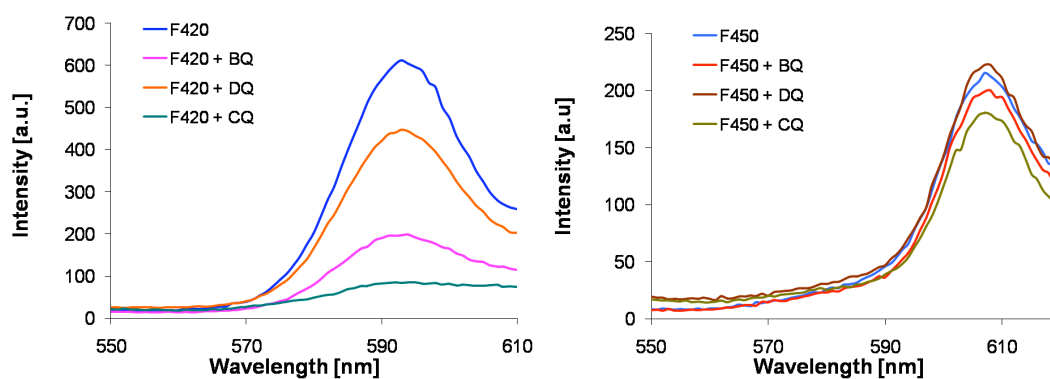


Figure 35. Fluorescence spectra of ZnP450_{cam} (1×10^{-6} M) excited at 420 nm and (left) at 450 nm (right) in aerated solution in the presence of quinones (5×10^{-5} M) at pH=7.4.

Table 7. Normalized fluorescence intensity of forms F420 and F450 in the presence of quinones.

	I/I_0
F420	1
F420+DQ	0.74
F420+BQ	0.34
F420+CQ	0.15
F450	1
F450+DQ	1.03
F450+BQ	0.92
F450+CQ	0.84

In addition to the oxidative ET quenching by the quinones, we also investigated the reductive quenching of the F420 and F450 triplet states by strong electron donors. The interaction of the photoexcited F420 with ferrocene and its more soluble derivative, ferrocene dicarboxylic acid, results in efficient reductive quenching of the protein triplet state. (Table 6, Figure 36).

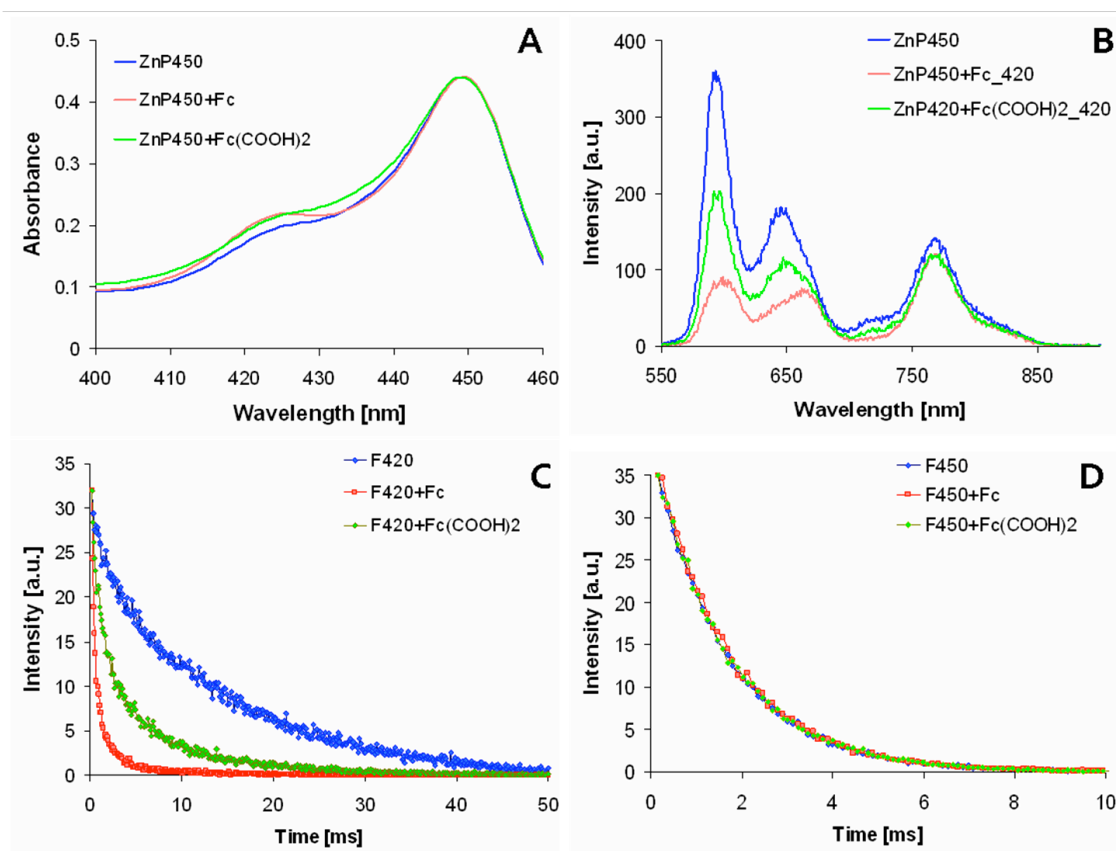


Figure 36. The results of reductive quenching of the excited state of $\text{ZnP450}_{\text{cam}}$ (1×10^{-6} M) in the presence of electron donors (saturated solution of ferrocene and 1.5×10^{-4} M solution of $\text{Fc}(\text{COOH})_2$ in 40 mM KPi, 0.1 mM camphor at pH = 7.4): (A) Absorption spectrum of $\text{ZnP450}_{\text{cam}}$; (B) phosphorescence spectrum of $\text{ZnP450}_{\text{cam}}$ excited at 420 nm; (C) phosphorescence decay of $\text{ZnP450}_{\text{cam}}$ excited at 420 nm and monitored at 590 nm; (D) phosphorescence decay of $\text{ZnP450}_{\text{cam}}$ excited at 450 nm and monitored at 768 nm.

In contrast, no quenching at all was observed for $^3\text{F450}$ in the presence of the same donors. These results could be explained by the difference in the driving force between the $^3\text{F450}$ and $^3\text{F420}$ reactions (both reductive ET reactions are slightly endothermic). However, the driving force in the $^3\text{F420}+\text{Fc}$ redox pair is nearly identical to the $\text{F450}+\text{Fc}(\text{COOH})_2$ pair. While in the first case the ET reaction is quite efficient, in the second one electron transfer does not proceed at all. This indicates that not only the

thermodynamic parameters but also other factors, such as the active site accessibility and the distance between the Zn-porphyrin and the redox partner, play a role in the quenching of the triplet state of the ZnP450's conformers. Indeed, if we use the Marcus equation to evaluate the D-A distance between the ferrocene and the zinc porphyrin in the form F420 we obtain separations of 7.6 to 8.3 Å for ferrocene and $\text{Fc}(\text{COOH})_2$, respectively. Naturally, such estimates are very sensitive to the driving force (Table 6), as well as the values of the total reorganization energy λ_{tot} and the distance attenuation factor β , which in our calculation were set to 1.1 eV and 1.1 Å.

It is worthwhile to point out that Fülöp *et al*⁸⁰ determined the crystal structure of an interesting post-translationally modified P450_{cam} bearing a covalently tethered ferrocene moiety, which was shown to fold deep into the substrate channel of the enzyme, with the closest part of ferrocene located 5.3 Å from the heme group,¹ corresponding to the Fe-Fe distance of approximately 7 Å, *i.e.* in a good agreement with our rough estimate based on the kinetics of the reductive electron transfer reaction.

The two conformations of ZnP450 exhibit widely differing electron transfer dynamics with the same redox partners. In the case of ZnP450_F420, the ET behavior is consistent with the binding of small hydrophobic redox partners deep inside the access channel of the enzyme, while the behavior of ZnP450_F450 suggests only a loose association with the ligand. Furthermore, form F420 exhibits the typical photophysical characteristics of other Zn-porphyrin proteins, including Zn-cytochrome *c* and myoglobin. The spectral properties and ET activity and of form F450 agree very well with the observations Morishima *et al*,⁵⁴ who found, very surprisingly, that the zinc substituted P450_{cam} did not at all undergo excited state ET reactions with small organic

redox ligands with dimensions similar to camphor.⁵⁴ Based on those results it can be concluded that form F420 corresponds to the open structure of the native cytochrome P450_{cam}, while form F450 has a closed or partially closed channel that is characteristic of the camphor-bound cytochrome P450_{cam}.

Bidirectional photoinduced electron transfer studies of zinc substituted cytochrome P450_{cam} with tethered ligands

The structural investigations of cytochrome P450 have shown protein conformational diversity in the presence of “wire ligands”.^{58,59} In these complexes, the protein displays more open structure compared to the camphor-bound stage similar to the protein conformation when it is weakly ligated with a water molecule. Spectroscopic evaluations of ZnP450 suggest structural changes also in the zinc substituted cytochrome P450_{cam} upon ligation of compounds possessing long hydrophobic tethers as coenzymes or FTMA (Figure 37 and 38). In the presence of selected ET ligands the protein absorption around 420 nm is enhanced and at the same time the one at 450 nm is reduced. As a result the fluorescence emission and excitation spectrum of the F420 change as well. The addition of coenzymes CoQ2 and CoQ4 increase the fluorescence intensity of F420, while FTMA causes decrease and 3 nm red shift in the ¹F420.

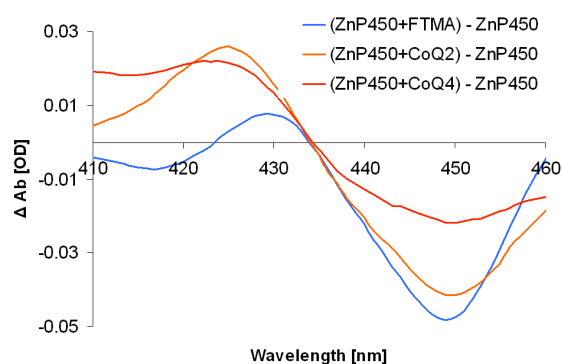


Figure 37. Protein absorption changes induced by the quenchers.

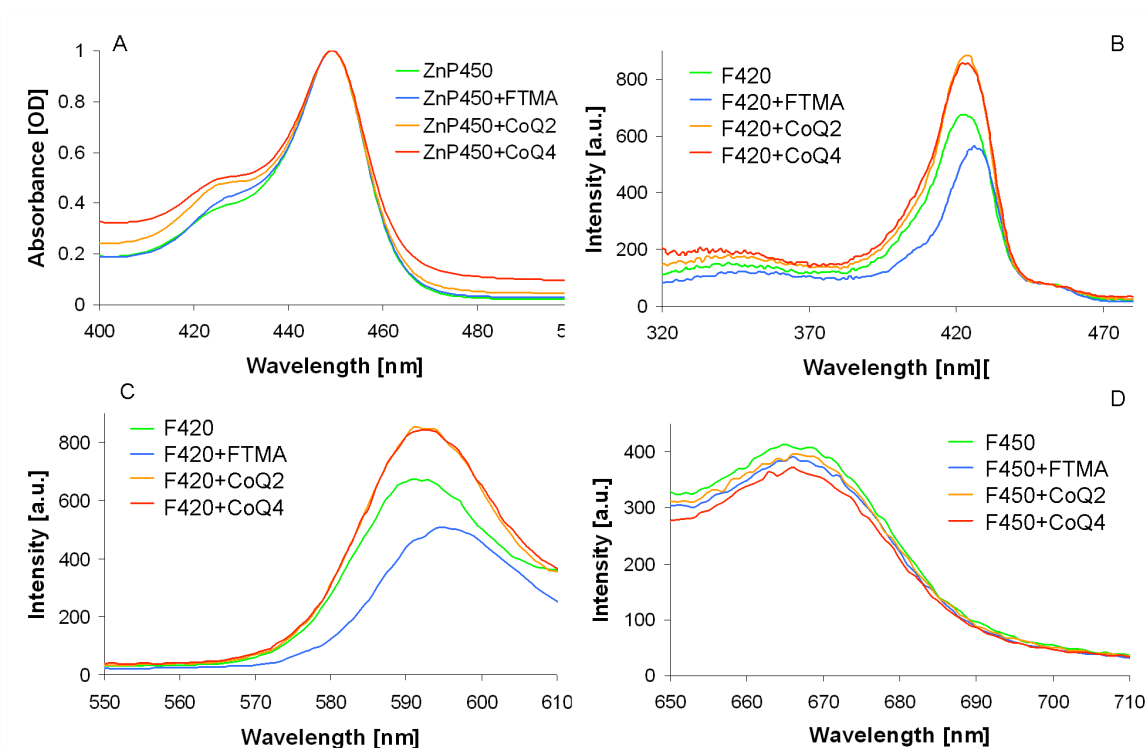


Figure 38. The quenching results for ZnP450_{cam} (1×10^{-6} M) in the presence of tather ligands (5×10^{-5} M) in 40 mM KPi, 0.1 mM camphor at pH = 7.4): (A) The absorption spectrum of ZnP450; (B) Fluorescence excitation of ZnP450, emitted at 590 nm; (C) Fluorescence emission spectra of ZnP450 (1×10^{-6} M) excited at 420 nm and (D) at 450 nm in the presence of FTMA, CoQ2 and CoQ4 (5×10^{-5} M) at pH=7.4.

In addition, the conformational conversions were monitored by titration of FTMA, which is much more soluble in aqueous buffers than coenzymes Q2 and Q4, or by titration of dodecyl trimethyl ammonium chloride (TMA) (Figure 39). In both cases as the substrate concentration increases in protein solution the absorption around 420 nm grows while diminishes at 450 nm indicating a transition from F450 to F420 structure.

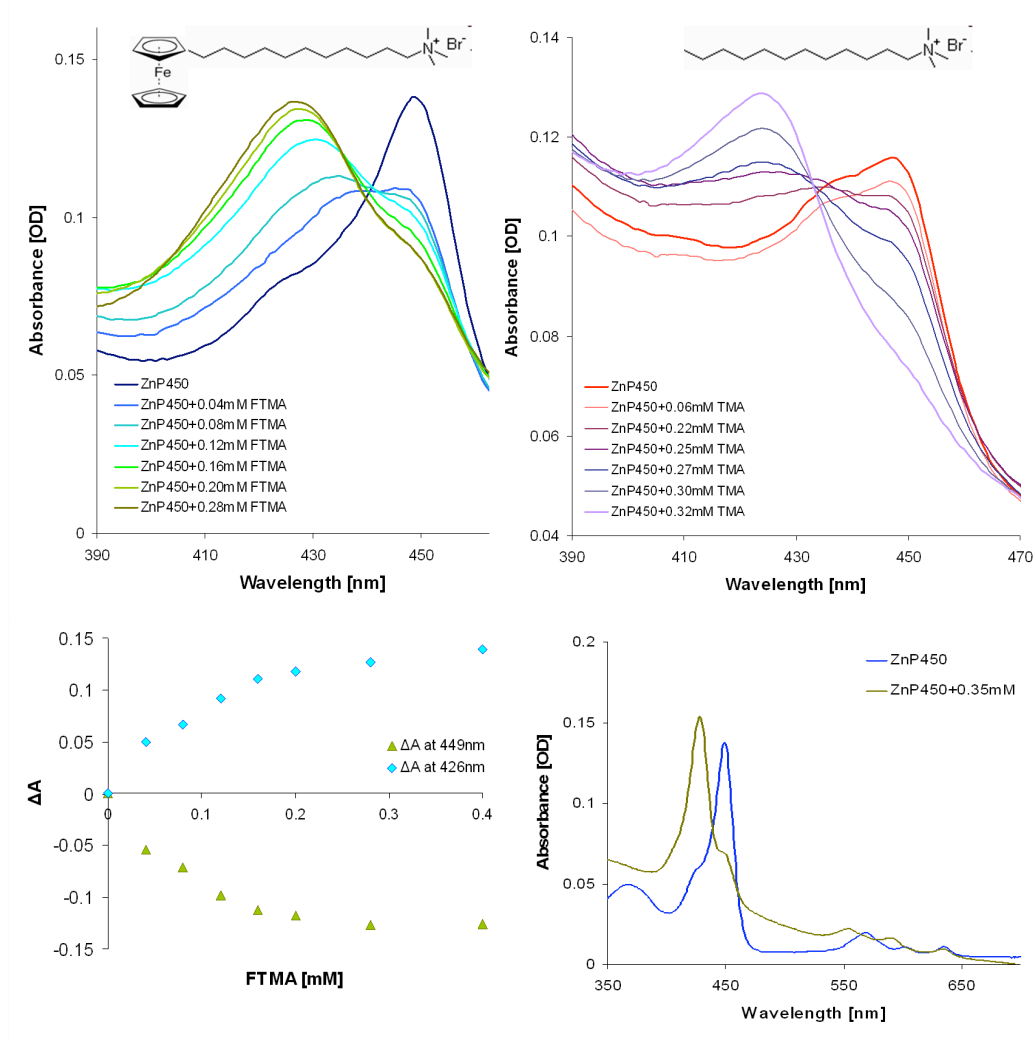


Figure 39. Titration of ZnP450 by FTMA (upper row, left) and TMA (upper row, right) in 40 mM KPi, 0.1 mM camphor at pH = 7.4, absorption differences (ΔA) of ZnP450+FTMA and ZnP450 at 426 and 450 nm and the spectrum of ZnP450 after equilibration with 0.35 mM FTMA (bottom).

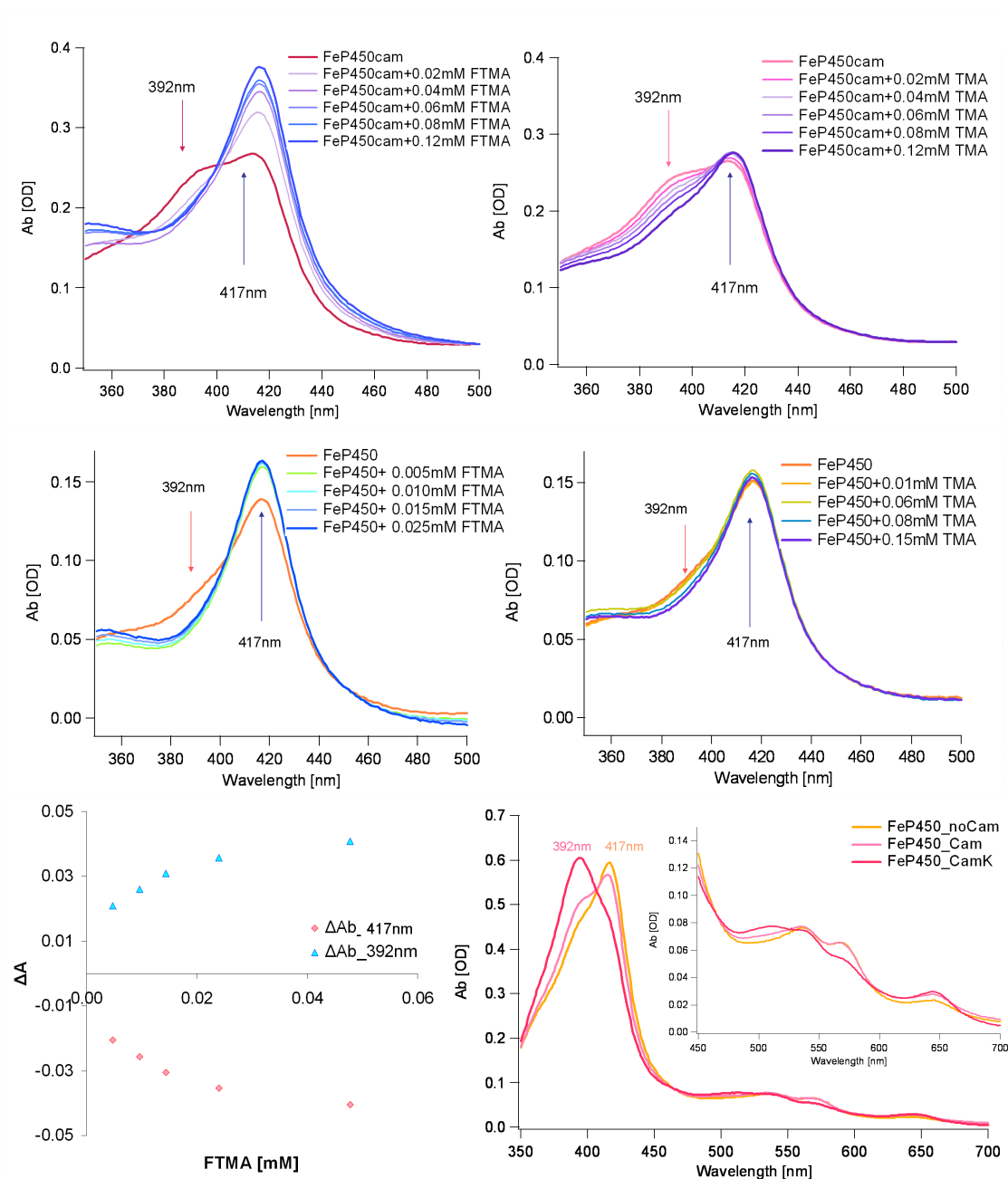


Figure 40. Titration of FeP450 by FTMA (left) and TMA (right) in 40 mM KPi, at pH = 7.4, with 1 mM camphor (FeP450_{cam}, upper row) or without camphor (FeP450, middle row); absorption differences (ΔA) of FeP450 and FeP450+FTMA at 392 and 417 nm (lower row, left) and the spectrum of FeP450 with (_Cam) or without (_noCam) camphor, as well as in the presence of 0.4mM K⁺ ions (_CamK) in 40 mM KPi, pH=7.4 (lower row, right).

The same titrations were also repeated for native P450 (FeP450) and as expected, the absorption at 392 nm, characteristic for camphor bound 5chs species, decreases while that at 418 nm, related to open 6cls FeP450, increases in the presence of FTMA or TMA (Figure 40).

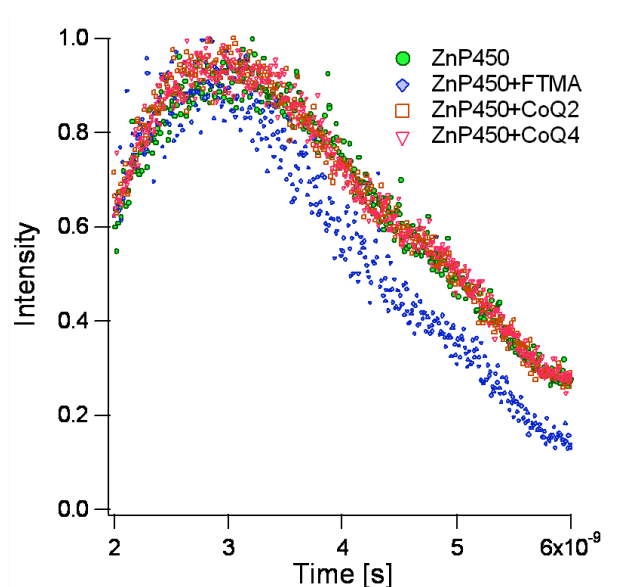


Figure 41. Normalized decay kinetics of $^1\text{F420}$ (1×10^{-6} M), excited at 420 nm and emission monitored at 590 ± 10 nm in the presence of quenchers (5×10^{-5} M).

Although the singlet state of F420 was affected by all three quenchers, time resolved measurements of the protein singlet state displayed a reduction of the $^1\text{F420}$ lifetime only in the presence of FTMA (Figure 41, Table 8, and Appendix 3). The shorter lifetime and lower fluorescence intensity in the presence of this substrate, as well as the fluorescence increase by coenzymes suggest some structural rearrangement due to ligation close to protein active site of F420 and confirm ligands association inside the protein channel.

Table 8. Fluorescence lifetime of F420 (when excited at 420 nm) and F450 (when excited at 450 nm) estimated by fitting to convoluted reference sample (± 0.1 ns) with single exponential functions (Supporting information, (Appendix 6, 7)).

	Fluorescence lifetime [ns]	
	F420	F450
ZnP450	1.2	0.3
ZnP450+FTMA	0.8	0.3
ZnP450+CoQ2	1.2	0.3
ZnP450+CoQ4	1.2	0.3

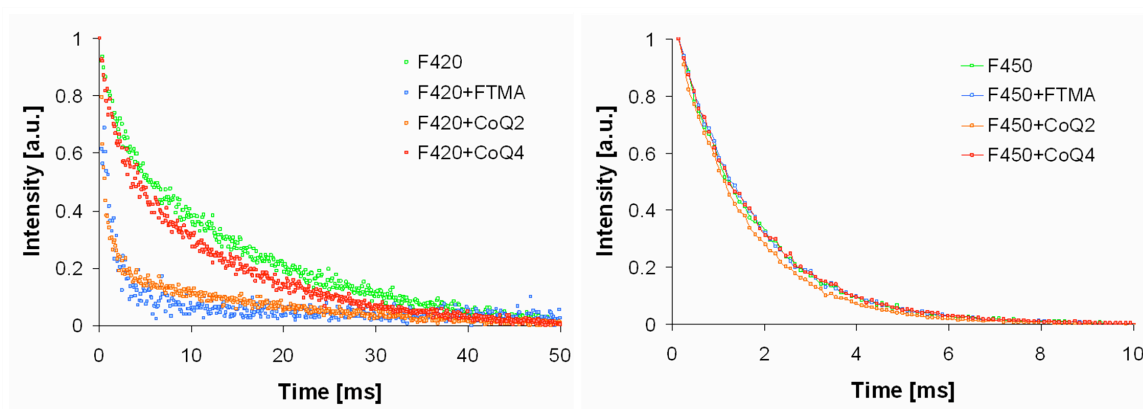


Figure 42. Normalized emission decay profiles of 2×10^{-6} ZnP450 in the presence of FTMA, CoQ2 and CoQ4 (5×10^{-5} M) when excited at 420 nm, with emission monitored at 590 nm (left) and when excited at 450 nm and emission monitored at 768 nm (right) at pH=7.4.

The fluorescence decay of $^1\text{F450}$ as well as phosphorescence lifetimes of F450 was unchanged in all studied complexes (Table 8, Figure 42 and Appendix 8). The minor decrease in emission intensity of F450 as a result of absorption changes ($450\text{nm} \downarrow$ and $420\text{nm} \uparrow$) upon the addition of coenzymes or FTMA imply ligation with F450 and conformational conversions of this form to the more open structure, the same as is also formed in F420 in the presence of these quenchers (Figure 43).

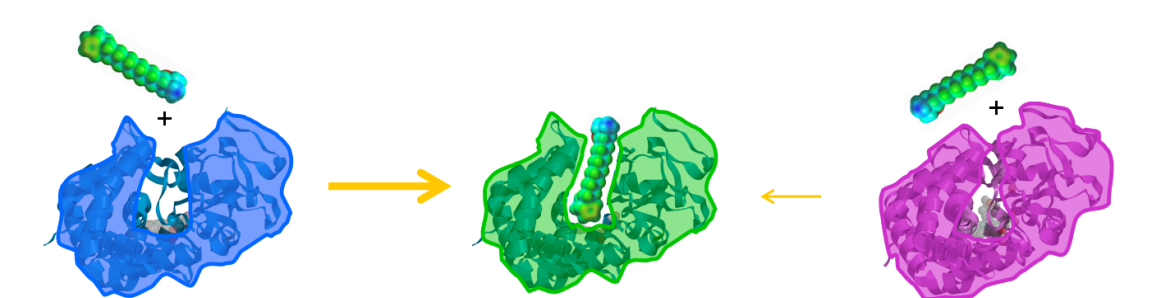


Figure 43. Ligand association with ZnP450. Both forms F420 and F450 display the same conformation upon ligation with a tether-bearing partner.

Due to the fact that ZnP450 associated with a quencher possesses similar spectral feature as the open form of ZnP450, the F420, all further presented results were obtained by excitation at 420 nm. Spectroscopic characterization of ZnP450 in the presence of redox inactive TMA (Appendix 5) indicates that association of a tether-bearing substrate inside the protein's channel alter the absorption spectrum, but does not change the phosphorescence lifetime, which is the same as in the sample without a quencher.

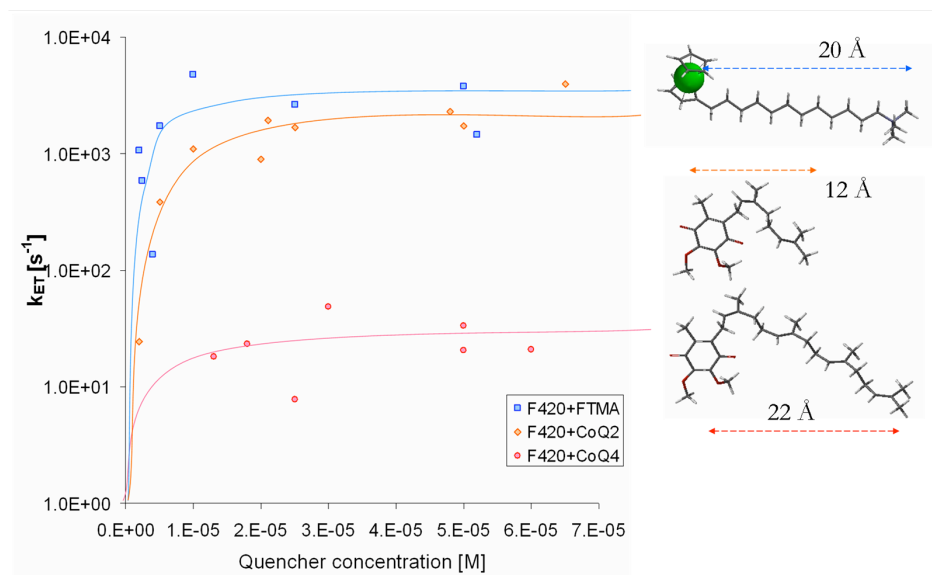


Figure 44. Concentration dependence of electron transfer kinetics of $^3\text{F420}$ (1×10^{-6} M) with FTMA, CoQ2 and CoQ4 at pH=7.4. Ligand structures and the tether lengths are shown on the right.

More detailed ET studies of protein triplet state were performed in various quenchers' concentrations (Figure 44). These data allow one to estimate maximum reaction rates (k_{ET}), association constants (K_a) and corresponding binding energies (E) for protein-quencher complexes (Table 9).

The traces in Figure 44 exhibit sharp initial increase of the quenching rate with the rising concentration of the quencher followed by a plateau. The increase is faster than would be observed for a diffusion controlled process, indicating ligand's association with the protein. In spite of the fact that the F420+CoQ2 complex is thermodynamically more stable than F420+FTMA, the determined maximum reaction rate in the presence of CoQ2 was almost two times slower than with FTMA. Moreover, FTMA appears to bind F420 more strongly than the coenzymes with the association constant $K_a = 1.3 \times 10^5 \text{ M}^{-1}$ and corresponding binding energy of $7.1 \text{ kcal mol}^{-1}$. The coenzymes CoQ2 and CoQ4, which vary from one another in the chain length by about 10 \AA , display similar ET kinetics with slightly higher binding energy in the case CoQ4. This can be explained by the longer chain and consequently larger hydrophobic area which is able to interact with the protein's active channel.

Table 9. Experimental rates, association constants, binding energies and thermodynamic parameters for the electron transfer reaction between $^3\text{F420}$ and the quenchers: FTMA, CoQ2 and CoQ4.

	$\Delta G^\circ [\text{eV}]$	$K_a [\text{M}^{-1}]$	$E [\text{kcal mol}^{-1}]$	$k_{ET} [\text{s}^{-1}]$	$\lambda_{Tot} [\text{eV}]$	$R_{DA} [\text{\AA}]$
F420+FTMA	0.23	1.3×10^5	7.1	3.2×10^3	1.1	5.8
F420+CoQ2	-0.62	6.9×10^4	6.6	1.5×10^3	1.2	18.1
F420+CoQ4	-0.62	8.7×10^4	6.7	2.8×10^1	1.2	21.7

The reactions rates obtained from the photoinduced ET measurements and the classical Marcus equation were used to estimate the donor-acceptor distances (R_{DA}) and consequently binding preferences for the ligands. The value of the attenuation coefficient β of 1.1 \AA^{-1} was determined by Gray *et al.*⁴⁸ on the basis of ET measurements on Fe^{III} -cytochrome *c* with electron donors covalently attached to specific sites on its surface. The magnitude of the reorganization energy for the ligand-protein complexes, $\lambda = \lambda_{\text{sol}} + \lambda_{\text{i}}$ was based on MO calculations and Born theory of solvation (Materials and Methods).

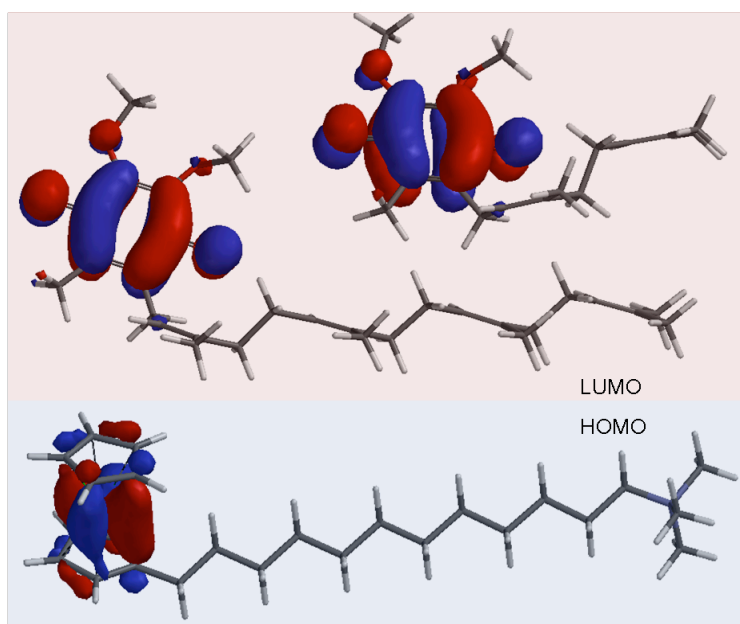


Figure 45. The relevant molecular orbitals participating in the ET reactions with ZnP450: HOMO of FTMA and LUMO of CoQ2 and CoQ4.

In the native P450_{cam} camphor is separated from the heme by about 4.3 \AA .⁸¹ Fülöp *et al.*,⁸⁰ who determined the crystal structure of P450 with the covalently attached ferrocene, showed that the closest part of ferrocene is located 5.3 \AA from the heme, corresponding to Fe-Fe distance of about 7 \AA . Our results suggest 5.8 \AA separation between F420 and FTMA, which is consistent with the value obtained by Fülöp *et al.*⁸⁰

As was shown in Figure 45, the relevant molecular orbitals participating in the ET reaction with F420 are located on the ligand “head” groups. The fact that the tail in the FTMA is 20 Å long and the calculated distance between Fe in FTMA and Zn from the porphyrin is less than 6 Å, indicates that this substrate enters the protein channel head-first, so the redox-active ferrocene is positioned close to the protein active site. On the other hand the 18 Å and 22 Å distances obtained for the coenzymes CoQ2 and CoQ4, respectively, imply opposite orientation, with the hydrocarbon “tail” entering the channel. The smaller R_{DA} separation in the F420 + CoQ2 pair suggests deeper than with the CoQ4 penetration onto the protein’s channel. The illustration of ligand binding to ZnP450 is shown in Figure 46.

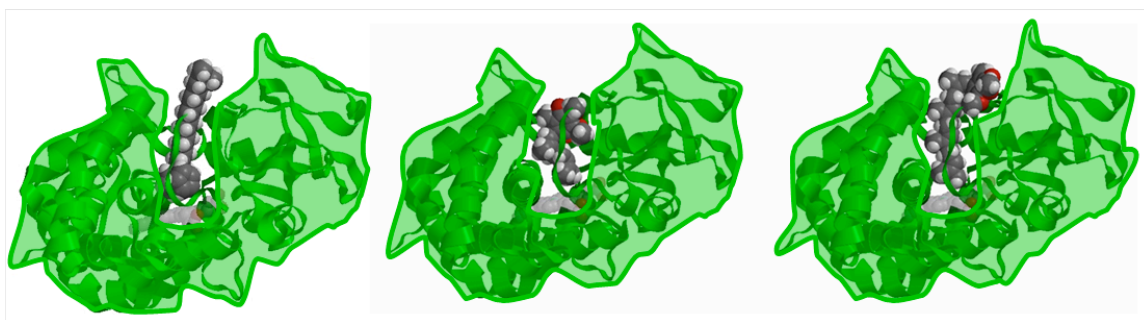


Figure 46. Proposed binding preferences of FTMA (left), coenzyme CoQ2 (middle) and coenzyme CoQ4 (right) to ZnP450 deduced from the ET results.

These binding preferences show that substrates are favored to enter the channel from their more hydrophobic side. If the quinones would associate with the protein from the head side- like FTMA does, both coenzymes should have very similar ET rates, both of which should be considerably higher than in the case of FTMA because of much larger driving force. Moreover, some changes in protein fluorescence lifetime should be seen as well as it was previously observed when the small quinones quenched the ZnP450 in the

direct vicinity of the active site (Figure 35, Table 7). The preferred orientation of FTMA does not come as a surprise, since one would expect that cationic tetraalkylammonium terminus to be more stabilized by the aqueous medium than by the hydrophobic pocket of the protein. However, the strong preference for the “tail-first” binding of coenzymes could not be as readily predicted and underscores the subtle nature of the protein ligand interaction.

Triplet - triplet energy transfer reactions of zinc substituted cytochrome P450_{cam}

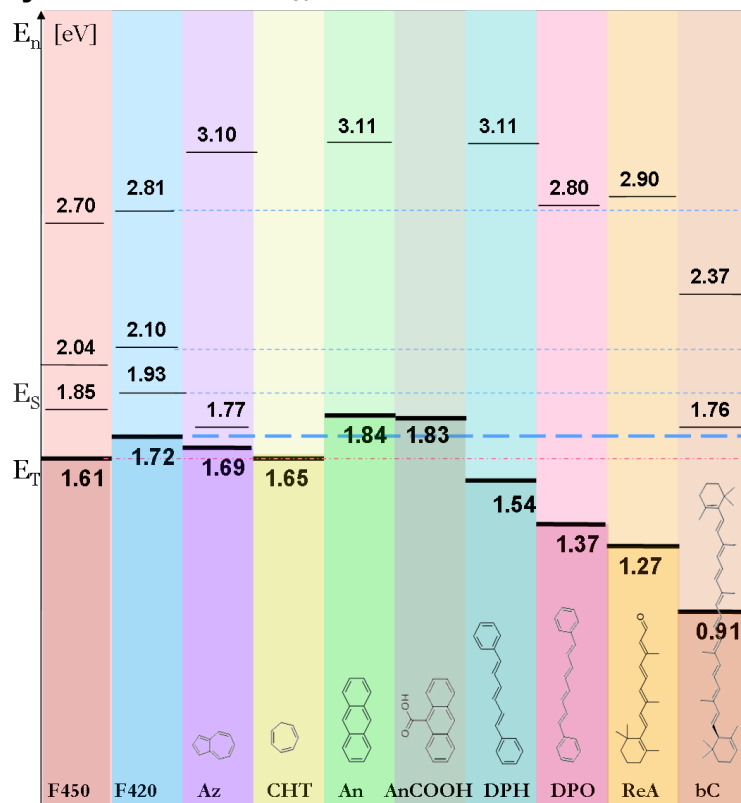


Figure 47. Energy levels of the triplet (E_T) and singlet (E_S) states of the selected acceptors and the F420 and F450 forms of ZnP450.⁸²

Figure 47 shows the energy levels of selected acceptors to illustrate the thermodynamic feasibility of TT energy transfer from $^3\text{ZnP450}$ to triplet states of these

quenchers. The TT energy transfer is possible from F420 as well as F450, thus spectroscopic properties of both forms were evaluated in the presence of these substrates. The TT ligands quenched only the triplet state of F420 with the highest reaction rate of 5.6×10^3 obtained in the presence of azulene (Figure 48, Table 10 and Appendix 9).

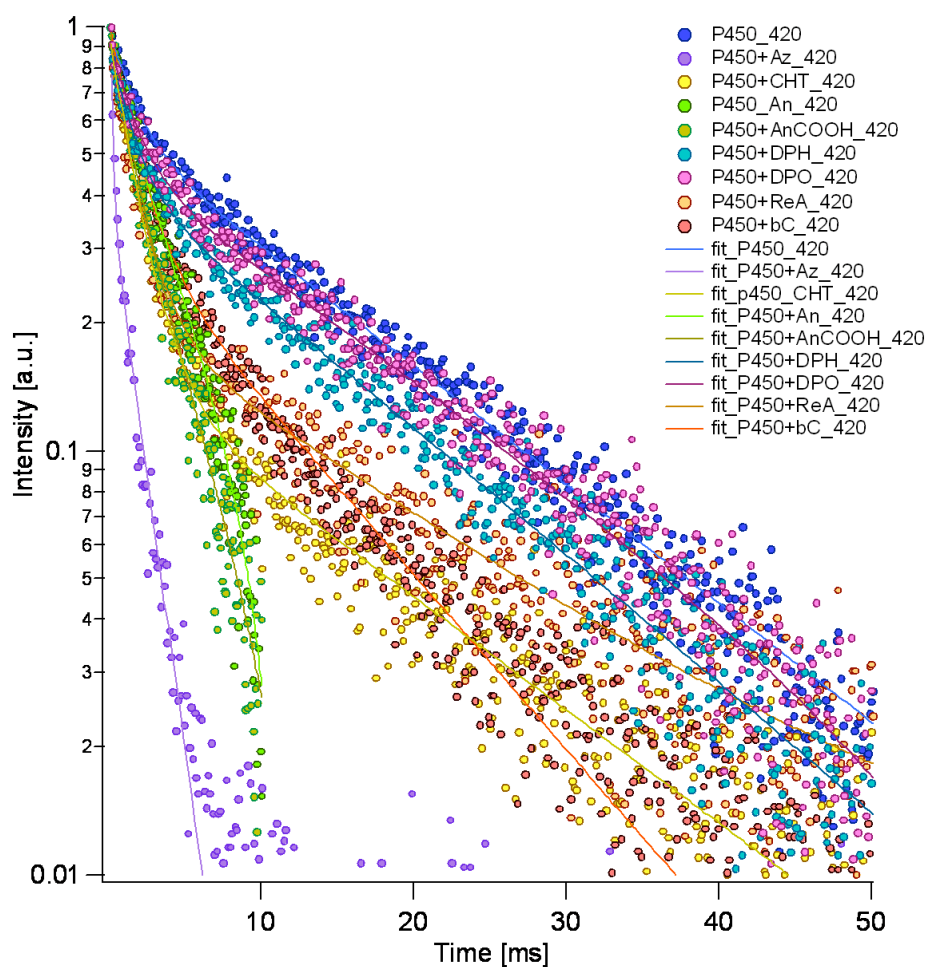


Figure 48. TT energy transfer results for $^3\text{F420}$.

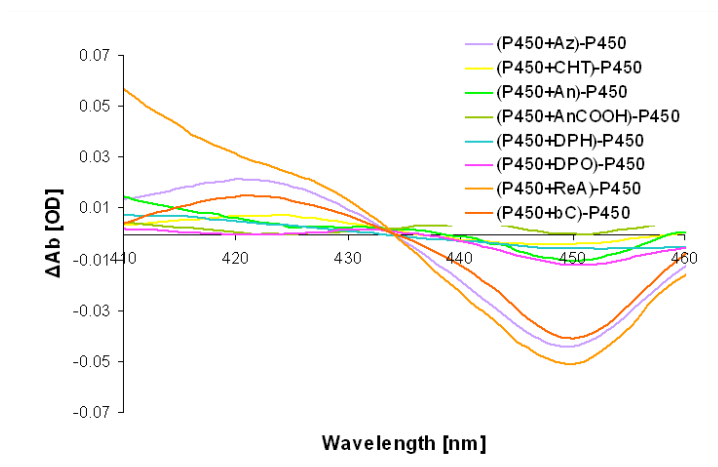


Figure 49. Absorption differences (ΔAb) of ZnP450+quencher subtracted from reference spectrum of ZnP450

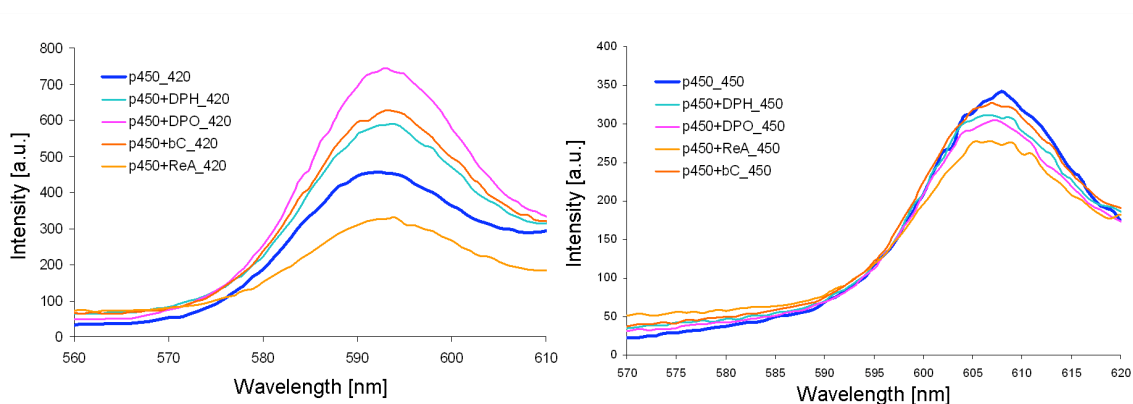


Figure 50. Fluorescence spectra of ZnP450 excited at 420 (left) and 450nm (right) in the presence and absence of triplet energy acceptor.

As in previous ET studies, the quenchers affect the protein absorption and emission spectra. In the presence of energy acceptors the absorption around 420 nm increases while the one at 450 nm is reduced (Figure 49). Additionally, some changes in the fluorescence intensity of F420 and minor alteration in $^1F_{450}$ are seen as well (Figure 50). In the case of DPO, DPH and β -carotene, the fluorescence of F420 is intensified while in the presence of retinal the emission of $^1F_{420}$ is suppressed. In all cases these suggest some changes close to porphyrin center of F420. Since the triplet- triplet energy transfer

(TT) occurs via overlap of electron clouds, these spectral variations indicate ligand associations in the direct vicinity of protein active site.

The temperature dependence studies of protein triplet state in the presence of quencher indicates temperature dependents of electron exchange energy transfer and linear decrease of $\ln(k_{TT})$ versus $1/T$, as shown in Figure 51 for F420+Az complex.

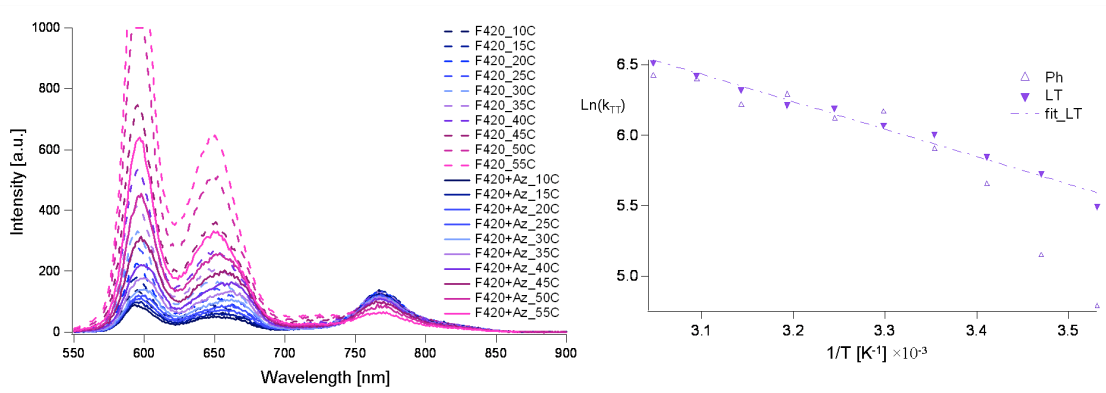


Figure 51. Temperature dependent triplet energy transfer in the F420+Az complex.

As in ET, the rate of TT may be described by the nonadiabatic Marcus formalism and can be expressed by coupling matrix element V , free energy of reaction ΔG° and the reorganization energy λ . In contrast to electron transfer, triplet energy transfer does not involve a major redistribution of charges between the donor and the acceptor. As a result the the solvent reorganization energy λ_{sol} is much smaller, less than 5 kcal/mol.⁸³ We have assumed that it constitutes about 10 % of total reorganization energy and used the average value of the internal reorganization energy for the entire set of donors and acceptors, $\lambda_{sol} \approx 0.1\text{eV}$. On the other hand, the magnitude of λ_i associated with the $S_0 \leftrightarrow T_1$ transitions is much larger and dominates the overall reorganization energy in triplet transfer. The total reorganization energies for each F420-triplet acceptor complex are summarized in Table 10. Since the TT reaction is a simultaneous electron and hole

transfer, the distance decay constant β_{TT} is a sum of distance decay constant for these processes ($\beta_{HT} + \beta_{ET}$).^{38,39} With this in mind, if the distance decay constant in biomolecules is close to 1 \AA^{-1} ,⁴⁵ it can be concluded that the distance decay constant for the protein- triplet acceptor will be doubled, $\beta_{TT} = 2 \text{ \AA}^{-1}$. The center-to-center donor-acceptor separations calculated based on this approximation are shown in Table 10.

Table 10. Energy transfer rates (k_{TT}), ΔG°_{TT} and donor-acceptor separation (R_{DA}) for $^3\text{F420}$ –triplet energy acceptor complexes.

	$k_{TT} [\text{s}^{-1}]$	$\Delta G^\circ_{TT} [\text{eV}]$	$\lambda_{Tot} [\text{eV}]$	$\ln (V[\text{eV}])$	$R_{DA} [\text{\AA}]$
F420+Az	5.6×10^3	-0.03	0.86	-10.48	6.7
F420+CHT	2.9×10^2	-0.07	1.32	-10.02	6.4
F420+An	2.1×10^2	0.12	0.92	-10.26	6.5
F420+AnCOOH	3.4×10^2	0.11	0.90	-10.24	6.5
F420+DPH	4.8×10^1	-0.18	1.29	-12.01	8.4
F420+DPO	2.9×10^1	-0.35	1.38	-13.18	9.6
F420+ReA	2.2×10^2	-0.45	1.51	-12.13	8.6
F420+bC	1.7×10^2	-0.81	1.72	-13.63	10.1

The obtained results divide examined quenchers into two groups: for Az, CHT, and anthracene derivatives the triplet transfer occurs in 6 -7 \AA range, while complexes of DPO, DPH, ReA, bC with F420 have the R_{DA} close to 8 - 10 \AA . In the case of small cyclic compounds the obtained results clearly imply association in a manner similar to the protein's natural partner. The distances obtained for the long wire like ligands can be explained by examining on ligand's spin density.

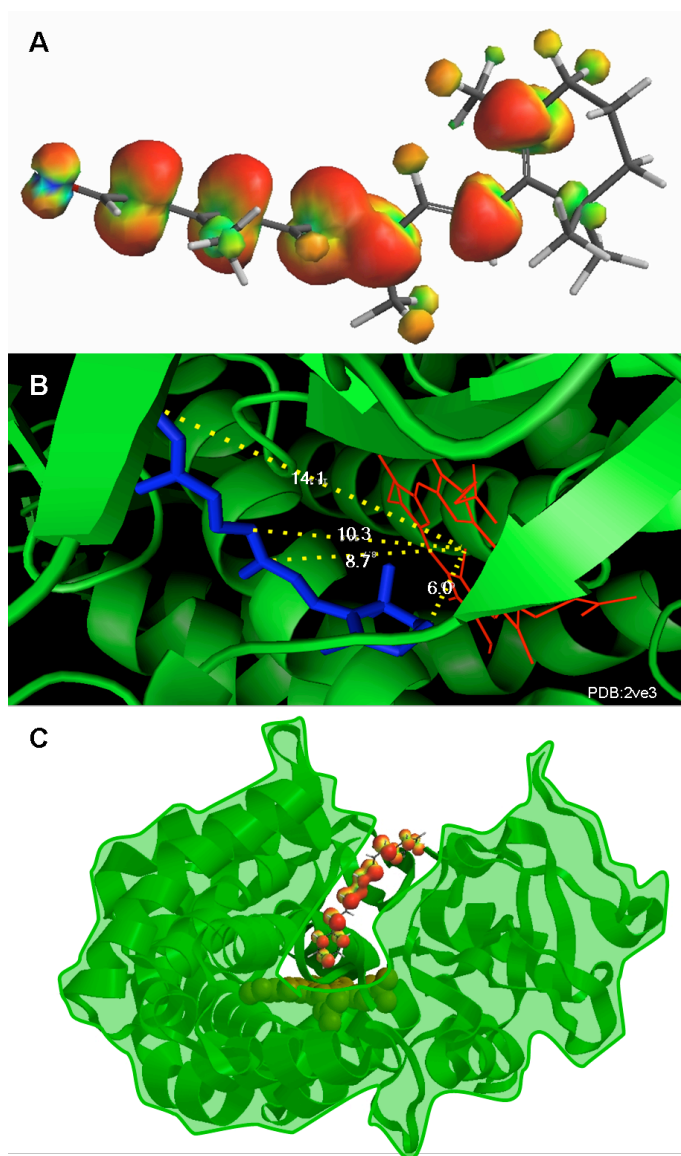


Figure 52. Spin density distribution in retinal molecule (A); retinoic acid association inside the hydrophobic channel of cytochrome P450 (CYP120A1), PDB: 2VE3⁸⁴ and (C) propose ligand association with ZnP450: DPO with its spin density (orange) inside the protein hydrophobic channel (PBD: 3L62).

The relevant electrons density is delocalized quite uniformly along the entire length of the tether (Figure 52A). As a result, the coupling is very effectively mediated by the chain from either end of the acceptor. In this respect they are very different from the coenzymes, in which the charge was well localized on the quinone. If we look at the

structure of native cytochrome P450 (Figure 52B) crystallized in the presence of retinoic acid determined by Schlichting *et al.*⁸⁴ we notice that those orbitals are about 7-14 Å away from the porphyrin center, which qualitatively agree with our calculations (Figure 52C). What is interesting, that in contrast with the coenzymes, in which the head group is slightly polar, retinal binds “head-first”, i.e. in opposite orientation than the coenzymes, once again, pointing to a very delicate balance of interactions between the protein and the ligand.

More detailed analysis of these data leads to additional conclusions. The coupling matrix for F420-triplet acceptor complex calculated from the experimental rate and Marcus equation (Table 10) is higher for small triplet acceptor than for tether ligand, as shown in Figure 53.

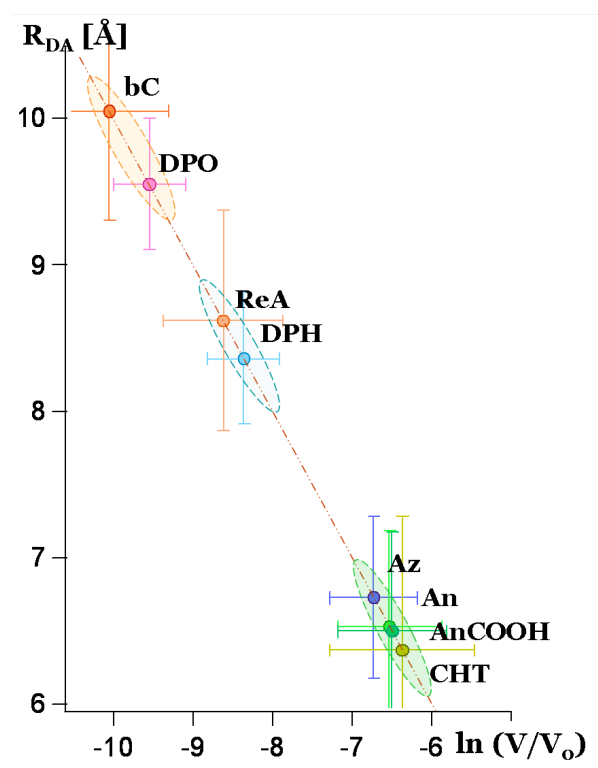


Figure 53. The logarithm of (V/V_0) versus donor- acceptor separation (R_{DA}).

If the distance dependence of coupling matrix H_{AB} is given by equation 23:

$$\ln \frac{H_{DA}}{H_0} = -\frac{\beta}{2}(R - R_0) \quad (23)$$

where the R_{DA} is expressed as $(R - R_0)$, R is the edge-to-edge distance between the porphyrin of ZnP450 and triplet acceptor, H_0 is the coupling matrix element for a donor-acceptor pair at van der Waals separation. When H_0 is the value of H_0 then $R = R_0$, which has been here defined to be 3.67 Å.

By looking at the acceptor spin distributions, and its ΔG°_{TT} , it could be also conclude that ReA will bind to F420 in similar manner as bC, and DPH more like DPO, which is not observed. These results suggest that the length of a tether chain in quenchers and at the same time the range of hydrophobic interactions between the probe molecule and the enzyme are the key factors that influence ligand association inside the protein hydrophobic channel.

2.3 Conclusions

Spectroscopic investigation of carefully and repeatedly purified ZnP450 revealed the existence of two forms of substituted cytochrome P450_{cam}, form F450 and F420, which possess different photophysical and photochemical properties. While it is difficult to draw definitive conclusions about the structure of forms F420 and F450 on the basis of time resolved electron transfer experiments, the existence of two conformers with distinct spectroscopic signatures is consistent with the recent findings of Goodin *et al.*⁵⁷ who obtained X-ray structures of two forms of the native cytochrome P450_{cam}. Our spectroscopic and quenching results on ZnP450_{cam} correlate form F420 with the substrate

free, more open and flexible conformation of the native P450_{cam}, while form F450 appears to be more similar to Goodin's "closed" conformation of the enzyme.

Conformer F450, which has been the subject of an earlier electron transfer study, has an abnormal spectrum containing a red shifted Soret band and a strong hyper-band.¹² The hyper-band is characteristic of sulfur ligation to ZnPP and is indicative of cysteine ligation to the ZnPP in F450. The short lifetime of the T₁ state of F450 is also consistent with strong axial ligation. In contrast, variant F420 exhibits the classical spectroscopic properties and triplet excited state lifetime that are typical of other zinc substituted heme proteins such as Zn-cytochrome *c* and myoglobin.

The photoinduced electron transfer experiments of ZnP450 with small ligands display different ET behavior of the studied protein conformer, which is most striking in the case of ferrocene, which is the bulkiest among the studied redox partners. The oxidation of ferrocene is mildly endoergic for both F420 and F450 triplet states, yet in the case of F420 it proceeds with a rate of $3.6 \times 10^3 \text{ s}^{-1}$, while in the case of F450 it cannot be detected at all. Similarly, only F420 undergoes substantial fluorescence quenching in the presence of the quinones, showing that in the case of this conformer the electron transfer reaction competes effectively with the short lifetime of the S¹ state.

The ET studies of zinc substituted cytochrome P450_{cam} with ligands possessing hydrophobic chains demonstrated that the wire-like ligands induce conformational changes in ZnP450 similar to those observed in native P450_{cam}.^{57,58,61} The bidirectional ET studies of ³ZnP450 and the obtained ET rates allowed calculating D-A separations which are consistent with X-ray structure determination of related systems and indicate that the ligands prefer to enter the channel from their more hydrophobic side.

The properties of ZnPP and structure of ZnP450 with the active site located inside the long channel make this protein ideal for TT studies. The obtained D-A separations calculated from the measured TT rates agree very well with the distances determined from the X-ray structures of ligand-bound cytochrome P450, proving that triplet-triplet energy transfer can be used in a similar manner as FRET to evaluate short range interactions. To our knowledge this is the first example of applying intermolecular TT energy transfer to study biological systems.

The present contribution can be very useful for researchers who are interested in employing metal substitution in their studies of electron or energy transfer in cytochromes P450, as well for those who are interested in spectroscopic investigation of intra or intermolecular interactions.

2.4 References II

-
- ⁴⁹ S. Franzen, L. Kiger, C. Poyart, and J-L. Martin Heme photolysis occurs by ultrafast excited state metal-to-ring charge transfer *Biophysical Journal*, 2001, 80, 2372–2385.
- ⁵⁰ G. C. Wagner, M. Perez, W. A. Toscano Jr. and I. C. Gunsalus Apoprotein formation and heme reconstitution of cytochrome P450cam *J. Biol. Chem.* 1981, 256, 6262-6265.
- ⁵¹ C-A. Yu, and I. C. Gunsalus Cytochrome P450cam III. Removal and replacement of ferriprotoporphyrin IX *J. Biol. Chem.* 1974, 249, 107-110.
- ⁵² G. C. Wagner, I. C. Gunsalus, M.-Y. R Wang. and B. M. Hoffman Cobalt-substituted cytochrome P450cam *J. Biol. Chem.* 1981, 256, 6266-6273.
- ⁵³ M. H. Gelb, W. A. Toscano, Jr. and S. G. Sligar Chemical mechanisms for cytochrome P450 oxidation: Spectral and catalytic properties of a manganese-substituted protein *Proc. Natl Acad. Sci. USA* 1982, 79, 5758-5762.
- ⁵⁴ Y. Furukawa, K. Ishimori, and I. Morishima Electron transfer reactions in Zn-substituted cytochrome P450cam *Biochemistry* 2000, 39, 10996 -11004.
- ⁵⁵ K. Auclair, P. Moënne-Loccoz, and P. R Ortiz de Montellano Roles of the proximal heme thiolate ligand in cytochrome P450cam *J. Am. Chem. Soc.* 2001, 123, 4877-4885.
- ⁵⁶ O. Pylypenko and I. Schlichting Structural aspects of ligand binding to and electron transfer in bacterial and fungal P450s *Annu. Rev. Biochem.* 2004, 73:991–1018.
- ⁵⁷ Y-T. Lee, R. F. Wilson, I. Rupniewski, and D. B. Goodin P450cam visits an open conformation in the absence of substrate *Biochemistry* 2010, 49, 3412–3419.
- ⁵⁸ A. R. Dunn, I. J. Dmochowski, A. M. Bilwes, H. B., Gray, and B. R. Crane Probing the open state of cytochrome P450cam with ruthenium-linker substrates *PNAS* 2001, 98, 12420–12425.
- ⁵⁹ A. R. Dunn, A. M. Hays, D. B. Goodin, C. D. Stout, R. Chiu, J. R., Winkler, and H. B. Gray Fluorescent probes for cytochrome p450 structural characterization and inhibitor screening *J. Am. Chem. Soc.* 2002, 124, 10254–10255.
- ⁶⁰ A. M. Hays, A. R. Dunn, R. Chiu, H. B. Gray, C. D. Stout and C. B. Goodin Conformational states of cytochrome P450cam revealed by trapping of synthetic molecular wires *J. Mol. Biol.* 2004, 344, 455–469.

-
- ⁶¹ Y-T Lee, E. C. Glazer, R. F. Wilson, C. D. Stout, and D. B. Goodin Three clusters of conformational states in P450cam reveal a multistep pathway for closing of the substrate access channel *Biochemistry* 2011, 50, 693–703.
- ⁶² T. L. Poulos Cytochrome P450: molecular architecture, mechanism, and prospects for rational inhibitor design *Pharm Res.* 1988 5, 67-75.
- ⁶³ B. O. Yang, S. S. Pochapsky, G. M. Pagani, and T. C. Pochapsky Specific effects of potassium ion binding on wild-type and L358P cytochrome P450cam *Biochemistry* 2006, 45, 14379–14388.
- ⁶⁴ T. C. Pochapsky, T. A. Lyons, S. Kazanis, T. Arakaki and G. Ratnaswamy A structure-based model for cytochrome P450cam-putidaredoxin interactions *Biochimie* 1996, 78, 723-733.
- ⁶⁵ W. Zhang, S. S. Pochapsky, T. C. Pochapsky and N. U. Jain Solution NMR structure of putidaredoxin–cytochrome P450cam complex via a combined residual dipolar coupling–spin labeling approach suggests a role for Trp106 of putidaredoxin in complex formation *J. Mol. Biol.* 2008, 384, 349–363.
- ⁶⁶ S. Shaik and S. P. De Visser Cytochrome P450: Structure, Mechanism, and Biochemistry by Paul R. Ortiz de Montellano, 3rd edition, *Kluwer Academic/Plenum Publisher, New York* 2005, 48-49.
- ⁶⁷ H. Nohl, W. Jordan, and R. J. Youngman Quinones in biology: Functions in electron transfer and oxygen activation *Advances in Free Radical Biology and Medicine* 1986, 2, 211-279.
- ⁶⁸ K. I. Jankowska, C. V. Pagba, E. L. Piatnitski Chekler, K. Deshayes, and P. Piotrowiak Electrostatic docking of a supramolecular host-guest assembly to cytochrome c probed by bidirectional photoinduced electron transfer *J. Am. Chem. Soc.* 2010, 132, 16423–16431.
- ⁶⁹ H. J. Fromm, and M. Hargrove Essentials of biochemistry 1st Edition, *Springer-Verlag New York, LLC*, 2012, 224-228.
- ⁷⁰ E. Haas The study of protein folding and dynamics by determination of intramolecular distance distributions and their fluctuations using ensemble and single-molecule FRET measurements *Chem Phys Chem* 2005, 6, 858 – 870.
- ⁷¹ B. Fierz, K. Joder, F. Krieger, T. Kiefhaber Using triplet–triplet energy transfer to measure conformational dynamics in polypeptide chains *Methods Mol Biol* 2007, 350, 169-187.
- ⁷² W. C. Galley and L. Stryer Triplet-triplet energy transfer in proteins as a criterion of proximity *PNAS* 1968, 60, 108-114.

-
- ⁷³ C. A. Ghiron, J. W. Longworth and N. Ramachandran Triplet-triplet energy transfer in α -Trypsin *PNAS* 1973, 70, 3703-3706.
- ⁷⁴ B. P Unger, I. C. Gunsalus, and S. G. Sligar Nucleotide sequence of the *Pseudomonas putida* cytochrome P450cam gene and its expression in *Escherichia coli* *J. Biol. Chem.* 1986, 261, 1158-1163.
- ⁷⁵ G. L. Closs, L. T. Calcaterra, N. J. Green, K. W. Penfield, J. R. Miller Distance, stereoelectronic effects, and the Marcus inverted region in intramolecular electron transfer in organic radical anions *J. Phys. Chem.* 1986, 90, 3673-3683.
- ⁷⁶ J. Daub, R. Engl, J. Kurzawa, S. E. Miller, S. Schneider, A. Stockmann, and M. R. Wasielewski Competition between Conformational Relaxation and Intramolecular Electron Transfer within Phenothiazine-Pyrene Dyads *J. Phys. Chem. A* 2001, 105, 5655-5665.
- ⁷⁷ M. Di Valentin, A. Bisol, G. Agostini, P. A. Liddell, G. Kodis, A. L. Moore, T. A. Moore, D. Gust, and D. Carbonera Photoinduced Long-Lived Charge Separation in a Tetrathiafulvalene-Porphyrin-Fullerene Triad Detected by Time-Resolved Electron Paramagnetic Resonance *J. Phys. Chem. B* 2005, 109, 14401-14409.
- ⁷⁸ A. Verras, A. Alian and P. R. Ortiz de Montellano Cytochrome P450 active site plasticity: attenuation of imidazole binding in cytochrome P450_{cam} by an L244A mutation *Protein Engineering, Design & Selection* 2006, 19, 491-496.
- ⁷⁹ J. E. Kim, M. A. Pribisko, H. B. Gray, and J. R. Winkler, Zinc-porphyrin solvation in folded and unfolded states of Zn-cytochrome c *Inorg. Chem.* 2004, 43, 7953-7960.
- ⁸⁰ K. D. Gleria, D. P. Nickerson, H. Allen, O. Hill, L-L. Wong and V. Fülöp Covalent attachment of an electroactive sulfhydryl reagent in the active site of cytochrome P450cam as revealed by the crystal structure of the modified protein *J. Am. Chem. Soc.* 1998, 120, 46-52.
- ⁸¹ W. Yang, S. G. Bell, H. Wang, W. Zhou, N. Hoskins, A. Dale, M. Bartlam, L.-L. Wong, and Z. Rao Molecular Characterization of a Class I P450 Electron Transfer System from *Novosphingobium aromaticivorans* DSM12444 *The Journal of Biological Chemistry* 2010, 285, 27372-27384.
- ⁸² S. L. Murov, I. Carmichael, and G. L. Hug Handbook of Photochemistry, 2nd Edition, *Dekker, New York, USA* 1993.
- ⁸³ I. Place, A. Farran, K. Deshayes, and P. Piotrowiak Triplet energy transfer through the walls of hemicarcerands: Temperature dependence and the role of internal reorganization energy *J. Am. Chem. Soc.* 1998, 120, 12626-12633.

⁸⁴K. Kühnel, N. Ke, M. J. Cryle, S. G. Sligar, M. A. Schuler and I. Schlichting Crystal Structures of Substrate-Free and Retinoic Acid-Bound Cyanobacterial Cytochrome P450 CYP120A1 *Biochemistry*, 2008, *47*, 6552–6559.

Chapter 3. Electrostatic Docking of a Supramolecular Host-Guest Assembly to Cytochrome c Probed by Bidirectional Photoinduced Electron Transfer

Supramolecular assemblies continue to attract great interest in recent years due to their promising application in chemistry and biology. The concept of incarcerating small molecules into larger container compounds was introduced by Cram's group in the early 1980-ties.^{85,86} They synthesized the first carcerand, in whose interior organic molecules were trapped as permanent guests.⁸⁷ A few years later the same group reported a new class of container molecules called hemicarcerands which are capable of reversibly complexing guest compounds⁸⁸ and releasing them upon thermal activation, irradiation⁸⁹ or under chemical stimulus. Hemicarcerands are closed-shell fully encapsulating hosts.⁹⁰ They consist of two bowl-shaped units (cavitands) connected together by linking groups. The length of the linkers determines the size of cavity of the hemicarcerand and hence the maximum size of the guest that can be trapped inside.^{91,92} The linkers can be tailored to endow the hemicarcerand with the desired properties, e.g. solubility in a particular medium or photolability. When guests become imprisoned inside these molecular capsules, complexes called hemicarceplexes are formed. They are stabilized by "intrinsic" and "constrictive binding energy".^{93, 94} Intrinsic binding energy is the standard free energy difference due to the encapsulation within the host's cavity. It consists of both attractive and repulsive interactions between the host and the guest, as well as of the changes in the solvation energy of both partners. Depending on the balance of these interactions, its overall value can be negative or positive. "Constrictive binding energy" on the other hand is the energy barrier associated with the exit of the guest. If the barrier

is much higher than $k_B T$, the host-guest complex prepared at high temperature or pressure may persist for weeks and behave like a distinct, stable chemical species, even if the intrinsic binding energy is positive.

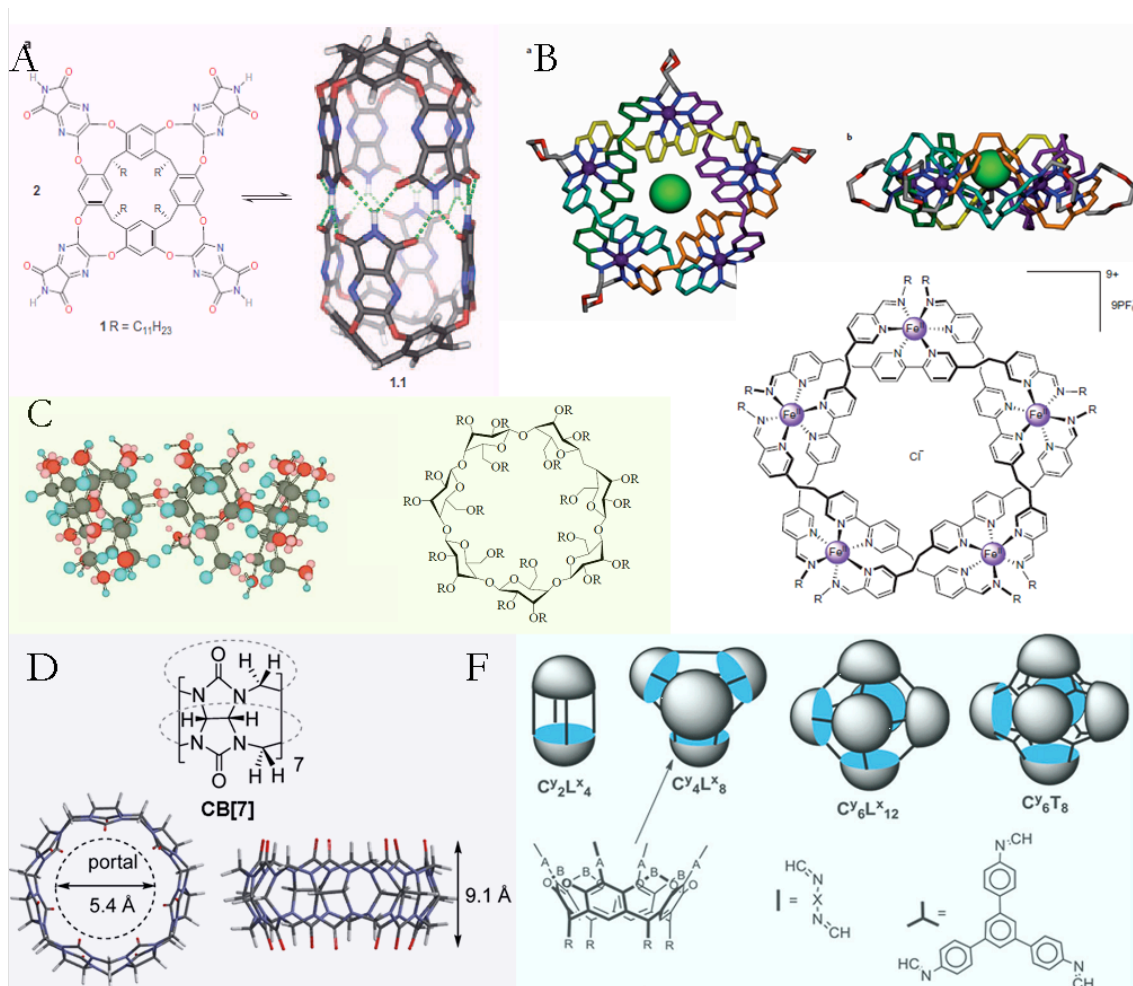


Figure 54. Examples of host molecules: (A) resorcinarene,⁹⁵ (B) knot,⁹⁶ (C) cyclodextrin,⁹⁷ (D) cucurbituril⁹⁸ (D) hemicarcerands and polyimine capsules made from cavitands C^y , and di- (L^x) and triamines T.⁹⁹

Hemicarcerands offer much tighter binding than cyclodextrins with ΔG^0 values of ~ 10 kcal/mol vs. ~ 4 kcal/mol,^{100,101} and far more complete protection of the guest from contact with the external environment. They are the only carriers that can fully insulate

small species such as for example the isotopes of I₂, Xe and Rn from the contact with biological medium. The size-selectivity of a hemicarcerand is much higher than that of liposomes, calixarenes or cyclodextrins. Many host molecules with diverse structures and applications were developed over the past decades (Figure 54). Nanoscale capsules large enough to accommodate multiple guests¹⁰² and self-assembling hydrogen-bonded molecular capsules that trap guest molecules in a reversible entropy-driven process were synthesized.¹⁰³ Encapsulation was used both to stabilize short-lived intermediates,^{104,105} as well as to accelerate the rates of chemical reactions and to control their regio- and stereoselectivity.^{106,107} The encapsulation within the hemicarcerand prevents damaging contact with molecular oxygen and blocks free radical quenching reactions such as hydrogen abstraction.¹⁰⁸ Moreover, electron and energy transfer mediated by the walls of hemicarcerands of different size and composition were investigated in solution^{109,83,110} and at interfaces.¹¹¹ More recently, the use of hemicarcerands in nanodevice fabrication¹¹² and in drug delivery¹¹³ has been demonstrated.

In this report we present the application of a Cram-type water-soluble octacarboxy-hemicarcerand¹¹⁴ (Figure 55) as a “molecular shuttle” capable of transporting hydrophobic molecules across the aqueous medium and binding to the target biomolecule. The cage contains two aromatic caps joined together by four phthalic acids. The eight carboxylic groups solubilize the molecule in the aqueous medium, as well as enable the association with basic partners via electrostatic attraction, while the aromatic interior provides the perfect hydrophobic shelter with spherical cavity of a diameter 11 Å and capacity of about 200 Å³. As a result, the water-soluble hemicarcerand spontaneously encapsulates small molecules within its hydrophobic void. Depending on the size and

polarity of the guest molecule the host-guest dissociation constants fall in the 10 nM - 100 μ M range, with binding free energies exceeding 10 kcal/mol in favorable cases.

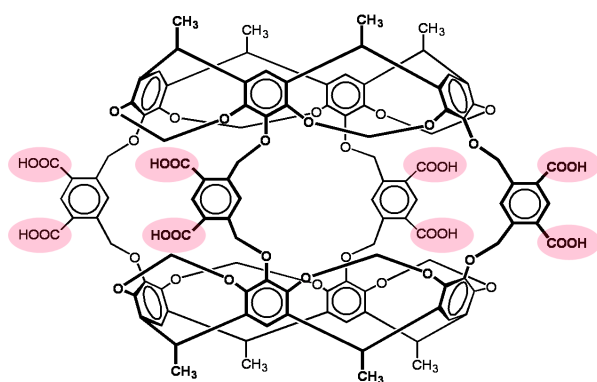


Figure 55. Cram-type water soluble hemicarcerand used in this study. Note four 1,3-methoxyphenyl linkers flanking the “portals” of the hemicarcerand and eight carboxylic group which solubilize it in the aqueous medium, as well as enable the association with basic partners.

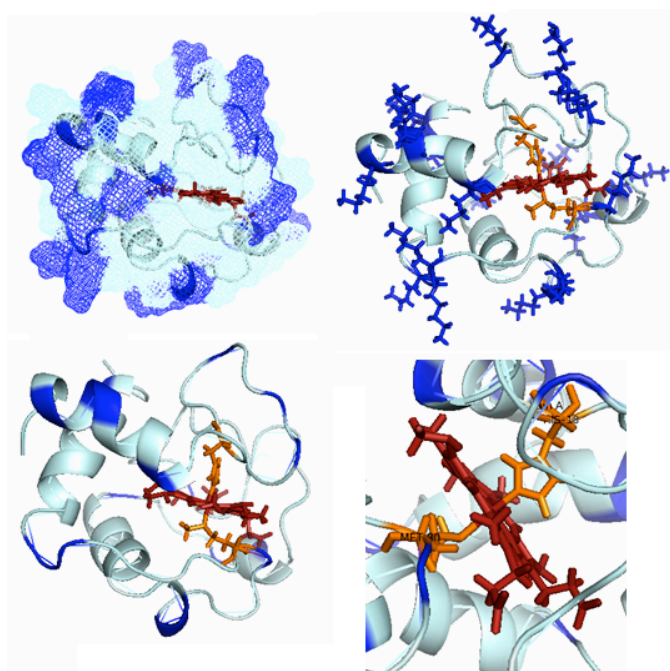


Figure 56. The X-ray structure of cytochrome *c* showing the basic lysine residues (blue) distributed on its surface (upper row) and the heme (red) axially ligated with histidine and methionine residues (orange) (PDB file: 1AKK).

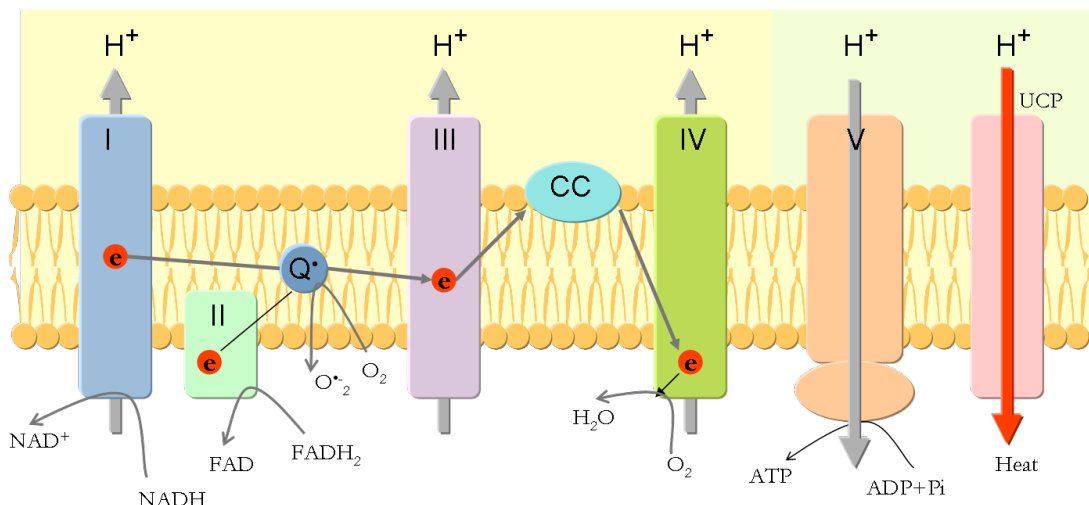


Figure 57. The mitochondrial electron-transport chain carried out by four inner membrane-associated enzyme complexes, cytochrome *c* and the mobile electron carrier ubiquinone (Q). NADH donates electrons to NADH:ubiquinone oxidoreductase (complex I). Then complex I transfer its electrons to ubiquinone Q. Ubiquinone can also be reduced by electrons donated from several FADH₂-containing dehydrogenases, including succinate:ubiquinone oxidoreductase (complex II) and glycerol-3-phosphate dehydrogenase. Electrons from reduced Q are then transferred to cytochrome *c* oxidoreductase (complex III) by the ubisemiquinone radical-generating Q cycle. Complex III transport the electron through cytochrome *c* to cytochrome *c* oxidase (complex IV) and, finally to molecular oxygen (O₂). Electron transfer through complexes I, III and IV generates a proton gradient that drives ATP synthase (complex V).¹¹⁵

When cytochrome *c* associates with the inner membrane of the mitochondrion, it plays an essential role in the electron transport chain and is responsible for accepting electrons from the b-c₁ complex (complexes III) and transfers electrons to the cytochrome oxidase complex (complexes IV).^{116,117,118} In the cytoplasm CC is involved in the initiation of apoptosis by binding to the apoptotic protease activating factor (Apaf 1).¹¹⁹

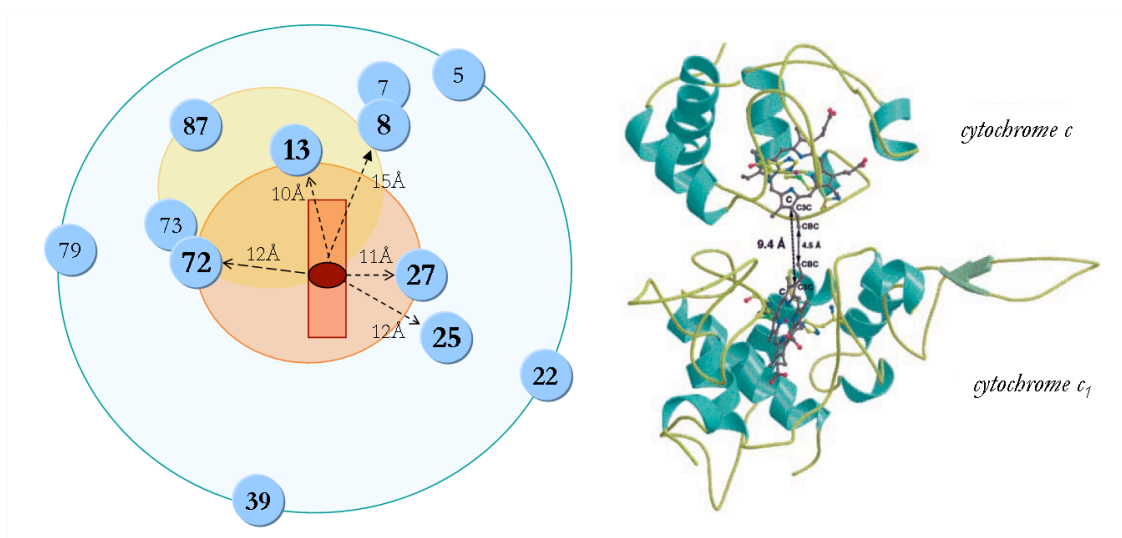


Figure 58. Left: Schematic planar projection of the front hemisphere of CC indicating the high affinity binding domain for cytochrome peroxidase (orange circle), cytochrome c oxidase (dark yellow) with some distances between the heme (red rectangular) and lysine residues involved in binding CC's partners (blue circle);¹²⁰ Right: The structure of cytochrome c-cytochrome c₁ complex determined by Lange and Hunte. Note that the short edge-to-edge distance (CBC) between cytochrome c and cytochrome c₁ is 4.5 Å, while the distance between the irons in their heme groups (center-to center) is 17.4 Å.¹²¹

The interactions of cytochrome c with its protein partners are driven primarily by electrostatic interactions. Cytochrome c is positively charged at neutral pH and contains 19 lysines and 2 arginines versus 12 acidic residues (glutamic or aspartic acid). The basic amino acids which are mainly located close to the heme are directly involved in protein association (Figure 56, Figure 58). It was shown by Jain *et al.* that surface ligands containing an appropriate combination of charge and hydrophobic groups associate to cytochrome c with higher affinity than the ligands which colligate only through the same number of anionic groups.¹²² The binding between the supramolecular host-guest assembly and its partner can rely on a variety of specific and nonspecific interaction. In the current system we exploited the electrostatic (ionic) interaction between the eight

carboxylic groups of our hemicarcerand and the numerous basic residues present on the surface of cytochrome *c* (Figure 58). The isoelectric point of cytochrome *c* is 10, while the pK_a values of the *m*-phthalic acid “portals” of the hemicarcerand are 3.54 for the singly and 4.60 for the doubly deprotonated species, respectively. As a result, both partners can exist in a broad range of protonated and deprotonated states and a pronounced ionic association between the protein and the supramolecular cage can be expected at neutral and moderately basic pH values. It is also important to note the comparable dimensions of the cytochrome and the hemicarcerand. The effective radius of the former is 14.3 Å, and of the latter 7.8 Å. As a consequence of the similar size and the flexible surface charge distribution, the association between the hemicarceplex and the cytochrome resembles more closely the complex, multivalent interaction between two proteins, rather than the binding of a small ligand.

The hemicarceplex-protein association was monitored by photoinduced electron transfer between the encapsulated donor or acceptor and Zn-substituted cytochrome *c*. The heme unit of native cytochrome *c* can act as an effective quencher in electron and excitation transfer experiments, however, due to its extremely short excited state lifetime (50 fs or less),⁴⁹ it is not a very useful light absorbing chromophore. For these reasons, Zn-Fe substitution has been used frequently in electron transfer studies on heme proteins.^{123,124,125} NMR structural studies of zinc substituted cytochrome *c* have shown that both zinc and Fe(II) cytochrome *c* share the same overall structure, including axial ligands, environment in the porphyrin vicinity, and the same binding interface with redox partners.¹²⁶ Zn-cytochrome *c* has a long-lived emissive triplet excited state, whose lifetime varies from 7 to 15 ms depending on the preparation and experimental

conditions.^{127,124,128} Furthermore, the $^3\text{ZnCC}$ triplet is easily oxidized and reduced.^{129,130,131,132} Therefore, it can act both as an electron donor in ET reactions with strong acceptors (quinones, nitro-aromatics) and as an acceptor with easily oxidized donors (ferrocene, aryl amines). The measured bi-directional ET rates combined with the known distance dependence of electron across proteins allowed us to identify the approximate binding region of the hemicarcerand on the surface of the protein. While other hosts such as cyclodextrins or cavitands have been used in conjunction with biomolecules in the past,^{133,134,135} the application of a fully encapsulating hemicarcerand to deliver both oxidizing and reducing partners to a redox-active protein has not been demonstrated.

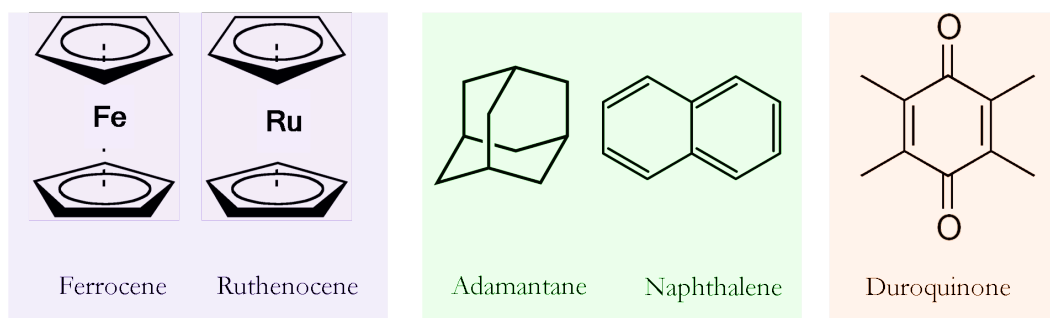


Figure 59. The encapsulated ligands: electron donors (ferrocene and ruthenocene), electron acceptor (duroquinone) and redox inactive guests (adamantane and naphthalene).

The guests used in our study (Figure 59) were selected on the basis of size and redox activity. Ferrocene and ruthenocene are good electron donors and their molecular volume of $180\text{-}190 \text{ \AA}^3$ is close to the maximum which can be accommodated within the cavity of the hemicarcerand. Duroquinone, $V_{mol} = 180 \text{ \AA}^3$, is a potent electron acceptor, while naphthalene and adamantane, which cannot undergo electron transfer reactions with $^3\text{ZnCC}$, served as the reference redox-inactive guests. The photophysical properties

of the selected guests preclude possibility of ZnCC* quenching by either singlet or triplet energy transfer. As a result, any observed emission quenching can be unambiguously attributed to electron transfer. In order to better understand the docking of the hemicarceplex to the cytochrome and its role in mediating the electron transfer reaction, control experiments on $^3\text{ZnCC}$ in the presence of free ferrocenedicarboxylic acid, sparingly water-soluble quinones and the redox inactive carboxynaphthalenes were performed. Electron transfer quenching of the ZnCC excited state by the protein-bound supramolecular host-guest complex was in all instances much faster than it was in the case of the corresponding free donors and acceptor in solution.

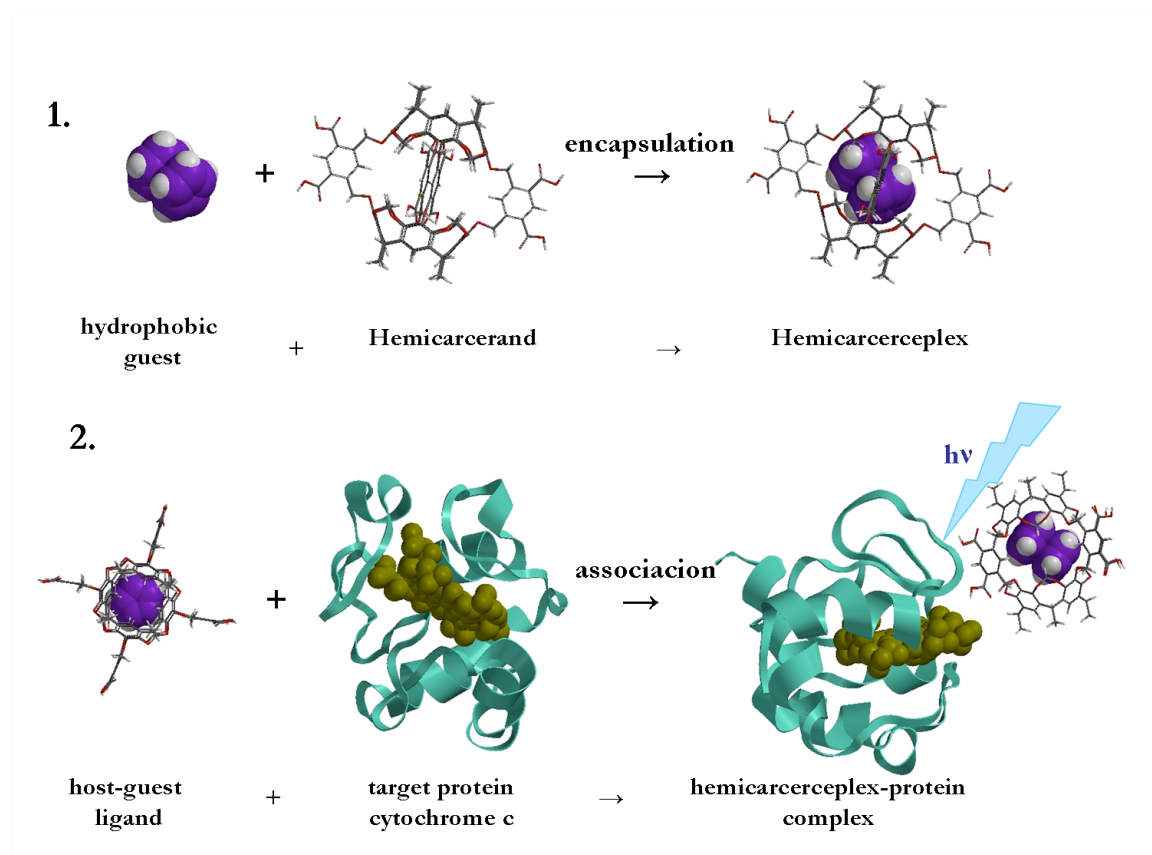


Figure 60. Schematic representation of: (1) encapsulation of the guest molecule within the hydrophobic cavity of octacarboxyhemicarcerand; (2) binding of the complete hemicarceplex to the target protein.

The general approach used in these studies is presented in Figure 60. First, the selected guest was encapsulated inside the hemicarcerand at room temperature and equilibrated. Then the desired concentration of the hemicarceplex was equilibrated with the zinc substituted cytochrome *c*. The association between ZnCC and the encapsulated guest was probed by electron transfer quenching of the long-lived triplet phosphorescence of ZnCC.

3.1 Materials and methods

Materials: Horse heart Type III cytochrome *c*, anhydrous CoF₂, zinc acetate, ferrocene, 1,1'-ferrocenedicarboxylic acid, 1,4,5,8-naphthalenetetracarboxylic acid, adamantane, benzoquinone and chloranil were used without further purification. Duroquinone was purified by sublimation and recrystallisation. All these chemicals were purchased from Sigma Aldrich Co. Ruthenocene was kindly provided by Prof. Frieder Jäkle. The octacarboxyhemicarcerand was prepared following the published procedure.¹³⁶ Anhydrous hydrogen fluoride gas was obtained from Matheson Tri-Gas, Inc.

Zinc-substitution of cytochrome *c*: The first batch of zinc cytochrome *c* was prepared as described by Vanderkooi and Erecinska^{137,16} by modifications of the methods of Flatmark and Robinson¹³⁸ and Fisher *et al.*¹³⁹. Later this method was modified. About 6 ml of anhydrous HF was condensed for about 25 min over anhydrous CoF₂ in a Teflon container of home-build HF apparatus at 77 K. The liquefied HF was allowed to evaporate and condense into another Teflon beaker at 77 K containing 50 mg of horse-heart Fe-cytochrome *c* and a Teflon coated magnetic spin bar. The liquefied HF-

protein mixture was stirred gently by the magnetic stirrer for about five minutes and then the unreacted HF was pumped off into a trap containing CaO. The metal-free protein was dissolved in 10 ml of 10 mM phosphate buffer at pH = 7.4 and treated with excess zinc acetate at 40 °C. The reaction was followed by monitoring the disappearance of characteristic absorption band of the free base-porphyrin and the emergence of the absorption bands of zinc cytochrome c (Figure 61).

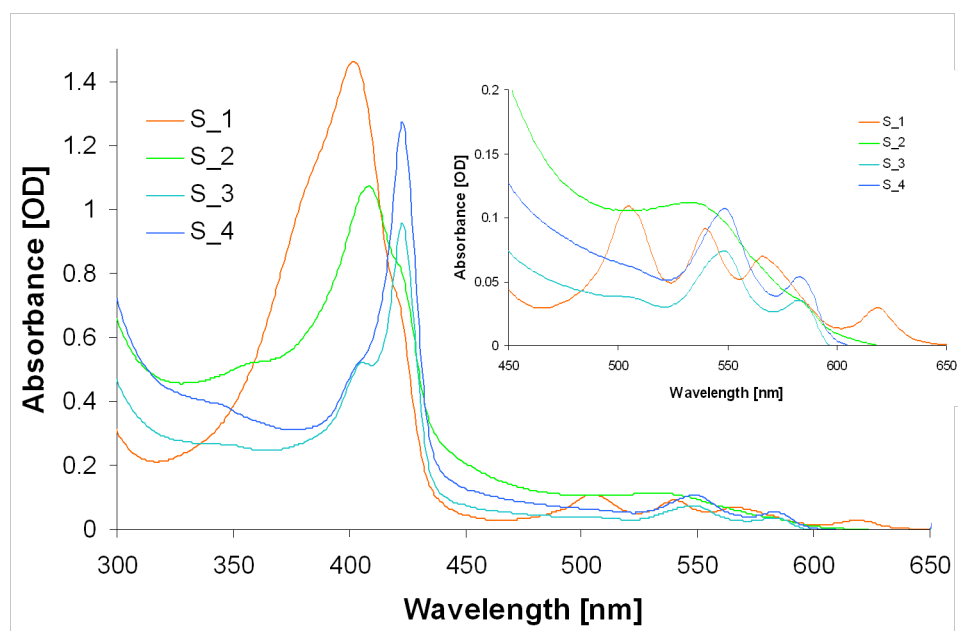


Figure 61. UV-Vis spectrum monitored during the metal exchange in cytochrome *c*.

The reaction was largely completed within 4 hours. The product was dialyzed at room temperature against 10 mM phosphate buffer (pH = 7.4) for 3 h and then twice with distilled water. The dialyzed protein was purified by HPLC using Water Protein-Pak Diol (OH) 10 μ m, 19 \times 300 mm column using ammonium acetate (pH = 6.5- 6.7) as the eluent. Only fractions with the absorbance ratios $A_{423}/A_{549} > 15.8$ and $A_{549}/A_{585} < 2.0$ were collected and used in the subsequent measurements (Figure 62). The purified protein was

then isolated by lyophilization. All manipulations involving zinc-substituted cytochrome *c* were performed in the dark or under minimal light exposure. Protein solutions were prepared using 20 mM phosphate buffer (pH = 7 - 10) containing 0.1 M NaCl in 20% glycerol.

Two concentrations of ZnCC were used: All samples prepared to investigate the interaction of the protein with the empty cage were 1×10^{-6} M in the protein, with the ratio ZnCC:Cage = 1:100. The initial electron transfer measurements were also performed at these concentrations. 2×10^{-6} M protein samples were used to study the quenching rate dependence on the concentration of Fc@Cage and DQ@Cage. The higher protein concentration was necessary for the time resolved measurements using photon counter and was kept constant throughout these measurements. The ZnCC:Cage ratio was varied from 1:1 to 1:50.

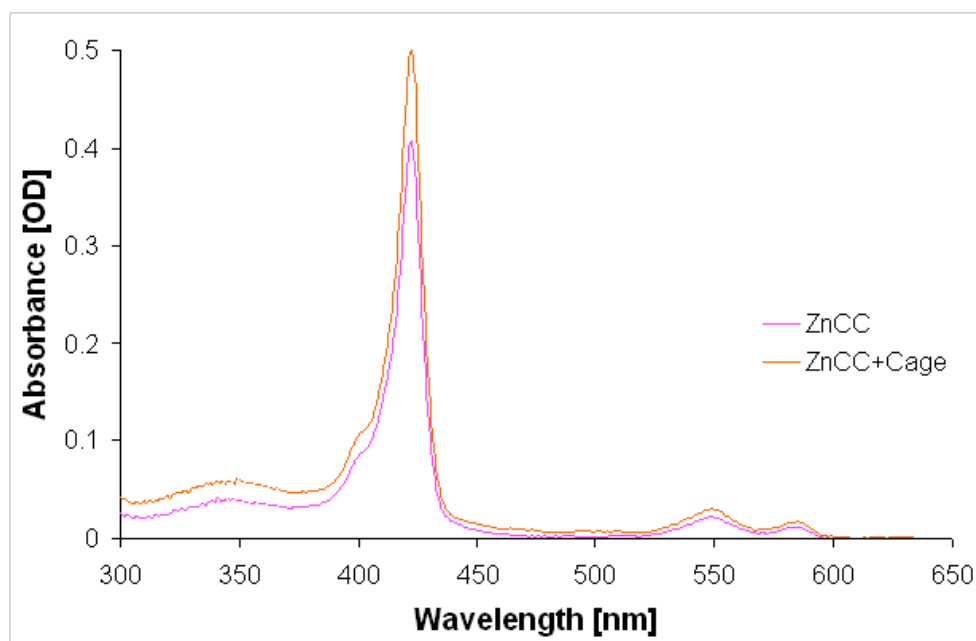


Figure 62. UV-Vis spectrum of ZnCC and ZnCC+Cage with ratio 1:10 after purification and lyophilization, dissolved in phosphate buffer at pH = 7 to achieve the desired concentration. Note that in both samples the $A_{423}/A_{549} > 16$.

Guest encapsulation and binding to the protein: The host-guest complex was prepared by adding appropriate amount of the guest's crystals to aqueous, slightly basic solution of the hemicarcerand of known concentration (2×10^{-4} M, 5×10^{-5} M, 2×10^{-5} M) to get final host-guest ratio 1:1. The encapsulation time depended on the guest compound. The reaction was spectroscopically monitored for at least 24 h and allowed to fully equilibrate. The resulting mixture was filtered prior to mixing with an equal volume of the protein solution (4×10^{-6} M, 2×10^{-6} M).

Photophysical properties: Absorption spectra were recorded using a Cary 500 UV-Vis NIR spectrometer. Emission spectra were measured with a Varian Cary Eclipse fluorescence spectrometer. Spectra were recorded following excitation at 420 nm.

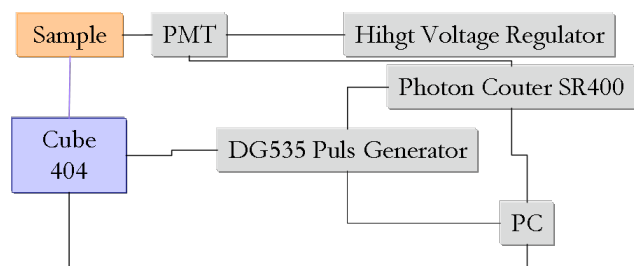


Figure 63. Homebuilt photon counting system with Cube 404 nm diode laser as a light source.

Time-resolved phosphorescence experiments were carried out on the Varian Cary Eclipse fluorescence spectrometer or using a homebuilt photon counting system which employed either a Hamamatsu Xe flash lamp or a Cube 404 nm (Figure 63), 100 mW diode laser (Coherent) as the excitation source. The lamp provided ~ 2 μ s wide broadband pulses which were filtered by a bandpass filter (427 nm, 10 ± 2 nm FWHM).

The duration of the diode laser pulse was varied from 0.5 to 10 μ s as needed. The emitted photons passed through a 550 nm longpass filter and were detected by a cooled R928 Hamamatsu PMT and counted by a SR400 photon counter (Stanford Research System). The system was operated at 40 Hz repetition rate with the synchronization provided by a DG535 delay generator (Stanford Research Systems). The solutions for the time-resolved and phosphorescence measurements were exhaustively degassed by freeze-pump-thaw cycles until no change in the recorded lifetime was observed.

Data analysis: Time resolved measurements of Zn-cytochrome c emission show that the delayed fluorescence exhibits the same lifetime as the 3ZnCC* phosphorescence. Therefore, either phosphorescence or delayed fluorescence can be used to monitor the triplet lifetime. Since the phosphorescence quantum yield is low, it was more convenient and reliable to analyze data recorded at the delayed fluorescence wavelength. The decay of 3ZnCC was not a pure single exponential, although it can be fit satisfactorily with a monoexponential function. Biexponential fitting revealed the presence of a minor, $\sim 10 \pm 2\%$ component with a considerably shorter lifetime, $\tau = 1.5 \pm 0.5$ ms, in all reference samples with and without the hemicarcerand. Since the short-lived component accounts for only 10% of the overall phosphorescence amplitude, it was decided to analyze the kinetic data in terms of a single exponential function. The resulting error is minor. It should be clarified that the $\sim 10\%$ short-lived component in the transient is not synonymous with the presence of a 10% impurity in our protein samples. The fixed 404 nm wavelength of the diode laser lies closer to the absorption maximum of the free-base porphyrin (404 nm) rather than of the ZnCC (423 nm). As a result, the contribution of the residual free-base CC to the transient is greater than its content in the sample, which on

the basis of the A423/A549 ratio we estimate at no more than 2%. Throughout the photon counting experiments the integrity of the protein was controlled by monitoring A423/A549 ratio in the UV-vis absorption spectrum. We did not observe any growth of absorption in the vicinity of 404 nm or spectral shifts which would indicate leaching out of the zinc ion or other protein degradation.

3.2 Results and discussion

Electrostatic association between Zn-cytochrome *c* and the hemicarcerand

Addition of the empty octacarboxyhemicarcerand to the ZnCC solution induces pronounced changes in the position of the absorption and emission peaks, as well as in the radiative lifetime of the triplet excited state. These effects confirm that association between the supramolecular cage and the cytochrome takes place and leads to the modification of the photophysical properties of the latter. At 1×10^{-6} M cytochrome concentration and 1:1 hemicarcerand:ZnCC ratio an approximately 2 nm hypsochromic shift of the Soret band of ZnCC is observed. The shift reaches its maximum value of 5 nm at 30:1 cage:protein ratio (Appendix 10). Smaller, approximately 3 nm blue shifts in the fluorescence and phosphorescence spectra of ZnCC were also observed in the presence of the empty hemicarcerand. Hypsochromic shifts in the absorption spectrum of native cytochrome *c* were observed upon binding to liposomes and membranes.^{140,141} This spectral change was attributed to the alteration in the Zn-porphyrin environment brought about by the interaction of the protein with these acidic substrates. A blue shift in the phosphorescence maximum of ZnCC bound to cytochrome *c* peroxidase (CcP) was

also reported.¹⁴² It was explained in terms of the increased torsion of the porphyrin ring upon binding to the peroxidase.

No changes in the fluorescence intensity and lifetime of ZnCC in the presence of the empty hemicarcerand were detected. However, the behavior of the long-lived triplet state is significantly altered. A dramatic, more than twofold increase of phosphorescence intensity is observed upon binding of the hemicarcerand to the protein, with a parallel decrease in the triplet lifetime (Figure 64). It could be argued that the increased phosphorescence intensity is due to the protection from residual quenchers, e.g. O₂, offered by the bulky cage bound to the surface of the protein. However, if this were the case, a corresponding increase in the triplet state lifetime of cytochrome *c* would have to occur. This was not observed. On the contrary, the ZnCC triplet lifetime decreased from 9.9 ms in free solution to 5.8 ms in the presence of the cage. The simultaneous growth of emission intensity and the decrease of lifetime point to the increase of the T₁-S₀ transition moment and as a consequence, acceleration of the radiative decay rate. The behavior of the T₁ state of zinc porphyrins is known to respond strongly to the planarity of the ring, as well as to small changes in the distance and orientation of the axial ligands, in this case the His18 residue.^{143,20} Both factors are influenced by the complexation. As a consequence, the observed pronounced lifetime and intensity changes are strong indications that the hemicarcerand binds to cytochrome *c* in the vicinity of the heme pocket and modulates the axial ligation of the Zn center.

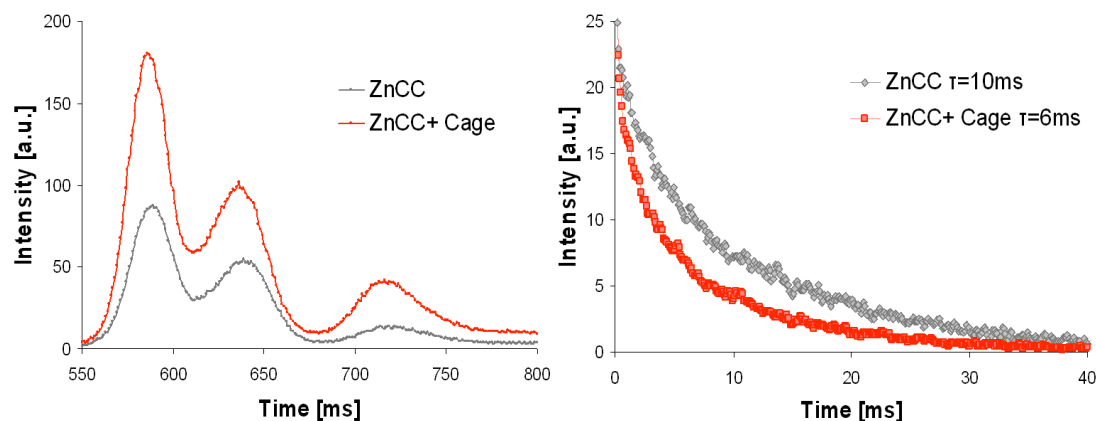


Figure 64. Phosphorescence spectra and normalized decay profiles of 1×10^{-6} M ZnCC in the absence and presence of 1×10^{-4} M of the empty hemicarcerand at pH = 7. The phosphorescence peak is at 720 nm, while the 570 and 635 nm peaks are due to delayed fluorescence.

Table 11. Single exponential phosphorescence lifetime ($\tau_{\text{reference}}$) of zinc substituted cytochrome *c* (1×10^{-6} M) in the presence and absence of empty hemicarcerand (1×10^{-4} M - 3×10^{-5} M) at different pH and room temperature.

	pH = 7	pH = 9	pH = 10
	τ [ms]		
ZnCC (1×10^{-6} M)	9.85 ± 0.05	9.63 ± 0.08	9.52 ± 0.14
ZnCC + Cage (1×10^{-4} M)	5.81 ± 0.12	7.14 ± 0.07	9.41 ± 0.03
ZnCC + Cage (8×10^{-5} M)	8.00 ± 0.07	-	-
ZnCC + Cage (3×10^{-5} M)	9.08 ± 0.08	-	-

The effect of the presence of the hemicarcerand is most pronounced under neutral and slightly basic conditions (Table 11). It diminishes in increasing pH and disappears altogether at pH = 10, indicating that the association of the supramolecular cage with cytochrome *c* is driven primarily by electrostatic interactions between the negatively

charged hemicarcerand and the positively charged protein. Variable temperature measurements of the T_1 lifetime of ZnCC and ZnCC+Cage further underscored the strong pH dependence of the association between the cage and cytochrome *c*.

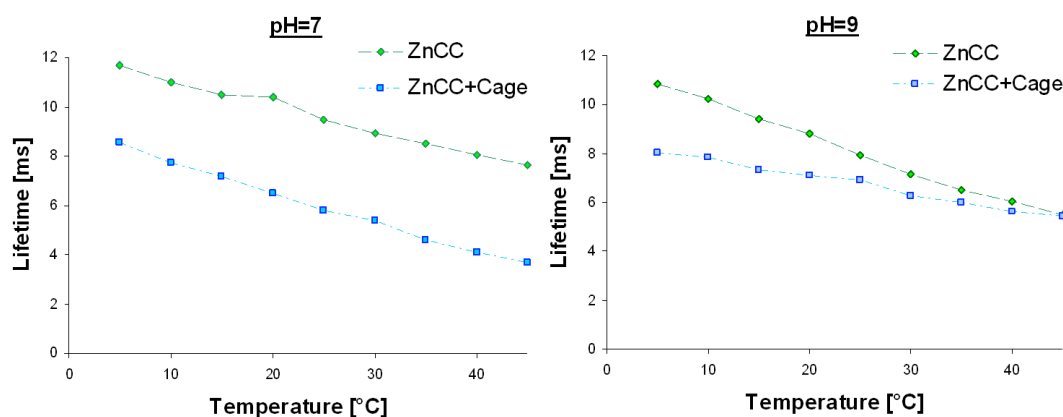


Figure 65. Temperature dependence of the triplet lifetime of ZnCC (1×10^{-6} M) in the absence and presence of the empty octacarboxyhemicarcerand (1×10^{-4} M) at pH = 7 (a) and pH=9 (b).

As can be seen in Figure 65, the $^3\text{ZnCC}$ lifetime decreases with increasing temperature both in the presence and in the absence of the hemicarcerand. The $^3\text{ZnCC}$ and $^3\text{ZnCC+Cage}$ lifetimes give rise to distinct lines with slopes determined primarily by the thermal repopulation of the S_1 state, which is a significant triplet decay pathway in Zn-porphyrins. At neutral pH, the ZnCC+Cage complex remains stable over the entire 5 – 45 °C temperature range, as evidenced by the two distinct lines. At pH = 9, electrostatic attraction between the cage and ZnCC is greatly diminished. The complex is much more labile and at 45° the $^3\text{ZnCC}$ and $^3\text{ZnCC+Cage}$ lifetime traces coalesce, indicating that above that temperature, only the free, uncomplexed ZnCC is present. Importantly, spectral shifts and lifetime changes similar to these described above were not observed at

any pH when small molecules bearing multiple carboxylic groups, for example 1,4,5,8-tetracarboxynaphthalene, were added to the ZnCC solution. This suggests that the binding to cytochrome *c* depends not only on the acidity of the ligand, but also on its size, conformational flexibility and ability to participate in multivalent interactions.

Photoinduced electron transfer between Zn-cytochrome c and the encapsulated guests

Photoinduced electron transfer was used in this study to probe the association between the supramolecular host-guest assembly and cytochrome *c*. Since $^3\text{ZnCC}$ can act both as an electron donor and acceptor depending on its redox partner, it was possible to demonstrate that the same molecular container can be used to transport reducing and oxidizing guest ligands and position them in the vicinity of the active site of the cytochrome. The choice of the guest molecules was dictated primarily by the size of the hemicarcerand cavity. Despite this restriction, guests spanning a nearly 1 eV range of driving force (ferrocene, ruthenocene and duroquinone) were studied. In addition, adamantane and naphthalene which are not capable of oxidizing or reducing $^3\text{ZnCC}$, were also encapsulated. This set of molecules allowed us to fully characterize the ET parameters and to identify the location of the hemicarceplex-cytochrome binding interface.

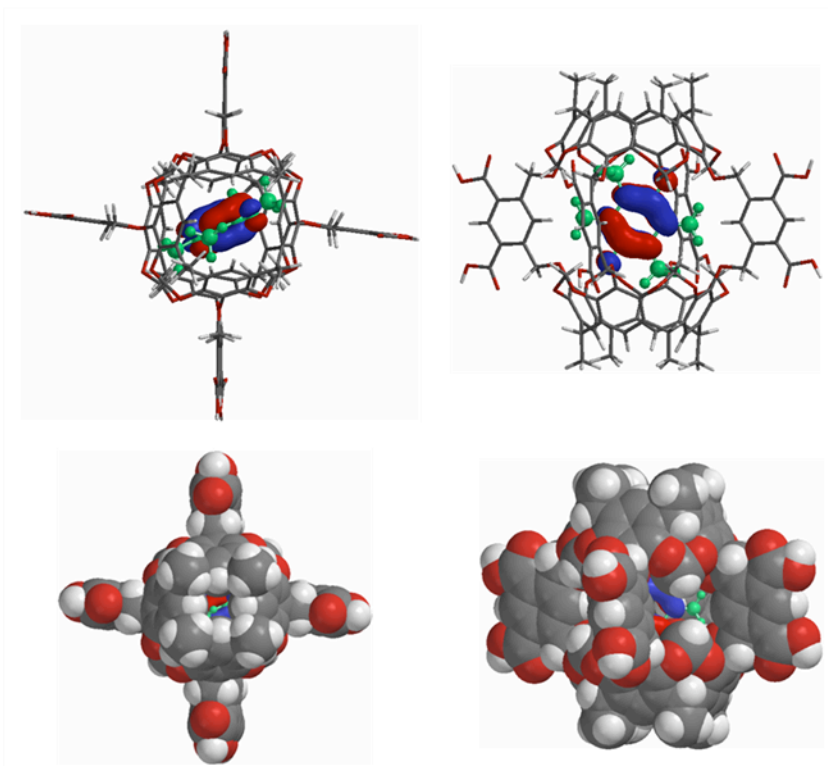


Figure 66. Duroquinone encapsulated within the octacarboxyhemicarcerand. The cage distorts slightly away from the ideal D_{4h} symmetry in the presence of the guest. Note that the LUMO orbital of the host-guest complex is fully localized on duroquinone (global AM1 optimization). The space-filled model demonstrates that the encapsulated guest molecule cannot come into direct contact with the surface of the cytochrome.

As can be seen from Figure 66, the relevant molecular orbitals participating in the electron transfer reaction (LUMO of duroquinone and HOMO of ferrocene) are fully localized on the guest molecule and do not extend onto the hemicarcerand. As a result, the electron transfer reaction between the Zn-substituted heme group and the redox-active guest satisfies the conditions of a weakly-coupled process mediated by superexchange and can be analyzed in terms of the Marcus theory.

The encapsulation of guest molecules within the octacarboxyhemicarcerand has been investigated in detail in the past.^{88,136} It should be emphasized that the

hemicarceplexes studied in this work are thermodynamically stable in the aqueous medium and do not rely on Cram's "constrictive binding". The affinity depends upon the shape and the hydrophobicity of the guest, the latter being favored by the hydrophobic nature of the inner wall of the hemicarcerand. The binding constants for large nonpolar guests such as naphthalene and ferrocene, whose size closely matches the 200 \AA^3 internal volume of the host, exceed $1 \times 10^8 \text{ M}^{-1}$, with the corresponding free energies in excess of -12 kcal/mol .¹³⁶ Smaller and more polar guests, such as trimethoxybenzene and quinones exhibit binding free energies of approximately -5 kcal/mol . The driving force for the encapsulation by the water-soluble hemicarcerand and hence the stability of the host-guest complex can be also predicted on the basis of the free energy change associated with the reduction of hydrophobic surface exposed to water. The 178 \AA^2 hydrophobic surface of ferrocene combined with Honig's $47 \text{ cal}\cdot\text{mol}^{-1}\cdot\text{\AA}^{-2}$ hydrophobic energy¹⁴⁴ yields an encapsulation free energy of -8.4 kcal/mol . A similar treatment of the more polar duroquinone yields net stabilization energy of -5.6 kcal/mol . In this case one has to account for the 2.9 kcal/mol loss of hydration energy of duroquinone (Spartan calculation). These estimates are remarkably close to the calorimetrically determined binding energies reported by Cram and Deshayes^{88,114, 136} and provide useful guidance in the design of the encapsulation experiments.

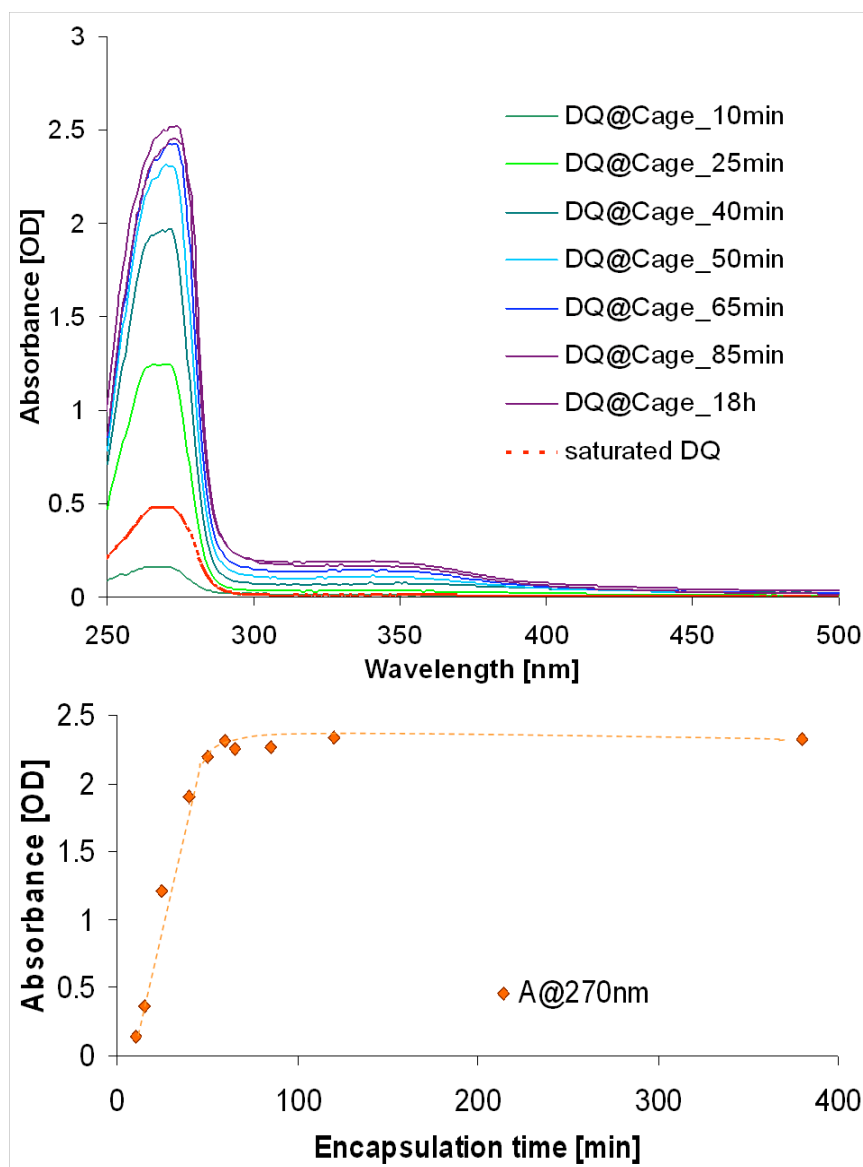


Figure 67. Room temperature kinetics of the incarceration of duroquinone (DQ): (a) formation of the hemicarceplex monitored by UV-vis spectroscopy; (b) encapsulation time established from the growth of the 270 nm band, $\epsilon_{\text{DQ@270nm}} = 21.64 \text{ mM}^{-1} \text{ cm}^{-1}$.¹⁴⁵

Encapsulation of guest molecules occurs spontaneously within minutes to hours indicating the presence of an activation barrier associated with the ingress and egress from the cage.^{114,146} The incarceration kinetics depends on the size of the guest and its solubility in the aqueous medium. For example, the encapsulation of duroquinone (Figure

67), which is slightly soluble in water and whose shape facilitates the passage through the portal, is relatively rapid. Its progress and the formation of the 1:1 host-guest complex were monitored by UV-VIS absorption. The encapsulation of the nearly insoluble ferrocene, ruthenocene and adamantane was considerably slower and required overnight equilibration.

The interaction of the photoexcited Zn-cytochrome *c* with the encapsulated redox-active guests (ferrocene, ruthenocene and duroquinone) results in all cases in efficient quenching of the triplet state of the former. As it can be seen in Figure 68, the reduction of the phosphorescence intensity is accompanied by a corresponding decrease of the triplet state lifetime. The quenching rates follow the expected thermodynamic trend and increase as the ΔG_{ET}^0 of the electron transfer reaction becomes more negative (Table 12). The triplet state lifetime of the cytochrome was not measurably altered in the presence of encapsulated naphthalene or adamantane, for both of which the electron transfer to or from $^3\text{ZnCC}$ is energetically unfavorable by more than 1 eV. Encapsulated ruthenocene, for which the electron transfer to $^3\text{ZnCC}$ is slightly endoergic, did cause substantial phosphorescence quenching, albeit at rates approximately 10-times slower than the Fc@Cage (Figure 68, 69 Table 12 and Appendix 11).

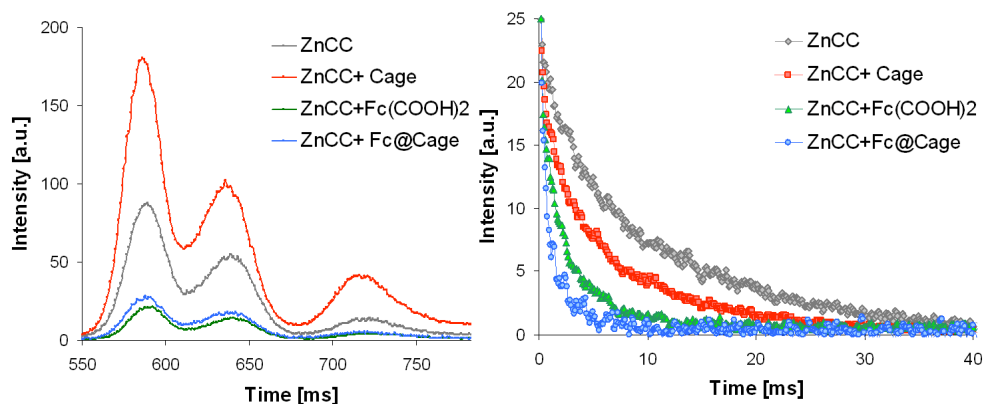


Figure 68. Phosphorescence spectra (a) and emission time profiles of cytochrome *c* ($1 \times 10^{-6} \text{M}$) with empty cage ($1 \times 10^{-4} \text{M}$), encapsulated ferrocene ($1 \times 10^{-4} \text{M}$) and in the presence of ferrocene dicarboxylic acid ($1 \times 10^{-4} \text{M}$) at pH=7.

Remarkably, in cases in which direct comparison is possible, electron transfer rates observed for the redox-active host-guest complexes are considerably higher than these for the corresponding free acceptors and donors in solution. For example, the encapsulated duroquinone, DQ@Cage, quenches $^3\text{ZnCC}$ 20 times faster than free duroquinone (DQ) at a similar concentration (Figure 70, Table 12). The reductive quenching of $^3\text{ZnCC}$ by the Fc@Cage is 3 times faster than quenching by the same concentration of free ferrocene dicarboxylic acid (Figure 68, 69, Table 12). Since the walls of the cage impose an additional barrier for the tunneling of electrons between the encapsulated guest and the protein, these results confirm that the hemicarceplex binds to cytochrome *c* and positions the redox active guest in the vicinity of the Zn-substituted heme. The difference between the free vs. encapsulated quenching rates is larger in the case of DQ and DQ@Cage, because duroquinone is not likely to associate with cytochrome *c*.

Table 12. Experimental rates and thermodynamic parameters for the electron transfer reaction between $^3\text{ZnCC}$ and host-guest complexes as well as free donors and acceptors in solution.

Quencher	E_{ox} [V]	E_{red} [V]	$\Delta G^0_{\text{ET}}^z$ [eV]	k_{ET} [s^{-1}] ^{aa}	ET direction
Fc@Cage	0.31 ^{bb}	-	-0.10	8.9×10^2	reduction
Ru@Cage	0.69 ^{bb}	-	0.28	7.0×10^1	reduction
DQ@Cage	-	-0.24 ^{cc}	-0.64	1.1×10^5	oxidation
Naph@Cage	1.54 ^{dd}	-2.49 ^{dd}	1.14 (1.61) ^{ee}	-	-
Ada@Cage	2.72 ^{ff}	-	2.32	-	-
Fc(COOH) ₂	0.64 ^{gg}	-	-0.10	3.2×10^2	reduction
DQ	-	-0.24 ^{cc}	-0.64	5.4×10^3	oxidation
CQ	-	0.65 ^{hh}	-1.53	9.8×10^2	oxidation
BQ	-	0.08 ^{hh}	-0.96	1.0×10^2	oxidation
Naph(COOH) ₄	1.54 ⁱⁱ	-2.49 ⁱⁱ	1.14 (1.61) ^{ee}	-	-

^z The free energy change for the reaction of ZnCC with the quencher is given by: $\Delta G = E_{\text{ox}}(\text{D}) - E_{\text{red}}(\text{A}) - E_{0-0}(\text{triplet})$ Where: $E_{\text{ox}}(\text{Zn/Zn}^+) = 0.8 \text{ V}$; $E_{\text{red}}(\text{Zn/Zn}^-) = -1.3 \text{ V}$; $E_{0-0}(\text{triplet}) = 1.7 \text{ V}$ (reference 47; *Inorg. Chem.* 1996, 35, 2780).

^{aa} The quenching rate for ZnCC ($1 \times 10^{-6} \text{ M}$) in the presence of quencher at pH = 7; the quencher concentration for presented results was equal $1.0 \times 10^{-4} \text{ M}$ except for DQ, BQ and CQ ($1.5 \times 10^{-4} \text{ M}$).

^{bb} The values for free donors: Kuwana, T.; Bublitz, D. E.; Hoh, G. *J. Am. Chem. Soc.* 1960, 82, 5811-5817.

^{cc} The value for free duroquinone: Meisel, D.; Czapski, G. *J. Phys. Chem.*, 1975, 79, 1503-1509.

^{dd} The value for free naphthalene: Murov, S. L.; Carmichael, I.; Hug, G. L. *Handbook of Photochemistry*, 2nd Ed., Dekker, New York, USA 1993.

^{ee} Driving force for the reduction of naphthalene.

^{ff} Oxidation potential of adamantane: Mella, M.; Freccero, M.; Soldi, T.; Fasani, E.; Albini, A. *Org. Chem.*, 1996, 61, 1413-1422.

^{gg} The value taken from: Quaranta, D.; McCarty, D. R.; Bandarian, V.; Rensing, C. *Journal of Bacteriology*, 2007, 189, 5361-5371, corresponds to neutral Fc(COOH)₂. Under the pH conditions of our experiments the compound is present as the easier to oxidize monoanion Fc(COOH)(COO⁻).

^{hh} Arno G. Siraki, Tom S. Chan, and Peter J. O'Brien; *Toxicological Sciences* 2004 81(1):148-159

ⁱⁱ The values for unsubstituted naphthalene from footnote "bb" were used.

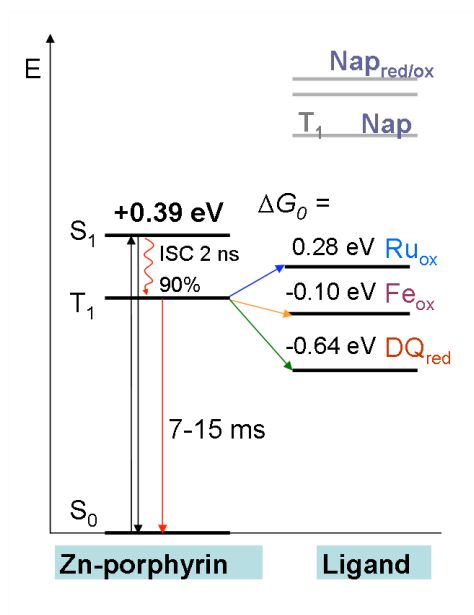


Figure 69. The free energy diagram for the reaction of $^3\text{ZnCC}$ with DQ@Cage, Fc@Cage, Ru@Cage and the redox inactive Naph@Cage.

Ferrocene dicarboxylic acid on the other hand can bind electrostatically to the cytochrome and as a consequence, the ratio of the Fc@Cage to Fc(COOH)₂ quenching rates is smaller. Nevertheless, in view of the attenuation of the ET rate by the walls of the hemicarcerand, Fc(COOH)₂ must bind to the protein not as strongly, or at a less favorable site than the Fc@Cage does.

The concentration dependence of the ET quenching rate of $^3\text{ZnCC}$ by Fc@Cage and DQ@Cage is shown in Figure 70. The rates were measured in $1\text{-}2 \times 10^{-6}$ M solutions of ZnCC in which the hemicarcerand-guest ratio was always kept at 1:1, regardless of the overall concentration. Both traces in Figure 70 show initial increase of the quenching rate with increasing concentration of the quencher followed by a plateau region, in which further increase of the concentration has little effect on the rate of electron transfer. In both cases the region of rate increase is steeper than it would have been in the case of a

diffusion controlled process, indicating that the hemicarcerands carrying redox-active guests bind to the cytochrome. The presence of the plateau is a further confirmation of the formation of a complex between the protein and the hemicarceplex. Electron transfer rates in the plateau region are approximately 25-times higher for DQ@Cage than for Fc@Cage and are consistent with the much higher driving force for the former, $\Delta G^0 = -0.64$ eV, vs. -0.10 eV. Increasing the concentration of the hemicarceplex beyond the onset of the plateau leads to only a slight further acceleration of the rate. This suggests that the guest@Cage complexes continue to bind to cytochrome *c* forming higher than 1:1 protein-hemicarceplex aggregates, however, the successive dockings occur further away from the heme site and make only a minor contribution to the overall quenching rate.

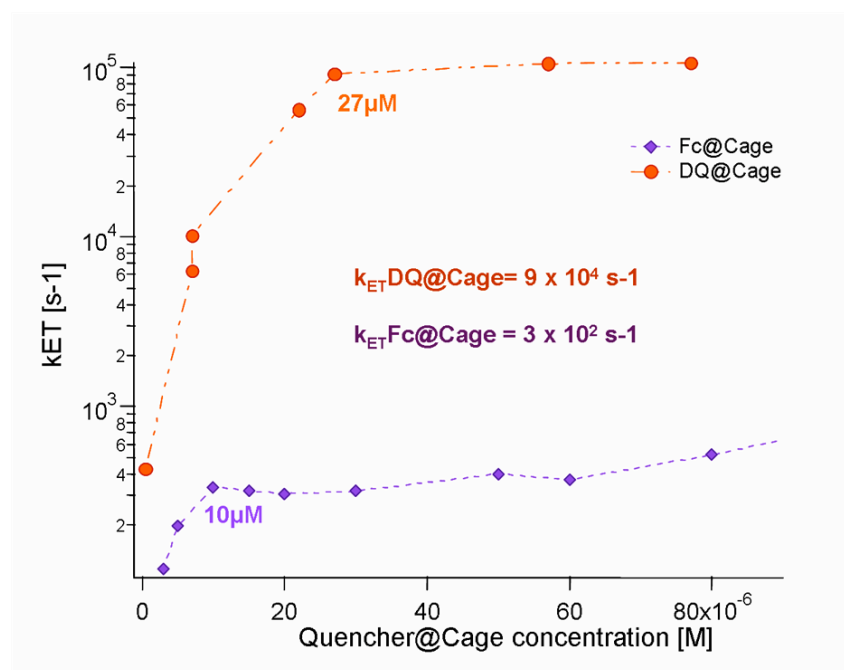


Figure 70. Electron transfer kinetics of $^3\text{ZnCC}$ with Fc@Cage and DQ@Cage. The DQ@Cage trace has been corrected for the quenching by the free duroquinone, $k_{DQ@Cage} = k_{measured} - k_{DQ}$.

It is significant that the DQ@Cage and Fc@Cage traces differ markedly from one another in the onset of the plateau region. In the case of the incarcerated ferrocene, leveling off occurs very early, at approximately 10 μM , while for encapsulated duroquinone it takes place much later, at nearly 30 μM . The divergence results from the difference in the affinity of the hemicarcerand towards the highly hydrophobic, completely insoluble ferrocene and the comparatively polar and somewhat water-soluble duroquinone. The octacarboxyhemicarcerand traps ferrocene with a very high binding constant, $K_{\text{encaps}} > 10^8 \text{ M}^{-1}$. As a consequence, even at the lowest concentrations, ferrocene is present in solution exclusively in the encapsulated form. The saturation point of the Fc@Cage curve most likely corresponds to the concentration at which the 1:(1:1) ternary complex of cytochrome *c* with the Fc@Cage hemicarceplex is the predominant species. Therefore, this point can be used to estimate the binding constant between the hemicarceplex and the cytochrome, $K_{\text{assoc}} = 1 \times 10^5 \text{ M}^{-1}$. Similar affinity, $K_{\text{assoc}} = 2 \times 10^5 \text{ M}^{-1}$, was reported by Fisher *et al.* for the binding of tetracarboxyphenylporphyrin with the native cytochrome *c*.¹⁴⁷

Duroquinone is considerably more soluble in water than ferrocene. Absorbance measurements in the same buffer as used in the above experiments yield saturated concentration of free duroquinone of $2.3 \times 10^{-5} \text{ M}$ (Figure 67). As a result, at low concentrations, the $\text{DQ} + \text{Cage} \leftrightarrow \text{DQ@Cage}$ equilibrium favors free duroquinone and empty hemicarcerand. Indeed, the quenching rates obtained with duroquinone concentrations below 20 μM are very similar regardless whether the hemicarcerand is present in the solution or not. When the concentration increases, the equilibrium shifts to the right, however, the DQ@Cage host-guest complex becomes the dominant form only

at a concentration that is higher than that corresponding to the formation of a 1:1 hemicarcerand-ZnCC complex. As a consequence, in the case of DQ@Cage, the onset of the plateau in Figure 70 signifies the point at which all hemicarcerands bound to the surface of the protein become occupied by duroquinone. The duroquinone encapsulation constant estimated on this basis is $K_{encaps} \approx 4 \times 10^4 \text{ M}^{-1}$.

In order to verify the electrostatic nature of the association between the hemicarceplex and cytochrome *c* experiments at different pH values were conducted (Table 13). The efficiency of quenching by both Fc@Cage and Fc(COOH)₂ is diminished in increasingly basic solutions. At pH = 10, when approximately ~25% of the positive charges on the surface of cytochrome *c* are neutralized, the rate of electron transfer quenching of ³ZnCC by Fc@Cage reduced by a factor 3 in comparison the rate at pH = 7. Solutions with pH > 10 were not investigated because of the possible aggregation and precipitation of cytochrome *c*, nevertheless, even the limited accessible pH range confirms that the hemicarceplex-cytochrome *c* association is driven primarily by ionic interactions. The electrostatic potential on the surface of hemicarcerand, Fc(COOH)₂ and quinines is shown in Figure 71.

Table 13. Quenching rates in the presence of encapsulated ferrocene and 1,1'-ferrocenedicarboxylic acid ($k_{ET} = 1/\tau_{observed} - 1/\tau_{reference}$) at different pH and room temperature.

	pH = 7	pH = 9	pH = 10
	$k_{ET} [\text{s}^{-1}]$		
ZnCC + Fc(COOH) ₂ ($1 \times 10^{-4} \text{ M}$)	3.2×10^2	2.8×10^2	1.5×10^2
ZnCC + Fc@Cage ($1 \times 10^{-4} \text{ M}$)	8.9×10^2	6.8×10^2	3.2×10^2

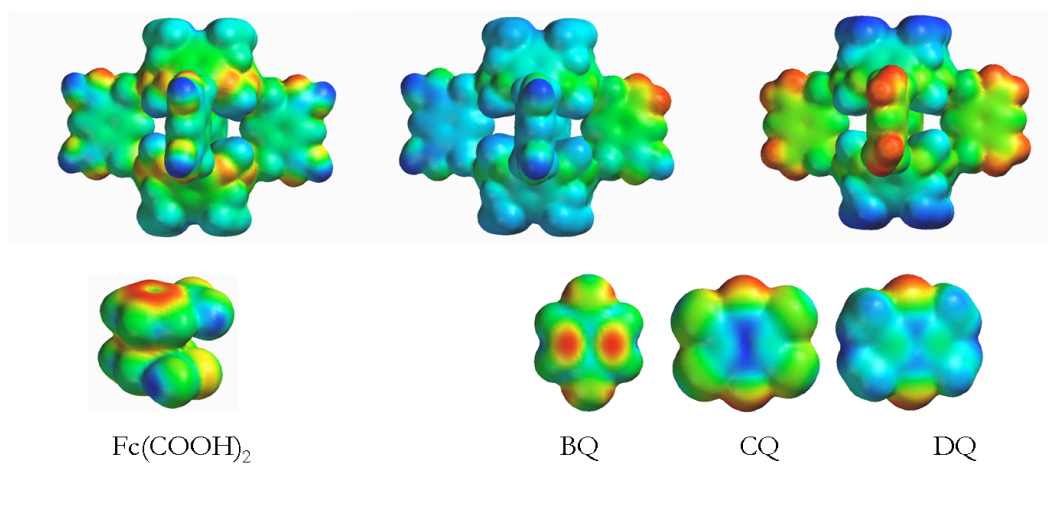


Figure 71. Electrostatic potential on the surface of fully protonated, singly ionized and fully deprotonated hemicarcerand (upper row) as well as $\text{Fc}(\text{COOH})_2$ and quinones.

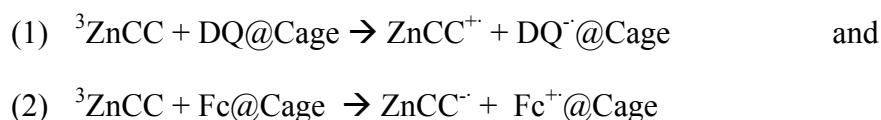
The binding site

The known thermodynamic parameters and distance dependence of electron transfer can be used to determine the distance between the donor and acceptor in a manner similar to FRET (Förster resonance energy transfer).^{148,149} Therefore, we can identify the location of the binding interface between the hemicarceplex and cytochrome *c* on the basis of the plateau electron transfer rates measured in the presence Fc@Cage and DQ@Cage (Figure 70). The electron transfer Franck-Condon factors are estimated with the help of the classical Marcus equation. The value of the attenuation coefficient β has been determined for a variety of intervening media in covalently linked donor-acceptor model systems, in monolayers, in frozen glasses including water, and in proteins. For the purpose of this work we treat the protein and the wall of the cage as a homogeneous tunneling barrier with effective β of 1.1 \AA^{-1} . This attenuation factor was determined by Gray *et al.*⁴⁸ on the basis of ET measurements on Fe^{III} -cytochrome *c* with electron donors covalently attached to specific sites on its surface. Since the hemicarcerand is not

covalently bound to the guest, the corresponding attenuation factor for electron tunneling must be greater than that found for covalently bound systems with unsaturated bridges. Indeed, Pina and Balzani reported 100-200-fold reduction of ET rates due to tunneling across the wall of a different, partially saturated hemicarcerand.¹⁵⁰ As a consequence, the accepted average β of 1.1 Å⁻¹ should be a satisfactory approximation for electron transfer in our ternary protein-(host-guest) assembly. This relatively steep distance dependence corresponds to 3-fold ET rate reduction per 1 Å. Since the electron transfer reactions between Zn-cytochrome *c* and ferrocene and duroquinone lie well within the “normal” thermodynamic region, the classical Marcus equation was used in the analysis.

The magnitude of the reorganization energy, λ , is a necessary parameter for the determination of the donor-acceptor separation. It can be calculated from the known ΔG^0 values and the experimental ET rates or taken from literature. Since the R_{DA} is sensitive to the value of λ , we used both approaches.

The electron transfer rates k_1 and k_2 measured for the reactions



were used to set-up the set of coupled equations:

$$k_1 = \left(\frac{\pi}{\hbar^2 \lambda k_B T} \right)^{1/2} \cdot |V|^2 \cdot e^{-\frac{(\Delta G_1^0 + \lambda)^2}{4\lambda k_B T}} \quad k_2 = \left(\frac{\pi}{\hbar^2 \lambda k_B T} \right)^{1/2} \cdot |V|^2 \cdot e^{-\frac{(\Delta G_2^0 + \lambda)^2}{4\lambda k_B T}}$$

in which the only unknowns are λ and $|V|$, both of which must be positive. The inherent assumption that the same average values of λ and $|V|$ can be used for both reactions is used frequently in electron transfer studies in which the ΔG^0 was varied. The set of equations can be solved iteratively or fitted. This procedure yielded for our system an

average $\lambda = 0.8$ eV, which is consistent with the reduced solvation of the encapsulated redox partners of $^3\text{ZnCC}$.

The solvation energy of $\text{Fc}^+@\text{Cage}$ and $\text{DQ}^-@\text{Cage}$ is considerably reduced in comparison with free Fc^+ and DQ^- since the redox partners of $^3\text{ZnCC}$ are encapsulated within the hydrophobic cage and cannot be directly solvated by the buffer. As in many other electron transfer studies, Born theory was applied to estimate the upper limit for the solvent reorganization energy associated with the oxidation of $\text{Fc}@\text{Cage}$ and reduction of $\text{DQ}@\text{Cage}$.^{75,151,76,77} Using the 7.8 Å effective radius of the guest@Cage, the static dielectric constant of water $\epsilon = 80.1$, and the refractive index of dimethoxy benzene $n = 1.52$, which is representative of permittivity of the hemispherical walls, the Born equation predicts the maximum reorganization energy of 0.19 eV at $R_{\text{DA}} \rightarrow \infty$.

The internal, or vibrational, reorganization energy for duroquinone and ferrocene was calculated at the B3LYP DFT level with the 6-31G* basis set (Spartan '06). We followed the standard procedure of first calculating the unrelaxed energy of the product species in the optimized geometry of the neutral species and then allowing the product species to relax. The resulting values of 17 meV for the Fc/Fc^+ and 27 meV for the DQ/DQ^- reaction are small and account for less than 3% of the total magnitude of λ recovered from the electron transfer data. The overall reorganization energy of the guest@Cage assembly, $\lambda_{\text{sol}} + \lambda_{\text{vib}}$ is less than 0.2 eV. Since $\lambda_{\text{vib}} \ll \lambda_{\text{sol}}$, and the reorganization energy of cytochrome *c* has been estimated at 0.6-0.7 eV by various groups.^{152,153} The $\lambda_{\text{total}} = 0.8$ eV retrieved from our data is both reasonable and consistent with the assumption that the reorganization energy in our system is similar for both guests. This value is lower than most reorganization energies reported for electron

transfer reactions between zinc-substituted cytochrome *c* and redox partners exposed to aqueous solution. Such an outcome is reasonable since ferrocene and duroquinone are encapsulated within the hydrophobic cage and cannot be directly solvated by the buffer. The solvation energy of $\text{Fc}^+@\text{Cage}$ and $\text{DQ}^-@\text{Cage}$ must be considerably reduced in comparison with free Fc^+ and DQ^- . Estimated on this basis, the Zn-to-Fe and Zn-DQ center-to-center distance in the hemicarceplex-cytochrome complex is 16.5 Å. This conservative value is significantly lower than the average center-to-center separation in a random encounter complex between the hemicarceplex and the cytochrome, which based on effective radii of the protein and of the supramolecular cage is 22.1 Å (Figure 72). The latter value would lead to ET rates at least 500 times slower than those observed experimentally. This strongly suggests that the binding of hemicarceplex, while not site-specific, has a pronounced preference for the region of the surface proximal to the heme pocket, which is the ET pathway in the self-exchange reaction of cytochrome *c* and has been invoked in its interaction with several metal complexes,²⁵ the copper-containing plastocyanin^{154,155} and the negatively charged cytochrome b_5 .¹⁵⁶ If a reorganization energy larger than 0.8 eV is used in the analysis, the extracted distance between the redox centers of the protein and of the hemicarceplex is further reduced. For example, if we use $\lambda = 1.2$ eV taken from the work of Gray et al. on ZnCC modified with covalently bound electron donors,¹⁵⁷ a R_{DA} value of 13.0 Å is obtained. Such short donor-acceptor distance places the hemicarceplex in the immediate vicinity of the heme pocket. Therefore, it is reasonable to conclude that distance between the redox centers of the protein and of the host-guest assembly lies in the 13 to 17 Å interval.

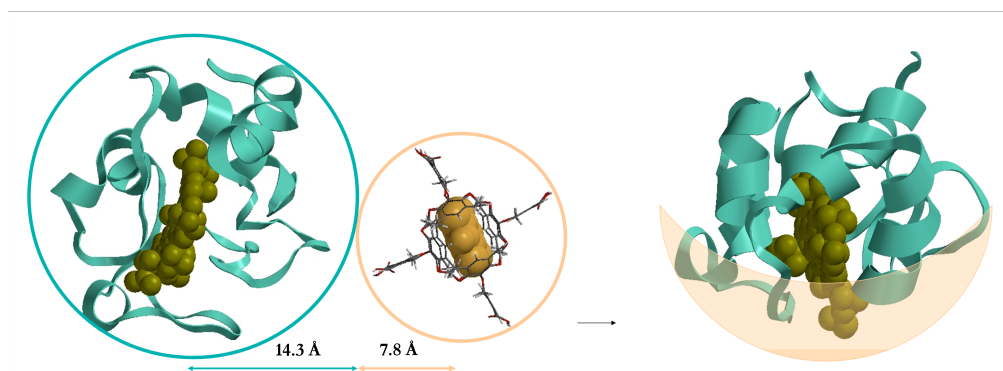


Figure 72. Left: The effective radii of cytochrome c and the hemicarceplex. Right: The location of the hemicarceplex–cytochrome c binding interface based on the R_{DA} radius of 16.5 Å.

Simple AM1 semiempirical calculations can help to understand why the supramolecular cage binds more strongly to its protein target than small ligands with similar pK_a values do. Under the mildly basic conditions of the reported experiments, on average one carboxylic group on each *m*-phthalic acid ‘portal’ exists in the ionic form. The possible distinct, not related by symmetry locations of the negative charges on the surface of the hemicarceplex are shown in Figure 73 (a). The AM1 gas phase energy differences between the four arrangements are small, in part because the flexible cage relaxes in order to accommodate multiple charges on its surface. All four forms become practically isoenergetic in aqueous medium as a result of solvation and screening by the high dielectric constant of water. The existence of multiple nearly isoenergetic and readily interconverting charge distributions allows the hemicarceplex to match the surface electrostatics of its binding partner. The last entry in Figure 73 (a) shows that the introduction of a second negative charge onto the same *m*-phthalic ‘portal’ carries a much larger energetic penalty of 32 kcal/mol (in vacuum). This is a significant amount, consistent with the considerably higher second pK_a of *m*-phthalic acid (4.60 vs 3.54 for

the first one). Such higher energy quadruply charged forms may become important in interactions with sufficiently basic sites and regions.

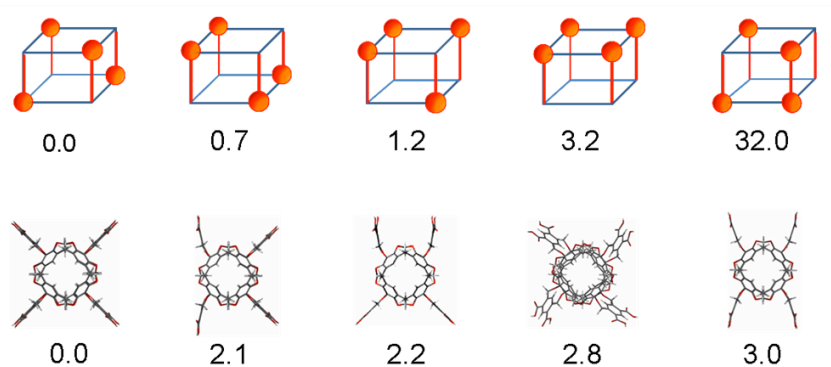


Figure 73 (a) Location of the negative charges and the relative fully relaxed energies of the distinct quadruply de-protonated octacarboxyhemicarcerand (in kcal/mol, AM1 in vacuo). In the first four structures only one carboxylic group per *m*-phthalic acid ‘portal’ is charged. In the last structure one of the portals is doubly deprotonated giving rise to a sharp increase in the energy, consistent with the pK_a difference between the first and second deprotonation of *m*-phthalic acid. **(b)** Examples of the distorted fully protonated hemicarcerand with corresponding energies relative to the D_{4h} minimum (in kcal/mol, AM1 in vacuo).

The variety of surface charge distributions is augmented by the structural flexibility of the outer section of the hemicarcerand. As shown in Figure 73 (b), pivoting of the ‘portals’ dramatically alters the shape of the host molecule at the expense of only a modest energy increase. The distortions change the spacing between the carboxylic groups and expose hydrophobic regions on the sides of the ‘portals’, enabling the hemicarcerand to interact also with the hydrophobic regions of the target. In addition to facilitating the binding, the distortion can reduce the distance between the redox-active guest and the heme group of the cytochrome. Importantly, the volume of the inner void of the cage is for the most part independent of the position of the portals. As a result, the

encapsulation of the guest is not significantly affected by the distortions of the outer region, however, the hemicarcerand does become somewhat more rigid when it holds a large molecule whose size is close to the volume of the internal cavity. The described combination of conformational and electrostatic flexibility allows the octacarboxyhemicarcerand to adapt itself to match the surface of the binding partner in manner that is not possible for small, rigid ligands with similar pK_a values, which not posses such electrostatic and conformational flexibility and for this reason exhibit a binding preference determined purely by the basicity of the available sites. This behavior is consistent with the findings of Jain *et al.* and points to the importance of multivalent interactions in the binding of large synthetic molecules with biological targets.¹²²

The hemicarcerand favors binding regions which allow for the optimization of distributed multivalent electrostatic and hydrophobic interactions, while small anionic ligands bind preferentially to individual positively charged residues. The most basic residues on the surface of cytochrome *c*, which are the most likely sites for the $\text{Fc}(\text{COOH})_2$ binding, are arginines R38 and R91, located 16.5 and 19.2 Å away from the Zn^{2+} center, respectively. As a consequence, $\text{Fc}(\text{COOH})_2$ tends to bind either at the boundary or outside of the 13.1 to 16.5 Å docking zone of the hemicarceplex. This binding preference explains the observed difference in electron transfer rates.

While we focused on demonstrating that the same hemicarcerand can deliver both reducing and oxidizing partners to the target protein, the reported results have broader implications for the design of supramolecular carrier molecules. The dynamic behavior of the hemicarcerand-guest-protein ternary assembly is determined by the relative host-guest and host-protein affinities. The differences in the solubility of the guest molecules

and their affinity towards the hemicarcerand and the long lifetime of the excited triplet state of ZnCC enabled us to investigate two distinct regimes: one of tight encapsulation and one of rapid guest exchange. In both cases the role of the hemicarcerand is more complex than that of a conventional solubilizer or phase transfer catalyst. In the simpler to probe and analyze tight encapsulation limit, $K_{\text{encaps}} \gg K_{\text{assoc}}$, the hemicarcerand transports the ligand to the desired target while protecting it from the aqueous medium. This case, in which the hemicarceplex behaves as distinct stable species, is represented in Figure 59. On the other hand, if $K_{\text{assoc}} > K_{\text{encaps}}$, the more thermodynamically stable hemicarcerand-protein complex is formed first and only at higher concentrations of the guest, the surface-bound cage becomes occupied. As a consequence, in this regime the cage docked to the surface of the protein acts as an artificial receptor which intercepts the ligand from solution and positions it in the vicinity of the active site of cytochrome *c* (Figure 74).

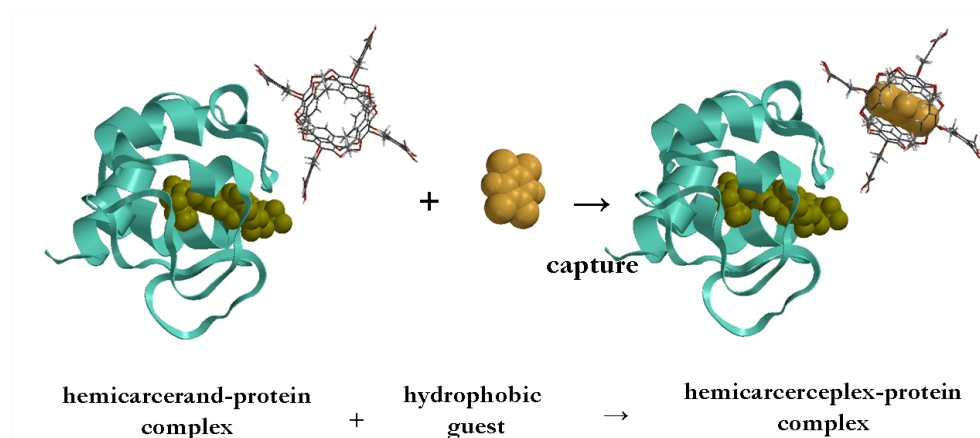


Figure 74. Capture of the guest by the octacarboxyhemicarcerand associated with cytochrome *c*.

In this regime the cage docked to the surface of the protein acts as an artificial receptor which intercepts the ligand from solution and positions it in the vicinity of the

active site of cytochrome *c*. This situation is more challenging from the kinetic point of view, however, it opens fascinating possibilities for the design of hybrid bio-synthetic systems. For example, one can envision how suitably engineered host molecules could be used to selectively intercept substrates from solution and increase the number of turnovers of a biocatalytic reaction. The tight encapsulation limit is relevant to transporting drugs and contrast agents and protecting them from the contact with the biological medium until they reach the selected target. The reversibility of the assembly-disassembly process and its sensitivity to stimuli such as temperature and pH mimics the behavior of biological systems and allows for fine adjustments of the binding equilibria and kinetics.

3.3 Conclusions

We employed a water-soluble Cram type octacarboxyhemicarcerand to dock reducing and oxidizing ligands to the surface of zinc-modified cytochrome *c*. To our knowledge, this is the first demonstration of bidirectional redox chemistry between a protein and a supramolecular host-guest assembly. The cytochrome and the supramolecular cage exhibit affinity driven primarily by electrostatic interactions between the positively charged protein and the negatively charged hemicarcerand. Changes in the spectroscopic properties of ZnCC observed in the presence of the hemicarcerand, as well as the analysis of the electron transfer rates, suggest that the supramolecular cage binds close to the heme site of the cytochrome in the area of the ‘hydrophobic patch’. The binding is aided by the flexibility of the hemicarcerand and the presence of hydrophobic areas on the surface of its portals. As a result, the hemicarcerand is capable of exhibiting ‘induced fit’ behavior that is characteristic of protein-protein

interactions. The kinetic behavior of the complete ternary protein-hemicarcerand-guest assembly depends on the relative strength of the protein-hemicarcerand and guest-hemicarcerand interaction. In the tight encapsulation limit the hemicarcerand transports the ligand to the desired target while protecting it from the aqueous medium. If on the other hand, the affinity of the hemicarcerand for the protein is stronger than that for its guest, the docked cage can act as an artificial receptor (Figure 75). The ability of synthetic macromolecules to act as labile receptor sites which enhance the protein-ligand interaction in a substrate and site selective manner deserves further exploration and may lead to novel biological and biomedical applications. It should be emphasized that the association between the hemicarcerand and the protein, as well as the encapsulation of the guest are fully reversible and can be controlled by varying the concentration of the components of the ternary assembly, as well as the pH, ionic strength and the temperature of the medium. Such capacity to undergo multiple self-assembly/disassembly cycles mimics the dynamic behavior of natural systems more closely than hybrid constructs with permanently appended exobiotic cofactors.

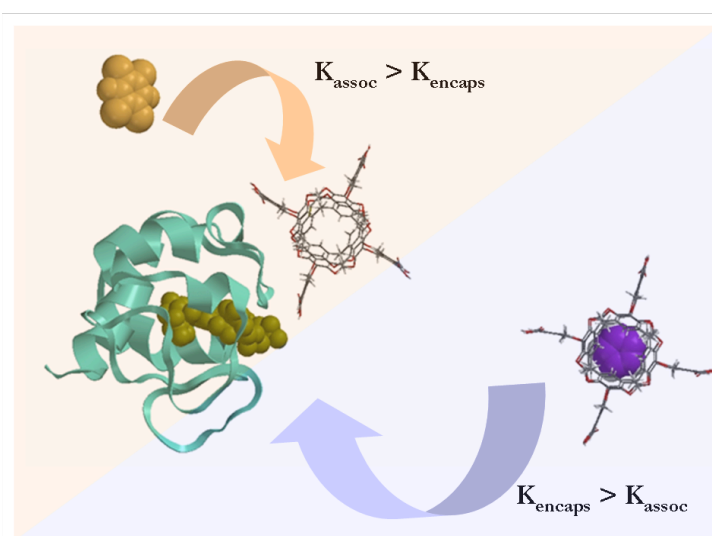


Figure 75. Novel applications of the hemicarcerand: a molecular shuttle (purple) or an artificial receptor (orange).

3.4 References III

-
- ⁸⁵ D. J. Cram, J. M. Cram Host-Guest Chemistry: Complexes between organic compounds simulate the substrate selectivity of enzymes *Science* 1974, *183*, 803-809.
- ⁸⁶ Cram, D. J. The design of molecular hosts, guests, and their complexes *Science* 1988, *240*, 760-767.
- ⁸⁷ D. J. Cram, S. Karbach, Y. H. Kim, L. Baczynskyj, K. Marti, R. M. Sampson, G. W. Kallemeyn Host-Guest Complexation. 47. Carcerands and Carcplexes, the First Closed Molecular Container *J. Am. Chem. Soc.* 1988, *110*, 2554-2560.
- ⁸⁸ M. L. C. Quan, and D. J. Cram Constrictive Binding of Large Guests by a Hemicarcerand Containing Four Portals *J. Am. Chem. Soc.* 1991, *113*, 2754-2755.
- ⁸⁹ Piatnitski, E. L.; Deshayes, K.; Hemicarceplexes that release guests upon irradiation. *Angew. Chem. Int. Ed.* 1998, *37*, 970-972.
- ⁹⁰ D. J. Cram, J. M. Cram In Monographs in Supramolecular Chemistry; In Container Molecules and Their Guests *Stoddart, J. F., Ed.; RSC: Cambridge*, 1994; 149-216 and references therein.
- ⁹¹ R. C. Helgeson, K. Peak, C. B. Knobler, E. F. Maverick, and D. J. Cram Guest-Assisted and Guest-Inhibited Shell Closures Provide Differently Shaped Carceplexes and Hemicarceplexes *J. Am. Chem. Soc.* 1996, *118*, 5590-5604.
- ⁹² D. J.; Cram, R.; Jaeger, K.; Deshayes, Hemicarcerands that encapsulate hydrocarbons with molecular weights greater than two hundred *J. Am. Chem. Soc.* 1993, *115*, 1011-10116.
- ⁹³ A. Jasat, and J. C. Sherman Carceplexes and hemicarceplexes *Chem. Rev.* 1999, *99*, 931-967.
- ⁹⁴ R. Warmuth, J. Yoon Recent highlights in hemicarcerand chemistry *Accounts of Chemical Research*, 2001, *34*, 95-105.
- ⁹⁵ D. Ajami and J. Rebek, Jr Compressed alkanes in reversible encapsulation complexes *Nature Chemistry* 2009, *1*, 89-90
- ⁹⁶ J.-F. Ayme, J. E. Beves, D. A. Leigh, R. T. McBurney, K. Rissanen and D. Schultz A synthetic molecular pentafoil knot. *Nature Chemistry* 2012, *4*, 15–20.
- ⁹⁷ C. M. Fernandes, R. A. Carvalhob, S. Pereira da Costac, F. J.B. Veigaa Multimodal molecular encapsulation of nicardipine hydrochloride by b-cyclodextrin, hydroxypropyl-

b-cyclodextrin and triacetyl-b-cyclodextrin in solution. Structural studies by H NMR and ROESY experiments *European Journal of Pharmaceutical Sciences* 2003, 18, 285–296.

⁹⁸ M. Freitag, L. Gundlach, P. Piotrowiak, and E. Galoppini Fluorescence enhancement of di-p-tolyl viologen by complexation in cucurbit[7]uril *J. AM. CHEM. SOC.* 2012, 134, 3358–3366.

⁹⁹ J. Sun and R. Warmuth Rational design of a nanometre-sized covalent octahedron *Chem. Commun.*, 2011, 47, 9351–9353

¹⁰⁰ E.E. Tucker, and S.C. Christian Vapor pressure studies of benzene-cyclodextrin inclusion complexes in aqueous solution *J. Am. Chem. Soc.* 1984, 106, 1942-1945.

¹⁰¹ H.-J. Schneider, and A. Yatsimirski Principles and methods in supramolecular chemistry *Wiley&Sons, Chichester*, 2000.

¹⁰² X. Liu, Y. Liu, G. Li, R. Warmuth One-Pot, 18-Component Synthesis of an Octahedral Nanocontainer Molecule *Angew. Chem. Int. Ed.* 2006, 45, 901 –904.

¹⁰³ D. Ajami, J. Rebek Jr Compressed alkanes in reversible encapsulation complexes *Nature Chemistry* 2009, 1, 87-90.

¹⁰⁴ D. J. Cram, M. E. Tanner, R. Thomas The Taming of Cyclobutadiene *Angew. Chem., Int. Ed. Engl.* 1991, 30, 1024-1027.

¹⁰⁵ R. Warmuth, and S. Makowiec Photochemical and Thermal Reactions of Intermediates in the Phenylnitrene Rearrangement Inside a Hemicarcerand *J. Am. Chem. Soc.* 2007, 129, 1233-1241.

¹⁰⁶ J. Kang, J. Rebek Jr. Acceleration of a Diels-Alder reaction by a self- assembled molecular capsule *Nature* 1997, 385, 50-52.

¹⁰⁷ R. Warmuth, J-L. Kerdelhué, S. Sánchez Carrera, K. J. Langenwaller, and N. Brown Acceleration through Dispersion Interactions: Effect of a Hemicarcerand on the Transition State of Inner Phase Decompositions of Diazirines *Angew Chem Int Ed.* 2002, 41, 96-99.

¹⁰⁸ Z. S. Romanova, K. Deshayes, and P. Piotrowiak Remote Intermolecular “Heavy-Atom Effect”: Spin-Orbit Coupling Across the Wall of a Hemicarcerand *J. Am. Chem. Soc.* 2001, 123, 2444-2445

¹⁰⁹ P. Piotrowiak Photoinduced electron transfer in molecular systems: recent developments *Chem. Soc. Rev.*, 1999, 28, 143–150

-
- ¹¹⁰ P. Piotrowiak, K. Deshayes, Z. S. Romanova, C. Pagba, S. Hore, G. Zordan, I. Place, and A. Farrán Electron and excitation transfer in hetero-supramolecular assemblies and at molecule–nanoparticle interfaces *Pure Appl. Chem.* 2003, 75 (8), 1061–1068.
- ¹¹¹ Z. S. Romanova, K. Deshayes, and P. Piotrowiak Triplet excitation transfer through the walls of hemicarcerands: Dependence of the electronic coupling on the size of the molecular cage *J. Am. Chem. Soc.* 2001, 123, 11029–11036.
- ¹¹² E. Menozzi, R. Pinalli, E. A. Speets, B. J. Ravoo, E. Dalcanale, and D. N. Reinhondt, Surface-confined single molecules: assembly and disassembly of nanosize coordination cages on gold (111) *Chem. Eur. J.* 2004, 10, 2199–2206.
- ¹¹³ C. L. D. Gibb, and B. C. Gibb, Well-defined, organic nanoenvironments in water: The hydrophobic effect drives a capsular assembly *J. Am. Chem. Soc.* 2004, 126, 1408–11409.
- ¹¹⁴ J. Yoon, and D. J. Cram The first water-soluble hemicarceplexes *Chem. Commun.* 1997, 497–498.
- ¹¹⁵ M. Brownlee Biochemistry and molecular cell biology of diabetic complications *Nature* 414, 813–820, 2001.
- ¹¹⁶ S. S. Gupte, and C. R. Hackenbrock, Multidimensional diffusion modes and collision frequencies of cytochrome c with its redox partners *J. Biol. Chem.* 1988, 263, 5241–5247.
- ¹¹⁷ H. Pelletier, and J. Kraut Crystal structure of a complex between electron transfer partners, cytochrome c peroxidase and cytochrome c *Science* 1993, 258, 1748–1755.
- ¹¹⁸ J. S. Zhou, and B. M. Hoffman Stern-Volmer in reverse: 2:1 stoichiometry of the cytochrome c-cytochrome c peroxidase electron-transfer complex *Science*, 1994, 265 (16) 1693–1696.
- ¹¹⁹ S. J. Riedl, W. Li, Y. Chao, R. Schwarzenbacher and Y. Shi Structure of the apoptotic protease-activating factor 1 bound to ADP *Nature* 2005, 434, 926–933.
- ¹²⁰ S. H. Speck, S. Ferguson-Miller, N. Osheroff, and E. Margoliash Definition of cytochrome c binding domains by chemical modification: Kinetics of reaction with beef mitochondrial reductase and functional organization of the respiratory chain. *PNAS* 1979, 76, 155–159.
- ¹²¹ C. Lange and C. Hunte Crystal structure of the yeast cytochrome bc1 complex with its bound substrate cytochrome c *PANS* 2002, 99, 2800–2805.
- ¹²² R. K. Jain, L. K. Tsou, A. D. Hamilton Macrocyclic chemistry: Current trends and future perspectives *Springer* 2005, 267–275.

-
- ¹²³ S. Papp, J. M. Vanderkooi, C. S. Owen, G. R. Holtom, C. M. Phillips Reactions of excited triplet states of metal substituted myoglobin with dioxygen and quinine *Biophys. J.* 1990, 58, 177-186.
- ¹²⁴ N. Sudha, B. P. Dixit, V. T. Moy, and J. M. Vanderkooi Reactions of excited-state cytochrome c derivatives. Delayed fluorescence and phosphorescence of zinc, tin, and metal-free cytochrome c at room temperature *Biochemistry* 1984, 23, 2103-2107.
- ¹²⁵ T. Horie, G. Maniara, J. M. Vanderkooi Interaction of electron acceptors with the excited triplet state of Zn cytochrome c *FEBS Letters*, 1984, 177, 287-290.
- ¹²⁶ H. Anni, J. M. Vanderkooi, and L. Mayne Structure of zinc-substituted cytochrome c: Nuclear magnetic resonance and optical spectroscopic studies *Biochemistry* 1995, 34, 5744-5753.
- ¹²⁷ H. Elias, M. H. Chou, and J. R. Winkler Electron-transfer kinetics of zn-substituted cytochrome c and its Ru(NH₂)(Histidine-33) derivative *J. Am. Chem. Soc.* 1988, 110, 429-434.
- ¹²⁸ B. P. S. N. Dixit, A. J. Waring, J.M. Vanderkooi Triplet absorption and phosphorescence emission in Zinc cytochrome c *FEBS Letters*, 1981, 125, 86-88.
- ¹²⁹ E. Magner, and G. McLendon Ground-state and excited-state electron-transfer reactions of zinc cytochrome c *J. Phys. Chem.* 1989, 93, 7130-7134.
- ¹³⁰ L. Qin and N. M. Kostic Photoinduced electron transfer from the triplet state of zinc cytochrome c to ferricytochrome bs is gated by configurational fluctuations of the diprotein complex *Biochemistry* 1994, 33, 12592-12599.
- ¹³¹ C. Shen, and N. M. Kostic, Photoinduced electron transfer from zinc cytochrome c to cationic ruthenium(III) complexes within silica glass prepared by the sol-gel method *Journal of Electroanalytical Chemistry*, 1997, 438, 61-65.
- ¹³² C. Shen, and N. M. Kostic Reductive quenching of the triplet state of zinc cytochrome c by the hexacyanoferrate(II) anion and by conjugate bases of ethylenediaminetetraacetic Acid *Inorg. Chem.* 1996, 35, 2780-2784.
- ¹³³ I. Hamachi, H. Takashima, Y.Z. Hu, S. Shinkai, and S. Oishi Cyclodextrin-appended myoglobin as a tool for construction of a donor-sensitizer-acceptor triad on a protein surface *Chem. Commun.* 2000, 1127-1128.
- ¹³⁴ D. A. Uhlenheuer, D. Wasserberg, H. Nguyen, L. Zhang, C. Blum, V. Subramaniam, and L. Brunsveld Modulation of protein dimerization by a supramolecular host-guest system *Chem. Eur. J.* 2009, 15, 8779-8790.

-
- ¹³⁵ R. Zadnırd, T. Schrader, Nanomolar protein sensing with embedded receptor molecules *J. AM. CHEM. SOC.* 2005, *127*, 904-915.
- ¹³⁶ E. L. Piatnitski, R. A. Flowers II; K., Deshayes Highly organized spherical hosts that bind organic guests in aqueous solution with micromolar affinity: Microcalorimetry studies *Chem. Eur. J.* 2000, *6*, 999 – 1006.
- ¹³⁷ J. M. Vanderkooi, and M. Erecinska Cytochrome c interaction with membranes absorption and emission spectra and binding characteristics of iron-free cytochrome c *Eur. J. Biochem.* 1975, *60*, 199-207.
- ¹³⁸ T. Flatmark, A. B. Robinson Structure and function of cytochromes. (K . Okunuki, Kamen, M. D. & Sekuzu, I., eds) 1968, *University Park Press, Baltimore*, 383 – 387.
- ¹³⁹ W. R. Fisher, H. Taniuchi, and C. B. Anfinsen On the role of heme in the formation of the structure of cytochrome c *J. Biol. Chem.* 1973, *248*, 3188-3195.
- ¹⁴⁰ E. K. J. Tuominen, C. J. A. Wallace, and P. K. J. Kinnunen Phospholipid-cytochrome c interaction: Evidence for the extended lipid anchorage *J. Biol. Chem.* 2002, *277*, 8822–8826.
- ¹⁴¹ I. L. Nantes, M. R. Zucchi, O. R. Nascimento, and A. Faljoni-Alario Effect of heme iron valence state on the conformation of cytochrome C and its association with membrane interfaces: A CD and EPR investigation. *J. Biol. Chem.* 2001, *276*, 153–158.
- ¹⁴² H. Koloczek, T. Horie, T. Yonetani, H. Anni, G. Maniara, J. M. Vanderkooi Interaction between cytochrome c and cytochrome c peroxidase: excited-state reactions of zinc- and tin-substituted derivatives *Biochemistry*, 1987, *26*, 3142–3148.
- ¹⁴³ B. M. Hoffman Triplet State Electron Paramagnetic Resonance Studies of Zinc Porphyrins and Zinc-Substituted Hemoglobins and Myoglobins *J. Am. Chem. Soc.* 1975, *97*, 1688–1694.
- ¹⁴⁴ K. A. Sharp, A. Nicholls, R. F. Fine, B. Honig Reconciling the magnitude of the microscopic and macroscopic hydrophobic effects *Science* 1991, *252*, 106-109.
- ¹⁴⁵ M. P. Merker, R.D. Bongard, G. S. Krenz, H. Zhao, V. S. Fernandes, B. Kalyanaraman, N. Hogg, S. H. Audi Impact of pulmonary arterial endothelial cells on duroquinone redox status *Free Radical Biology & Medicine*, 2004, *37*, 86 – 103.
- ¹⁴⁶ C. Pagba, G. Zordan, E. Galoppini, E. L. Piatnitski, S. Hore, K. Deshayes, and P. Piotrowiak Hybrid photoactive assemblies: electron injection from host-guest complexes into semiconductor nanoparticles *J. Am. Chem. Soc.* 2004, *126*, 9888–9889.

-
- ¹⁴⁷ K.K. Clark-Ferris, J. Fisher Topographical mimicry of the enzyme binding domain of cytochrome c *J. Am. Chem. Soc.* 1985, *107*, 5007-5008.
- ¹⁴⁸ G. D. Scholes, Long- Range resonance Energy Transfer in Molecular Systems *Annu. Rev. Phys. Chem.* 2003, *54*, 57–87.
- ¹⁴⁹ L. Cristian, P. Piotrowiak, and R. S. Farid Mimicking Photosynthesis in a Computationally Designed Synthetic Metalloprotein *J. Am. Chem. Soc.* 2003, *125*, 11814–11815.
- ¹⁵⁰ A. J. Parola, F. Pina, E. Ferreira, M. Maestri, V. Balzani Photoinduced Electron- and Energy-Transfer Processes of Biacetyl Imprisoned in a Hemiacarcerand *J. Am. Chem. Soc.* 1996, *118*, 11610-11616.
- ¹⁵¹ M. D. Johnson, J. R. Miller, N. S. Green, G. L. Closs Distance dependence of intramolecular hole and electron transfer in organic radical ions *J. Phys. Chem.* 1989, *93*, 1173–1176.
- ¹⁵² D. W. Dixon, X. Hang, S. E. Woehler, A. G. Mauk, B. P. Sistrup Electron-Transfer Self-Exchange Kinetics of Cytochrome b5 *J. Am. Chem. Soc.* 1990, *112*, 1082-1088.
- ¹⁵³ S. M. Andrew, K. A. Thomasson, S. H. Northrup Simulation of Electron-Transfer Self-Exchange in Cytochromes c and bs *J. Am. Chem. Soc.* 1993, *115*, 5516-5521.
- ¹⁵⁴ M. M. Ivković-Jensen, N. M. Kostić Effects of Viscosity and Temperature on the Kinetics of the Electron-Transfer Reaction between the Triplet State of Zinc Cytochrome c and Cupriplastocyanin *Biochemistry* 1997, *36*, 8135-8144.
- ¹⁵⁵ J. S. Zhou and N. M Kostić Photoinduced Electron-Transfer Reaction in a Ternary System Involving Zinc Cytochrome c and Plastocyanin. Interplay of Monopolar and Dipolar Electrostatic Interactions between Metalloproteins *Biochemistry* 1992, *31*, 7543-7550.
- ¹⁵⁶ G. L. McLendon, J. R. Winkler, D. G. Nocera, M. R. Mauk, A. G. Mauk, H. B. Gray Quenching of zinc-substituted cytochrome c excited states by cytochrome b5 *J. Am. Chem. Soc.* 1985, *107*, 739–740.
- ¹⁵⁷ J. R. Winkler and H. B. Gray Electron transfer in ruthenium-modified proteins *Chem. Rev.* 1992, 389-479.

Chapter 4. Gas trapping inside the water soluble Cram-type hemicarcerand.

Molecular recognition of gases is a rising area of chemistry that has multiple applications in biomedicine, science and technology.^{158,159} Studies of the supramolecular chemistry by investigating intermolecular interactions and assembly of molecules helps us to understand how gases interact with biological molecules and offers insights into the mechanisms of their physiological activity. Host-guest chemistry has been applied for to gas purification, gas storage and gas conversion^{160, 161, 162,163} as well as for gas sensing. More recently studies have been undertaken for labeling to provide knowledge about the structure and dynamics of complexes.^{164,165,166} The sensitivity of techniques employed in studies of gases such as magnetic resonance imaging (MRI) are usually much weaker than in liquids, because gas density is much lower than the density of fluids under normal conditions.¹⁶⁷ Gas trapping inside highly porous materials raises its adsorption, host molecules can increases its solubility in liquid phase, which helps to enhance the signal and consequently improves its detection. The fact that gases comprise the atmosphere of the Earth and continuously circulate between different phases and are absorbed or emitted due to chemical processes, necessitates the development of novel methods for gas recognition under variety of conditions. A number of materials for gas trapping have been developed and applied.^{168,169,170} Gas encapsulation in the solid and liquid phase has been extensively investigated,^{171,172} but still the molecular detection of gases deserves more attention. Many industrially important gases, such as natural hydrocarbons are hydrophobic. At the same time, their applications require water. The problem with solubility appears also when the hydrophobic gases have to be applied in biosystems.

Use of an organic framework does not increase the gas solubility in liquid phase since the assembly of porous solids is usually filled with solvent molecules. Cyclodextrin or cucurbituril do not fully encapsulate the gas molecules, while the self-assembling capsules require delicate balancing of conditions such as specific concentration or a temperature range to assemble the capsule and to trap a gas molecule. Rudkevich *et al.*¹⁷³ has shown that Cram hemicarcerands made from two lipophilic resorcin[4]arene hemispheres connected by three *o*-xylyl bridges form stable complexes with hydrocarbons in aqueous solution (Figure 76).

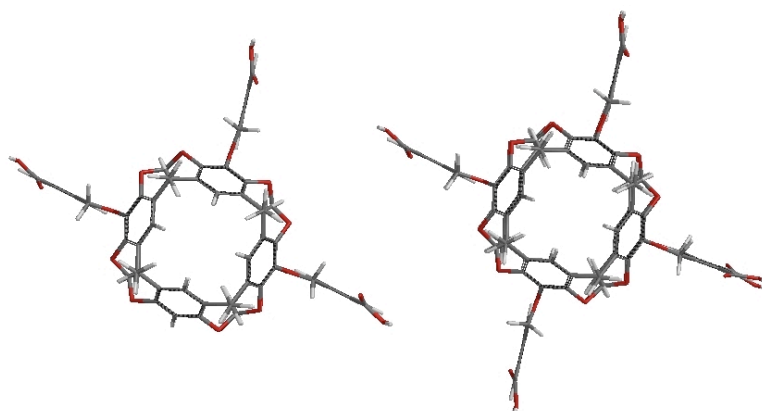


Figure 76. Cram-type hemicarcerand used by Rudkevich *et al.*¹⁷³ (left) vs the Cram-type hemicarcerand used for butane and SF₆ trapping in work reported here (right).

Here we present encapsulation studies of hydrophobic gases such as butane and sulfur hexafluoride inside the more closed water soluble Cram-type hemicarcerand possessing four *o*-xylyl bridges, a carrier that can fully insulate small molecules. The encapsulation process has been probed by nuclear magnetic resonance spectroscopy (NMR). NMR plays a very important role in studying various interactions in solution thanks to the ability to detect inter- and intra- nuclear coupling. During NMR studies, the local magnetic field experienced by a nucleus is affected by neighboring magnetic nuclei.

There are direct and indirect types of magnetic interactions between nuclei. The direct transfer of nuclear spin polarization from one nuclear spin population to another via cross-relaxation generate Nuclear Overhauser Effect (NOE, dipole-dipole coupling). The indirect, through-bond interaction (spin-spin splitting: J) is caused by a spin of one nucleus which perturbs (polarizes) the spins of the intervening electrons, and the energy levels of neighboring magnetic nuclei.¹⁷⁴ Thanks to the fact that hydrogen and fluorine atoms have fractional spins (Table1), the encapsulation of butane or SF₆, as well as structural changes of the cage upon this process can be easily monitored by detecting their nuclear resonance.

The general scheme for an encapsulation of gas molecule in aqueous solution within the water soluble Cram-type hemicarcerand is presented in Figure 77. The goal here is to investigate in molecular detail the interaction between the guest and the host as well as the dynamics of the guest exchange by applying several NMR techniques.

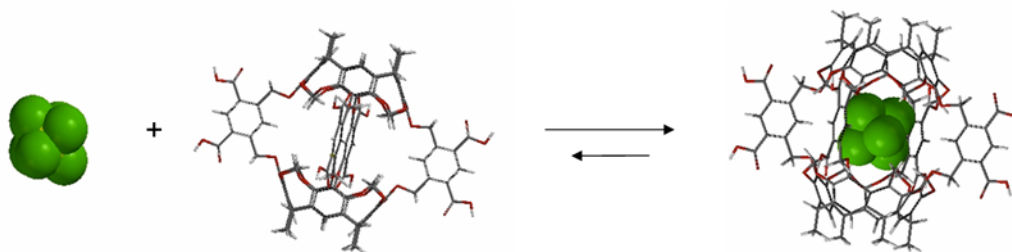


Figure 77. The general scheme.

Since both gases, SF₆ and butane, are hydrophobic, the driving force for the encapsulation by the water-soluble hemicarcerand and hence the stability of the host-guest complex can be predicted on the basis of the free energy change associated with the reduction of hydrophobic surface exposed to water. The 101 Å² hydrophobic surface of SF₆ and 112 Å² hydrophobic surface of butane combined with Honig's 47 cal·mol⁻¹·Å⁻²

hydrophobic energy¹⁴⁴ yields encapsulation free energy of -4.7 kcal/mol and -5.3 kcal/mol for SF₆ and butane respectively. The encapsulation process should change the NMR spectrum of the cage as well as of the guest molecule. Gas encapsulation raises also the more fundamental question of the state of trapped matter. Cram *et al.* suggested that the inner phase of a host molecule is a mixture of vacuum and guest occupation of volume and can be designed to be vacuum-like, liquid-like, or even solid-like, depending on the balance of space occupied by guest and free space.^{175, 176} In these experiments the gas molecule not only changes its environment but becomes imprisoned inside the volume which restrict its freedom of translational and even rotational movement. The space offered by the cage molecule may not be sufficient for the gaseous guest to maintain its properties as to the ideal gas law states that each molecule occupies 37 nm³ at standard temperature and pressure. This may force a gas molecule(s) to start behaving more as a liquid guest(s) in the “inner” phase environment.

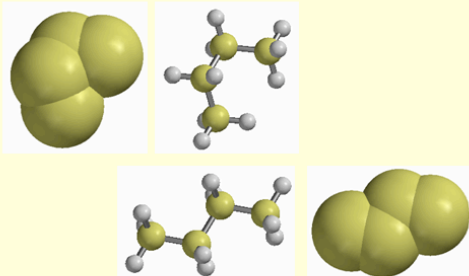
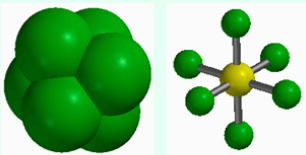
Butane C ₄ H ₁₀	Sulfur hexafluoride SF ₆
	
MW: 58.12 g mol ⁻¹	MW: 146.06 g mol ⁻¹
Volume: 88.3 Å ³	Volume: 72.9 Å ³
Density in gas phase: 2.48 g/l	Density in gas phase: 6.17 g/l
Density in liquid phase: 600 g/l	Density in liquid phase: 1888 g/l
Solubility in water: 61 mg/l	Solubility in water: 29 mg/l

Figure 78. Properties of butane and sulfur hexafluoride.

The sizes and properties of the selected gases are summarized in Figure 78. The lipophilic inner cavity of the host molecule with a volume of about 200 Å³ is large enough to trap at least one molecule of butane as well as of the slightly smaller SF₆. Butane was chosen for these investigations because its volume is perfect for this cage, it is commercially available and as a member of natural gases is a good representant of hydrocarbons. The second candidate, sulfur hexafluoride (SF₆), possesses excellent dielectric and insulating properties and is used extensively in the electric and electronic industries. Importantly, SF₆ has a global warming potential thousand times greater than carbon dioxide and has been put on a list of greenhouse gases. As a result, researchers have started to search for a method to capture this gas from the atmosphere. Recent studies on SF₆ have also focused on its potential use in medical science as an alternative to ¹²⁹Xe. SF₆ is nontoxic and chemically inert at room temperature. The octahedral molecular geometry of SF₆ with six chemically equivalent ¹⁹F nuclei is a major advantage in ¹⁹F NMR. ¹⁹F NMR has been frequently applied in biological systems for structural and binding studies^{177, 178} as well as due to its imaging applications. ¹⁹F imaging of inhaled sulfur hexafluoride (SF₆) allows quantitative studies of lung function on the basis of signal intensity or longitudinal relaxation time measurements.¹⁷⁹ Recently, the binding of SF₆ into the hydrophobic cavity of organic host molecules such as cucurbit[6]uril, α-cyclodextrin or metal-hyphen capsule in aqueous solutions have been reported.^{180, 181} The detection limit of dissolved SF₆ by ¹⁹F NMR is in the μM range for measurement times of a few minutes with standard equipment. The ¹⁹F longitudinal relaxation time of SF₆ dissolved in diamagnetic solutions ranges between a few hundreds of milliseconds and about 1 s. It is much shorter than the longitudinal relaxation time of monatomic ¹²⁹Xe.

Short relaxation times T_1 allow multiple accumulation of the NMR signal over relatively short time to improve the signal-to-noise ratio. Similar detection level and range of T_1 are expected for a butane molecule in liquid phase.

In addition to chemical shift measurements, the investigation of a trapped butane and SF₆ molecule has included ¹H and ¹⁹F longitudinal relaxation time measurements of butane and SF₆ molecules respectively, inside and outside the cage. Additionally, the selective magnetization transfer experiments through homo or heteronuclear dipole-dipole cross relaxation and some 2D nuclear coupling measurements have been used to probe the binding of the gas, its phase and to characterize the geometry of the host / guest complex. The description of applied experiments has been summarized in the methods section below.

4.1 Materials and methods

Materials: Sulfur hexafluoride $\geq 99.75\%$ and butane 99% gas were purchased from Sigma Aldrich Co. Deuterium oxide (99.9%) was obtained from Cambridge Isotope Laboratories. The water soluble Cram-types hemicarcerand (cage) was a gift from Dr. Eugene L. Piatnitski Chekler.¹⁸²

Sample preparation and encapsulation: The appropriate amount of Cage was dissolved in D₂O at pD= 8.5 (adjusted by $\sim 0.2\text{M}$ Na₂OD and DCl solutions) in order to obtain $2.5 \div 3.0 \times 10^{-4}$ M solution of the cage solution.

The NMR samples were prepared in 5 mm NMR tubes, closed by silicon cork by gently bubbling SF₆ or butane gas through the needle immersed in approximately 1ml of the cage/D₂O solution for about 30 minutes. In parallel, two control samples were

prepared as well: Gas/D₂O and Cage. The cage only sample was made by gently bubbling argon gas through the solution in order to remove oxygen, the presence of which would affect the NMR relaxation times (Figure 79). All the samples were allowed to fully equilibrate for at least 24 h.

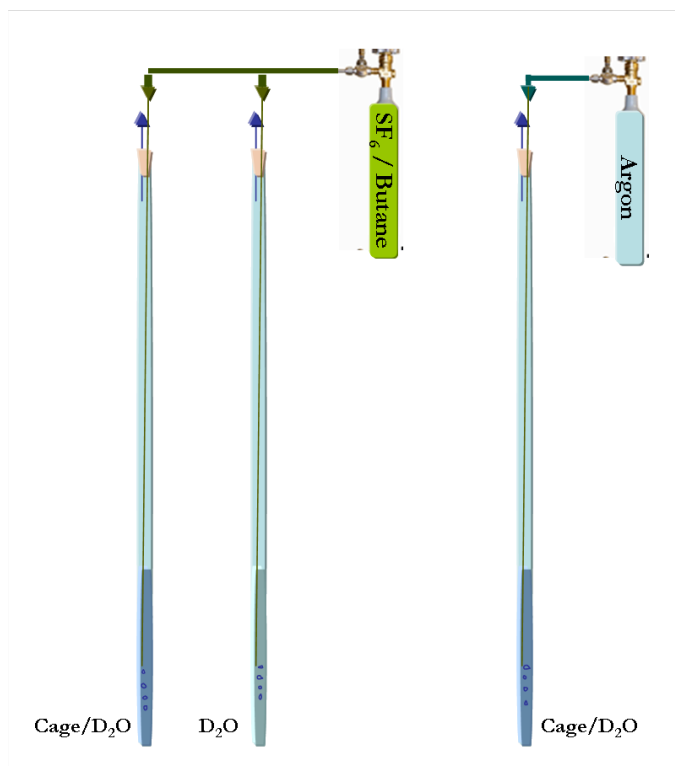


Figure 79. The set up for the encapsulation of hydrophobic gases.

Measurements: NMR spectra were recorded at different temperatures on either a Varian VXR 500 or AS600 spectrometer operating at proton frequencies of 500 and 600 MHz, respectively. The samples were left to reach equilibrium at the desired temperature within the magnet for at least 30 min before the NMR measurements.

1D ¹H NMR: spectra were recorded at 499.7 and 599.7 MHz for ¹H with spectral width of 16 ppm centered at 4.7 ppm for ¹H with respect to the major signal of HDO.

1D ^{19}F NMR: spectra were recorded at 470.5 MHz for ^{19}F with spectral width of 58 ppm using 64 transients. The chemical shift scale was calibrated with respect to the major signal of pure CFCl_3 used as an external reference.

Proton longitudinal relaxation times T_1 : The spin-lattice relaxation time T_1 was measured in the inversion recovery experiment in a simple two-pulse sequence (Figure 80). First the nuclei are allowed to relax during d_1 then a 180° pulse is applied which inverts the magnetization vector along the negative z axis. As a result, the magnetization vector M_z gradually increases until it is back to the original value M_0 . Since the magnetisation along the z axis is not observable, the recovery is monitored by placing the vector in the xy plane by applying a 90° pulse after a suitable period, t_1 , to measure its magnitude as a function of time. Mathematically, this recovery process is described by the Bloch equations for the z –component (24)¹⁸³:

$$dM_z/dt = (M_0 - M_z)/T_1 \quad (24)$$

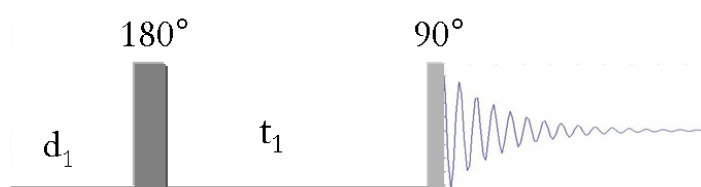


Figure 80. The inversion recovery sequence.

T_1 finding involves measurements of the signal amplitude for several different t_1 intervals (Figure 81) and the curve fitting according to formula (25).

$$M_t = M_0 (1 - 2\exp(-t_1/T_1)) \quad (25)$$

where M_0 corresponds to equilibrium magnetization, such as that recorded at t_∞ .

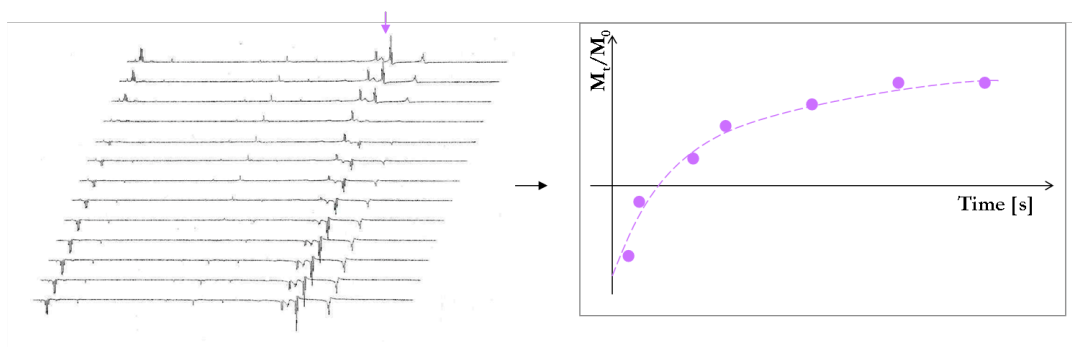


Figure 81. The inversion recovery experiment and the exponential growth of the longitudinal magnetization with increasing t_1 .

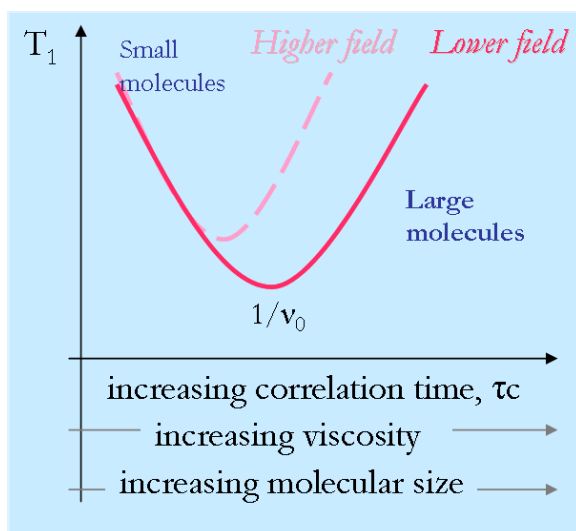


Figure 82. The dependence of longitudinal relaxation times T_1 on the correlation time τ_c , viscosity and molecular size.

^1H spin-lattice relaxation times were measured at 600 MHz using the inversion-recovery pulse sequence with 512 transients and 14 recovery delays ranging between 0.01 and 10 s. ^1H pulse widths were calibrated on 1 pulse (s2pul) experiments. The measurements were repeated at differed temperatures: 5 and 25. The T_1 values were determined using integrated intensities and a three parameter nonlinear fit.

Fluorine longitudinal relaxation times T_1 : ^{19}F spin-lattice relaxation times were measured at 470 MHz using the inversion-recovery pulse sequence with 256 transients, 10 s repetition time, and 10 recovery delays ranging between 0.02 and 14 s. The measurements were repeated at differed temperatures: 5, 20, 25 and 30°C. T_1 data were determined using integrated intensities and a three parameter nonlinear fit.

2D COSY: Two-dimensional COSY (CORrelation SpectroscopY) experiment performed to determine which protons are spin-spin coupled detects only protons with J-coupling over two or three bonds. 2D COSY was recorded at 600 MHz at 5°C with spectral window of 10000 Hz in both dimensions, 64 repetition and 2×256 transients. Water suppression was applied (Figure 83).

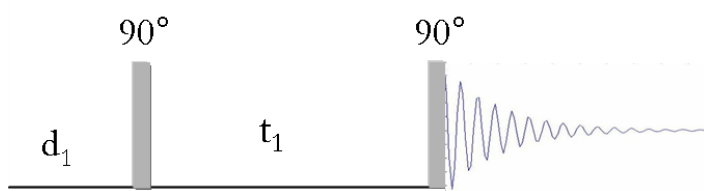


Figure 83. Puls sequence for COESY.

1D ^{19}F cycle-NOE Difference Experiment is a steady-state NOE difference experiment in which a selected peak (here, corresponding to the ^{19}F of the SF_6 inside the cage) is saturated by low power RF saturation for a designated time (t_s). NOE peaks (here, corresponding to the ^{19}F of the SF_6 outside the cage) are revealed and phased positive and the saturated peak phased negative.

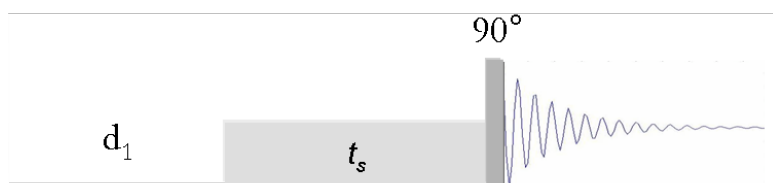


Figure 84. The cycle-NOE sequence.

The relationship between exchange rate and saturation transfer is measured by monitoring the intensity I of the unsaturated resonance when an exchanging resonance is saturated for a given length of time as follows (26):

$$\frac{I(t) - I_{\infty}}{I_0} = \exp(-kt) \quad (26)$$

1D ^{19}F cycle-NOE were measured at 470 MHz using pulse sequence presented at Figure 84 with 256 transients, 10 s repetition time, and 11 different saturation times ranging from 0.01 to 16 s at 25 °C.

2D TOCSY: Two-dimensional Total Correlation Spectroscopy yields homonuclear proton correlation spectra based on scalar couplings but is also able to establish correlations between protons within the same spin system, regardless of whether they are themselves coupled to one another. 2D TOCSY was recorded at 600 MHz at 5°C with spectral window of 10000 Hz in both dimensions.

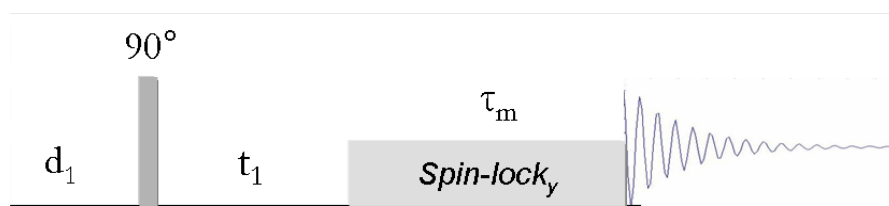


Figure 85. The TOCSY sequence. The spin-lock mixing time, τ_m , replaces the single mixing pulse of the basic COSY experiment.

The experiment was recorded with resolution of 256 points in the t_1 dimension and 1024 points in the t_2 dimension with 0.5 s mixing time and 256 transients (Figure 85). Water suppression was applied.

2D NOESY: Two-dimensional Nuclear Overhauser Enhancement Spectroscopy detects correlations through-space. The intensity of the NOE is proportional to the distance between two nuclei in its invert sixth power ($1/r^6$) and is usually detected for the distance smaller than 5 Å. 2D NOESY was recorded at 600 MHz at 5°C and 500 MHz at 25°C with spectral window of 10000 Hz in both dimensions. The experiment was recorded with resolution of 256 points in the t_1 dimension and 1024 points in the t_2 dimension with 0.3 and 0.6 s mixing time and 256 transients (Figure 86). Water suppression was applied.

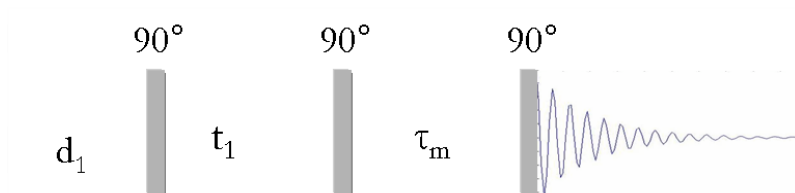


Figure 86. The NOESY pulse sequence.

Data Analysis: Data sets were processed on the Varian NMR Spectrometer system equipped with VNMR 6.1B Software, as well as using NMRPipe and NmrView.^{184, 185}

4.2 Results and discussion

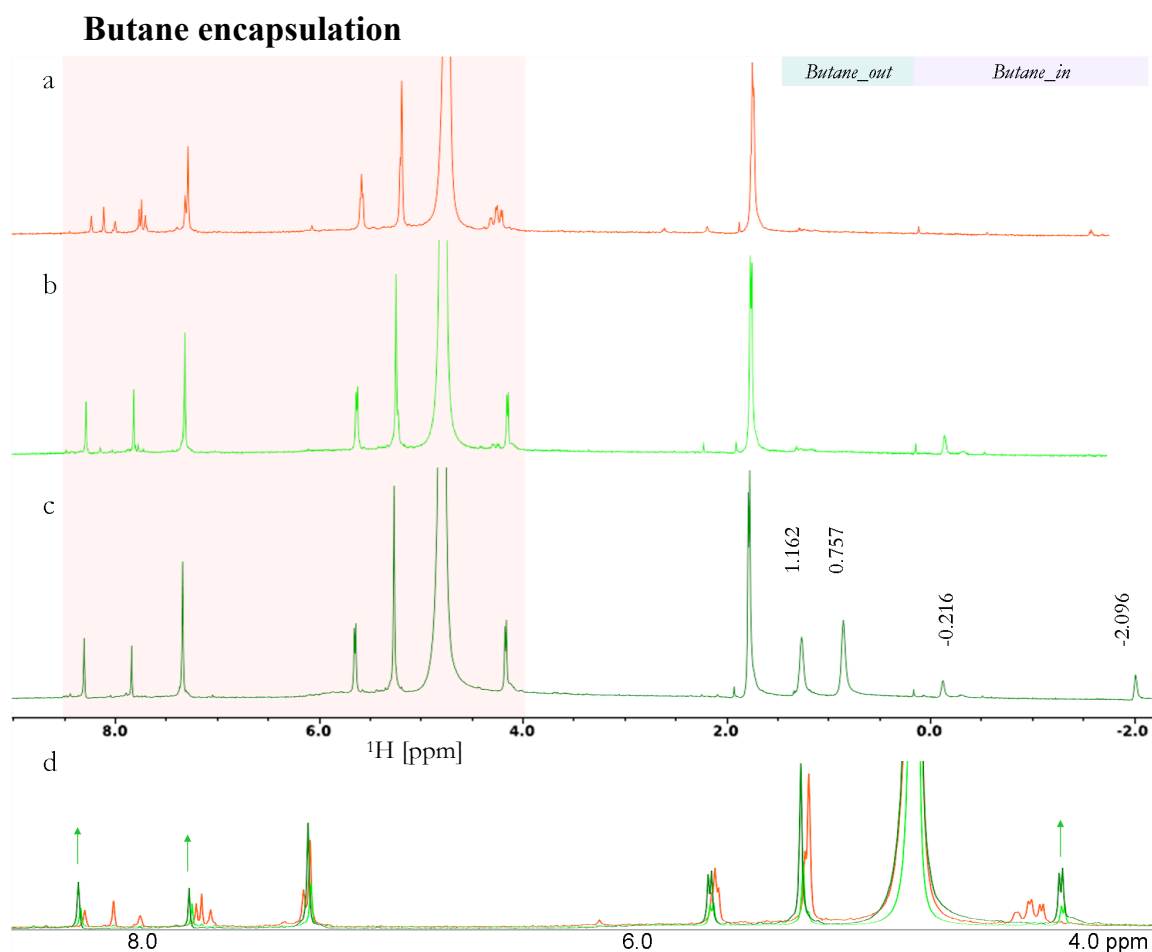


Figure 87. 1D ^1H NMR for: a) free cage (orange), b) the same solution of cage after bubbling with butane (green); c) gas-saturated sample obtained by additional bubbling with butane (dark green); and d) the highlighted region (4-8.5 ppm) for all three spectra (a,b and c) together, green arrow indicate the signal increase upon encapsulation. No water suppression.

The 1D ^1H NMR spectrum of Cram type hemicarcerand in aqueous solution is shown in Figure 87a. Upon the bubbling of a butane gas through this solution the cage spectrum changed which clearly demonstrate its affinity toward the hydrocarbon (Figure 87b). It was the most evident by changes in aromatic region of a spectrum (7.0 - 8.5

ppm). The spectrum of free cage displays multiple peaks in this region, which collapse when butane has been added, instead the single peaks appear, slightly shifted to the low field region. These changes may imply that the cage which exists as a mixture of different conformations or is occupied either by argon or water molecules displays one dominant structure when it binds the butane. The almost complete disappearance of the multiple peaks suggests that most of the host molecules are already occupied by a guest. No free butane was observed (~ 1.2 and ~ 0.8) by that time but an additional peak which appeared at -0.2 ppm is assumed to correspond to bound butane. The additional NMR spectral changes were detected when an excess of gas was used (Figure 87c). The cage spectrum appeared to be even more homogeneous suggesting complete gas encapsulation. Additionally two signals appeared at 1.2 and 0.76 ppm corresponding to free butane and by increasing spectral width the missing peak for alkyl protons from bound butane was found at -2.1 ppm. The significant difference in chemical shifts between nuclei of free and encapsulated gas implies the slow exchange processes on the NMR time scale as well as high exchange barriers.

The more detailed 2D NMR experiments, COSY (Figure 89), TOCSY (Figure 90) and NOESY (Figure 91) helped us to identify every proton in the spectrum (Figure 88).

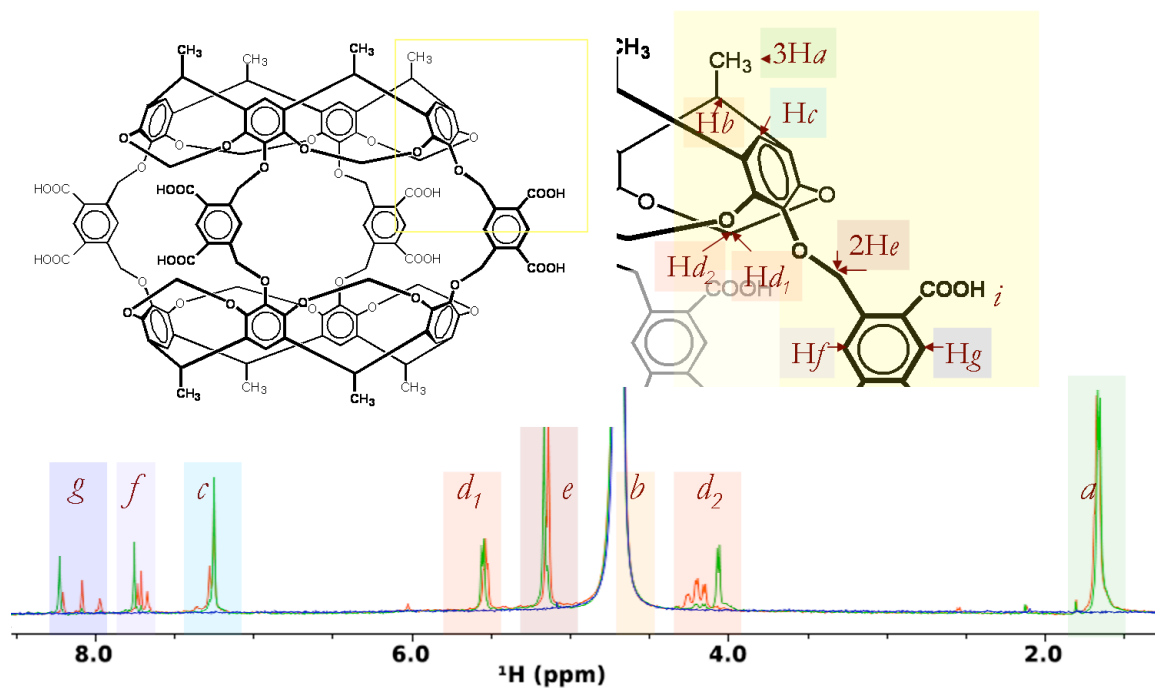


Figure 88. Cram-type hemicarcerand (upper left) with labeled protons (a-i; upper right) and 1D ^1H NMR for cage (orange) and cage in the presence of butane (green) with assigned protons. Note that the nucleus b is here invisible because the water peak.

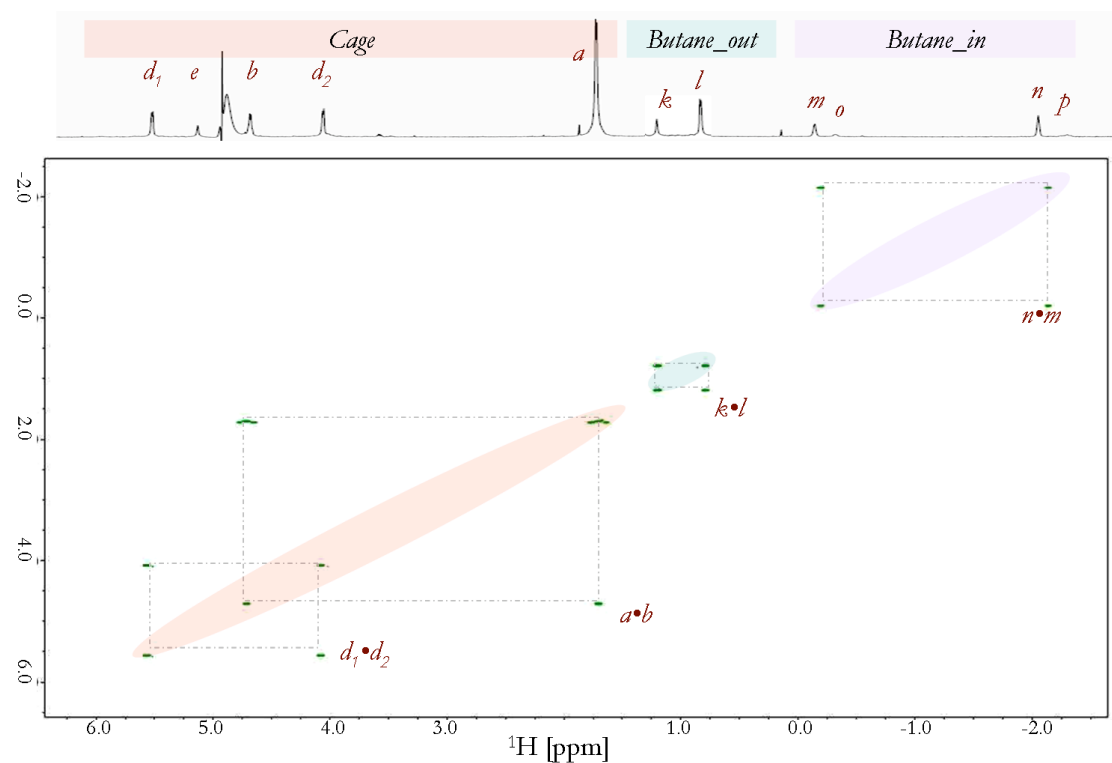


Figure 89. 2D COSY for the cage+butane sample at 5°C.

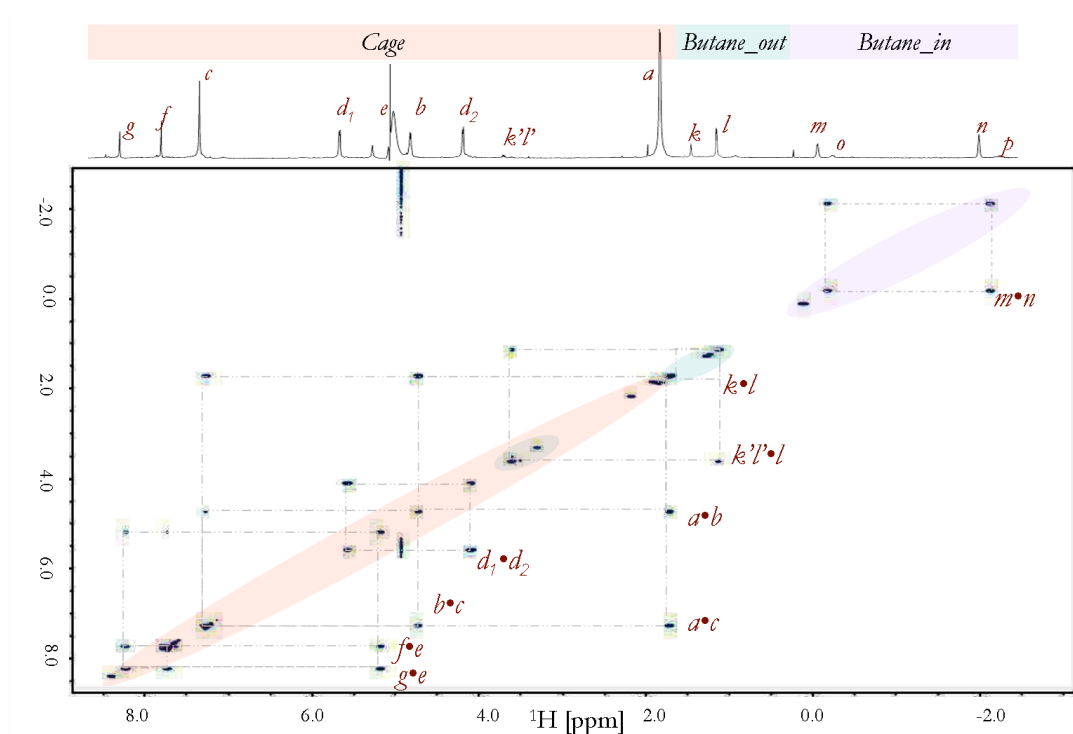


Figure 90. 2D TOCSY for the cage+butane sample at 5°C. Note, that there is an additional cross peak for free butane (k) at ~3.5 ppm (label $k'l'$).

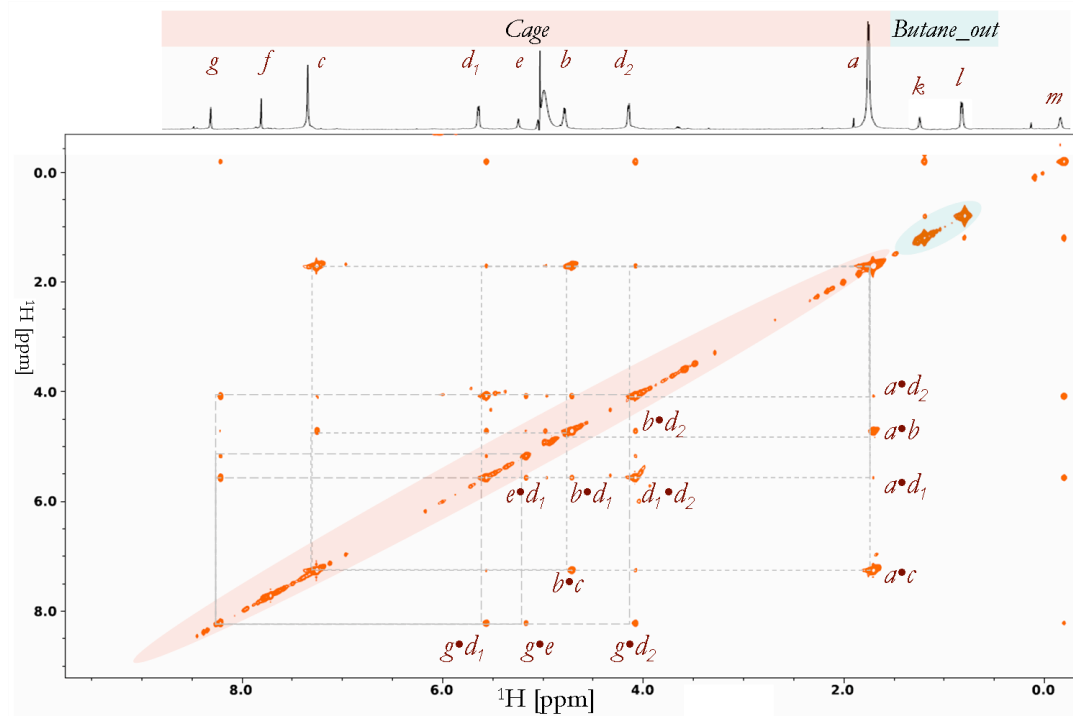


Figure 91. 2D NOESY for the cage+butane sample at 5°C showing the interaction of the cage protons.

These results explain why the aromatic region appeared to be so different upon butane binding. The protons *g* and *f* which are located on four *o*-xylyl bridges of the cage are directly involved in host binding. This part of the cage is also most flexible, which was shown in previous section of this thesis. The 2D experiments show also that the *d* nuclei are not equivalent. The *d*₁ is the one which is directed out of cage while *d*₂ is the inward-facing proton of the -OCH₂O- bridge and thus appears to be more sensitive to the presence of the gas in the cavity (Figure 87d). In empty cage, these protons were seen as doublets at around 4.2 ppm, and they transform into one doublet shifted 0.3 ppm upfield upon encapsulation.

NOESY also reveals a number of interactions between the free (labeled *k* for the CH₂ and *l* for the CH₃ group) and bound butane (labeled *m* for the CH₂ and *n* for the CH₃ group) (Figure 92). The strong cross signals between the protons of in free (*k•l*) and bound (*m•n*) butane were seen, as well as cross peaks between the same type of nuclei inside and outside the cavity (*k* and *m* or *l* and *n*), which imply proton exchange between inner and outer sphere of the cage. Additionally, the free butane nuclei display cross peaks with two other peaks, labeled *o* and *p*, located next to the bound butane signals, *m* and *n* peaks respectively, about 0.2 ppm upfield. These cross-peak signals suggest that there is a second butane molecule inside the cage. The upfield position of these nuclei implies that they are shielded by the cavity aromatic rings. Since these peaks are broader it may suggest that rapid rotation of the guest on the ¹H NMR time scale takes place.

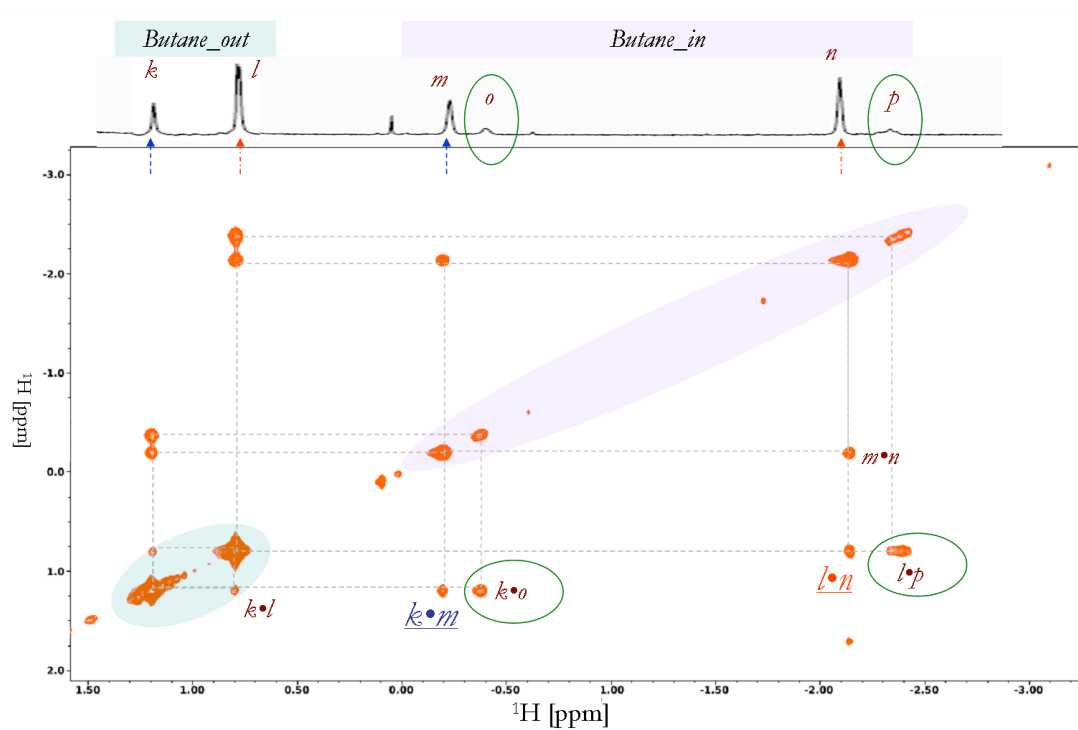


Figure 92. 2D NOESY for cage+butane at 5°C showing the butane region (-2.0-1.5 ppm) with labeled cross-peaks between the butane protons outside and inside the cage.

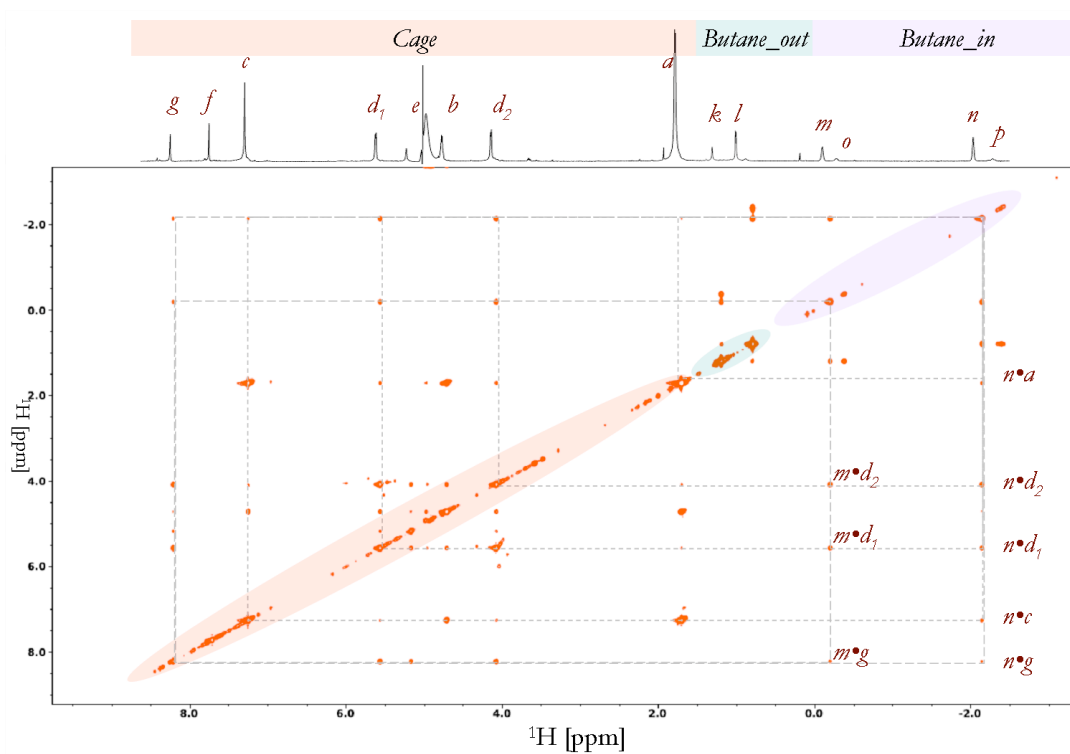


Figure 93. 2D NOESY for the cage+butane sample at 5°C showing the interaction between a cage and butane molecules.

The number of interactions between cage protons and butane peaks verify the butane encapsulation (Figure 93). Both nuclei, *m* and *n*, displayed the interaction with the *g* and *d* protons of cage molecule. Additionally, the methyl group of the bound butane (peak *l*) give the cross signal with nuclei *a* and *c*. These results imply that the butane molecule is aligned along the long north-south axis of a cage and explain the chemical shift of the nuclei from the trapped gas. The methylene groups of the trapped gas (-0.2 ppm) are more in the center of cavity, partially covered from water solution, which result in $\Delta\delta=1.4$ ppm with respect to position of methylene groups from gas without the cage. The methyl groups appear under the cavity aromatic rings which cause larger shielding and almost 3 ppm shift with respect to position of methyl group from butane without the cage. (Figure 94a). The same alignment was previously suggested by Rudkevich *et al.* for encapsulated hydrocarbon inside cage.¹⁷¹ Our simple AM1 calculation shown in Figure 94 b, c, d display that the butane either in *trans* or *cis* conformation may form complex with a cage with low cost of energy. The cage exhibits almost the same conformation regardless is occupied by *cis*- or *trans*- butane aligned either along the long north-south or west-south axis of a cage. The calculated gas-phase energy differences between these complexes are smaller than 2 kcal/mol (Figure 94). The encapsulation of the second butane molecule leads to some distortion in the capsule structure (Figure 94 e) and a 13 kcal/mol increase in energy.

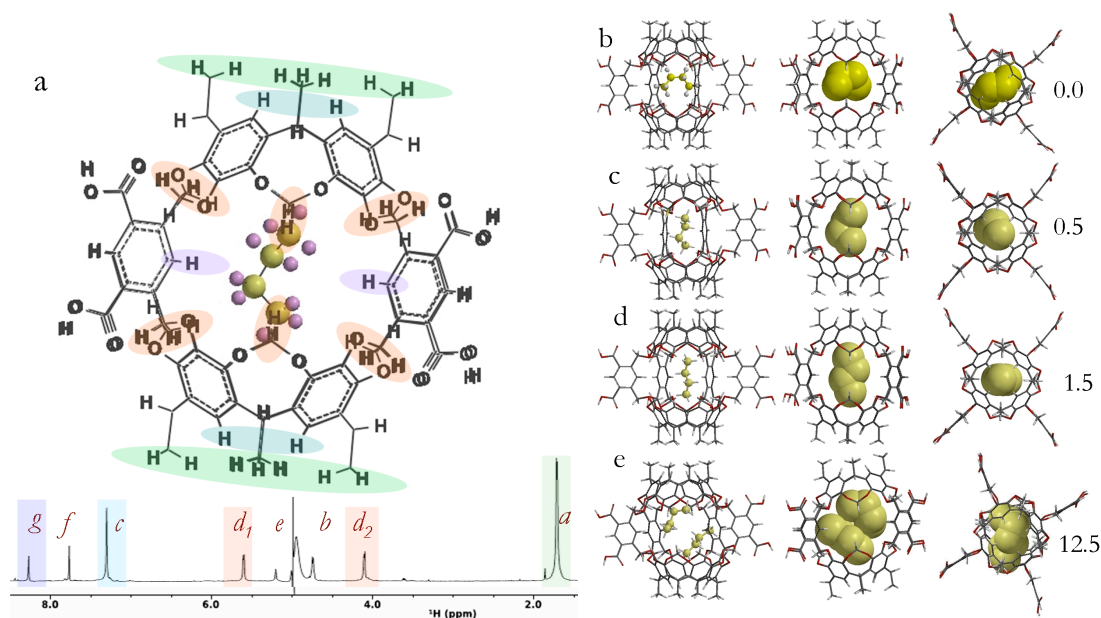


Figure 94. Encapsulated butane inside the cage: a) The hemicarcerand with highlighted cage protons giving the cross-peak with bound butane aligned along the long north-south axis of a cage. Side and upper view of entrapped butane in b) cis-conformation aligned along the south-west axis of a cage, c) cis- and d) trans- conformation aligned along the long north-south axis of a cage; e) two butane molecules trapped inside the cage in their equilibrium geometries (in cis and trans conformation) as well as the corresponding energy difference between the complexes in kcal/mol (AM1 in vacuo).

After the cage-butane complex reached equilibrium, much larger signals for bound butane was seen (Figure 95 c) and some additional peaks appeared in aromatic spectrum of the 1D ¹H NMR (Figure 95 b) even more shifted downfield. This suggests that some fraction of occupied cage changes its conformation, possibly due to the binding of the second butane molecule. This was observed both at 5 and 25°C (Figure 95).

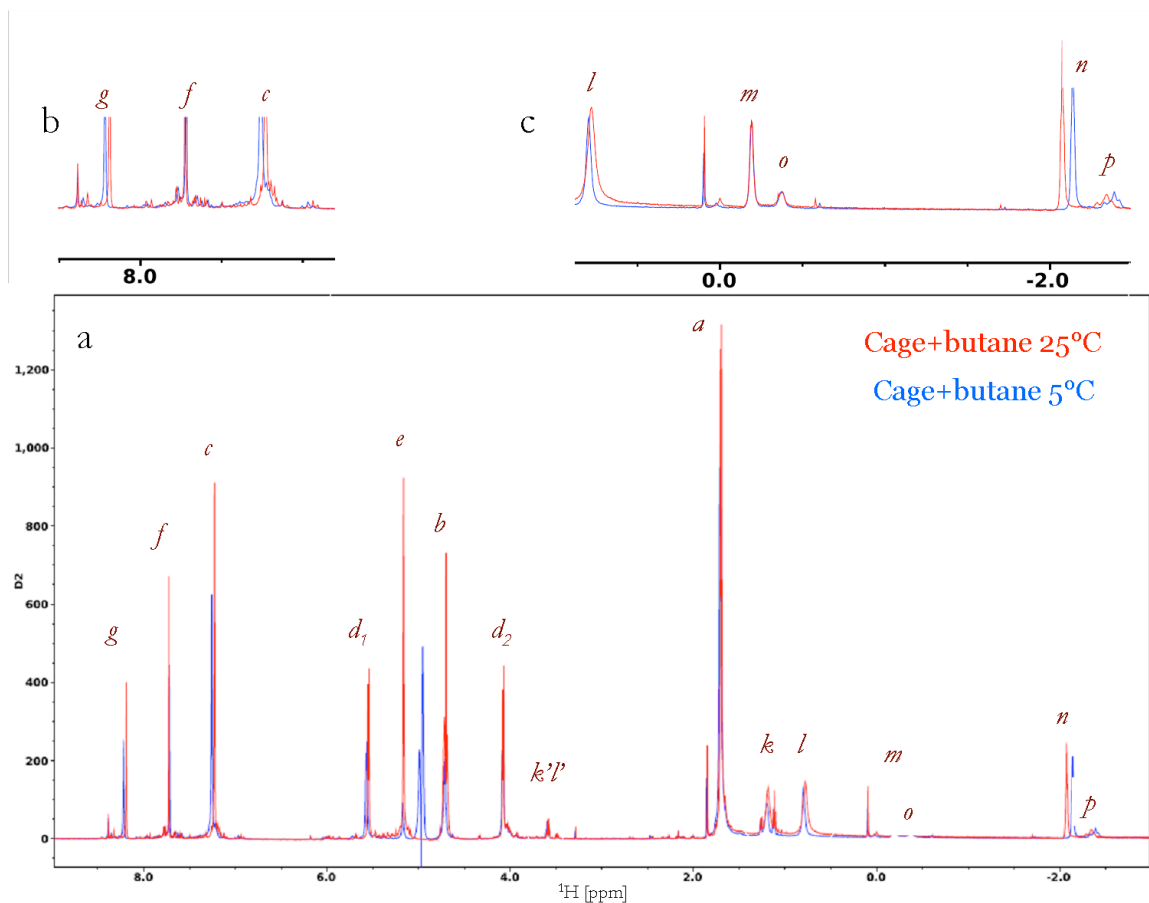


Figure 95. 1D ^1H NMR spectra of the cage and butane at 5°C (blue) and 25°C (red). Free butane signal is highlighted by light blue circles. Arrows shows the increased intensity after the sample reaches equilibrium; orange for the cage protons (b), pink for the bound butane (c).

The longitudinal relaxation times for butane and a cage (Figure 96, Table 14 and 15) at various temperatures were measured. The results show that the T_1 times for the methyl and methylene groups gradually increase for the encapsulated butane molecule as the temperature raise. The longer T_1 means a lesser mobility for the trapped guest inside the cage. Higher T_1 observed in the *o* and *p* peaks (2.44 and 2.45 s respectively) compare to *m* and *n* peaks further verify that some faction of a cage is encapsulated by two butane molecules.

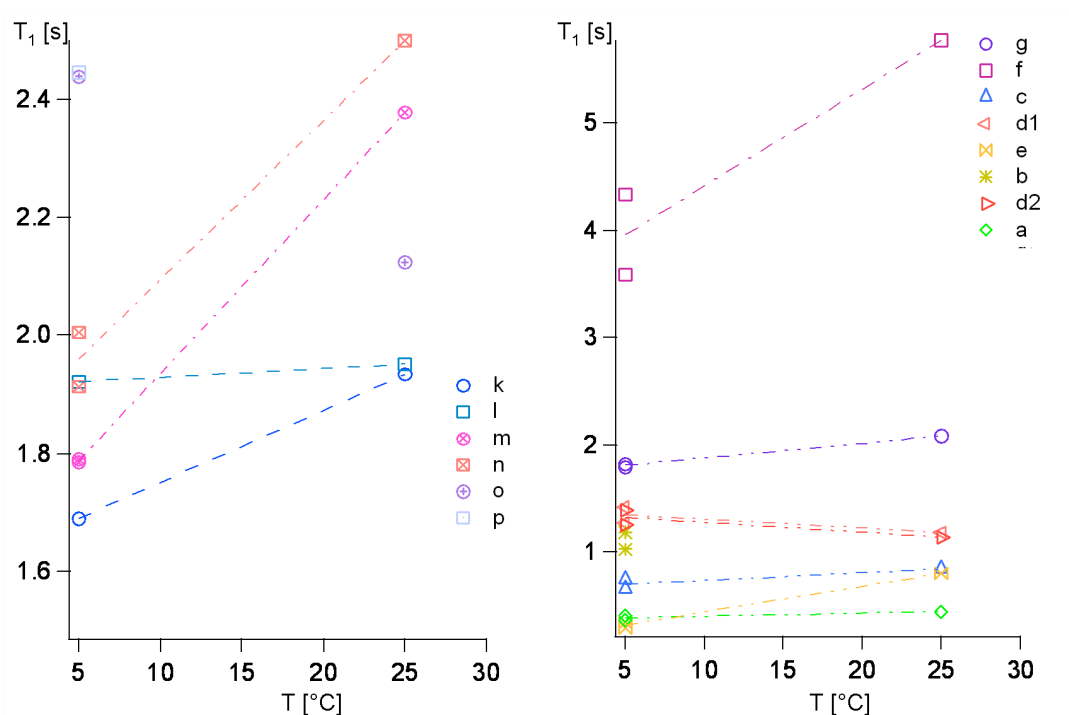


Figure 96. Longitudinal relaxation time for bound and free butane (left) and a cage (right) at 5 and 25°C. The a-h letters correspond to the different nuclei characterized.

Table 14. ^1H longitudinal relaxation time for butane in the presence of cage.

	T_1 [s]				
T [°C]	$\text{CH}_{2_out}(k)$	$\text{CH}_{3_out}(l)$	$\text{CH}_{2_in}(m)$	$\text{CH}_{3_in}(n)$	$\text{CH}_{3_in2}(o;p)$
5	1.69	1.92	1.79	2.01	2.44; 2.45
25	1.93	1.95	2.39	2.5	

Table 15. ^1H longitudinal relaxation time for cage nuclei (a-g) in the presence of butane.

	T_1 [s]							
T [°C]	<i>g</i>	<i>f</i>	<i>c</i>	<i>d₁</i>	<i>e</i>	<i>b</i>	<i>d₂</i>	<i>a</i>
5 ^{jj}	1.81	3.97	0.71	1.35	0.32	1.11	1.33	0.39
25	2.09	5.77	0.84	1.18	0.80	-	1.14	0.45

The comparison of T_1 values for free butane in the sample with and without the cage was not possible because the T_1 obtained for butane in aqueous solution gave inconclusive results. This is partially because chemically equivalent protons are not

^{jj} The average value from two measurements.

magnetically equivalent. Furthermore, the butane spectrum was changing in time and after a few days additional peaks were seen close to original butane peak (k) and ~ 3.5 ppm, ($k'l'$). This was observed both in the sample containing the cage (Figure 95a, light blue circle) and for free butane (Appendix 14, 15). 1D NMR spectra compute on Spartan indicate that additional butane molecules cause spectral changes and appearance of new signals across the spectrum (Appendix 13).

Integration of the NMR signals at 5 and 25°C showed the predominant of 1:1 stoichiometry for the cage-butane inclusion complex (Appendix 16, 17) and imply that over 80% of host molecules are occupied by guest. The additional butane signal (peaks o and p) detected next to m and n nuclei may imply that same small fraction of the guest molecules (less than 15%) exists as an enclosure dimer. The packing coefficient ($PC = V_{\text{guest}}/V_{\text{host}}$) for 1:1 complex is equal to 0.44 which is more close to the occupancy factor for a liquid butane ($PC_{\text{liquid}} = 0.47$) rather than supercritical butane ($PC_{\text{supliq}} = 0.19$).¹⁸⁶ These results are opposite to those obtained by Cribb *et al*, where the butane appeared to behave as a supercritical liquid inside the nano-capsules.¹⁸⁶ The packing coefficient for 2:1 of butane@cage complex is equal to 0.88^{kk, ll}. This is higher than the average 55% value observed for encapsulation of organic guests in solution and would suggest that the butane molecule start to behave as molecules in a solid phase.

^{kk} So high PC value, higher than any other reported in literature, is due to the fact that the packing coefficient for this complex was calculated using the same volume of cage's interior (200\AA^3) as for 1:1 butane:cage complex. Since the cage witch traps two butane expands its volume, the correct PC for 2:1 butane:cage complex should be slightly smaller.

^{ll} The density for butane at 1atm and 0°C is equal 0.6 g/ml; packing coefficient 0.55.

SF₆ trapping

Bubbling SF₆ through a solution of cage in D₂O resulted in the formation of the SF₆-Cage complex, as observed by ¹H NMR. Similarly as in case of butane, the aromatic nuclei as well as proton *d*₂ of the cage displayed a shift (Figure 97), although not so pronounced as previously.

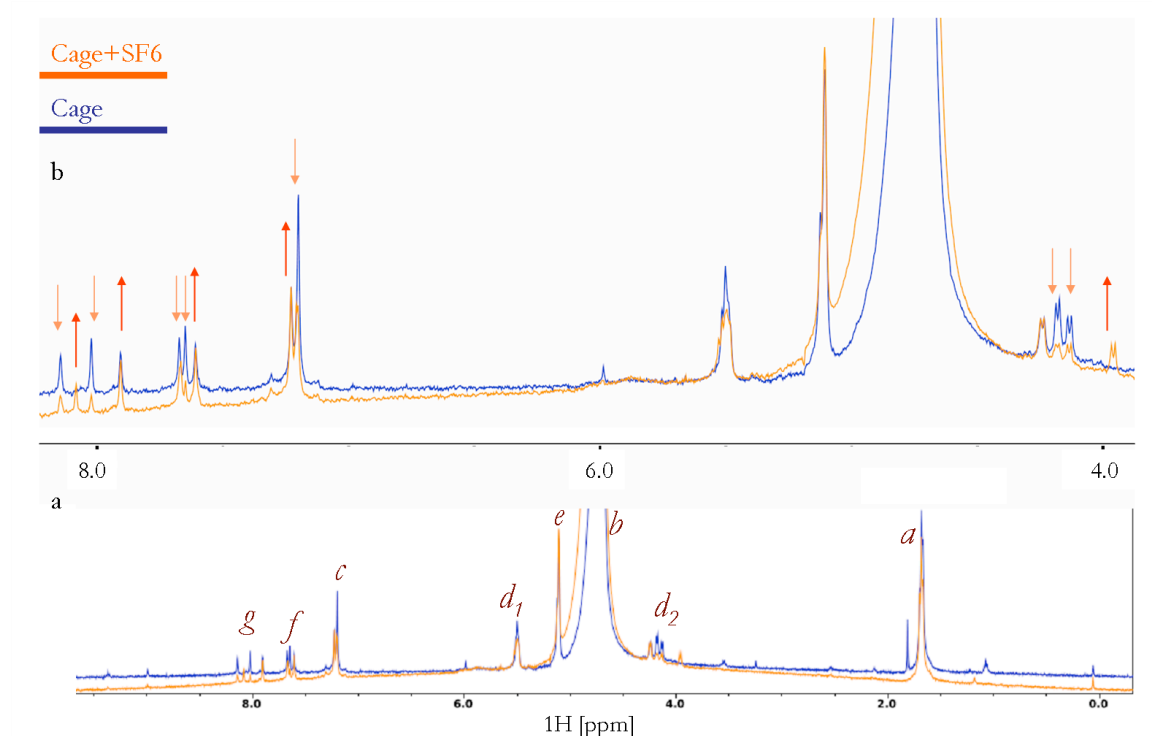


Figure 97. 1D ¹H NMR for a) free cage (blue) and cage after bubbling with SF₆ (orange) with labeled protons (a-g) and b) the 4-8 ppm region showing the spectral changes upon gas encapsulation at 20°C. Note that the nucleus *b* is not invisible because the water peak was not suppressed.

Signals corresponding to the SF₆ were observed in the ¹⁹F NMR spectrum (Figure. 98, Table 16) in the presence and absence of cage. In the absence of the cage only single peak at about 58.2 ppm corresponding to the dissolved gas was observed. Two singlets, one at the same frequency of 58.2 ppm and another shifted 0.2 ppm upfield were

observed in the sample containing the cage confirming the encapsulation. The positions of the fluorine peaks are only slightly affected by temperature changes (Table 16).

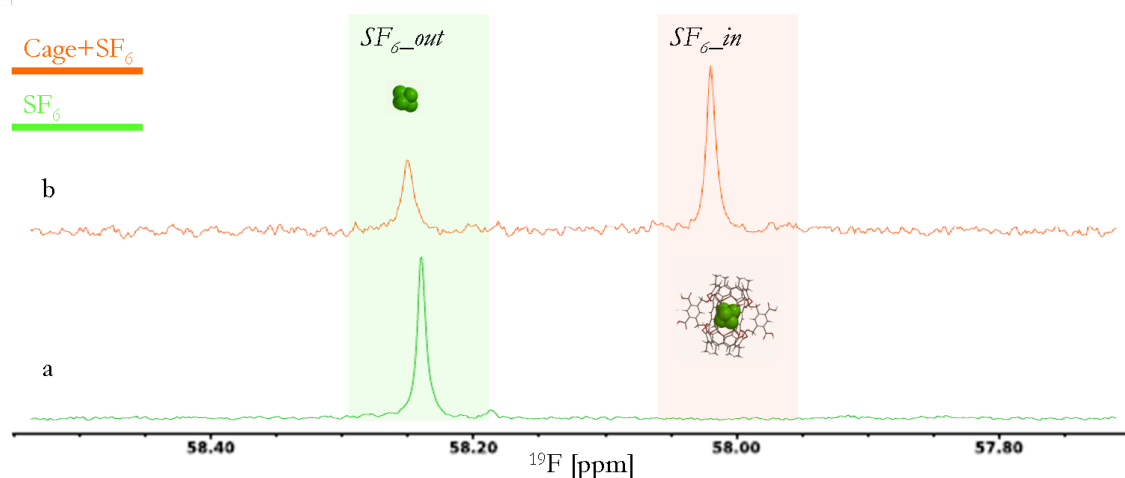


Figure 98. 1D ^{19}F NMR for a) SF_6 in D_2O solution (green); b) SF_6 in the presence of the cage (orange) at 20°C .

Table 16. Chemical shifts δ in the ^{19}F NMR and the ^{19}F longitudinal relaxation times for the SF_6 in the absence and presence of cage.

T [$^\circ\text{C}$]	δ [ppm]				T_1 [s]		
	SF_6		Cage + SF_6		SF_6		Cage + SF_6
	out	out	in	$\Delta \delta_{\text{in-out}}$	out	out	in
5	57.83	57.84	57.58	0.26	1.03 ± 0.07	1.01 ± 0.11	0.56 ± 0.02
20	58.12	58.13	57.90	0.23	0.89 ± 0.02	0.88 ± 0.04	0.54 ± 0.01
30	58.31	58.32	58.11	0.21	0.85 ± 0.05	0.86 ± 0.04	0.57 ± 0.05

The ^{19}F longitudinal relaxation time (T_1) measurements were carried out at 5, 20 and 30°C for saturated SF_6 dissolved in D_2O and in a 2.0×10^{-4} M solution of the cage (Table 16, Figure 99). The longitudinal relaxation times measured for the free SF_6 in the absence and in the presence of cage are almost the same and close to 1s, while for the encapsulated guest the relaxation times are almost two times shorter. Very similar values were obtained by Luhmer *et al.* (0.99 s for the free and 0.46 s for the trapped SF_6 at 25°C

inside the cucurbit[6]uril).¹⁸⁷ The longitudinal relaxation of SF₆ in D₂O solution is dominated by the spin-rotation interaction, which is mediated by molecular collisions, as indicated by shorter values at higher temperature.¹⁸⁸ When confined to cage interior, additional collisions of molecules with the cage walls substantially change T_1 .^{189, 190}

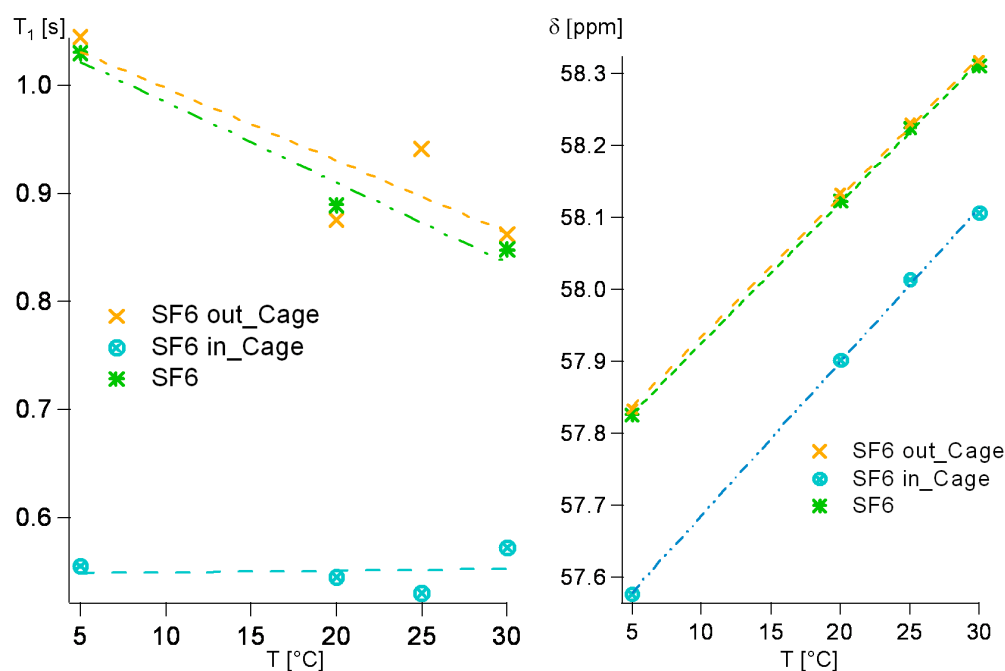


Figure 99. Temperature variation of ¹⁹F longitudinal relaxation time (T_1) (left) and the ¹⁹F chemical shift of SF₆ (right) in the absence (green) and the presence of cage.

The small differences in chemical shifts between free and encapsulated gas implies that the guest is only slightly shielded by the cage and indicates association in the center of cage cavity. This also implies that the cage is occupied by one molecule of SF₆. The packing coefficient for the 1:1 cage:SF₆ complex is equal to 0.37 which is close to the occupancy factor for liquid SF₆ ($PC_{liquid} = 0.40$)^{mm} rather than supercritical SF₆ ($PC_{supliq} = 0.23$)ⁿⁿ.

^{mm} Density of liquid SF₆ at T=25 °C is equal 1.33 g/mL

ⁿⁿ Critical density of SF₆ at T=45.6 C and P=36.6 atm is equal 0.755 g/mL

For the 1:1 stoichiometry of SF₆ encapsulation the equilibrium is written as (27):



where k_i and k_e are the kinetic rate constants for the inclusion and escape of SF₆, respectively. The corresponding equilibrium constant, K_{eq} , is defined by (28):

$$K_{eq} = \frac{[SF_{6in}]}{[SF_{6out}][Cage_0]} = \frac{k_i}{k_e} \quad (28)$$

where $[SF_{6in}]$ is equal to the molar concentration of the inclusion complex. The residence time of SF₆ within the cavity of cage, τ_{in} , and the residence time of SF₆ free in solution, τ_{out} , can be expressed by line widths measured for SF₆ inside ($\Delta\nu_{1/2in}$), outside the cage ($\Delta\nu_{1/2out}$), and in the solvent without the cage ($\Delta\nu_{1/2s}$):

$$\tau_{in} = \frac{1}{k_e} \approx \frac{1}{\pi(\Delta\nu_{1/2in} - \Delta\nu_{1/2D_2O})} \quad (29)$$

$$\tau_{out} = \frac{1}{k_i[Cage_0]} \approx \frac{1}{\pi(\Delta\nu_{1/2out} - \Delta\nu_{1/2D_2O})} \quad (30)$$

Based of these approximations, the residence time of SF₆ inside the cage is $\tau_{in}=1.6$ s, while the equilibrium constant for SF₆ encapsulation into cage yields $K_{eq}=4 \times 10^4 \text{ M}^{-1}$. This value is larger than the value of $K_{eq}=3.1 \times 10^4 \text{ M}^{-1}$ reported by Luhmer *et al.* for encapsulation of SF₆ in cucurbit[6]uril¹⁸⁷ and much higher than for equilibrium constant of SF₆ encapsulation inside α -cyclodextrin, $K_{eq}=28 \text{ M}^{-1}$.¹⁸⁰

The saturation transfer experiment, in which the ¹⁹F peak corresponding to SF₆ inside the cage was saturated for a given length of time-resolves the NOE signal corresponding to ¹⁹F from SF₆ outside the cage (Figure 100). The exchange rate and residence time determined based on these measurements give values of $k_i=0.7 \text{ s}^{-1}$ and τ_{in}

=1.4 s, respectively, and agree very well with the values based on the linewidth analysis (previous page).

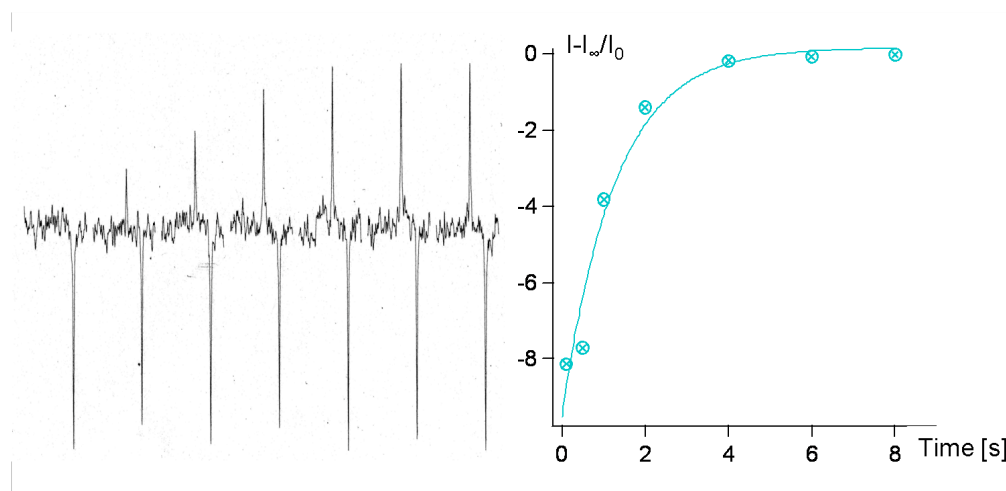


Figure 100. The saturation transfer experiment. Left graph shows 1D ^{19}F cycle-NOE NMR spectrum for the SF_6 inside the cage. NOE peak corresponding to the SF_6 outside the cage is phased positive and the saturated ^{19}F peak corresponding to SF_6 inside the cage is phased negative. Right plot shows the intensity of the unsaturated resonance when the exchanging resonance is saturated for a given length of time.

4.3 Conclusions

We have demonstrated the ability of the water soluble Cram-type hemicarcerand to encapsulate hydrophobic gases such as butane and sulfur hexafluoride. Both gases have a similar volume of about 80 \AA^3 which perfectly fits to 200 \AA^3 cavity of the cage. The NMR results imply that the SF_6 locates itself in the center of the cavity and thus only slightly affect the conformation of the host. On the other hand, butane molecules prefer to align themselves along the long north-south axis forcing the host molecule to undergo larger structural adjustment, reflected by bigger changes in the 1D ^1H NMR spectrum of the cage.

The spin–lattice relaxation times depend significantly on the nature of the gas molecule and the dominant relaxation mechanism. The T_1 for butane was longer for molecules trapped inside the cage than in solution, while for the SF_6 the T_1 decreased upon encapsulation as a result of the dominant spin-rotation interaction contribution to the relaxation mechanism.

The 1:1 host:guest ratio dominates for both gas molecules, however additional signals in the case of butane indicate that encapsulation of two guests is feasible. The encapsulation of a second molecule is possible thanks to structural flexibility of the cage molecule which can adapt to the guest. The calculated packing coefficients for butane and SF_6 in the 1:1 complexes suggest liquid-like behavior. The encapsulation of the second butane molecule forces the guest molecules to accept solid state packing. These observations agree with Cram's conjecture that the cage interior can be viewed to be vacuum-like, liquid-like, or even solid-like, depending on the volume of the guest relative to the size of the void.

In conclusion, this work demonstrates the new possibility of using Cram-type hemicarcerand as gas-capture device for gas purification, storage or sensing. The potential use of hemicarcerand in the biomolecular context was shown in previous chapter, here we increase the range of applications and at the same time present possibility of using solution state ^{19}F NMR of trapped SF_6 inside a cage for biomedical sciences where the trapped gas could be directed to a biomedically relevant protein target to act as biosensor.

4.4 References IV

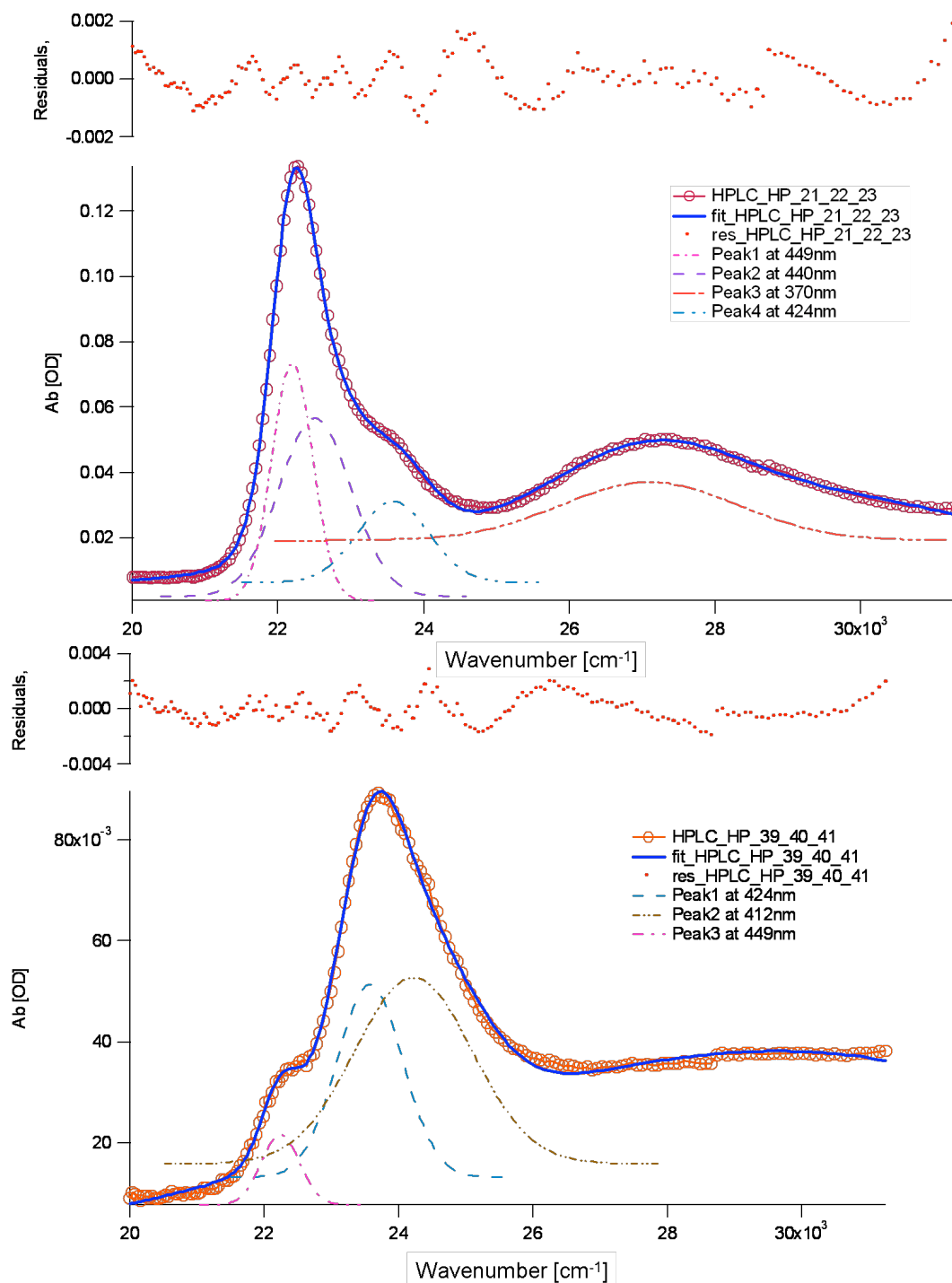
-
- ¹⁵⁸ D. M. Rudkevich and A. V. Leontiev Molecular encapsulation of gases *Aust. J. Chem.* 2004, *57*, 713-722.
- ¹⁵⁹ D. M. Rudkevich Emerging Supramolecular Chemistry of gases. *Angew. Chem. Int. Ed.* 2004, *43*, 558-571.
- ¹⁶⁰ C. Boulart, M. C. Mowlem, D. P. Connelly, J.-P. Dutasta, and C. R. German A novel, low-cost, high performance dissolved methane sensor for aqueous environments *Optics Express*, 2008, *16*, 12607-12617.
- ¹⁶¹ R. E. Morris and P. S. Wheatley Gas storage in nanoporous materials *Angew. Chem. Int. Ed.* 2008, *47*, 4966 – 4981.
- ¹⁶² W. Hölderich, M. Hesse, F. Nümann Zeolites: Catalysts for organic syntheses *Angew. Chem. Int. Ed.* 1988, *27*, 226–246.
- ¹⁶³ D. M. D'Alessandro, B. Smit, and J. R. Long Carbon dioxide capture: Prospects for new materials *Angew. Chem. Int. Ed.* 2010, *49*, 6058 – 6082.
- ¹⁶⁴ S. Zhang and L. Echegoyen Selective anion sensing by a tris-amide CTV derivative: ¹H NMR titration, self-assembled monolayers, and impedance spectroscopy *J. Am. Chem. Soc.*, 2005, *127*, 2006–2011.
- ¹⁶⁵ B. Chen, L. Wang, F. Zapata, G. Qian and E. B. Lobkovsky A luminescent microporous metal–organic framework for the recognition and sensing of anions *J. Am. Chem. Soc.*, 2008, *130*, 6718–6719.
- ¹⁶⁶ B-P Jiang, D-S Guo, and Y. Liu Self-assembly of amphiphilic perylene–cyclodextrin conjugate and vapor sensing for organic amines *J. Org. Chem.*, 2010, *75*, 7258–7264.
- ¹⁶⁷ P. J. Prado, B. J. Balcom, I. V. Mastikhin, A. R. Cross, R. L. Armstrong, and A. Logan Magnetic resonance imaging of gases: A single-point ramped imaging with T1 enhancement (SPRITE) study *Journal of Magnetic Resonance* 1999, *137*, 324–332.
- ¹⁶⁸ J.-H. Yoon, M.-W. Huh Encapsulation of simple gases in zeolites *J. Phys. Chem.*, 1994, *98*, 3202–3206.
- ¹⁶⁹ P. A. Hill, Q. Wei, T. Troxler and I. J. Dmochowski Substituent effects on xenon binding affinity and solution behavior of water-soluble cryptophanes *J. Am. Chem. Soc.*, 2009, *131*, 3069–3077.

-
- ¹⁷⁰ Y. Finkelstein, A. Saig, A. Danon, and J. E. Koresh Encapsulation of He and Ne in carbon molecular sieves *Langmuir* 2003, 19, 218-219.
- ¹⁷¹ A. V. Leontiev and D. M. Rudkevich Encapsulation of gases in the solid state *Chem. Comm.*, 2004, 13, 1468-1469.
- ¹⁷² M. A. Albiter, R. M. Crooks, and F. Zaera Adsorption of carbon monoxide on dendrimer-encapsulated platinum nanoparticles: Liquid versus gas phase *J. Phys. Chem. Lett.* 2010, 1, 38–40.
- ¹⁷³ A. V. Leontiev, A. W. Saleh, and D. M. Rudkevich Hydrophobic encapsulation of hydrocarbon gases *Org. Lett.*, 2007, 9, 1753–1755.
- ¹⁷⁴ T. D.W. Claridge High-Resolution NMR Techniques in Organic Chemistry 2nd Edition, *Elsevier Ltd.* 2009.
- ¹⁷⁵ D. J. Cram, J. M. Cram Container molecules and their guests *Royal Society of Chemistry*, 1997, 203-205.
- ¹⁷⁶ J. C. Sherman, C. B. Knobler, and D. J. Cram Syntheses and properties of soluble carceplexes^{1,2} *J. Am. Chem. Soc.* 1991, 113, 2194-2204.
- ¹⁷⁷ D. Keidel, M. Bonaccio, N. Ghaderi, D. Nicks, D. Borchardt, and M. F. Dunn {¹⁹F} NOE NMR structural signatures of the insulin R6 hexamer: Evidence of a capped HisB10 site in aryl- and arylacryloyl-carboxylate complexes *ChemBioChem* 2009, 10, 450 – 453.
- ¹⁷⁸ L. Fusaro, E. Locci, A. Lai, and M. Luhmer Highlighting cavities in proteins by NMR using sulfur hexafluoride as a spy molecule *J. Phys. Chem. B* 2010, 114, 3398–3403.
- ¹⁷⁹ N. L. A. and D. O. Kuethe Quantitative mapping of ventilation-perfusion ratios in lungs by ¹⁹F MR imaging of *T₁* of inert fluorinated gases *Magnetic Resonance in Medicine* 2008, 59, 739–746.
- ¹⁸⁰ L. Fusaro, E. Locci, A. Lai, and M. Luhmer Probing systems in solution by NMR using sulfur hexafluoride as a spy molecule *J. Phys. Chem. B*, 2009, 113, 7599–7605.
- ¹⁸¹ I. A. Riddell, M. M. J. Smulders, J. K. Clegg and J. R. Nitschke Encapsulation, storage and controlled release of sulfur hexafluoride from a metal–organic capsule *Chem. Commun.*, 2011, 47, 457–459.
- ¹⁸² J. C. Sherman, C. B. Knobler, D. J. Cram Host-guest complexation. 56. Syntheses and properties of soluble carceplexes *J. Am. Chem. Soc.* 1991, 113, 2194–2204

-
- ¹⁸³ V. I. Bakhmutov Practical NMR relaxation for chemists *John Wiley & Sons*. 1st Edition, 2005, 7-28.
- ¹⁸⁴ F. Delaglio, S. Grzesiek, G. W. Vuister, G. Zhu and J. Pfeifer, et al. NMRPipe: A multidimensional spectral processing system based on UNIX pipes *J. Biomol. NMR* 1995, 6, 277-293.
- ¹⁸⁵ B. A. Johnson and R. A. Blevins NMR View: A computer program for the visualization and analysis of NMR data *J. Biomol. NMR* 1994, 4, 603–614.
- ¹⁸⁶ C. L.D. Gribb and B. C. Gribb Templated assembly of water soluble nano-capsules: Inter-phase sequestration, storage, and separation of hydrocarbon gases *J. Am. Chem. Soc.* 2006, 128, 16498-16499.
- ¹⁸⁷ L. Fusaro, E. Locci, A. Lai, and M. Luhmer NMR study of the reversible trapping of SF₆ by cucurbit[6]uril in aqueous solution *J. Phys. Chem. B* 2008, 112, 15014–15020.
- ¹⁸⁸ J. DeZwaan and J. Jonas Density and temperature effects on motional dynamics of SF₆ in the supercritical dense fluid region *J. Chem. Phys.* 1975, 63, 4606-4612.
- ¹⁸⁹ D. O. Kuethe, R. Montaña, T. Pietrass Measuring nanopore size from the spin–lattice relaxation of CF₄ gas *Journal of Magnetic Resonance* 2007, 186, 243–251.
- ¹⁹⁰ V. I. Bakhmutov Solid-state NMR in materials science: Principles and applications *Taylor & Francis, Inc.* 2012, 170-175.

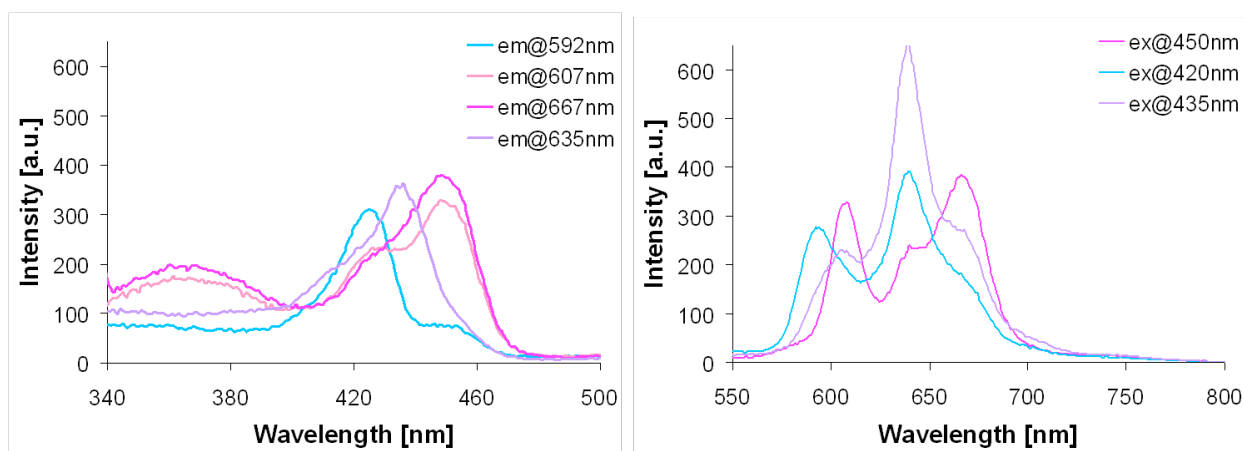
5. Supporting Information

Supporting information for chapter 2



Appendix 1. Gaussian line shape analysis of the contributions of conformers F420 and F450 to the overall spectra of the HPLC fractions of ZnP450 rich in F450 (top) and F420 (bottom).

Fitting gaussian functions to the UV-Vis spectra reveals in detail the spectral contribution of the conformers to the overall spectra of fractions rich in F420 and F450, respectively (Appendix 1). It was found that gaussian functions reproduce the experimental line shapes significantly better than lorentzians. The peaks at 449 and 370 nm belong to form F450 and the peak at 424 nm to form F420. The features at 440 and 635 nm appear when the sample was exposed to oxygen. This phenomenon was previously described by Morishima *et al.* The presence of oxygen disturbs the fluorescence spectrum of the protein as well and leads to increased intensity at 640 nm (Appendix 2). As described in the main text, all samples used in the electron transfer measurements were thoroughly degassed.



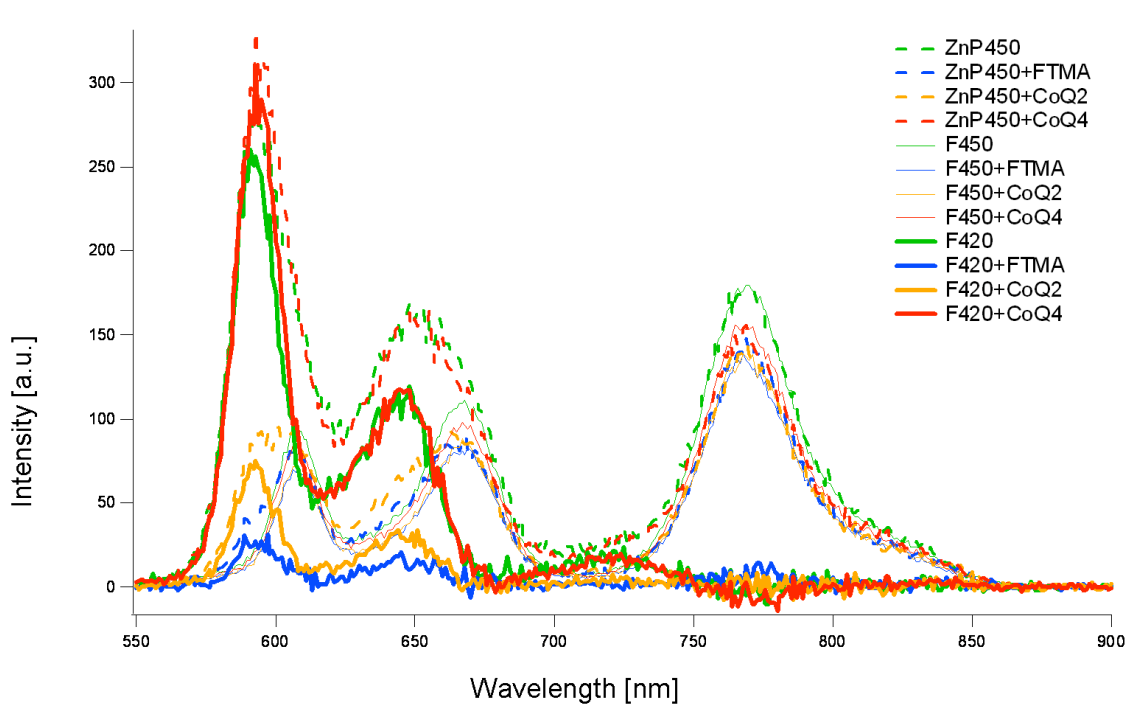
Appendix 2. Fluorescence excitation and emission spectra of ZnP450 collected under aerobic conditions.

Appendix 3. The thermodynamic parameters for both forms of ZnP450 complexed with the quenchers.

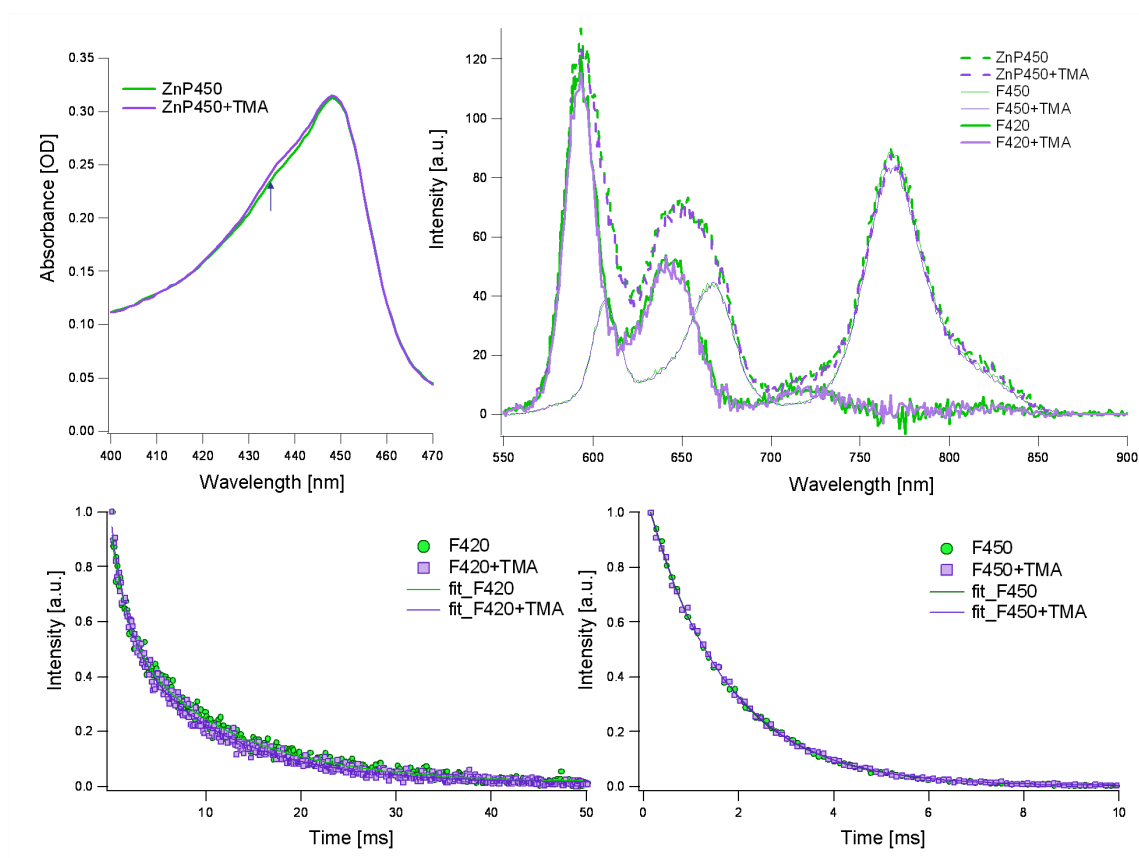
	E^0 [V]	ΔG^0 for F450 [eV]	ΔG^0 for F420 [eV]
FTMA	E_{ox} [V] = 0.64 ^{oo}	0.33	0.23
Q2	E_{red} [V] = 0.3 ^{pp}	-0.51	-0.62
Q4	E_{red} [V] = 0.3 ^b	-0.51	-0.62

^{oo} T. Komura, T. Yamaguchi, K. Noda, S. Hayashi, *Electrochimica Acta* 2002, 47, 3315-3325

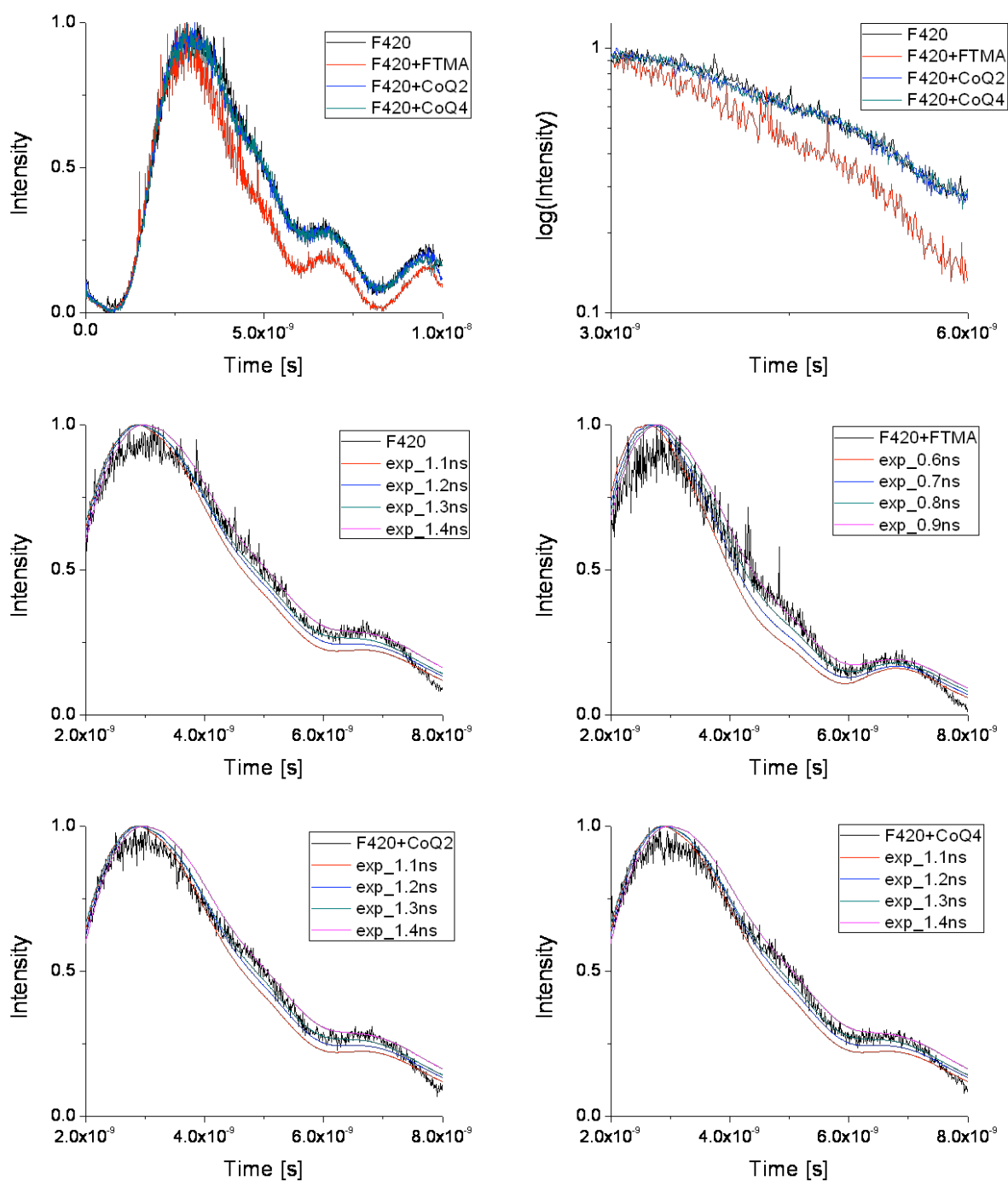
^{pp} G. J. Gordillot, and D. J. Schiffrin, *J. Chem. Soc. Faraday Trans.* 1994, 90, 1913-1922.



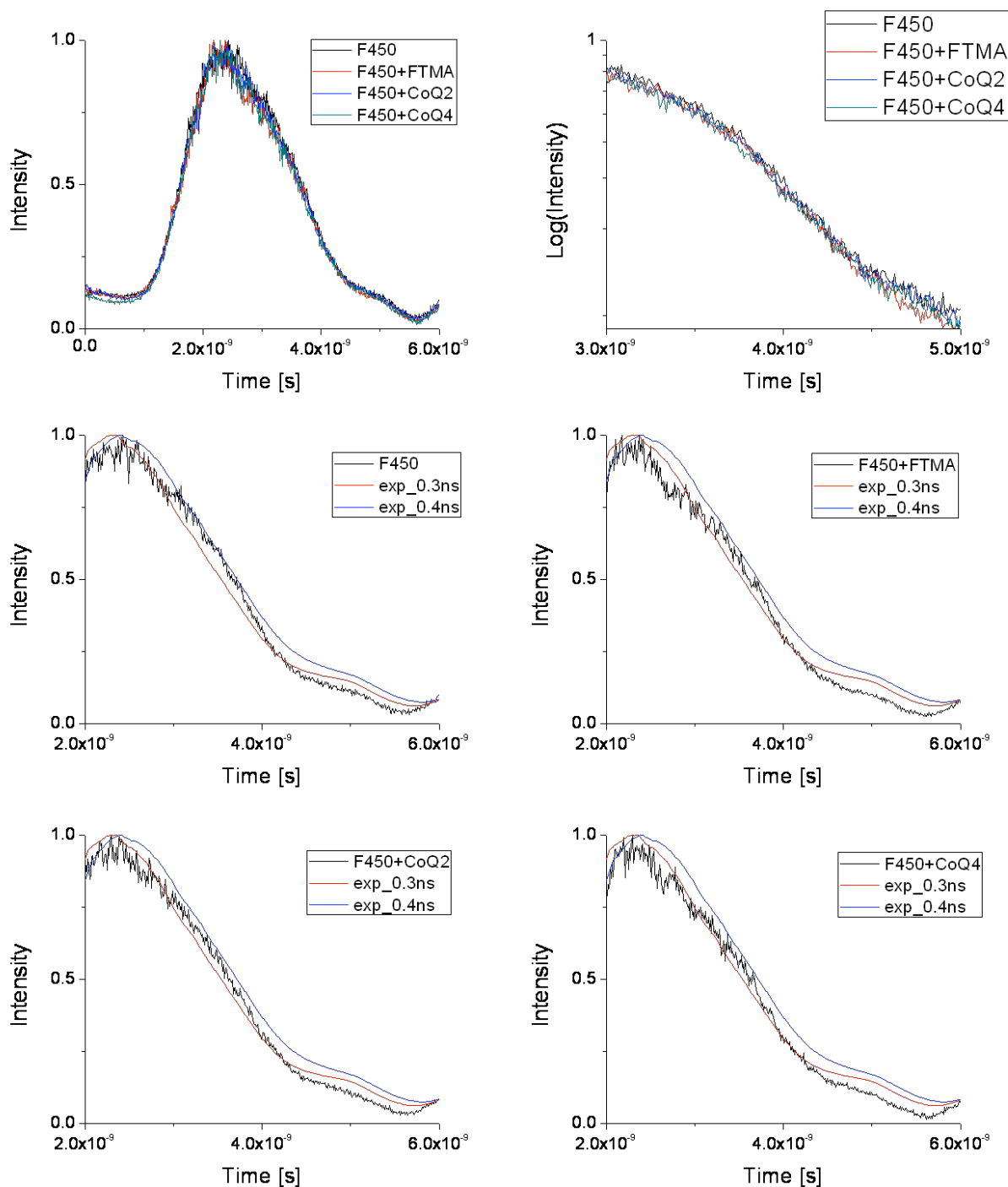
Appendix 4. Phosphorescence spectra of ZnP450 (2×10^{-6} M) in the presence of FTMA, CoQ2 and CoQ4 (5×10^{-5} M). The protein spectrum excited at 420 nm which possess emission maxima characteristic for a F420 (at 590 and 640 nm) and F450 form at 768 nm (dotted line, ZnP450+quencher). Form F450 when excited at 450 nm, with maximum at 768nm normalized to the spectrum of ZnP450 excited at 420 nm (light line, F450 + quencher) and the F420 form obtained by deconvolution of F450 from the spectrum of ZnP450 when excited at 420 nm with phosphorescence maximum at 723 nm.



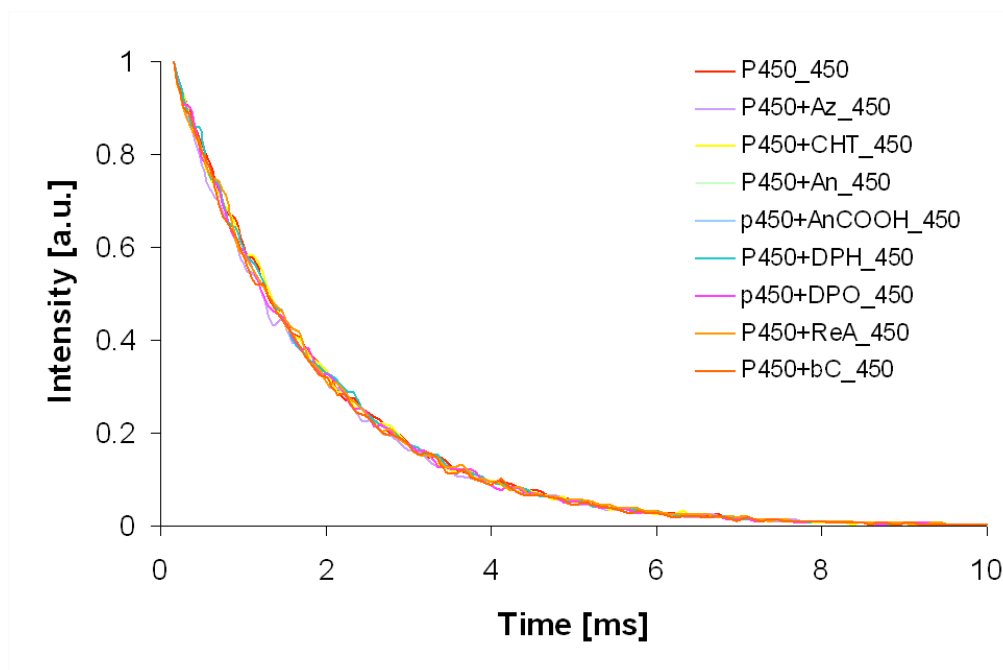
Appendix 5. Spectral features of ZnP450 (2×10^{-6}) in the presence of TMA (5×10^{-5} M); (A) Protein absorption spectrum (B) The protein phosphorescence excited at 420 nm which possess emission maxima characteristic for a F420 (at 590 and 640 nm) and F450 form at 768 nm (dotted line, ZnP450+quencher). Form F450 when excited at 450 nm, with maximum at 768 nm normalized to the spectrum of ZnP450 excited at 420 nm (light line, named F450 + quencher) and the F420 form obtained by deconvolution of F450 from the spectrum of ZnP450 when excited at 420 nm with phosphorescence maximum at 723 nm. Normalized emission decay profiles of ZnP450 in the presence of TMA when excited at 420 nm and emission monitored at 590 nm (C) and when excited at 450 nm and emission monitored at 768 nm (D) at pH=7.4.



Appendix 6. Normalized fluorescence decays of $^1\text{ZnP450}$ (F420) (40 mM KPi, 0.1M camphor, pH=7.4) in the presence of FTMA, CoQ2 and CoQ4 (5×10^{-5} M) at pH=7.4, excited at 420 nm with 590 ± 10 nm band pass filter, fitted to the single exponential functions to convoluted reference sample.



Appendix 7. Normalized fluorescence decays of ¹ZnP450 (F450) (40 mM KPi, 0.1M camphor, pH=7.4) in the presence of FTMA, CoQ2 and CoQ4 (5×10^{-5} M) at pH=7.4, excited at 450 nm with 670±10 nm band pass filter, fitted to the single exponential functions to convoluted reference sample.



Appendix 8. Normalized emission decay profiles of 2×10^{-6} ZnP450 in the presence of energy transfer quenchers (saturated solutions except of AnCOOH (20 μ M), ReA (70 μ M) and bC (70 μ M)) excited at 450 nm and emission monitored at 768 nm pH=7.4.

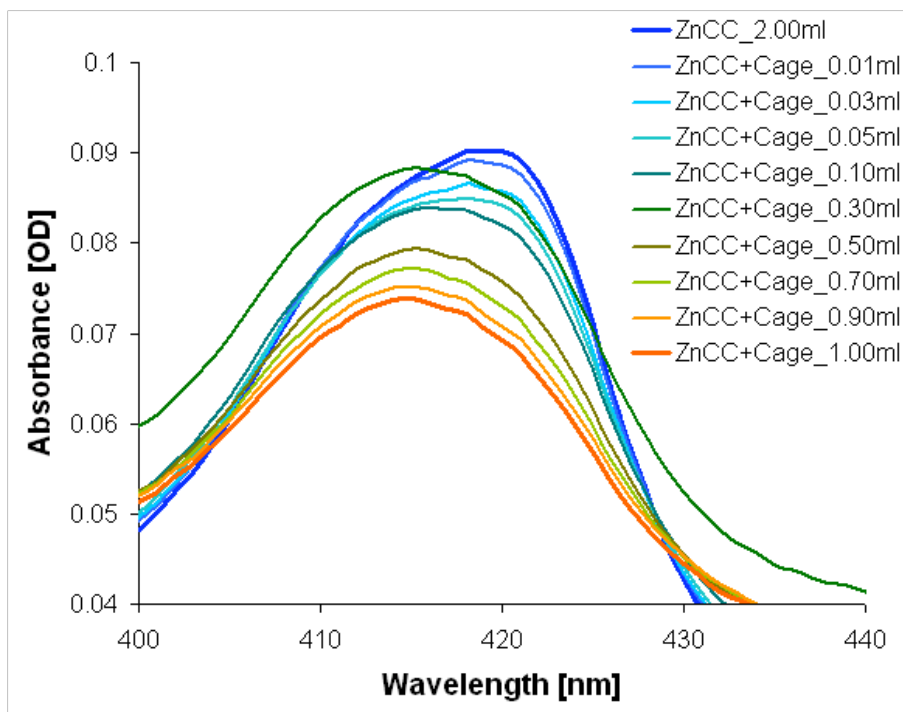
Appendix 9. Thermodynamic parameters for F420 complexed with the triplet energy acceptors and computational values of internal reorganization energies λ_i for redox partners.

	E^0 [V] ^{qq,rr}	ΔG^0 for F420 [eV]	λ_i [eV]
ZnPP	$E_{ox} = 0.80$ $E_{red} = -1.30$		0.366
Az	$E_{ox} = 0.95$ $E_{red} = -1.41$	0.53 0.49	0.397
CHT	$E_{red} = -2.90$	1.68	0.850
An	$E_{ox} = 1.09$ $E_{red} = -1.95$	0.67 1.08	0.824
AnCOOH	$E_{ox} = 0.95$ $E_{red} = -1.75$	0.53 0.83	0.437
DPH	$E_{red} = -1.72$	0.80	0.827
DPO	$E_{red} = -1.62$	0.70	0.910
ReA	$E_{red} = -1.41$	0.50	1.043
bC	$E_{red} = -1.63$	0.71	1.251

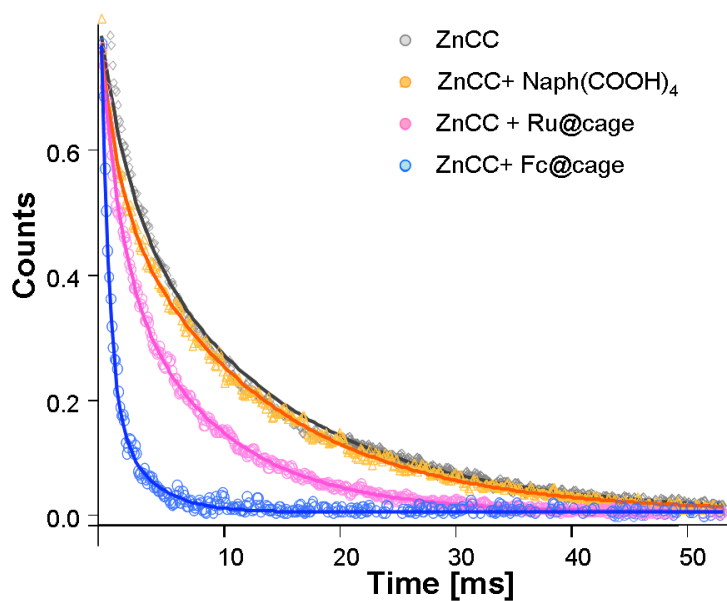
^{qq} Murov, S. L.; Carmichael, I.; and Hug, G. L.; *Handbook of Photochemistry*, 2nd Ed., Dekker, New York, USA 1993

^{rr} Shen, C.; Kostić, N. M. *Inorg. Chem.* **1996**, 35, 2780-2784.

Supporting information for chapter 3

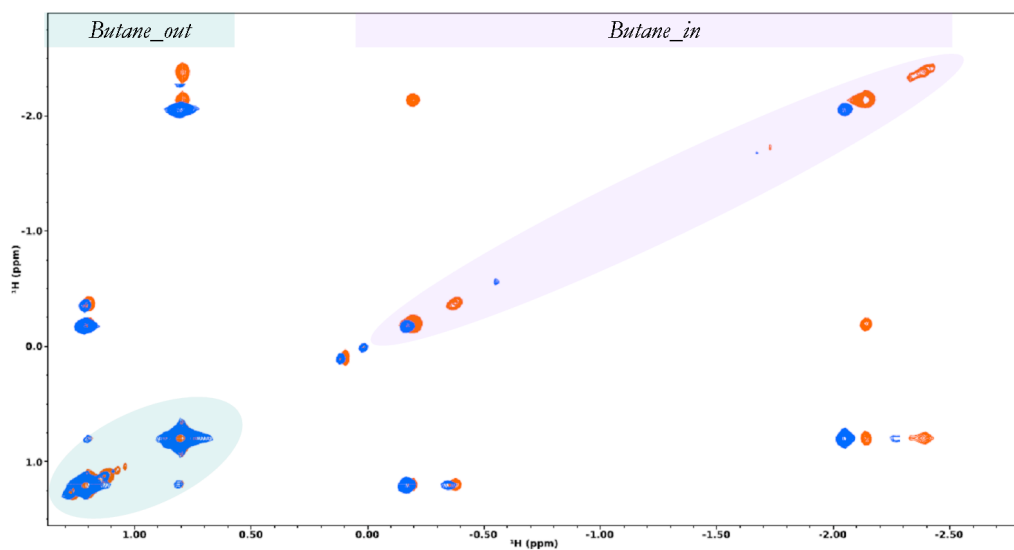


Appendix 10. Titration of Zn-cytochrome *c* (1×10^{-6} M) with the empty cage (2×10^{-4} M) at pH = 9 monitored by UV-Vis spectroscopy.



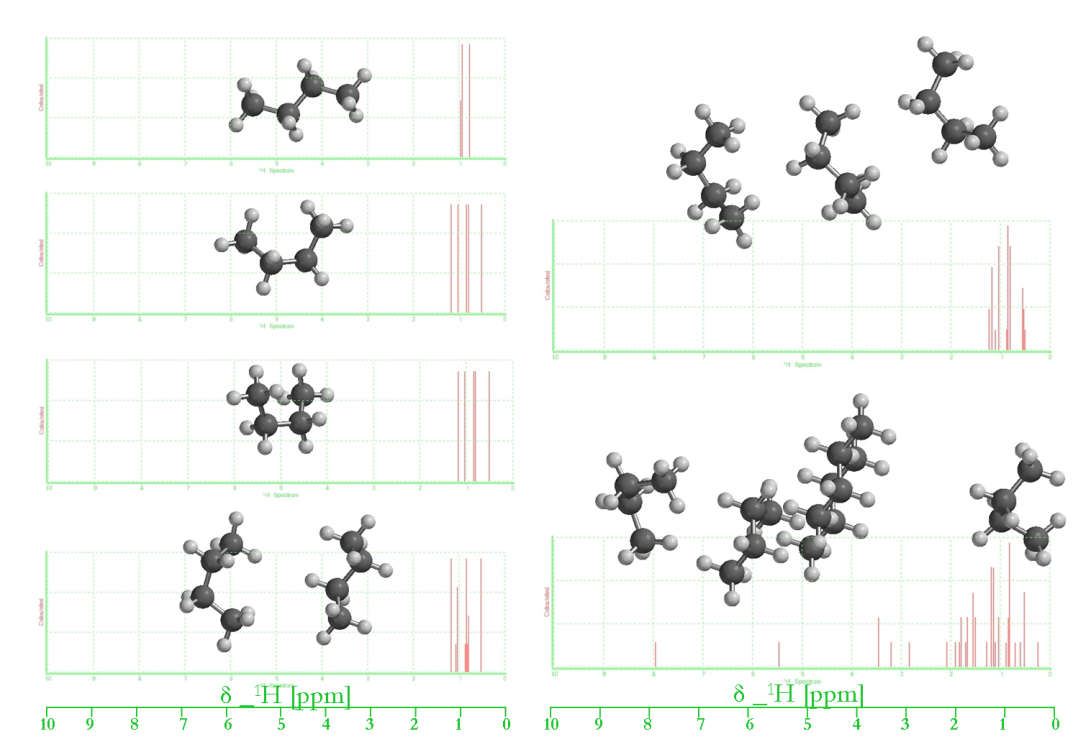
Appendix 11. ET quenching of Zn-cytochrome *c* (1×10^{-6} M) phosphorescence by tetracarboxynaphthalene (1×10^{-4} M), encapsulated ruthenocene (1×10^{-4} M) and ferrocene (1×10^{-4} M) at pH = 7, T = 25 °C.

Supporting information for chapter 4

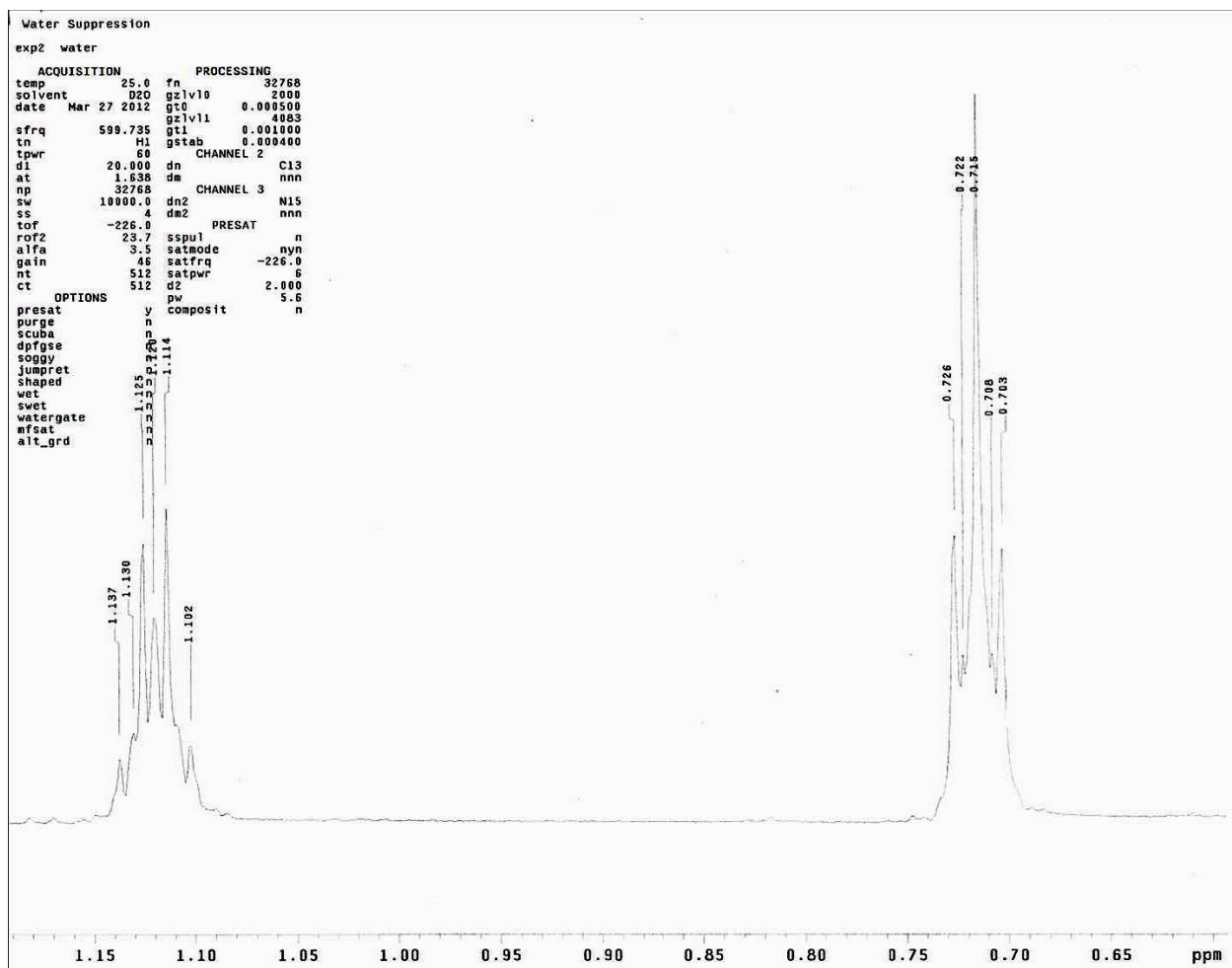


Cage_butane 25C Cage_butane 5C

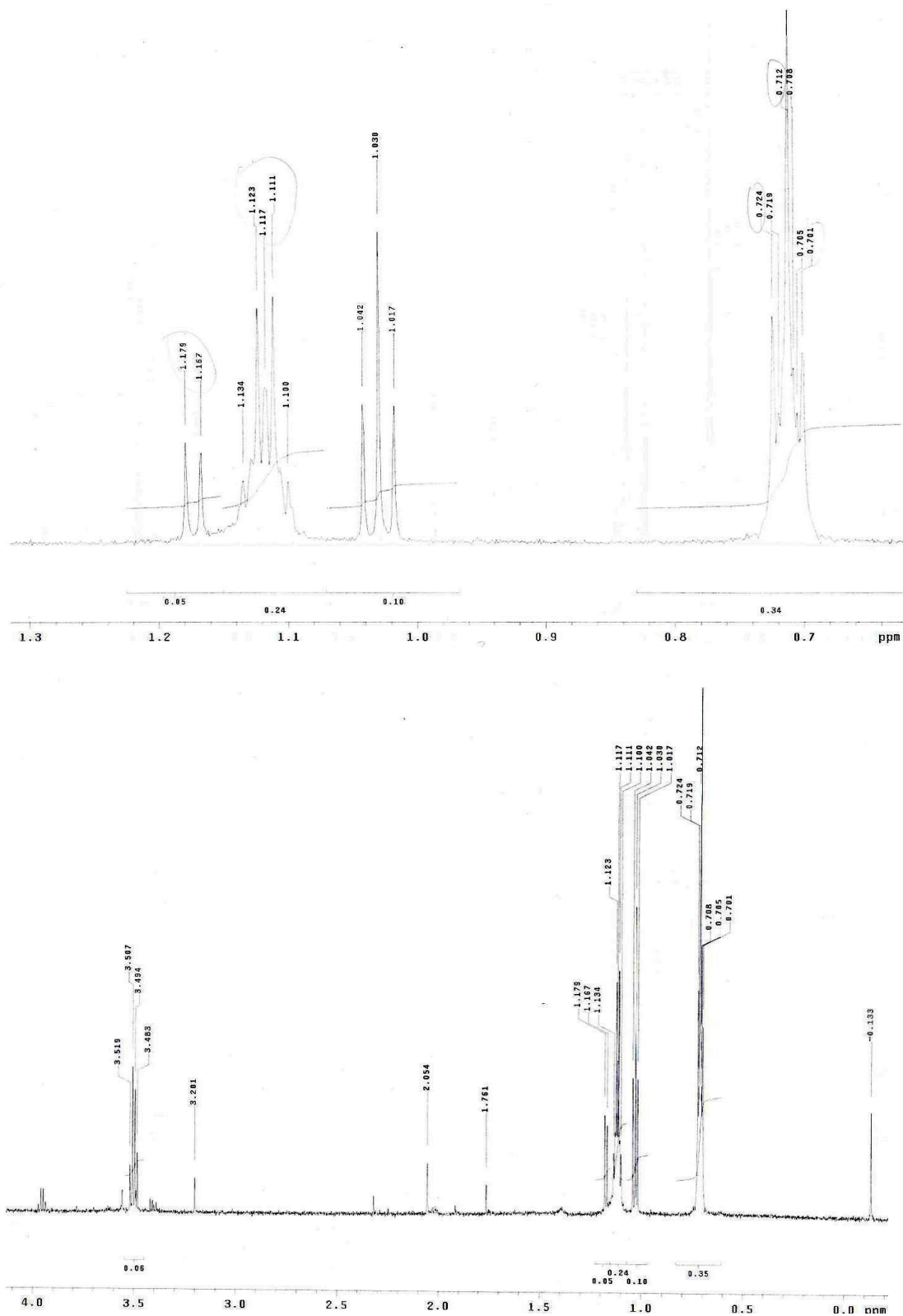
Appendix 12. 2D NOESY for cage+butane sample at 5°C and 25°C, showing the butane region.



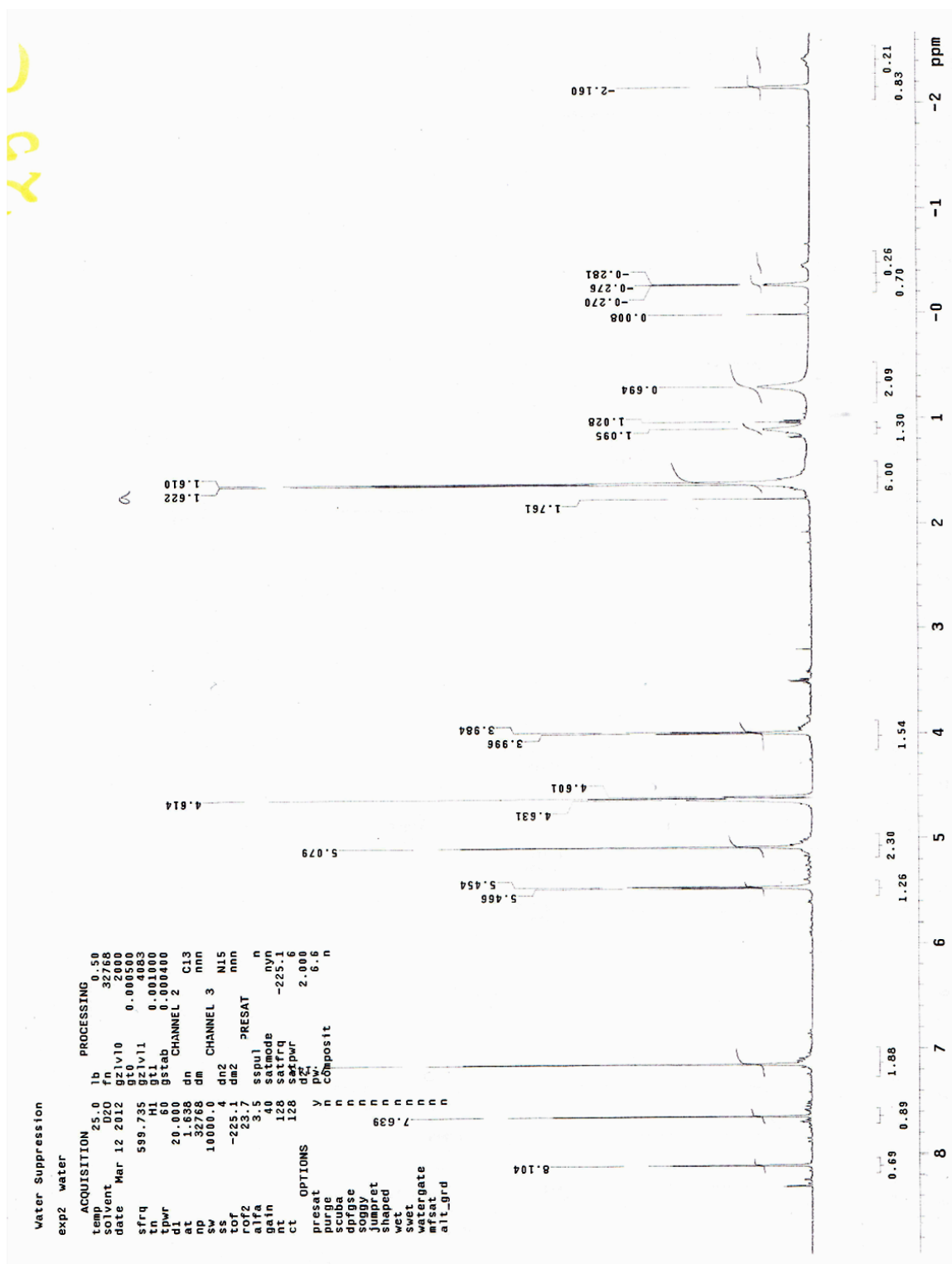
Appendix 13. NMR spectra comput at the Hartree-Fock level, 3-21G basis set using the Spartan 06 software packing by Wavefunction, Inc.



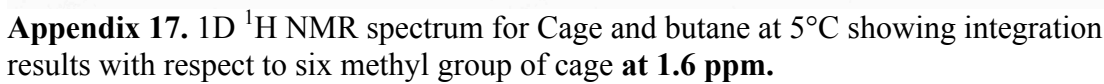
Appendix 14. 1D ^1H NMR for butane in D_2O at 25°C two days after gas bubbling.



Appendix 15. 1D ^1H NMR for butane in D_2O at 25°C week after gas bubbling. (upper spectrum shows the 0.5-1.4 ppm range, lower spectrum shows the -0.5-4.5ppm range)



Appendix 16.1D ^1H NMR spectrum for Cage and butane at 25°C showing integration results with respect to six methyl group of cage at 1.6 ppm.



Curriculum Vitae

Katarzyna I. Jankowska (Paruch)

Date of Birth: April 15, 1980

Place of Birth: Stalowa Wola, Poland

Education

Doctor of Philosophy, Chemistry

2006-2012

Rutgers University, Newark, NJ

Department of Chemistry

Advisor: **Prof. Piotr Piotrowiak,****Master of Science, Biotechnology**

1999-2005

Warsaw University of Technology, Warsaw, Poland

Faculty of Chemical and Process Engineering

Advisor: **Prof. Krzysztof W. Szewczyk,**Supervisor: **Andrzej Piasek, PhD**Research Experience

2003-2005**Research Staff, Laboratory of Virology**

National Institute of Public Health, Warsaw, Poland

Advisor: Andrzej Piasek, PhD

Publications

K. I. Jankowska and P. Piotrowiak, *Triplet - Triplet Energy Transfer Reactions of Zinc Substituted Cytochrome P450cam*, in preparation.K. I. Jankowska, C. V. Pagba, and P. Piotrowiak, *Zinc substituted cytochrome P450cam: characterization of protein conformers F420 and F450 by photoinduced electron transfer*, *Biochemistry*, 2012, 51, 1431–1438K. I. Jankowska, C. V. Pagba, E. L. Piatnitski Chekler, K. Deshayes and P. Piotrowiak *Electrostatic Docking of a Supramolecular Host-Guest Assembly to Cytochrome c Probed by Bidirectional Photoinduced Electron Transfer*, *J. Am. Chem. Soc.* 2010, 132, 16423–16431M. Bretner, A. Najda, R. Podwińska, A. Baier, K. Paruch, A. Lipniacki, A. Piasek, P. Borowski, T. Kulikowski, *Inhibitors of the NTPase/helicases of hepatitis C and related Flaviviridae viruses*, *Acta Pol Pharm.* 2004, 61, 26-28.